Investigating the role of microglia risk genes in Alzheimer's disease

Marieta Vassileva

Thesis presentation for the degree of Doctor of Philosophy

(Medicine)

2023

Acknowledgements

First and foremost, I would like to offer my biggest gratitude to my supervisor Prof Philip Taylor, for giving me the opportunity to be a part of his team, for continually letting me pursue my scientific interests and for pushing me to be a better scientist. I will always be thankful for your feedback, advice, and unsolicited support in and outside the lab. Doing this project over a pandemic was challenging for everyone involved but I always knew I can rely on your support irrespective of the circumstances.

My most genuine thank you goes to my family and especially my parents, who raising me always encouraged me to follow my interests and supported me moving to the other side of Europe to pursue my dreams. Thank you for being so understanding and for all the sacrifices you have made along the way in my interest. To my brother, Dimitar for being an amazing friend and one of my biggest supporters through my whole life.

I would like to acknowledge my 3 closest friends, Sofi, Yana and Kari who I don't see nearly as much as I would like, but who I know are always there to support me when I need them. To my Cardiff squad, Rebekah, Alex and Carys, who have encouraged me since our days in undergrad providing unlimited wine supply in moments of crisis. I also want to thank my many other friends scattered all around the world that I can't possibly name here but your support and encouragement over the last 4 years meant more than you can imagine.

I would like to extend my gratitude to the wider Taylor group and every member that worked there during my PhD project. There is however, one member who requires more recognition than anyone else. Ruth without your help half of this project would have not existed or even been possible. Thank you for the continued belief and encouragement, for understanding and for showing me what a great scientist and friend truly is. Elena who I know I can always share my most honest thoughts with and she will be there to understand and provide some great Italian food. To Mark for knowing 'everything', kindly sharing it with me and for saving me numerous times when I was too scared to touch the mice.

I am so grateful to have conducted my PhD research in one of the friendliest places, so thank you to every Cardiff DRI member who has helped me in the lab and worked alongside me over this time. There are 3 people who deserve the highest praise, my tea break club, Laura, Katy, and Dina. I would have not mentally survived without all of you and our weekly

tea drinking breaks. Words are not enough to express how amazing you all are, and I am happy to say I will leave this PhD with some friends for life. To Antoine for being such an amazing friend and even though you never moved desk to the second floor I always knew you are not far away if I needed your help and support. Thank you for the memories and the experiences which I will always cherish. Thank you to the extended Dion group who always adopted me for their social activities. Thank you to the amazing IPMAR team and Roman, who made failing experiments bearable and who were always there to cheer me up. Finally, a special gratitude to Andrew for being the best lab manager. Your dedication and care mean more than you know.

Last but not least, my most heartfelt and sincere thank you goes to my partner James. For tolerating me over the last 4 years, for picking me up late at night from the lab and driving me back early in the morning without complaining, for making dinner when I couldn't and making sure I was always looking after myself. You have been the definition of what a partner is, and I will always be grateful for all your sacrifices during this time.

Contributions

Dr Mark Gurney helped with generation of the PLCG2 MOP cell lines (Chapter 3). Dr Magdalena Czubala generated the retrovirus used for the generation of the MOP cell lines (Chapter 3).

Dr Ruth Jones contributed to initial validation experiments and ScRNA-sequencing by designing, processing and analysing experiments (Chapter 5). All analysis of ScRNA-sequencing data is based on scripts developed by Dr Ruth Jones (Chapter 5 and 6).

ScRNA-sequencing analysis was performed by Dr Mateus Bernardo Harrington (Chapter 5) and Dr Carolina Toste (Chapter 6). In addition, Dr Carolina Toste developed the script for assigning microglia populations. Dr Elena Simonazzi, Dr Mark Gurney and Dr Ruth Jones for helping with processing of mouse microglia samples used for ScRNA-sequencing.

Dr Ryan Bevan for acquiring of histological images and processing of data using Imaris (Chapter 6).

Prof Nick Allen designed the first set of guides required for generation of the iPSC lines (Chapter 4).

All sorter experiments were completed by Mark Bishop, Roman Seliverstov and Jolene Twomey. Sequencing of generated libraries was performed by Joanne Morgan (Chapter 5 and 6). CNV analysis was carried out by Alexandra Evans and Patrick Weller (Chapter 4).

Summary

Alzheimer's disease (AD) is the most common form of dementia. It affects over 155 million people worldwide and represents a huge social and economic burden. Recent genetic advances have revealed that microglia play a key role in disease development and understanding how different microglia genes contribute to disease is crucial for future treatment development.

A single nucleotide polymorphism within paired immunoglobulin-like receptor alpha (PILRa) was identified to be protective against AD. The G78R variant alters the conformation of the receptor ligand binding pocket and reduces receptor activation. The function of the G78R variant was investigated through developing and validating novel microglia relevant *in vitro* models. Using functional approaches, the data suggests that PILRa might be involved in regulating crucial microglia functions such as cytokine release. In addition, utilising human relevant iPS derived microglia lines a brain relevant ligand of PILRa, PANP was functionally explored.

Another important gene for microglia function is the spleen tyrosine kinase (SYK) which can modulate the response of multiple core microglia pathways and is positioned downstream of important risk gene targets. Utilising a conditional knock-out (cKO) model of *Syk* in the APP^{NL-G-F} mouse model of AD the role of the gene in microglia was investigated. Some novel transcriptomic data identifies the initial cell response upon *Syk* deletion including metabolic changes and pathways linked to mitochondrial function. Additionally, investigating the response during disease progression in aged animals, identifies that *Syk* is involved in regulating microglia DAM transcriptomic signature. This is paired with pronounced morphological changes, including reduced number of microglia cells and diminished response to the presence of plaques.

The genes of interest in this thesis represent an important part of microglia activation and inhibition and demonstrate why it is important to understand microglia responses in more detail to develop better treatments.

Table of Contents

Table of Figures:

Table of Tables:

Chapter 1 General Introduction

1.1 Alzheimer's disease

1.1.1 Aetiology

Alzheimer's disease (AD) is a chronic age-related neurodegenerative condition which leads to progressive neuronal loss in the hippocampus and cortex (1). It was first identified by Alois Alzheimer in 1907 who studied the case of a 55-year-old female patient who presented with delusions, mania, memory loss and confusion. Later on, when performing postmortem brain analysis Alzheimer observed neurodegeneration, the presences of plaques and tangles as well as different morphology of the glia (2). All of these became the hallmarks of AD. Patients affected by the disease develop memory problems, confusion, speech impairment and even loss of motor functions in late stages. AD is usually classified in two categories: early-onset AD (EOAD) or late-onset AD (LOAD) depending on the age of onset and the genetic background of the patient.

Although there are multiple drug trials looking into different pharmacological treatments, currently there is no effective approach against the disease. The very few clinically available treatments only target the symptoms and aim to slow progression rather than treat the underlying cause. Development of these treatments was based on the limited understanding of AD in the 20th century. The mechanism of action of these drugs targets metabolism of acetylcholine, and in particular the enzyme which breaks it down, acetylcholine esterase (3). Due to the involvement of acetylcholine in learning and memory, the cholinergic hypothesis of AD was developed as reviewed in (4). Based on this knowledge it was believed that low levels of acetylcholine cause memory problems in patients. Therefore, increasing the concentrations of the neurotransmitter will improve symptoms of AD. However, with disease progression causing neuronal loss, the amount of acetylcholine is irrelevant as there is too much damage to the neuronal network to facilitate proper signalling. Although the understanding of AD significantly broadens since then, very little advancement has been made in terms of drugs available on the market. Just recently, for the first time in over 20 years a new drug against AD was approved by the Food and Drug Administration (FDA). Aducanumab, a monoclonal antibody aimed at targeting amyloid pathology demonstrated decrease in AD related markers in early onset AD (5).

One of the major hallmarks of AD is the presence of amyloid plaques. Amyloid plaques are a consequence of accumulated amyloid beta (Aβ) protein (6). Normally amyloid precursor protein (APP) is processed by two enzymes. First APP is cleaved by β-secretase, which is the rate-limiting factor in the pathway, followed by γ-secretase to produce multiple isoforms of Aβ (Figure 1.1). γ-secretase is known to be a multiunit enzyme consisting of the APH1, PEN2, nicastrin and presenilin 1 and 2 (PSEN1 and PSEN2) proteins. Mutations in the *APP*, *PSEN1* and *PSEN2* genes are associated with early-onset familial AD (fAD). The most abundant Aβ species end at position 40 ($Aβ_{1-40}$) or 42 ($Aβ_{1-42}$) depending on the splicing. The longer $Aβ_{1-42}$ isoforms are hydrophobic and fibrillogenic, making them more prone to aggregation (7). In addition, NMR-guided simulation of both forms suggested that the C-terminus of the $Aβ_{1-42}$ isoform was essential for oligomer formation (8). Furthermore, in patients with AD the ratio between $Aβ_{1-42}$ and $Aβ_{1-40}$ is significantly increased. The role of Aβ in AD led to the establishment of the Amyloid Cascade Hypothesis which prevailed in the field for over 20 years (9).

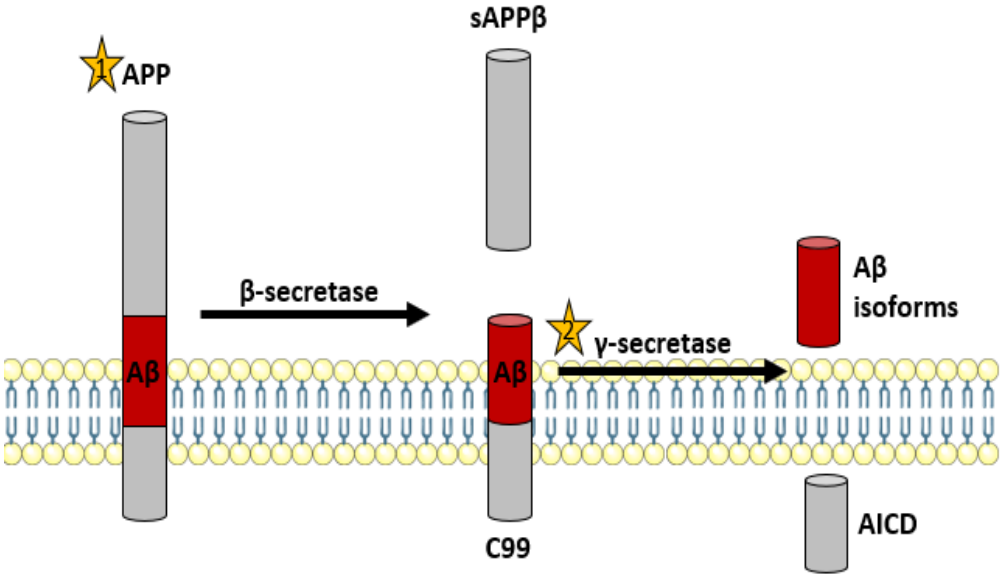

Figure 1.1: APP processing pathway. The amyloid precursor protein (APP) is first cleaved by β-Secretase which results in the release of a soluble APPβ fragment and C99 fragment. C99 is further cleaved by γ-Secretase. This produces multiple Aβ isoforms and the APP intracellular domain (AICD). The $Aβ_{1-42}$ isoform is more prone to aggregate and lead to plaque formation. Mutations in the APP gene or γ-Secretase enzymes (indicated by the stars) results in inappropriate cleavage and are associated with familial forms of AD.

Another classic hallmark of AD which is detected in postmortem brains are neurofibrillary tangles (NFTs). These tangles are a consequence of hyperphosphorylated protein tau (10). In healthy physiology the microtubule associated protein tau (MAPT) is important for maintaining axon integrity. The presence of tangles is believed to cause neuronal death and lead to cognitive decline. Furthermore, evidence suggests that the presence of tau is associated with the progression and onset of disease, rather than having a causative role. Wu *et al.* demonstrated in iPSC cultures that neurons can secrete and uptake tau (11). Tauopathy is thought to spread quickly through the brain due to the ability of the tau protein to transfer between neurons. Furthermore, studies propose that increased neuronal activity enhances this propagation and as it is known hyperexcitable neurons were previously documented in AD.

Studies of patients and mouse models show that AD manifests with increased occurrence of neuronal hyperexcitability. This hyperactivity leads to non-convulsive epileptic discharge (12). Between 10 and 22% of patients develop seizures, where this is increased in familial and early-onset forms of AD. Patients who present with seizures have faster rate of progression, more neuronal loss and greater cognitive decline. Palop *et al.* investigated the presence of hyperactivity in transgenic murine AD models expressing hAPP and revealed that seizure activity is present early in disease progression before any significant neuronal loss is observed (13). In addition, many studies on transgenic hAPP mice reveal a link between high levels of Aβ and alterations in neuronal circuits as reviewed in (14). Aβ has been associated with causing a decrease in some excitatory neurotransmitters in certain neuronal regions (15). These observations were confirmed in complex 2D and 3D hiPSC cultures (16). Aβ induced neuronal activity further leads to cognitive decline. The impaired activity in neuronal networks activates inhibitory responses to counteract and balance the aberrant neuronal activity. However, apart from regulating abnormal activity these responses might interfere with normal synaptic function which is required for learning and memory. The role of Aβ in abnormal neuronal function is further supported by the fact that incidence of unprovoked seizures is higher in patients with familial and EOAD. In these cases, the Aβ ratio is usually shifted towards a more aggregate prone form or increased production is observed. In addition, multiple mutations in the *PSEN1* gene are associated with epilepsy (17).

Apart from EOAD, risk genes for LOAD have also been associated with aberrant neuronal activity. APOE4 is associated with increased memory impairment and epilepsy exacerbation in patients (18). EEG alterations and sharp waves were reported in subjects with high risk of fAD (19). These findings reveal that impaired neuronal activity associated with genetic AD factors is present in patients without AD, therefore dysfunction in circuits might play a role early in disease development.

Microglia have an important role in regulating neuronal activity. Microglia express receptors for almost all neurotransmitters and can modulate synaptic transmission. These cells have a role in long term potentiation (LTP) which is an important molecular process underlying learning and memory. Mice stimulated with lipopolysaccharide (LPS), part of the outer membrane of gram-negative bacteria, showed deficits in learning and memory. LPS caused microglia activation and release of IL-1β which was suggested to play an important role in the observed cognitive deficits (20). In addition, mice with CXC3R1 loss-of-function mutations present with impaired LTP (21). Furthermore, loss of another important microglia receptor CD200, causes inhibition of LTP in mice, therefore supporting the role of microglia in this process (22). Collectively, these findings suggest that microglia are involved in neuron circuit regulation and since these cells are implicated in AD pathophysiology, they might contribute to the hyperexcitable networks observed.

More research is required to fully understand the aetiology of AD. Advances in research have revealed the complexity of AD in recent years. Now it is clear that AD is a polygenic multifactorial disease. Studies have shown that both genetic and environmental factors such as brain injury and obesity could play a role in disease development. In addition, up to date age remains the greatest risk factor for AD development, therefore a lot of effort is dedicated into understanding how this process impacts the disease. Further transcriptomic analysis and interactome studies showed that multiple pathways and processes are involved in the aetiology of AD. Therefore, the following part of the chapter will concentrate on the risk associated with identified AD genes.

1.1.2 Genetics

1.1.2.1 EOAD

Early-onset AD cases represent 5-10% of all AD cases. This form of AD is associated with heritable autosomal dominant mutations in the *APP*, *PSEN1* and *PSEN2* genes. These genes are part of the APP processing pathway and are thought to cause aggregation of Aβ (23). EOAD is more aggressive in comparison to the late form and presents earlier in life before the age of 65. The *PSEN1* and *PSEN2* genes are part of the γ-secretase complex. Mutations in these genes lead to production of the more aggregate prone $A\beta_{1-42}$ isoform which leads to plaque formation (24). However, mutations in these three highly penetrant genes explain only a small number of EOAD cases (around 5%). The rest of the cases are sporadic, and the causes remain unknown. Some recent research is focused on unraveling the full genetic landscape of sporadic EOAD. Mutations in *APP*, *PSEN1* and *PSEN2* contributed greatly towards the understanding of the Aβ cascade and the role it has on AD.

1.1.2.2 LOAD

1.1.2.2.1 APOE gene

The apolipoprotein family consists of three members: ε2, ε3 and ε4. The ε4 allele represents the strongest identified genetic risk factor for LOAD. One copy of the allele increases the risk with 2-3 times whereas two copies lead to up to a 12-fold increase in risk (25). Furthermore, the presence of the allele is consistently associated with earlier age of onset in patients. Evidence suggests that the association between APOε4 and Aβ has an important role in AD pathogenesis. In comparison, the ε2 allele is protective against AD. In addition, the ε4 allele has been linked to cardiovascular disease risk, decreased lifespan and metabolic syndrome (26).

The exact role of APOe4 in AD is not fully understood, however it is associated with lipid transport (27). It is known that APOE serves as a ligand for cell surface receptors which mediate lipoprotein update as well as a component of many lipid particles (28). In the central nervous system (CNS) APOe4 is predominantly produced by astrocytes and is crucial during the process of remyelination and axon regeneration during injury. A recent study using iPSC derived astrocytes

demonstrated that cultures expressing APOe4 accumulate more lipid droplets containing unsaturated triglycerides compared to isogenic APOe3 cultures in vitro (29). Mouse studies have previously demonstrated that APOe4 is required for Aβ deposition, and the effect is dose dependent. In addition, studies suggest that APOe4 influences disease progression independent of Aβ, meaning that combination of the two might cause neurodegeneration and promote disease development. Recent study showed that APOe4 advances BBB breakdown in the 5xFAD mouse model of AD with no impact on Aβ (30).

Finally, APOE is also thought to interact with another AD risk gene, TREM2. These genes are important at inducing a disease associated state in microglia and are thought to drive the transcriptional phenotype through shifting the expression profile of microglia (31).

1.1.2.2.2 Other AD risk genes

In recent years, a lot of effort has been dedicated to identifying the underlying genetics of AD. Large scale genome wide associated studies (GWAS) led to the identification of more than 30 loci which increase the risk of AD development. The first identified genes independently of *APOE4* included *CLU*, *CR1* and *PICALM* (32). Later work discovered more genes conferring to AD risk such as *CD2AP*, *ABCA7*, *CD33* and *EPHA1* (33, 34).

In 2013 Lambert *et al.* performed large scale meta-analysis identifying 11 new loci involved in AD risk. One of the identified risk genes was the *ZCWPW1* locus containing more than 10 genes, including *PILRa (*35*).* Following these discoveries, more recent work by Sims *et al*. 2017 revealed the rare coding variants *ABI3*, *PLCG2* and *TREM2* as AD risk genes, implicating the role of microglia and immunity in disease development (36).

In addition, Jansen *et al.* 2019 published a GWAS with over 600,000 samples confirming already existing risk genes and identifying 9 novel AD risk loci, such as *ADAM10* and *APH1B* (37). Just recently, the biggest GWAS meta-analysis up to date identified a total of 75 risk loci, with 42 new added to the already existing

ones, such as *ADAM17*, *MAF*, *SIGLEC11* and *CTSB*. Furthermore, additional 31 potentially disease-associated processes were identified (38).

Many of these genes encode for proteins which have a direct effect on signalling and cellular responses. However, studies also revealed that different transcription factors which are also identified risk genes could modify non-coding regions of the genome. An example of these are *Spi1* (39) and *Mef2c*. In addition, a large amount of the identified risk variants for AD are found in non-coding regions (40), making research and experimental approaches more difficult. Interestingly, sporadic AD variants are largely restricted to microglia enhancers (41). The importance of mapping identified genetic variants to the correct causative gene is high in terms of functional consequences when investigating a specific variant. Studies suggest that regions which are hundreds of base pairs apart might influence each other's expression which is hugely important in disease like AD.

This collective evidence shows the polygenic nature of AD and points to the fact that a more complex approach is required towards novel treatment development. Although individual disease-associated alleles contribute to disease risk only minimally, when combined they can provide a useful source for AD susceptibility prediction. Currently, the overall risk score which contains all identified SNPs across the genome, normalized to the effect size which has been estimated allows generation of polygenic risk score (PRS) (42). This understanding of genetics allows the prediction of LOAD using PRS with up to 90% accuracy (43). In addition, better understanding of genetic background allows research to intervene earlier on in disease progression. PRS represents a major advancement in identifying individuals with high risk of developing AD later in life. The knowledge of different genetic risk factors allows us to investigate how these genes impact proteins, which in turn influence signalling pathways and cell responses. The focus is now moving towards understanding how all the above identified genes impact cell responses response and how they link together to cause AD.

1.1.3 Link between genetic risk and biological understanding

Some early *in silico* work utilized databases containing genetic risk factors to predict functional pathways which may have a role in AD. Importantly pathways linking to the immune system, metabolism and endocytosis were identified (44). Later, GWAS studies were used to further reinforce these findings and identify further processes like cholesterol transport to be linked to AD. With advances in sequencing technologies, many studies used mRNA expression as an indicator of activated biological pathways. Overall, translating genetic findings to functional ones has led to identification of key lines of research, including the implication of the immune system.

1.3 Immune system in AD

Since it was suggested that immune system dysfunction might be key in AD, many studies demonstrated that neuroinflammation is a key hallmark of the disease. Multiple immune responses have been investigated in dementia. Firstly, several identified risk genes are associated with immune responses and pathways in microglia. These will be reviewed in more detail in section 1.7.4. Additionally, data from mouse models of AD and postmortem brain analysis reveals that microglial morphology changes in AD towards a more reactive phenotype (microgliosis). Various inflammatory pathways and processes are also elevated in AD. For example, complement pathway proteins regulate engulfment of synapses by microglia, therefore their activation in disease is considered crucial (45). Upregulation of various inflammatory cytokines and chemokines was observed in AD patients (46). Further evidence suggested that the immune system might not only be a consequence of AD but could be part of disease etiology. Another important link between the immune system and AD is aging. Currently the biggest identified AD risk factor is age. However, studies showed that age also impacts the immune system and leads to increase in inflammation (47). Consequently, a significant effort has been dedicated to understanding how the process of aging impacts the brain. All this evidence clearly highlights that the immune system is an integral part of AD, however the underlying mechanisms are not so well understood. The most accepted theory represents the immune system as a ‘’double-edged sword”. In early stages of disease when microglia detect neurodegeneration, they are beneficial. However, following chronic activation they become harmful and might exacerbate the condition.

1.3.1 Recruitment of peripheral cells to the CNS

Neurodegeneration has been identified as a trigger of peripheral cells infiltrating the brain. Besides microglia, which are the resident macrophages, studies reveal that many circulatory immune cells are also present in AD and might contribute to the pathology. A study by Scheld *et al.* identified in transgenic mouse models that upon neurodegeneration, peripheral immune cells are recruited to the forebrain (48). Work on APP mouse models shows that systemic monocytes and macrophages are directly involved in Aβ clearance (49, 50).

Additionally, the presence of T cell lymphocytes is also documented in AD. Both mouse models (51) and human postmortem tissue (52) shows that T cell populations are upregulated in the brain following neurodegeneration. However, the role these lymphocytes have in pathology and its development is poorly understood.

Cerebrovascular dysfunction and aging induce dysregulation of tight junctions which results in compromised BBB integrity (53). Therefore, peripheral cells infiltrate the perivascular space easily. Interestingly, vascular changes, including BBB breakdown and cerebral hypoperfusion, are well-documented in AD and patient data reveals they occur early during disease progression (54). These findings are further recapitulated in transgenic mouse models which demonstrate reduction of vascular density in hippocampal regions (55). Some recent findings used novel techniques to enrich microvessels from brain tissue and apply RNA sequencing to compare vascular changes in human and mouse tissue (56). Strikingly, the results demonstrated that many identified AD risk genes are expressed by vascular cells in humans, but by microglia in mice, highlighting some potential evolutionary differences.

1.4 Oligodendrocytes in AD

Oligodendrocyte primary function is myelin production which is used to ensheath axons in the CNS. Oligodendrocyte functions are essential for neuronal health and synapse survival (57). Multiple lines of evidence suggest that oligodendrocyte function in AD is impaired. Human MRI studies show that white matter (WM) is decreased in AD patients and suggest that WM microstructure alterations are an early pathological feature (58). These finds are also confirmed in mouse models (59). The role of oligodendrocyte in AD has been reinforced by implicating some genetic factors expressed by these cells in AD as well (60).

1.5 Astrocytes in AD

Multiple cell types are involved in maintaining brain homeostasis and they are all affected by disease development and might contribute to progression. Since astrocytes are another major glial cell group within the brain, their role in AD is of particular interest. Astrocytes express specific markers such as GFAP, glutamine synthase and others, which differentiate them from other cell groups. They represent a heterogenous group of cells with multiple homeostatic functions, hence their importance in disease.

Astrocytes were found to also participate in the process of clearance and removal of Aβ. It was identified that similar to microglia activation in AD, astrocytes also get activated during prolonged inflammation (61). Furthermore, in human primary astrocyte cultures treated with pro-inflammatory cytokines increased secretion of Aβ was observed (62).

Just recently single-nucleus RNA sequence identified a disease associated astrocytes (DAA) population (63). Similarly, to the distinct population of microglia present in AD, these astrocytes have different expression profile compared to homeostatic conditions. The genes overexpressed in DAAs, and DAMs overlap, suggesting a general transcription program might be initiated in response to pathology. Importantly, the presence of DAAs is observed early on disease progression in mouse models. Therefore, it is hypothesized that based on the wide range of functions these cells have an important role in disease progression.

1. 6 Metabolic dysfunction in AD

In recent years emerging evidence suggests that there is dysregulation of metabolic pathways in AD. Studies of patients report hypometabolism manifesting as altered brain glucose levels and switch to alternative energy sources such as fatty acids (64). In addition, *in vivo* models of AD demonstrate that metabolic pathways are altered early in disease progression specifically in areas affected by AD such as the hippocampus and cortex (65). One of the main organelles on a cellular level which controls metabolism is the mitochondria. Mitochondria, which contain their unique set of DNA, are responsible for the main energy supply of the cell, generating ATP via the electron transport chain (ETC) via a process also known as oxidative phosphorylation. Some believe that early changes in mitochondria and cell metabolism drive sporadic late-onset AD and refer to this idea as the mitochondrial cascade hypothesis.

Production of reactive oxygen species (ROS) has also been linked to AD. ROS can be generated by faulty ETC and in turn can lead to damage to mtDNA, proteins or lipids. Interestingly, cell lines which contain mtDNA from AD patients exhibit an increase in ROS production (66). Fault in the ETC in turn can be linked to expression of mitochondrial enzymes such as the cyclooxygenase enzymes (COX) subunits of which are encoded by mtDNA. Therefore, intrinsic mutations in mtDNA can cause mitochondrial dysfunction and damage over time.

Compellingly changes in brain metabolism are linked to normal aging, suggesting mitochondrial dysfunction might play a role in the increased susceptibility to AD associated with increase in age.

1.7 Microglia

1.7.1 Origin and characteristics

Microglia are the resident tissue macrophages in the central nervous system (CNS), accounting for 5-20% of all glial cells (67). The first reports of microglia date back to the late nineteenth century when Franz Nissl described rod cells with phagocytic, migratory, and proliferative properties. Rio-Hortega was the first one to introduce the name microglia in 1932. Initially microglia were viewed as neuroinflammatory in the context of brain injury, until later studies identified them to have neuroprotective roles as well. The origin of microglia populations has been a debate in the field for many years. Until the late 20th century, it was believed that microglia originate from the neuroectoderm as neurons and other macroglia cells (68). The first studies which suggested that microglia might originate from the mesoderm identified similarities in morphology which link microglia and macrophages and identified shared markers such as CD11b and F4/80 (69). Important work in mouse by Ginhoux *et al.* revealed that the innate immune cells of the CNS originate from erythromyeloid progenitors (EMPs) in the embryonic yolk sac (70). Around embryonic day 8.5 (E8.5) after conception EMPs emerge in blood islands in the extra-embryonic yolk sac. These primitive macrophages migrate to the brain through entering the circulation system between E8.5 and E10 and are finally seeded around day E10.5 during murine embryonal development, following which they ramify (71). This process is followed by a second wave of Hoxb8^{+} cells derived from the yolk sac, before closure of the blood brain barrier around E13.5 (72) (Figure 1.2). In humans, microglia are

present in the neural tissue around 5.5 weeks of gestation (73). Work by the same group showed that in comparison to blood monocytes and macrophages, microglia development is dependent on colony stimulating factor-1 receptor (CSF-1R) and its ligands (e.g. IL-34).

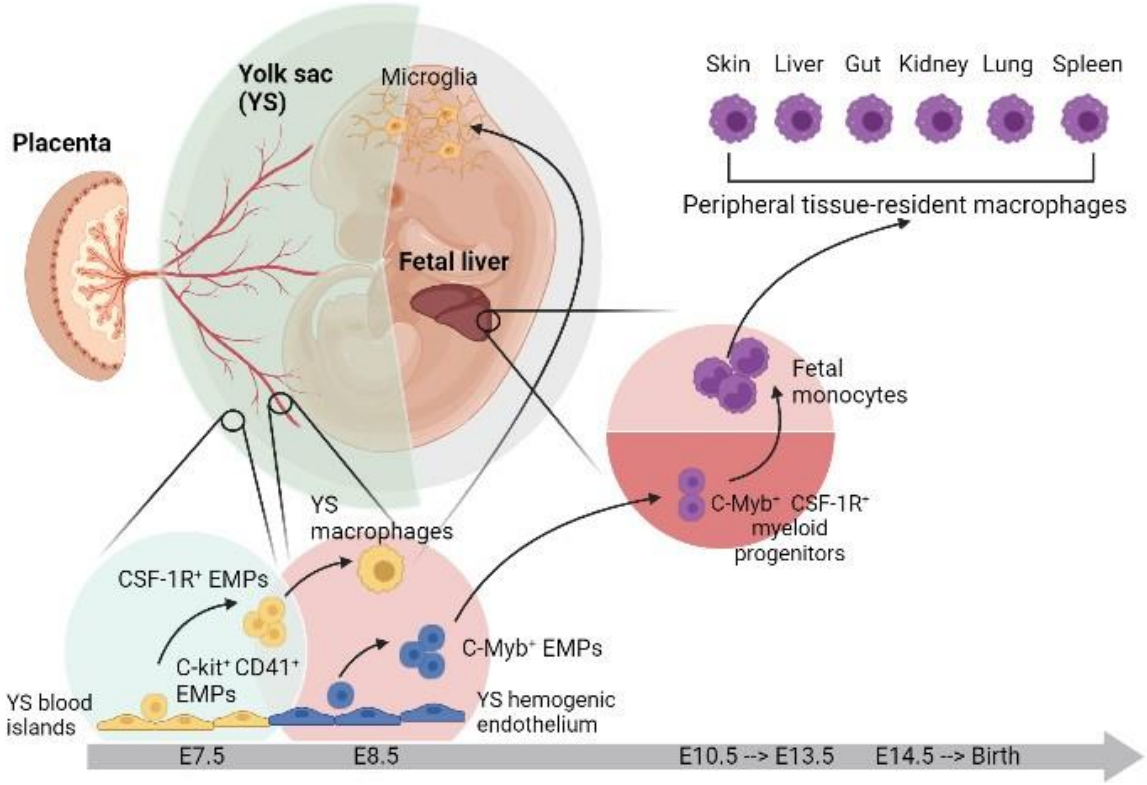

Figure 1.2: Origin of microglia. In mouse embryos on embryonic day 7.5 (E7.5) erythromyeloid progenitors (EMP) start to emerge from blood islands found in the yolk sac. These EMPs migrate and begin to express CSF1R and around E8.5 they enter the circulation as yolk sac macrophages. The yolk sac macrophages are transported to the brain where they seed the tissue and will later differentiate to functional microglia. In contrast, at E8.5 C-Myb+ EMPs emerge in the vessels from the yolk sac endothelium. These migrate to the fetal liver where they differentiate to myeloid progenitors and show CSF1R expression around E10.5. By E13.5 these form fetal monocytes which are later distributed to other organs and give rise to tissue-resident macrophages. Adapted from (74) and created using BioRender.

Microglia are the **most diverse and dynamic** CNS cell type, constantly adapting to the environment. Advances in transcriptomics revealed microglia heterogeneity depending on the brain region. Mouse studies show that microglia cell count, structure, molecular signature and function can all differ depending on the brain region as reviewed in (75). In

addition, large scale single-cell RNA-seq studies confirmed the regional heterogeneity of microglia within the brain (76). Microglia have an important role not only in the adult brain but also during development. Studies show that microglia functions are essential for the development of the CNS. The early infiltration of microglia during development which is followed by rapid expansion and colonization makes them well-suited to regulate critical brain development.

In the adult brain both in rodents and humans, the microenvironment is essential for driving the microglia phenotype (77). Diverse factors such as TGF-β, CSF-1, PGE2, IL-34 and others are released into different brain regions to promote or inhibit certain microglia functions. The role of TGF-β signalling in microglia is of particular importance. Butovsky *et al.* found that TGF-β is crucial for the development of microglia and expression of signature microglia genes, identified by RNA sequencing analysis. Some of these signature genes included *Tmem19*, *P2ry12* and *Siglech* (78). In addition, TGF-β and its receptors are highly expressed in microglia. Importantly, the same expression pattern was documented in humans as well.

In addition, other major regulators of resting microglia are Cx3cl1/Cx3cr1 and CD200/CD200R. Cx3cl1 which is either expressed on neurons or secreted, leads to inhibition of microglia activation after recognition by Cx3cr1 (79). The Cx3cl1 axis has been implicated in ageing as well as AD pathology. Downregulation or genetic deletion of Cx3cr1 led to cognitive deficits and reduced neurogenesis (21, 80).

Similarly, to Cx3cl1, CD200 stimulation leads to decrease in microglia activation. Microglia are the only brain cell type that expresses CD200R (81). The importance of CD200-CD200R interaction for microglia reactivity was first demonstrated by Hoek *et al*. in deficient mice which showed reduced ramifications and upregulation of CD11b (82). CD200 downregulation has been noted in AD patients (83).

Another important mediator of microglia functions are astrocytes. Cell culture experiments show that astrocyte-conditioned media supports the survival of microglia *in vitro* (84). In addition, other factors such as the macro environment and sex differences can also impact microglia function as reviewed in (85).

An important microglia transcription factor which regulates cell fate is PU.1 (*Spi1*). PU.1 binds purine-rich regions and promotes gene expression during microglia development. The transcription factor is essential for microglia maintenance and is continuously expressed on cells (72). PU.1 was identified as an AD risk factor. In addition to *PU.1, IRF8* and *CSF-1* were identified as critical regulators of early microglia development. Other important transcription factors involved in microglia maturation and regulation in later stages are *Mef2c, Sal1 and TGF-b* (86).

1.7.2 Microglia renewal

For many years it was believed that once seeded within the brain during development, microglia populations were long-lived and maintained via a slow turnover. It is now known that microglia can repopulate the mouse brain in less than a week after genetic ablation (87). The actual rate of microglia turnover and proportion of cells in S-phase of the cell cycle at any time remains a huge debate with conflicting evidence in the field. A study by Askew *et al*. demonstrated that within 95 days a complete renewal of microglia populations occurs within the mouse brain and further estimated up to 0.69 active cells (88). This is significantly higher compared to previous findings which report rates as low as 0.05% (89). There is no conclusive evidence but in humans this number has been reported to be as high as 2% (88). Interestingly, microglia turnover rate was shown to be increased 3-fold in models of AD. Cumulatively, these findings highlight some key differences in microglia populations between humans and mice. Furthermore, the exact mechanism which regulates microglia proliferative or quiescent state remains understudied. Unsurprisingly, key microglia factors such as CSF-1 have been implicated in the process (90). Additionally, microglia derived brain-derived neurotrophic factor (BDNF) has been linked as a regulator of microglia density in homeostasis (91). Further research is required to determine the exact pathways involved in microglia renewal.

1.7.3 Physiological functions of microglia

Under normal physiological conditions microglia have two central roles: immune defense and maintenance of tissue health. Microglia use mobile processes to survey the environment and the cells and play an important role in pathogen defense and injury response, therefore their impact in disease development is crucial. Furthermore,

microglia take part in shaping neural circuits through engulfing and removal of neurons and synapses.

1.7.3.1 Phagocytosis and synaptic remodeling

The endocytic pathway is essential for efficient sorting and recycling of cellular components. It represents the mechanism by which cells internalize either internal or plasma bound particles. Endocytosis is classified into 3 groups, clathrin mediated endocytosis, macropinocytosis and phagocytosis, each internalizing different cargo mainly based on size (Figure 1.3). The endocytic pathway is believed to have far more wide-reaching role and implications than cargo recycling.

The process of phagocytosis is essential both during development and in the adult brain. In development, excess neurons undergo programmed cell death to ensure that only essential number remain (92). In addition, removal of synapses and refinement of neural circuits aids the process of learning and memory. Phagocytosis by microglia is regulated through a fine balance between various signals. The process depends on expression of phagocyte signals and receptors as well as downstream signalling pathways which cause actin polymerization and reorganization (reviewed in (93). This complex sequence leads to engulfment of harmful particles or synapses. In general, there are two main groups of receptors involved in phagocytosis. The Toll-like receptors (TLR) which primarily bind to foreign pathogens (e.g. microbes) and triggering receptor expressed on myeloid cells 2 (TREM2) which is responsible for recognizing apoptotic neurons. In addition, complement receptors, Fc receptors, P2Y6 and others have also been associated with microglia phagocytosis (94).

TLRs are essential components of the innate immune system. They recognize structurally conserved microbial patterns and are important in CNS infections. In accordance with the innate immune system, TLRs in the CNS recognize neurodegeneration associated molecular patterns (NAMPs) such as Aβ. In particular, TLR4 and TLR2 were associated with mediating phagocytosis of Aβ fibrils. Mouse models expressing TLR4 mutations demonstrate that Aβ uptake and clearance was impaired compared to wild type controls (95).

The TREM2-DAP12 axis has a central role in microglia activation. TREM2 is a transmembrane receptor which belongs to the family of Triggering Receptors Expressed on Myeloid Cells glycoproteins. TREM2 consists of an extracellular domain, transmembrane region and a short cytoplasmic domain that lacks signalling properties. TREM2 associates with DAP12 (encoded by TYROBP), which encodes an immunoreceptor tyrosine-based activation motif (ITAM), short peptide sequence with 2 tyrosine residues which are 6-12 amino acids apart, and initiates signalling (96). Upon activation in microglia, DAP12 recruits Syk which triggers multiple intracellular signalling pathways downstream. Importantly, it initiates upregulation of chemokine receptors, activates the protein kinase ERK and triggers cytoskeletal changes (97).

Fc receptor-initiated phagocytosis is more efficient if the target particle has been opsonized by IgG. In normal physiological conditions Fc receptor expression on microglia is low, however studies show that they are upregulated in several CNS conditions (98). Fc receptor mediated phagocytosis of Aβ deposits has been studied in mouse models and cell culture, however the involvement of the receptor in this process remains controversial.

P2Y6 receptor belongs to the G-protein coupled receptor family. This receptor has gained attention after Koizumi *et al.* demonstrated that it triggers microglia phagocytosis (99). P2Y6 is able to recognize UDP signals which are released by injured neurons and act as a phagocytosis trigger. Activation of the receptor causes release of intracellular calcium and actin polymerization. Expression profiles of some members of the P2Y receptor family were altered in human AD brain samples (100). Further studies demonstrate that P2Y receptors might be involved in Aβ metabolism and neuroinflammation as summarized by (101).

The complement system has been widely studied regarding the identification and engulfment of synapses in the CNS. The classical complement cascade involves a chain of reactions which tags the target and consequently activates phagocytosis by binding complement receptor on phagocytic cells. C1q and C3 are critical components of complement which tag synapses for clearance. In addition, the C3 receptor on microglia is required to further engulf those synapses. Studies highlight the importance of complement in synaptic pruning because experimental models lacking

any of these components result in impaired neuronal function and spontaneous activity such as seizures (102). In addition, complement function is associated with elimination of synapses during aging. Experimental work by Stephan *et al.* demonstrates that C1q is upregulated in aging brains (103). Recently, genetic studies have identified complement components as risk for AD development as reviewed in (104). Synapse loss is a hallmark of AD and dysregulation of complement-initiated phagocytosis could be involved in this process.

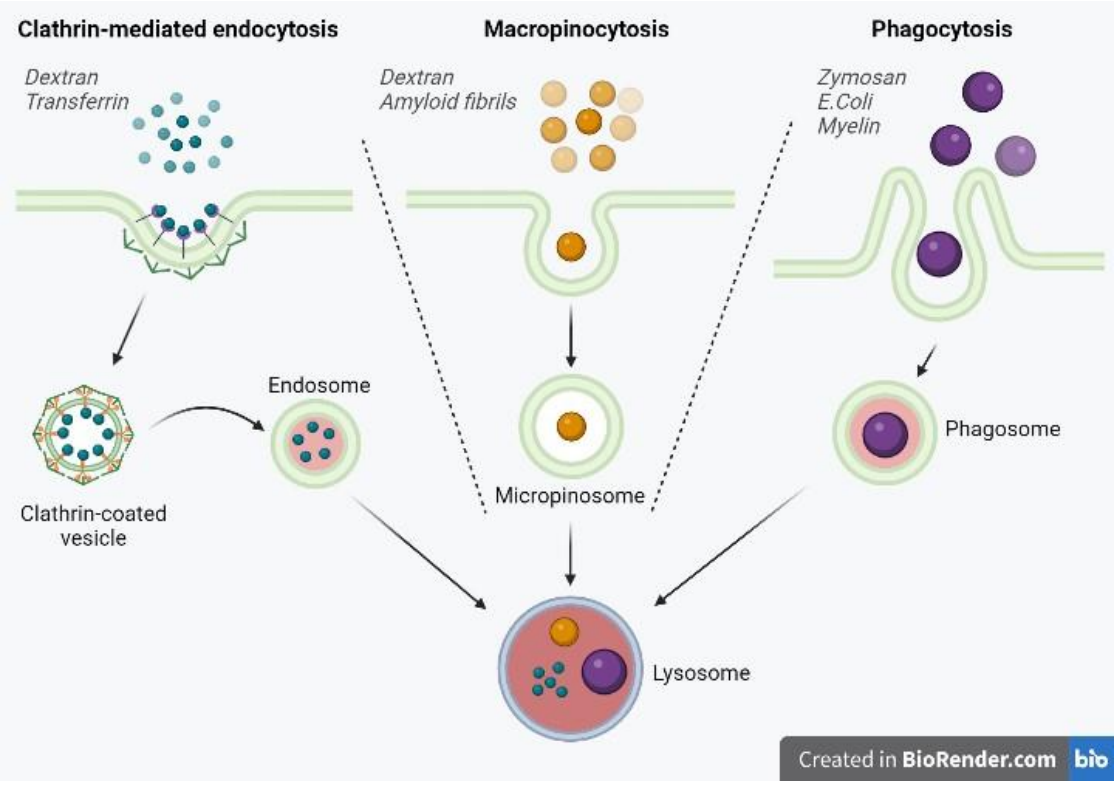

Figure 1.3: Schematic representation of the endocytic system. The 3 main pathways utilized by phagocytic cells to uptake cargo are presented. The overall induction of each pathway will depend on the size of the identified particle. Some example cargoes for each pathway are outlined. Independent of the pathway, all vesicles will fuse with a lysosome containing acidic enzymes which degrade the ingested cargo. Differences in the acidic environment are depicted by the strength of red background.

1.7.3.2 Neurogenesis

Microglia are particularly important for neurogenesis, as they regulate the microenvironment which determines whether newly synthesized neurons survive (reviewed in (105). By releasing various cytokines, microglia regulate the

differentiation and proliferation of neuron progenitor cells (NPCs). Studies demonstrate that TNF-α signalling is essential for neurogenesis (106). In addition, aging, microglia and neurogenesis are all connected since age shifts microglia into an inflammatory state which in turn reduces neurogenesis.

1.7.3.3 Angiogenesis

The majority of studies on angiogenesis concentrate on the role of microglia in the development of the retina. Studies show that microglia function is essential during early CNS development. Depletion of microglia causes decrease in retinal vasculature density (107). In support of these findings, work by Rigato *et al.* showed that microglia increase vascular branch points (108). However, there is contradictory data showing that in fact microglia might suppress vascular angiogenic branching through Wnt-signalling as reviewed in (109). Very recently, a publication revealed that microglia can regulate specific sets of endothelial cells and induce angiogenesis (110). The ScRNA-sequencing reveals that microglia promotes this process via SPP1 and IGF signalling.

Importantly, microglia can also impact the blood brain barrier (BBB). Microglia are in constant contact with endothelial cells and monitor the influx in the CNS. Their ability to secrete various cytokines, as detailed in section 1.7.3.5, allows them to modify BBB permeability (111). In addition, the breakdown of blood vessels and disruption in BBB function in various neurodegenerative conditions coincides with microglia activation (112).

1.7.3.4 Immune surveillance and synaptic pruning

Under normal physiological conditions, microglia are highly branched with processes extended in the space between neurons, usually with minimal to no overlap. Resting microglia are highly dynamic and two-photon imaging revealed that within several hours, the entire CNS space is sampled by microglia processes (113). More detailed live imaging revealed that microglia use filopodia structure at the tip of the process to sample the environment at a faster rate (114).

Microglia are in constant interaction with the other cells found within the CNS. The neuron-microglia interactions are particularly important for regulating neuronal

activity and synaptic transmission. Microglia have been implicated to have a role in regulating synapse development and pruning in health. A study by Miyamoto *et al*., revealed that contact with microglia are essential for synapse formation in early postnatal development (115). Genetic ablation of microglia resulted in a reduction in synaptic density and less functional neurons in these animals. Other studies have supported these findings and further demonstrated that microglia presence is key for maturation of synapses (116). Microglia are also involved in synapse elimination which is a key process during brain development and refinement.

More recently, two publications revealed that specific signals on neurons can tag synapses for phagocytosis. Studies focusing on the retina demonstrated that microglia are able to uptake synapses via phagocytosis (117). A number of publications by Stevens *et al*. and her team focused on unravelling some of the key mediators of this process including C1q and C3, components of the complement system and AD risk genes, once again reinforcing the involvement of the immune system in AD (118, 119). Some more recent publications identify phosphatidylserine (PS) as a signal on synapses which is recognized by microglia and triggers engulfment during development (120, 121).

1.7.3.5 Cytokine release and neurotransmitter regulation

Microglia produce and secrete interleukins (IL), interferons (IFN), tumor necrosis factors (TNF) and other molecules which regulate the cell environment and immune responses. Cytokines are crucial for mediating inflammatory responses and their release requires activation of inducible multiprotein complexes known as inflammasomes. The most well-studied inflammasome, NLRP3 is known to contribute to pathologies. Importantly, NLRP3 is thought to regulate the cleavage and activation of caspase-1 (122). Caspase-1 has an important role in activating and promoting the release of IL-1β and IL-18 into the extracellular space. Frontal cortex data from AD patients reveal that caspase-1 expression is elevated which correlates with reduction in Aβ peptide phagocytosis (123).

Cytokines can be categorized as pro and anti-inflammatory. Expression of various cytokines was documented in AD and some show altered profiles. IL-4, IL-10 and TGF-β are all anti-inflammatory and some of them show elevated levels in serum and CNS

in AD patients (124). In addition, expression of cytokines is thought to impact Aβ levels and clearance. On the contrary, TNFα, IL-6 and IL-1β are important pro-inflammatory mediators. These cytokines show increased expression in AD. In addition, IL-1β was found to be involved in a feedback loop with Aβ and IL-6 which could potentially regulate Aβ processing. IL-1β promotes the secretion of nitric oxide (NO) and TNF-α, which promotes neuronal damage and degeneration. GWAS identified SNPs in TNF-α in association with APOE are associated with sporadic forms of AD (125). Studies in fAD mice show that deletion of NLRP3 correlates with lower IL-1β and Aβ levels corelating with better cognitive performance (126). All this evidence suggests that cytokine production and release by microglia could have an important impact on pathology progression and development. Furthermore, the balance between pro and anti-inflammatory cytokines might be crucial for slowing down progression and mediating inflammation.

Importantly, cytokine release by microglia is involved in regulation of neurotransmitters within the brain. Studies demonstrate that IFN-γ is involved in glutamate removal (127). In addition, release of ATP by microglia was shown to aid astrocyte activation and promote neurotransmission (128). Microglia express receptors for all known neurotransmitters which allows them to detect neuronal activity and communicate with astrocytes (129).

1.7.4 Role in AD

During normal physiological conditions, microglia are distributed regularly with a ramified morphology throughout the CNS. However, in pathology and injury, microglia morphology and function transforms to hypertrophic and ameboid phenotype (130). The ameboid morphology is characterized by short and thick processes as well as enlarged soma. These changes are reflected by expression of specific cell surface markers, induction of cytokine release specific to the stimuli. Following activation, microglia are able to migrate to the site of injury in a matter of minutes, demonstrated by laser injury experiments (131). Although the classification of different microglia types in the past consisted of only neurotoxic (M1) and neuroprotective (M2), recent advances in transcriptomics revealed that microglia populations are highly heterogeneous and even in homeostatic state there are multiple different clusters of cells (132-134).

Traditionally neuroinflammation is defined as the innate immune response of the brain to injury. Neuroinflammation can be a persistent response leading to chronic activation of microglia and initiating feedback loops which sustain the release of inflammatory signals.

The exact role of microglia in AD has been discussed for a long time. When Alois Alzheimer first characterized the disease, he reported that changes in glia are visible and that they present with different morphological features. Since then, due to the challenges of studying immune cells within the brain, for long-time microglia were defined as a single population of cells during disease development. However, advances in research approaches, such as single cell RNA sequencing, have allowed the identification of a subset of microglia present in neurodegenerative disease. This group of microglia are known as disease-associated microglia (DAM) and show distinct transcriptomic profile (135). Similarly, to the central immune system response, it was proposed that microglia sense neurodegenerative damage through neurodegeneration-associated molecular patterns (NAMPs). An example of NAMP in AD could be the presence of Aβ. DAMs express a high number of genes identified through GWAS studies to alter the risk of AD development. Importantly, DAM populations investigated in the 5XFAD, and other mouse models reveal that expression is seen only in brain regions affected by the disease (136). The shift from homeostatic to disease associated state in microglia is a two-step sequential process. TREM2 is suggested to play an important role in DAM activation through association with APOE4 and mouse models deficient in TREM2 show no presence of DAM. In addition, TREM2 is required for the first step of DAM transitioning, however the second step is TREM2 independent. This transitioning in microglia is also associated with downregulation of the homeostatic genes discussed above such as *Tmem119*. However, the exact impact microglia have on disease progression is still poorly understood. Therefore, there is an urge to understand their role in AD as well as the contribution of individual SNPs to microglia response.

Apart from the core DAM signature microglia, there are studies which reveal additional groups of microglia with distinct transcriptomic signature in disease. For example, two sets of microglia, activated response microglia (ARMs) and interferon-responsive microglia (IRMs) have emerged from the APP^{NL-G-F} mouse model of AD associated with

amyloid pathology progression (137). ARMs are associated with high expression of MHC type II and tissue repair genes such as *Spp1* and are present during normal brain aging. ARMs appear to be highly enriched for APP^{NL-G-F} microglia demonstrating a strong response to amyloid and higher expression levels of *Apoe*. In contrast, the IRMs which express genes enriched for interferon response also appear in wild-type mice but seem to be less affected by the AD pathology. Interestingly, regional and sex differences are also revealed between different homeostatic microglia clusters, termed H1M and H2M, which recapitulate some previous reports (138).

Additionally, human AD microglia (HAMs) have also been documented (139). Identified HAM profile shows low similarity to DAMs. Although these findings highlight significant differences between mouse and human, the experimental variance used to derive different transcriptomic datasets should also be considered carefully before precise conclusions are formed. Using frozen or fixed samples can impact the transcriptome and comparing such findings with fresh tissue samples might lead to drawing entirely misleading hypothesis.

The role of various cytokines in AD has been studied as summarized in (140). Research shows that expression of certain pro-inflammatory cytokines such as IL-6 are upregulated in AD brains. In addition, the expression of certain cytokines is thought to impact APP processing and Aβ levels, however most of these results require further investigations. Interestingly, anti-inflammatory cytokines are also upregulated in AD. For example, IL-10 expression was shown to cause decrease in phagocytosis and increase in Aβ deposition (141). TGF-β levels were also elevated in the CNS which might have an important impact on microglia responses due to its central role in signalling as explained in section 1.7.1 (142).

Additionally, mouse model studies investigating the role of microglia in AD provide some useful cues about their involvement in disease. Historically, different pharmacological and genetic modifications were used to investigate if disrupting proper microglia function will impact different hallmarks of AD and progression. Some of the more common approaches targeted key microglia molecules such as Cx3cr1 or CSF1R. In a study conducted by Spangenberg *et al*., 5xFAD mice were treated with selective CSF1R inhibitor resulting in 80% decrease of microglia (143). Interestingly, this study reports no impact

on Aβ load however, suggests improved cognitive function. This increase in memory performance is attributed to decreased neuronal loss and reduction in dendritic spine loss. Additional studies have suggested that genetic knock out of Cx3cl1 in APP-PS1 mice leads to decrease in Aβ deposition, but conversely increase in neuronal deposition of tau (144). This effect on Aβ has been supported by other studies which suggest that Cx3cr1 may be involved in modulating the conformational state of Aβ and it turn impacting synaptic transmission (145). Although intriguing, most studies looking at microglia deficiency impact on AD use different mouse models and various ways to decrease presence of microglia. Furthermore, in most utilized models both macrophages and microglia will be targeted, raising the question about peripheral effects and specificity.

Interestingly, just recently a key publication in the field utilized a novel mouse model which lacks microglia but sustains peripheral macrophages (146). The study by Shabestari *et al*. investigated how microglia absence from birth will impact disease progression in the 5xFAD mouse model (147). The study revealed some very compelling evidence supporting the essential role of microglia during disease development. 5xFAD mice where no microglia were detected exhibited various transcriptional changes, brain calcification and premature lethality. More importantly, mice lacking microglia demonstrated a shift in amyloid distribution from parenchymal to blood vessels and meninges instead, demonstrating potential link to the vascular system.

Altogether, these findings conclusively support the role of microglia in AD and even more suggest that microglia can be essential cell type regulating processes linked to disease progression.

1.7.4.1 Other CNS macrophages and their role in AD

CNS macrophages populations consist of microglia, residing in the brain parenchyma and border-associated macrophages (BAMs) which occupy the meninges, choroid plexus and the perivascular space. Although microglia and BAMs both originate from the yolk sac, they show distinct ontogeny and gene signatures. Recent studies using fate-mapping identified that in the yolk sac two distinct populations are present (148). Interestingly, single-cell RNA sequencing reveals distinct transcriptomic profiles between microglia and BAMs. BAMs express high levels of *Mrc1, Siglec1, Mc4a7* and others which are not identified signature microglia genes (136).

In addition, there are differences between the various BAM populations. For example, meningeal macrophages and microglia share common prenatal progenitor whereas PVMs are derived after birth in an integrin-dependent manner (149). Perivascular macrophages (PVM), associated with the perivascular space, regulate important functions such as vascular permeability and offer first line defense to blood-borne pathogens. In addition, some BAM populations self-renew during adulthood whereas others such as choroid plexus BAMs can be replenished by infiltrating monocytes (150).

The role of BAMs in disease has not been well investigated until now. However, some recent publications point at the importance of these various macrophage populations within the brain and suggest crosstalk with microglia. For example, a recent publication identified secreted phosphoprotein 1 (SPP1), a protein derived from PVMs to be involved in phagocytosis regulation. Using the APP^{NL-F} mouse model of AD it was demonstrated that there is a functional crosstalk between microglia and PVMs which can result in modulation of phagocytosis and reduction in synapse loss (151).

Overall, the evidence suggests that CNS macrophages are a dynamic cell population with complex functions which yet remain to be fully understood. Studying the role that macrophages have in regulating microglia-relevant functions might reveal novel disease mechanisms and potential targets to aid microglia dysfunction.

1.7.4.2 Impact of LOAD risk on microglia

As summarized in section 1.1.2.2, in the past few years GWAS studies identified AD risk genes, many of which are primarily expressed on myeloid cells. The challenge in research is to understand how this genetic risk translates to a functional level and how it contributes to the pathology. Most of the functions of the identified risk genes are poorly understood and understudied. In addition, linking individual genes together in polygenic interaction networks is important to understand better the processes which might modify disease progression. Expression profiles of several risk genes show that the transition of homeostatic microglia to DAM is associated with upregulation of these genes. This evidence suggests that DAM could be protective in the AD pathology and its progression. For example, studies involving the APOe4 allele show that it is one of the earliest genes upregulated in DAMs (152). The role of some

identified risk genes was reviewed in (153). In the following section, AD risk associated with inhibitory and activation receptors on microglia which are relevant to this thesis will be discussed. Interestingly, a study by Shaw *et al*. revealed that genetic variation associated with ITAM/ITIM receptors, mainly present on microglia and linked to modulation of phagocytosis and inflammation, represents understudied genetic risk factor for AD (154). ITIM and ITAM containing proteins demonstrated protein QTLs (pQTLs) which were overrepresented as significant for AD, showing that the functional link in these molecules might be stronger than was GWAS studies identify.

1.7.4.2.1 Activation receptors

The R47H variant of TREM2 increases the risk of AD by 2 to 4-fold. Song *et al.* recently demonstrated in a 5XFAD mouse model, that defects in TREM2 cause impaired microglia (155). The proper function of TREM2 is required to associate the transition of homeostatic microglia to DAM, therefore these findings support the idea that DAM can be protective against AD. In addition, DAP12 which is essential for TREM2 signalling was also found to be upregulated in DAMs (156). The R47H variant of the gene causes slight reduction of the receptor in the cell surface as demonstrated in BV2 microglia cells (157). However, this effect was not seen in other cell lines such as bone marrow derived macrophages and HEK293T cells (158). The amino acid change leads to a slightly altered conformation, causing impaired interaction of the receptor with its ligands. The SNP causing arginine to histidine substitution is situated at the ligand binding pocket of the receptor. This amino acid change causes reduced positive charge of the domain (159).

TREM2 role in phagocytosing Aβ has been widely investigated. Murine 5xFAD models reveal that TREM2 is essential for microglia ability to surround plaques and limit neuron damage (160). Although the effect of TREM2 on plaque burden is unclear as reviewed in (161), its role in activating microglia and promoting their migration to plaques is conclusive. Due to the variety of roles the TREM2-DAP12 axis has on microglia it is suggested that its dysfunction might play a role in dementia. TREM2-DAP12 signalling regulates microglia activity and removal of

apoptotic cells, showing that defects can cause accumulation of toxic substances within the CNS and overstimulate microglia. Furthermore, evidence from mice studies shows that TREM2 expression in AD brains is upregulated (162).

Surprisingly the effect of the R74H mutation in iPS-derived microglia demonstrated very modest effects (163). Some detailed transcriptomic studies revealed more specific pathways such as adhesion defects but overall, these cultures lacked large phenotypic defects. These findings are particularly important as they highlight the difference between scientific models and also demonstrate that small SNP changes alone do not cause direct phenotypic differences in the absence of the brain environment and underlying genetic complexity.

1.7.4.2.2 Inhibitory receptors

The cluster of differentiation (CD33) is a classic member of the inhibitory family of receptors which encodes two ITIM domains and decreases intracellular signalling. *CD33* variants are associated both with increased and protective risk against AD (33). The risk variant of the gene which causes overexpression of CD33 was shown to be downregulated in DAM. On the contrary, the protective variants (rs3865444) resulting from alternative splicing of exon 2 encodes a non-functional CD33 protein (164). In addition, analysis of the impact of the protective form of CD33 shows that decreased expression of the receptor positively correlates with decrease in $A\beta_{42}$ in AD brains (165). This evidence further supports the idea that DAMs are important in AD and dysfunctional genes which contribute to activating microglia promote disease development whereas impairment of inhibitory genes has a protective effect. Two distinct isoforms, short and long, result from CD33 alternative splicing. The two isoforms appear to have opposing functions in terms of regulating core microglia functions, such as phagocytosis, migration and proliferation (166). Interestingly, a study investigating the functional role of CD33 in both mice and humans found some conflicting results. Using a variety of in vivo and in vitro models, the study suggests that deletion of CD33 in mice does not show alteration in phagocytosis, whereas human models demonstrate decrease in cargo uptake (167).

A large family of inhibitory immune receptors is the Sialic acid-binding immunoglobulin-like lectins (Siglec) family. Siglec receptors are usually split into two groups, CD33-like Siglecs and those which are conserved across mammals. The ones not belonging to this family include Sialoadhesin. Overall, there are 14 identified Siglecs in humans and 9 in mice. The majority identified Siglecs belong to the CD33-like family and contain at least one ITIM-domain. Recently some Siglecs have been identified as GWAS hits.

Siglec-11 is expressed on human macrophages and microglia and contains an ITIM domain (168). The receptor has been shown to have anti-inflammatory and neuroprotective properties *in vivo* in microglia (169). In vitro microglia cultures demonstrate decrease of pro-inflammatory cytokines and reduction in neuronal cell phagocytosis (170). Abud *et al*. showed that in iPSC derived microglia and neuron co-culture system *SEGLEC11* is upregulated which demonstrates that the receptor could be involved in microglia-neuron crosstalk most likely via ligands expressed on neurons. Recently, an SNP residing in the minor allele of *SEGLEC11* (rs9304690^{T}) has been associated with LOAD (38). It is believed that this mutation leads to increase in *SIGLEC11* expression, however the mechanism underlining AD pathology facilitation remains unclear.

Although not identified GWAS hits, other inhibitory Siglecs such as CD22 and Siglec-8 have also been identified to have important functions in the CNS and modulate responses in AD. CD22, which can be expressed on microglia in mice demonstrated that it could alter the phagocytic abilities of cells clearing myelin and Aβ *in vivo* (171). Additionally, CD22 null mice showed improved cognition. Another study recapitulated these findings and demonstrated that increased CD22 expression causes reduction in phagocytic clearance and cognitive decline (172). Importantly, these findings were translated to human iPSC lines where CD22 blockade rescued phagocytosis responses. In the case of Siglec-8, the phosphorylated ITIM-like motif was found in higher abundance in 3 different AD mouse models (173). Additionally, the study showed that not only the phosphorylated form, but Siglec-8 overall is upregulated in microglia, and this is recapitulated in human brains in age-dependent manner. Surprisingly,

overexpression of Siglec-8 in BV2 cells caused induction of pro-inflammatory cytokines and increase in phagocytosis.

Another inhibitory receptor whose dysfunction is associated with protection against AD is PILRα. The mechanisms through which PILRα modulates AD risk will be a main focus of this thesis and a more detailed introduction can be found in section 1.9.

1.8 Models to study microglia

With the emerging role of microglia in neurodegenerative disease many *in vivo* and *in vitro* techniques were developed to study closely their function. The complex developmental origin of microglia combined with the intricacy of the brain environment represents an ongoing challenge in the field for identifying the 'perfect' model. Advances in transcriptomics and identification of the ''signature'' microglia genes expressed in homeostatic state was of particular importance. These genes are markers for what ideally a microglia *in vitro* culture should express. Overall, the best approach involves a combination of models which accurately answer the scientific hypothesis and allow for translation of the findings. In the next sections, some historical and current models to investigate microglia functions in AD will be outlined.

1.8.1 Mouse models

The common effort to capture the complex clinical and biological aspects of AD in humans has led to the generation of multiple mouse models over the years. The mouse models of AD have allowed microglia labelling, depletion or altering gene expression using elegant genetic tools.

Some of the first generation transgenic (Tg) models include single, double or triple APP-Tg mice. These mice overexpress APP with or without fAD associated mutations. One of the most widely used models, the 5XFAD model is a double APP-Tg mouse. To generate the model, APP-Tg animals were crossed to mice containing PSEN1 mutations. The model contains APP^{SWE} mutation combined with Florida (I716V) and London (V717I) *APP* mutations as well as *PSEN1* M146L and L286V mutations (174). This leads to quicker amyloid deposition and acceleration of AD associated phenotypes such as synaptic degeneration and Aβ accumulation.

Overall, some drawbacks of the APP-Tg models include the random insertion of the transgene as well as the overexpression which does not accurately recapitulate human disease. Furthermore, the tau tangle pathology is not represented.

To overcome the issues associated with the APP overexpression, a second generation of models using humanized APP were generated. These mice contain either two (APP^{NL-F}) or three (APP^{NL-G-F}) fAD mutations. The model was generated using HDR approach by substitution of single base pairs to humanize the *APP* gene, hence these mice are known as APP KI mice (175). Mice from these models demonstrate Aβ deposition as early as 2 months and pronounced memory impairment (138).

Overall, there are some limitations which need to be considered with the use of animals to study AD irrespective of the model. Most strains lack the combination of all AD related characteristics focusing only on one hallmark, usually plaques or tangles. Ultimately this means that some important links and conclusions might be missed. Additionally, mouse studies demonstrate poor reproducibility and low translatability in humans. Most models demonstrate very early onset of symptoms as well as faster disease progression. Some of the advances in mouse model techniques have led to the generation of chimeric models which include the transplantation of human cells.

1.8.2 Cell culture

Although mouse models provide certain complexity, studies in mice are time consuming, expensive and require technical expertise. Therefore, the use of tissue culture allows a different approach to explore microglia functions but also provides flexibility allowing for multiple conditions and replicates.

1.8.2.1 Immortalized cell lines

Through the years, various microglia cell lines with either human or mouse origin were developed. These were mostly derived from primary microglia from the CNS through using viral transduction with various oncogenes (e.g. v-Myc, SV40 T antigen) to achieve immortalization. An example of a widely used microglia mouse cell line is the BV2 line. Another line derived similarly with human origin is the HMC3 line. Although these lines provide ease in the experimental design, recent

studies show that they significantly differ from primary microglia functionally and genetically (176). The development and characteristics of various microglia cell lines is reviewed in (177).

1.8.2.2 Primary microglia culture

Using primary microglia from brain tissues was valuable in the research of various microglial genes and their role in signalling. Obtaining human primary microglia is difficult due to the limited resource, therefore most primary microglia used in research is derived from rodents. In addition, there are available protocols for primary microglia cultures developed from non-human primates, to minimize the experimental differences (178).

Primary microglia cultures show upregulation of inflammatory and developmental genes. Importantly, these microglia transition back to standard *in vivo* gene expression profile when transferred into an adult brain (85). Studies by Turano *et al.* demonstrated that in immune challenged microglia *in vitro* expression of inflammatory genes varied depending on the presence of other neural cells in culture (179). These studies prove the importance of other neural cells in regulating microglial responses.

Although the human genes enriched in mouse microglia are only 30%, there are some key genes which are conserved between species (180). Based on some developmental similarities, the use of rodent microglia in research has been justified. Importantly, the timeline of microglia colonizing the human brain is similar as the one observed in rodents. In addition, microglia function is regulated by the microenvironment, although that can differ slightly between species (77). With advances in scientific approaches, these essential differences could be accounted for and minimized experimentally.

Although valuable and useful, murine cultures fail to translate fully to human pathologies due to key genetic and signalling pathway differences. In addition, obtaining healthy microglia cells from patients' brains postmortem or during operation is extremely difficult due to the limited material. Therefore, this led to

the development of human derived stem cell cultures, also known as induced Pluripotent Stem Cells (iPSC).

1.8.2.3 Stem cells

iPSCs could be generated from adult cells by reprogramming of few key transcription factors (181). The starting material could be obtained from various easily accessible sources. In the past 15 years multiple protocols for deriving microglia cells from pluripotent progenitors have been developed and recently some were reviewed in (182).

One of the main advantages is that these cells could be derived from patients carrying genetic alterations in the genes of interest, therefore the cultures will already express the desired characteristics. Due to the complex origin of microglia, they are considered to be as one of the hardest cell types to derive from stem cell precursors. There are various protocols developed ranging from 35 to 75 days for developing mature microglia. To resemble brain specific functions, the culture conditions of differentiated microglia-like cells should also match the brain microenvironment. There are several components which were defined as essential for microglia iPSC production. Colony stimulating factor-1 (CSF-1) is associated with microglia survival and proliferation, therefore most iPSC media is supplemented with M-CSF. In addition, TGF-β is also an important factor in microglia culture maintenance. Within the brain microglia are constantly exposed to serum, however as serum has high variability and is hard to ensure experimental reproducibility, Bohlen *et al.* identified cholesterol as a minimal requirement to maintain similar conditions (84). The development and advances in the iPSC field will be further discussed in more detail in Chapter 4 introduction.

1.9 PILRα

Paired immunoglobulin like type 2 receptor alpha (PILRa) belongs to the immunoglobulin receptor family. Fournier *et al.* first reported the presence of the receptor in cells of myeloid origin (183). The 44-kDa glycoprotein spans the membrane and contains a single Ig-like V-type extracellular domain. *PILRα* was mapped to chromosome 7q22. The receptor contains two immunoreceptor tyrosine-based inhibitory motifs (ITIM) intracellularly which inhibit signalling.

Another member of the paired immunoglobulin receptor family is PILRβ. In contrast to PILRα, it is an activation receptor and promotes intracellular signalling. PILRβ is the primary form expressed on NK cells. The receptor does not encode an ITAM domain and relies on DAP12 activation to induce signalling similar to TREM2.

The role of the PILR receptors is essential for regulating inflammatory responses which will be discussed further in more detail.

PILRα and PILRβ contain residues for sialic acid (SA) engagement and belong to the Siglec (SA-binding immunoglobulin-like lectin) family of receptors. Structural studies identified that both receptors have a typical Siglec-like fold important for ligand binding. In comparison to typical Siglecs, these receptors use hydrophobic interactions rather than disulfide bonds to confer stability (184). There are several identified ligands for PILRα, including mouse CD99, PILR-associating neural protein (PANP), NPDC-1 and collectin-12, all suggesting diverse immune functions of the receptor. Up to date, the only identified and functionally validated PILRβ ligand is CD99.

In combination, these receptors regulate the immune response by delivering opposing signals to cells. The balance between PILRa and PILRb signalling, and expression is most likely very tightly regulated and subtle changes might induce opposing responses. PILRβ was shown to regulate IL-27 production in PILRb (-/-) mice (185). Importantly, the receptor may play a role in regulating the balance between pro and anti-inflammatory cytokines. Some evidence from PILRb knock-out mouse models suggests that in the absence of PILRb, PILRa is overexpressed as detected by increased mRNA levels (185).

1.9.1 Structure and signalling

PILRα is an inhibitory receptor which upon activation uses its ITIM domains to recruit cytoplasmic phosphatases such as SHP-1 and SHP-2 via the Src homology -2 (SH2) domain. The phosphorylation of phosphatases causes dephosphorylation and inhibition of kinases such as Syk and prevents downstream signalling effects. PILRα consists of 7 exons and is a 303 amino acid long protein in humans (186). The protein has 3 reported isoforms, 1 membrane bound and 2 soluble. PILRa and PILRb share 83% amino-acid identity between their extracellular domains in humans and both compromise immunoglobulin superfamily V-set domain and stalk region (187).

Human and mouse PILRa demonstrate diverse biological functions and the identity between the protein structures can be seen in Figure 1.4. Interestingly, human PILRa does not interact with human CD99, but it can bind mouse CD99. These observations suggest that human and mouse PILRa have similar ligand recognition mechanisms. It was identified that PILRa ligand binding involves complex structures containing peptides and sugar antigen T (sTn). Furthermore, recognition of peptide regions by the receptor caused complex structural rearrangements. It is believed that ligand specificity of PILRa is determined by amino acid sequences, and C-terminal parts are essential since they are conserved across the majority of known PILRa ligands (188).

Figure 1.4: PILRa protein structure comparison between human and mouse. The human protein sequence (RefSeq ID NP_038467.2) and mouse protein sequence (RefSeq ID NP_705730.1) were 46% identical, using BLAST analysis.

1.9.2 Peripheral immune system role

Most of the prior knowledge referring to the function of PILRα relates to its role in innate immunity. The receptor is well-known for its function as a viral entry co-receptor. Studies by Satoh *et al.* first demonstrated that PILRα is essential for herpes simplex virus (HSV-1)

infection, and it aids the entry of the virus particles into cells (189). PILRa associates with glycoprotein B (gB) which promotes membrane fusion. Further investigation into this mechanism revealed that specific sialylated O-linked glycans residues on gB are required for the interaction with the receptor (190). In addition, PILRα functions as a coreceptor for other herpes viruses such as pseudorabies virus as demonstrated in (191).

PILRa function in innate immune responses in mice is related to neutrophil recruitment. Neutrophil infiltration to the site of infection was tested in Pilra(-/-) mice and revealed increased recruitment to infectious sites and susceptibility to endotoxin shock (192). This mechanism is regulated through integrin activation. Clustering of active PILRa leads to enhanced ITIM domain signalling and modulation of integrin β2 inside-out activation.

In addition to those studies, Pilra(-/-) mice were also studied to understand the role of PILRa in monocyte regulation. As demonstrated by Kohyama *et al.* PILRa regulates monocyte migration via integrin signalling like the one seen in neutrophils (193). In addition, these mice showed significantly higher numbers of macrophages in adipose and liver tissues. The authors suggest that the receptor plays an important role in obesity.

Although understudied, it was previously reported that PILRa works as a ligand for unknown receptors on a distinct population of NK cells. These interactions are crucial for activation and exerting cytotoxicity by the cells (194).

In terms of the role of PILRa in disease, it has been linked to inflammatory arthritis. Interestingly, under inflammatory conditions PILRa levels were shown to be increased in human samples. A study by Sun *et al*. utilized PILRa knock-out mice and revealed some important functions regulated by the receptor. $PILRa^{-/-}$ animals presented with more severe disease scores and modulation of the inflammatory response manifested by altered cytokine levels (195). Higher concentrations of IL-6 and IL-1β were reported which highlights that normal PILRa function might be required for regulating inflammation. Interestingly, the cytokine results demonstrated high variation between different immune cell types, and it was reasoned by the authors that this effect might be attributed to varying expression of PILRa across cells.

Recently a publication depicting the role of CD8 in T-cell quiescence identified that PILRa-CD8 interactions are crucial for maintaining $CD8^{+}$ T-cell pools (196). This interaction was

confirmed both in mice and humans and provides another example of the diverse range of responses where PILRa is involved. It also identifies another ligand for PILRa and shows that this interaction is conserved between species in comparison to other discussed PILRa ligands.

1.9.3 CNS function

In 2013 a meta-analysis by Lambert *et al.* identified the ZCWPW1 locus as risk for LOAD (35). *ZCWPW1* is found upstream of *PILRa,* and further analysis confirmed that the missense variant of PILRa is associated with AD risk (197). The causal link between the risk locus and the variant was further confirmed by additional GWAS and colocalization analysis using expression quantitative trait loci (eQTL) (198). Interestingly, risk associated with PILRa has been manifested in relation to another risk variant within NYAP1 (Neuronal Tyrosine Phosphorylated Phosphoinositide-3-Kinase Adaptor 1) (rs12539172). The study demonstrated that carriers of R78 PILRa show decreased blood concentrations of circulating PILRa and PILRb and suggest that this might contribute to the overall protective effect (199).

In the CNS, the receptor expression is mainly restricted to microglia, although some neuronal expression is detected. The allele frequency of PILRα is highly variable between populations, ranging from 10% in African populations to 65% in east Asian (200). The G78R variant of the receptor showed protective effect against AD development. The missense mutation caused decreased ligand binding and activation of the receptor, leading to increased intracellular signalling. The guanine (ggg) to arginine (agg) substitution alters the conformation of the ligand binding pocket, therefore modifying the amino acid sequence recognized by PILRα ligands. Rathore *et al.* tested the ligand binding of various exogenous and endogenous ligands to the G78 (risk) and the R78 (protective) variant of the receptor. The results showed significantly decreased activation of the R78 receptor. Consequently, this causes less intracellular inhibition and signalling (201). Due to the nature of arginine, amino acid with longer side chain, it forms a hydrogen bond with amino acid at position 140, therefore stabilizing the ‘’open’’ form. This conformational change and its effect on ligand binding are of high importance for cell response regulation. Furthermore, PILRα downregulation was observed in some brain regions of AD patients such as the entorhinal cortex (202). In addition, PILRα was

previously associated with modulating APP metabolism, however further investigation is required to validate these findings (203).

Previous identification of PILR-associated neural protein (PANP) which is expressed in neural tissues suggests that PILRα has a role in immune regulation in the CNS (204). PANP specifically binds PILRa but not PILRb, in comparison to other identified ligands such as CD99. The exact function of PANP and its interaction with the receptor is not known, however a variety of ligands might be involved in regulating PILRα function and cell response within the brain.

Previously a link between the protective (R78) variant of the receptor and HSV-1 titers in AD was reported. HSV-1 infects more effectively macrophages expressing the G78 form as compared to the R78. Comparison of patients with AD, mild cognitive impairment (MCI) and heathy controls revealed that those carrying the protective variant show increased IgG titers within the brain, therefore less brain damage (205). Interestingly, this study suggests a potential link between genetic and environmental risk for AD development.

A more recent publication identified PILRa to be enriched in microglia populations associated with amyloid and phospho-tau (pTau) in human postmortem tissue using single-nuclei RNA sequencing (206). In addition, using a program for identifying cell-cell interactions using the generated transcriptomic networks, an interaction between PILRa expressed on microglia and CD99 expressed on astrocytes was proposed. This potential cell crosstalk highlights the diverse functions that PILRa potentially regulates and why it might be particularly important during AD development. This diversity is further reinforced by additional structural work which revealed that PILRa contains calmodulin binding motifs (207).

Interestingly, PILRa has been associated with increased risk of age-related macular degeneration which is another disorder where progressive loss and accumulation of deposits is seen, which might suggest some common mechanisms exist (208). More importantly, PILRa was shown to negatively modulate the risk associated with identified AD risk genes *APOE* and *GM17* in large human cohorts. The observed effect was further

increased in homozygous individuals therefore suggesting a potential dose-dependent pattern (209).

Cumulatively, the presented studies demonstrate strong evidence about the role of PILRa in AD. However, up to date, no functional studies investigating the role of the identified G78R SNP in microglia have been published. Therefore, investigating the role of microglia in dementia relevant context might provide some novel insight into disease mechanisms and how they can be targeted.

1.10 Spleen tyrosine kinase

1.10.1 Structure and signalling

The spleen tyrosine kinase (SYK) is a 72kDa protein located intracellularly. The kinase contains two SRC homology 2 (SH2) domains and can be rapidly phosphorylated by ITAM domains on activated receptors (Figure 1.5). Some work in *Drosophila* models suggests that SYK functions are well conserved and originate from ancient evolutionary processes. Human and mouse SYK share 92% amino acid sequence homology. Downstream of SYK activation is a myriad of direct and indirect signalling intermediates, including PLCg2, PI3K and NFAT. Most often the activation of SYK is counteracted by phosphatases like SHP1. The ultimate signalling output is usually a product of the balance between Syk and SHP1.

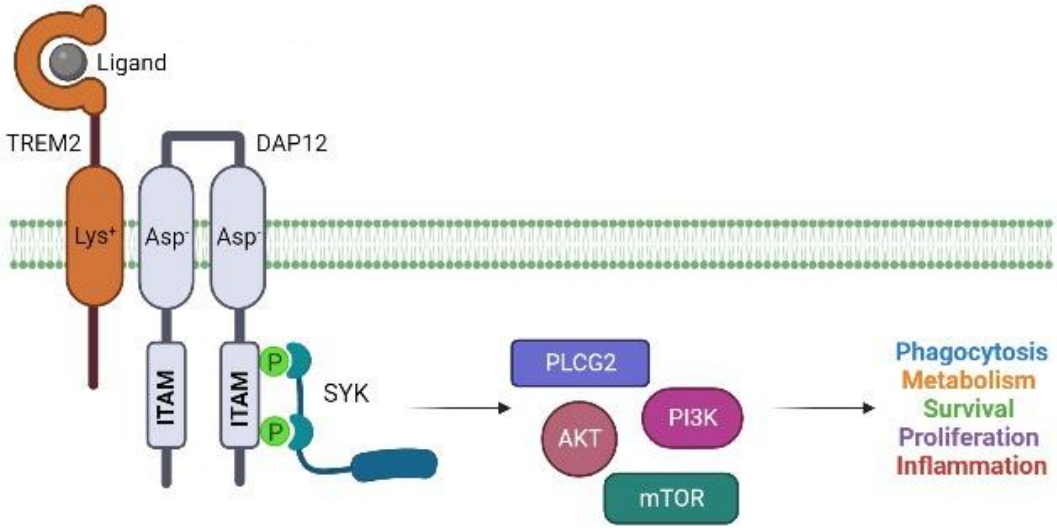

Figure 1.5: Activation and signalling of Syk. Receptor-ligand interaction can initiate activation of ITAM associated receptors such as TREM2. TREM2 activation recruits DAP12, which contains 2 ITAM domains. Direct interaction between DAP12 and Syk leads to phosphorylation of the SH2 domains and activates the kinase. SYK can initiate a complex response including interaction with

multiple signalling molecules which modulate cell function. SYK activity can alter phagocytosis, metabolism, cytokine release and many more.

SYK has 3 different activity states. Usually, in resting state the kinase domain is inactive and can be activated when both SH2 domains are bound to dually phosphorylated ITAM. Interestingly, the kinase can also be activated via phosphorylation of tyrosine residues in the linker region composed of interdomain A and B (Figure 1.6) which occurs in the absence of phosphorylated ITAM (210). The kinase domain is prone to autoinhibition in the absence of ITAM signalling which is achieved by binding between interdomain A, B and the kinase domain which contain the catalytic center in inactive state which was revealed from the crystal structure (211). In addition, SYK contains 10 autophosphorylation sites (212). Interestingly, there are 2 forms resulting from alternative splicing. The second isoform lacks 23 base pairs from interdomain B (213).

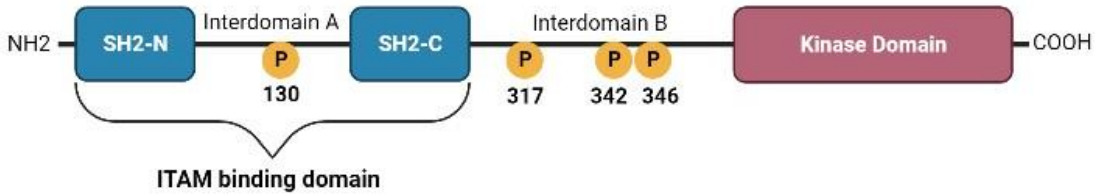

Figure 1.6: SYK protein domain structure. The kinase contains 2 SH2 domains, which function as ITAM binding site and bind phosphorylated receptors, and a kinase domain. Syk has the ability for autophosphorylation. Some key positions where phosphorylation occurs are indicated by the yellow circles. Image created with BioRender.

1.10.2 Peripheral immune system role

SYK function is wide and spans across different cell types and systems. The kinase is known to have a role in both adaptive and innate immunity as well as regulation of non-immune functions. Interestingly, SYK is known for mediating signalling not only via conventional ITAM containing receptors. Initially, SYK was characterized as an abundant kinase found in the spleen and thymus. SYK expression has been detected across multiple immune cells, including T-cells, B-cells, NK cells and macrophages.

SYK has been extensively studied for its role in B-cell maturation and transition. B-cell development undergoes a set of well-defined steps which are characterized by rearrangement of antigen receptors and expression of specific cell surface markers.

Studies demonstrate that *Syk* deficient mice present with lower pool of pre-B cells, with many pro-B cells failing to transition successfully (214). Furthermore, immature B cells were unable to complete maturation and effectively convert into recirculating B cells.

Importantly, SYK has been identified to have a major role in regulating macrophage inflammatory responses. Although initially studied for its role in adaptive immunity, studies present that SYK has a key role in regulating innate immune responses and especially macrophage-mediated inflammatory responses. Phosphorylation of SYK is demonstrated within several minutes after stimulation by TLR ligands in different macrophage cell lines (215). Interestingly, this signalling pathway can be initiated through exposure to minimally oxidized low-density lipoprotein (mmLDL) (216). This study demonstrates that in macrophages SYK can mediate lipid accumulation, cytokine expression and ROS production. Additionally, some of the cytokine release associated with SYK activation in macrophages has demonstrated some conflicting findings. The majority of publications report that SYK induction leads to secretion of inflammatory cytokines and mediators such as NO and promote activation of macrophages (217, 218). However, there are conflicting studies which show that SYK can mediate anti-inflammatory responses as well and suppress activation although these findings are less conclusive (219). Additionally, *Drosophila* studies indicate that immunoreceptor-Syk interactions are essential for phagocytosis, a key macrophage function (220). A more recent publication using Syk KO cells demonstrates that in the absence of the kinase insufficient phagosome acidification occurs due to impaired lysosomal fusion. The publication implies that SYK is involved in modulating actin remodeling during phagocytosis (221). This evidence demonstrates the essential role of SYK in modulating macrophage functions.

A particularly important role of SYK outside of its immune functions is its involvement in vascular development. *Syk* deficient fetuses present with blood-filled lymphatic vessels (222). This indicates that SYK function is essential for separation of the lymphatic system from general circulation during development. The exact role of the kinase was not well understood until a few publications suggested that this effect is attributed to platelet activation signalling via CLEC2, SYK and PLCg2, resulting in closure of blood-lymphatic

shunts (223). The role of SYK and CLEC2 signalling in platelets is further reinforced for the normal development of the brain vasculature (224).

Interestingly, SYK is also involved in osteoclast signalling. SYK function is mediated via FcRγ and DAP12 signalling and loss of function in this pathway results in Nasu-Hakola disease, where patients present with presenile dementia (156).

A wide variety of natural and synthetic SYK inhibitors exist and some are already applied for the treatment of disease. Due to the diverse immunological roles of SYK, most clinical effort has concentrated on autoimmune and hematological cancer treatments (225). Unsurprisingly, most synthetic SYK inhibitors used in the past demonstrate a wide range of off-target effects in clinical trials terminating future developments. In 2018, the first Syk inhibitor was approved by the FDA for the treatment of chronic immune thrombocytopenia (ITP) for patients showing insufficient response to other treatments (226).

Altogether these findings demonstrate the extremely varied nature of SYK induced signalling and its importance for key homeostatic cellular functions and processes.

1.10.3 CNS function

The role of SYK in the context of neurodegeneration and AD dates back to the late 20th century when a study by McDonald *et al*. utilized primary rat microglia and immortalized monocyte cultures. Exposure to Aβ fibrils revealed dose and time-dependent activation of SYK and associated nitric oxide production which was diminished by pharmacological inhibition of the kinase (227). Another study just a couple years later using very similar methodology further revealed that SYK is in fact essential for inducing cytokine responses, particularly TNF-α in microglia which in turn leads to elevation of iNOS expression (228).

For almost a decade there were no further advances towards understanding the role of SYK in the context of dementia. Lebouvier *et al*. was the first who demonstrated that SYK can phosphorylate tau, primarily at Tyr-18 residue (229). This led to a series of publications focusing on this direction. It was demonstrated that in the Tg Tau P301S mice inhibition of SYK leads to a reduction of tau phosphorylation which was proposed to be mediated via GSK3β and PKA signalling pathways (230). In addition, important

research dissecting the role of SYK in neurodegenerative models was carried out by Schweig and colleagues (231). In their first study, using overexpression mouse models of amyloid (Tg PS1/APP^{swe}) and of tau (Tg Tau P301S) it was demonstrated that pathological activation of Syk is present in the brain. The findings further reinforced the role of the kinase in terms of tau hyperphosphorylation demonstrating that SYK is present in neurons containing hyperphosphorylated and misfolded tau in the cortex and hippocampus *in vivo*. More importantly, neurons demonstrate worsening of pathology which correlates with high levels of SYK. The transgenic mouse model findings were further recapitulated in human AD samples which were immunopositive for SYK activation. Overexpression of SYK was also reported in other mouse models such as the Tg19959 (232).

These investigations were further carried out in other publications focusing on more detail about the pathways which SYK might regulate linking to tau phosphorylation. Interestingly, using neuronal model SH-SY5Y cell in vitro, it was demonstrated that hyperactivation of SYK increases hyperphosphorylated tau whereas genetic SYK inhibition leads to lowering of tau levels (233). The study further links the effects seen by SYK inhibition to the mTOR pathway and suggests autophagy is responsible for increase in total tau degradation. Taking these findings *in vivo* in the Tg Tau P301S model chronic SYK inhibition leads to improved locomotor functions and decreased mTOR activation. These mice also presented with decreased levels of Iba1 and iNOS which were used as markers of gliosis. Furthermore, a third publication by the same authors examined the neuroinflammatory effects induced by SYK caused by tau hyperphosphorylation using organotypic brain slices (234). Overall, cultures from Tg Tau P301S mice show increased cytokine production which is fully antagonized by SYK inhibition. In addition, LPS stimulation which causes increase of pro-inflammatory cytokines was also alleviated though inhibition of the kinase. Altogether the combination of these findings demonstrates that SYK has an important role in mediating tau hyperphosphorylation and inflammatory response but does not focus on its role in glia or on the effects of amyloid pathology.

Other reports link SYK function to processes which might be relevant in AD context. The function of SYK has been linked to formation of stress granules (SG). SG which contains

large complexes of mRNAs emerge during cellular stress when normal protein synthesis is halted. These complexes can induce apoptosis and have been noted in AD due to the chronic inflammation processes. A couple of publications indicate that SYK is recruited to SG and can modulate their clearance via autophagy (235, 236). In addition, in microglia cultures recruitment of SYK to SG was reported to inhibit the phagocytic abilities of cells. Additionally, using nilvadipine treatment, which lowers SYK activity, was shown to alleviate symptoms linked to traumatic brain injury including spatial memory and inflammation (237).

Just recently, two key publications in the field demonstrated the role of SYK in microglia using an amyloid model of AD (238, 239). Utilizing a conditional knock-out system in the 5XFAD mice, both papers used very similar experimental strategy to highlight transcriptomic, phenotypic and behavioral changes associated with deletion of *Syk* in microglia. The first publication by Wang *et al.*, links the response identified in the knock-out animals associated with TREM2 signalling. The presented work further reinforces the association of SYK with activation of the GSK-3β-mTOR pathway. Overall, conditional *Syk* deletion results in increased Aβ deposition, worsening of behavioral phenotypes and loss of DAM associated microglia signature. Detailed histological analysis reveals that microglia do not associate with plaques and phagocytic abilities are significantly impaired. Furthermore, exploring the effect of SYK in conjunction with known $TREM2^{R74H}$ risk variant revealed that activation of CLEC7A which promotes SYK activity can improve microglia activation and rescue TREM2 associated phenotypes.

Using a systemic model of demyelination caused by experimental autoimmune encephalomyelitis (EAE), Ennerfelt and colleagues demonstrate that *Syk* deficient mice present with significantly less oligodendrocyte precursor (OPC) cells which is mediated via microglia defects rather than direct effect of SYK on the oligodendrocyte lineage. This result highlights the broad spectrum of functions which SYK can modulate and reinforces the importance of cell crosstalk in neurodegeneration.

Overall, these publications highlight the importance of *Syk* for microglia responses during AD pathology and regulation of neuroinflammatory processes.

1.11 Hypothesis and general aims

The overarching theme in this project involved understanding how identified genetic risk variants can modulate microglia functions and how this can relate to the well documented role of microglia in AD. Using a combination of models and methods, the project focused on understanding the role of the PILRa receptor and the Syk kinase. Although a direct link between these does not functionally exist (up to date), they represent important molecules for microglia functions and studying in depth how they can impact microglia responses can provide novel insights. These genes highlight the complexity of microglia function and the balance between activation and inhibition which is key for microglia homeostasis and determines the ultimate functional outcomes. PILRa functions as an inhibitory receptor whereas Syk phosphorylation leads to activation of downstream signalling pathways. Therefore, it is important to understand how both activation and inhibition and the ultimate balance between these pathways can alter disease progression.

The more detailed aims of each chapter are highlighted below.

Chapter 1: Developing models to study PILRa *in vitro*

At the beginning of this project, although the G78R SNP within PILRa was genetically associated with risk of AD, no functional data about the role of the receptor in microglia specifically was available. This thesis aimed at providing a novel insight into how the G78R variant of PILRa regulates microglia-relevant functions which might provide cues as to how it can alter AD risk.

Due to the high expression of PILRa in myeloid cells, an immortalized mouse macrophage precursor (MOP) cell line was selected for preliminary studies. Combining molecular biology and viral techniques, the goal was to generate overexpression cell lines containing either G78 or R78 PILRa. The objective was to use these cell lines to optimize some of the assays required later in the project as well as all the reagents in a system that can be easily manipulated and allows to draw parallels between macrophage and microglia functions. The models used in this chapter were selected based on the required duration to validate, optimize, and produce preliminary data which can serve as a platform for more in-depth complex investigations. All assays were selected based on key microglia functions which we hypothesized can be altered by the presence of the hypofunctional variant.

Chapter 2: The role of human G78R PILRa in iPS derived microglia-like cells

Most published work suggests that PILRa functions as a negative regulator of microglia activation, therefore the protective effect of the variant lies with enhancement of microglia activity (201). However, no functional data testing this hypothesis has been published for microglia-specific models. With advances in the field throughout the project and the need to use more disease-relevant models, iPS derived microglia-like cells were introduced. This chapter focused on using CRISPR-Cas9 technologies to generate isogenic cell lines which mimic patient samples more closely and represent a more relevant model for microglia-specific functions. In this chapter, characterized microglia-like cells homozygous for G78, R78 or heterozygous PILRa were subjected to an array of phenotypic assays which explored the effect of the variant on microglia functions. Additionally, the PANP ligand was selected to investigate any differences between G78 and R78 cells upon activation.

Chapter 3: Validation of *Syk* cKO in APP^{NL-G-F} mouse model and associated early transcriptomic changes

When this thesis began, there was very limited knowledge of the role of *Syk* in AD specific context, but more importantly in microglia, with only a few publications focusing on tau mouse models or using non-immune immortalized cell lines (229).

The primary aim of this chapter was to establish the efficacy of the selected model and to validate the cKO of *Syk.* We hypothesized that using tamoxifen in the Cre-ERT expressing animals will lead to deletion of exon 1 of the *Syk* gene which will cause reduction in mRNA expression and protein levels of SYK (Figure 1.7). Additionally, the dosing regimen of the drug had to be established and evaluated since it has not been previously tested in this strain in our group. This model was selected based on its ability to produce targeted effects in Cx3cr1 expressing cell, including microglia and because it allows manipulation of the time at which cKO is induced. Furthermore, combining this model with the APP^{NL-G-F} AD model enables us to research the role of *Syk* in disease-relevant context focusing on the amyloid pathology since this is heavily understudied.

Some additional work included exploring and generating preliminary data about the role of *Syk* in microglia early in disease development using single-cell RNA sequencing. Identifying

genes which are altered on transcriptomic level in the cKO animals might provide some useful cues to pathways and molecular processes which are regulated by *Syk* in microglia.

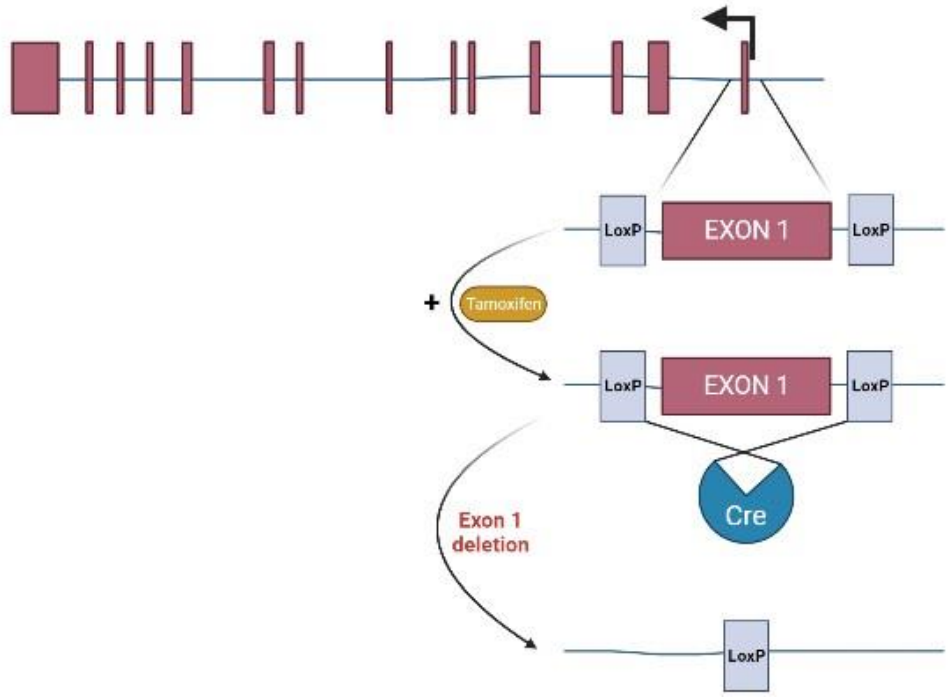

Figure 1.7: Mouse model used in this thesis. Exon 1 of the Syk gene (containing 14 exons in total) has been flanked with 2 loxP sites inserted into the sequence. When tamoxifen is administered, the Cre recombinase translocate to the nucleus where it facilitates site-specific recombination of the LoxP sites leading to deletion of exon 1.

Chapter 4: Syk cKO alters microglia transcriptional profile in microglia and modulate AD pathology in aged APP^{NL-G-F} mice

It is now well established that microglia have a pivotal role in AD development and onset. Therefore, how *Syk* will impact disease progression and disease relevant hallmarks such as amyloid deposition were key questions in the field. When this study commenced no work existed on how *Syk* deletion will modulate AD progression in terms of amyloid pathology. Just recently, at the final stages of the project, 2 publications using identical methodology were published answering some of these questions (238, 239). Both utilize the 5xFAD mouse model of AD. The aim of this chapter was to investigate *Syk* role using the APP^{NL-G-F} model which arguably mimics human disease better although still exhibiting faster disease development trajectory.

Furthermore, it is well documented that microglia undergo transcriptional changes which result in phenotypic and morphological differences in AD (152). This chapter focused on investigating if *Syk* cKO will affect different disease development microglia associated changes using transcriptomic approaches.

Chapter 2 General Methods

2.1 Methods

2.1.1 Buffers and Solutions

All reagents used were supplied by Thermofisher Scientific or Sigma Aldrich if not specified otherwise.

Table 2.1: List of solutions and reagents used in this thesis.

Solution	Ingredients
Mammalian Cell Lysis Buffer	100mM Tris pH 8.5 5mM EDTA 200mM NaCl 0.2 % (v/v) Sodium Dodecyl Sulphate (SDS) Nuclease free water
Lidocaine Solution	0.4g lidocaine-HCl 50mL DPBS 5mM EDTA
Tris- Acetate-EDTA (TAE) Buffer	50 x TAE stock solution Distilled water
0.1% Triton X-100 buffer	Triton – X – 100 1 x DPBS (Gibco)
FACS wash	1X DPBS 5mM EDTA 2mM NaN_3 0.5% BSA
FACS block	FACS wash 5% (v/v) filtered rabbit serum 2.4G2
MUSE staining solution	1X DPBS 625ng/mL Propidium Iodide (PI) 500ng/mL LDS 751
Freezing media	10% (v/v) DMSO 90% (v/v) heath inactivated filtered FBS
2% formaldehyde	1X DPBS 36.5-38 % formaldehyde solution with methanol
4% formaldehyde	4% (w/v) Paraformaldehyde powder 1 x PBS
MACS buffer	5mM EDTA 0.5% BSA 1X DPBS
MACS block	5% (v/v) filtered rat serum 5% (v/v) filtered rabbit serum 10µg/mL 2.4G2 MACS buffer
Pre-stimulation media	1X IMDM 15% heath inactivated filtered FBS Pen-Strep 10ng/mL IL-3 20ng/mL IL-6

	25ng/mL SCF
0.5mM EDTA	1 x DPBS 0.5M EDTA
iCell8 buffer	1 x DPBS (Ca^{2+}/Mg^{2+}) 0.5% BSA 5mM EDTA DNase I (30ul/mL) RNAsin (2ul/mL)
iCell8 block solution	1 x iCell8 buffer 3.5% BSA 4ug/mL TruStain FcX PLUS
MeOH rehydration solution	1 x DPBS (Ca^{2+}/Mg^{2+}) 0.01% BSA
MeOH wash solution	1 x DPBS (Ca^{2+}/Mg^{2+}) 0.1% BSA
Geltrex	Geltrex (Gibco) 1 x KO-DMEM
Fibronectin solution	Fibronectin (Gibco) 1 x DPBS
70% Formic acid (v/v)	Nucleic free water 100% formic acid
Histology blocking buffer	1 x PBS 0.05% Tween (v/v) 5% normal goat serum
Block (ICC)	1 x DPBS 5% serum 0.3% Triton X-100
Antibody dilution buffer (ICC)	1 x DPBS 1% BSA 0.3% Triton X-100
0.01% sodium azide	1 x DPBS 0.01% (v/v) sodium azide
Amyloid Glo solution	1% (v/v) AmyloGlo (Biosensis) 0.9% saline solution
Citrate antigen retrieval solution	Distilled water 1% citrate buffer (100X)
0.05% Tween	0.05% Tween (v/v) 1 x DPBS

2.2 Cell Culture Maintenance

2.2.1 Incubation and Media

All cell cultures were incubated at 37°C in humid incubator with 95% air 5% CO_2.Dulbecco's Modified Eagle Media (DMEM) and Roswell Park Memorial Institute 1640 (RPMI) were supplemented with 10% heat-inactivated filtered Fetal Bovine Serum (FBS) and 1% Penicillin-Streptomycin (PS) antibiotics. Cell lines were maintained in 6-well plates, T75 flask and T175 flasks.

2.2.2 Cryopreservation and Thawing

Cell suspensions were transferred to 50mL falcon tubes and centrifuged for 5 minutes at 350 x g. After discarding the supernatant, the cell pallet was resuspended in 1mL of freezing media per $3x10^6$ cells. The media was aliquoted in cryotubes adding 1mL to each and frozen in Mr. Frosty™ (Thermofisher) at -80^oC overnight. The stock was then transferred to liquid nitrogen for long term storage.

For iPS cells alternative freezing solution was used (Table 2.2). Cells were frozen from confluent 6-well plates, aliquoting $1x10^6$ cells per cryovial. After detaching the cells with EDTA as described in section 2.3.7, the cell pallet was resuspended in half the volume required for the cryovials with E8 (Gibco) and 2X freezing media was added at equal volume.

Table 2.2: iPSC 2xfreezing media.

2X Freezing media
20% (v/v) DMSO (Sigma)
20% (v/v) Knock-out DMEM (Gibco)
60% (v/v) ES-qualified FBS

Cells from the liquid nitrogen storage were placed in 37^oC water bath until ice crystals disappeared. The vial content was further transferred to 10mL of fresh media and centrifuged for 5 minutes at 350 x g, to remove any trace of DMSO. The cell pellet was resuspended in the appropriate media after removing the supernatant and placed in the correct culturing vessel. Additionally, for iPS cells, Y27632 dihydrochloride, also known as Rock inhibitor (RI) was added to each well at 1:1000 from stock solution (10mM)

2.2.3 Counting

Cells were primarily counted using the Muse Cell Analyzer (Merck Millipore). Muse tube was used to dilute cells at 1:10 or 1:20 ratio with MUSE staining solution and incubated for 5 minutes at room temperature (RT). Cell count was measured following manufacturer's instructions and recorded. Alternatively, in a separate tube Trypan Blue solution was mixed with some of the cells at ratio 1:1. Cells were counted using a standard 4x4 hemocytometer, adding 10µL on each side and counting only the light cells.

iPS cultures were counted with NucleoCounter® NC-250 (Chemometec) using NC-Slide A2 (Chemometec) Cells were prepared by mixing 1µl of DAPI solution (Chemometec) and 19µl

of cells suspension. The mixed cells were added to a slot on the slides and counted via the manufacturer's instructions.

2.3 Cell Lines

2.3.1 Jurkat Cell Line

Jurkat cells are immortalized human T-cell lymphocyte line derived from the peripheral blood of a leukemia patient (240). Jurkat cells are non-adhesive and were cultured in RPMI 1640 media. Cultures were passaged twice weekly at 1:10 or 1:20 ratio. Firstly, the cell suspension was centrifuged at 350 x g for 5 minutes and the supernatant was removed. The cell pallet was resuspended in fresh media and cells were aliquoted into new culture vessels.

2.3.2 Jurkat Lucia Cell Line (Invivogen)

Jurkat Lucia cells were derived from Jurkat line by stable integration of NFAT-inducible Lucia reporter construct. The Lucia gene encodes coelenterazine-utilizing luciferase which is secreted upon NFAT activation. Following stimuli treatment, measuring the levels of Lucia luciferase provides an indication of NFAT induction (Figure 2.1). Cells were cultured in IMDM media supplemented with Normocin (50µg/mL). In addition, to keep the selective pressure, Zeocin was added at 100µg/mL every other passage. Cells were passaged twice a week as previously described for standard Jurkat cell lines.

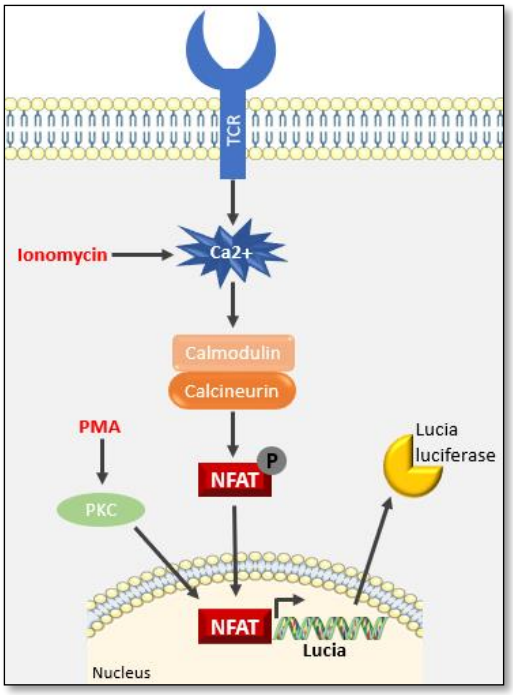

Figure 2.1: Induction of Jurkat Lucia cells. Upon stimulation via ionomycin/PMA, dephosphorylation of NFAT occurs, which promotes its translocation to the nucleus. NFAT further stimulates the expression of the Lucia gene, which leads to secretion of coelenterazine luciferase. (Adapted from Invivogen.)

2.3.3 HEK293T Cell Line

The Human Embryonic Kidney 293T cell line was generated from human embryonic cells through stable expression of SV40 T-antigen (241). The 293T cells were cultured in complete DMEM and passaged 2-3 times per week at ratio 1:20. Media was aspirated from the culture vessel and the cell monolayer was washed with Dulbecco's Phosphate Buffered Saline (DPBS). Next, pre-warmed 0.05% Trypsin-EDTA was added, and cells were incubated at 37°C for 5 minutes. After cell detachment, an equal volume of media was added to neutralize the trypsin. The cell suspension was transferred to a 50mL falcon tube and centrifuged for 5 minutes at 350 x g. Supernatant was removed, and the pellet resuspended in fresh media. Cells were gently mixed with the pipette to ensure good spread in a new culture vessel.

2.3.4 EcoPack

EcoPack cells were derived from the HEK293 embryonic kidney cell line. This cell line was utilized to produce retroviral stocks using transient transfection. Viruses produced using this

line can be applied to mouse and rat cells. All culture conditions and procedures for these cells were kept the same as for HEK293 cells as described above.

2.3.5 Macrophage Precursor (MOP) Cell Line

Polyclonal conditionally immortalized macrophage precursor (MOP) cells were originally derived from $CD117^+$ mouse bone marrow cells, which were transfected with retrovirus carrying a *HoxB8* gene, induced by oestrogen. These cells were maintained in standard RPMI media supplemented with 10µM oestrogen and 10µg/mL recombinant murine granulocyte-macrophage colony stimulating factor (GM-CSF). Cells were passaged at 1:10-1:40 dilutions as required, every 2-3 days.

Table 2.3: List and details of the mouse strains used to create MOP cell lines used in this thesis.
Both lines were created in parallel to minimize any potential experimental differences. Methods used to create these cell lines can be found in section 2.8.

Genotype	Age	Gender
PLCG2 WT	7 weeks	Male
PLCG2 KI	6 weeks	Male

2.3.5.1 MOP Differentiation

Oestrogen and GM-CSF were depleted from MOP cells by washing cultures 3 times with 10mL standard RPMI media. The cells were centrifuged at 350xg for 5 minutes and on the last wash they were counted as previously described. Cells were plated at $1x10^6$ per well of a 6-well plate with 5mL media supplemented with 20ng/mL macrophage colony stimulating factor (M-CSF). The differentiating cells were incubated for 4 days at 37^oC, and the media was replenished on day 2/3. Initially a lot of cell death was visible but by day 4 of incubation a monolayer of cells was formed. Differentiated cells were further harvested before used for downstream applications.

2.3.6 Ba/F3

The Ba/F3 cells are IL-3 dependent murine pro B-cell line derived from C3H mice. The exact origin of the line is not clear, however some evidence suggests it has a lymphatic background and is potentially a subclone of the earlier Ea3 cell line (242, 243). Ba/F3 cells were acquired from the Leibniz Institute DSMZ and cultured in RPMI media with 10% FBS, supplemented with 10ng/mL mouse IL-3 (Peprotech). Ba/F3 cells which are non-adherent

with doubling time of 20 hours were grown in T-75 flasks or 6-well plates. Cultures were split every 3 days at 1:10 ratio to keep optimal cell density and growth. Supernatant was collected and centrifuged at 350 x g for 5 minutes. The media was aspirated, and the cell pellet was resuspended in an appropriate volume of fresh cell media. Cells were mixed well and transferred to a new culture vessel.

2.3.7 Kolf2-C1 iPS cells

The Kolf2 iPSCs were generated from dermal fibroblast obtained from healthy volunteers by the Sanger Institute's Human Induced Pluripotent Stem Cell Initiative (HipSci) project. The lines were generated using the CytoTune 1 Sendai method. The Sendai virus reprogramming system includes particles which are employed to transduce target cells with replication-competent RNA molecules, and which encode the original set of four reprogramming factors. The Sendai method of reprogramming is highly efficient in comparison to other methods and kits are now commercially available to allow individual laboratories to perform the process independently. The Kolf2-C1 line used in this thesis is a well-characterised subline of the Kolf2 line (244). Both Kolf2 and Kolf2-C1 lines carry mutations in *COL3A1* and 19-bp deletion in *ARID2 (245)*. The Kolf2-C1 clone served as a parent to the more recently developed and characterised Kolf2-J1 line (246).

Kolf2 iPS cells were grown in 6-well plates with 2ml of E8 flex media (Gibco) to maintain pluripotency. Cells were passaged usually every 2-3 days or when large colonies started appearing. Cells were passaged 1:2 to 1:10 depending on the following applications. Colonies were washed with DPBS once media was aspirated and 1mL of 0.5mM EDTA was added. The plate was returned to the incubator for 6-7 minutes with regular monitoring for rounding up of the cells under microscope. EDTA was aspirated and appropriate volume of fresh E8 flex media was added to each well using zig-zag movements to gently detach the cells. The detached cells were transferred into new culture vessel pre-coated with Geltrex, by dripping slowly around the dish to achieve even distribution. The cells were left to adhere in the hood for 5-10 minutes before returning in the incubator.

2.3.7.1 Factory establishment

2.3.7.1.1 Embryoid body (EB) formation

To aid the formation of embryoid bodies (EBs) an established method using AggreWell (Stem Cell Technologies) plates was utilized. To prepare the plate prior to addition of cells,

the wells to be used were gently rinsed with DPBS, followed by 500uL of AggreWell Rinsing Solution (Stem Cell Technologies). The plate was centrifuged at 2500 x g for 3 minutes to eliminate microscopic air bubbles. Following this, the wells were rinsed with DPBS and 1mL of 2xEB media with 2uL RI per well was added and plate was returned to the incubator until cells were prepared.

Between 2-3 confluent wells of iPS cells from a 6-well plate were required for the set-up of 1 factory. Media was aspirated from the selected wells and cells were gently rinsed with DPBS. 1mL of pre-warmed TrypLE (Gibco) was added per well and plates were returned to the incubator for 5-7 minutes until colonies appeared rounded and detached from the surface. The detached cells were carefully collected using some DPBS and added to falcon tubes containing 30mL DPBS to dilute the detaching reagent. Aliquot was taken for counting as previously described in section 2.2.3. The cell suspension was spun at 400 x g for 5 minutes. DPBS was aspirated and pellets were resuspended with fresh pre-warmed E8 media to final concentration of $3.5x10^6$ cells/mL. 1mL of cell suspension was added to the AggreWell well and the plate was spun at 100 x g for 3 minutes with the break off. After centrifugation wells were inspected to ensure even distribution of cells around the microscopic wells and returned carefully to the incubator overnight avoiding disruption of the cells.

On the following day, the AggreWell plate was very carefully checked under a light microscope for the formation of EBs in each well. The wells containing EBs were given 75% media change with fresh pre-warmed EB media. 1mL of media per well was slowly aspirated and very gently dropwise 1mL of new media was added. This procedure was repeated once more, following which the plate was returned to the incubator.

The feeding procedure was repeated the following day again. After EBs received fresh media, 5mL serological stripette was used to gently lift and aspirate the EBs from the well. The EBs were split between 3 wells of a 6-well low-attachment plate (Thermofischer). Each well was topped up with 5mL of pre-warmed EB media and plates were transferred in the incubator and left with no interference for 4 days.

2.7.3.1.2 Harvesting EBs

T-175 flasks were prepared in advance by pre-coating with Gelatin (Gibco). 10mL of coating factor was added to each flask before transferring to the incubator for around 1 hour. After coating, the solution was aspirated and replaced with 20mL of factory media. Flasks were kept in the incubator until later.

The 6-well plate containing the EBs was carefully tilted to collect them on the edge of the well. Using a serological stripette as much media as possible was removed and replaced with 2mL per well of fresh pre-warmed factory media. EBs from all 3 wells were pooled together, collected with serological stripette and gently expelled into the already prepared flask. Alternatively, if too many EBs are available, they can be split equally between 2 flasks. The flask was gently swished to allow for even distribution of EBs around the surface after which it was carefully placed in the incubator and left undisturbed for a week.

Factories were fed with fresh factory media once weekly. In the first couple of weeks 10mL media was added, and once precursors start occurring 20mL or more of media was added. Always at least 20% of the original factory volume was left.

2.7.3.1.3 Harvesting of microglia precursors and terminal differentiation from factory

After enough monocytes started appearing in the factory, we proceeded with harvesting. Supernatant from the flask was gently harvested by aspiration while avoiding damaging or detaching any EBs and then passed through a 40µM cell strainer to eliminate any large clumps, debris or EBs which might have been collected by mistake. Aliquot for counting was collected. The supernatant was centrifuged at 400 x g for 5 minutes. The resulting pellet was resuspended in an appropriate volume of pre-warmed microglia media to yield the required cell concentration for the subsequent application. Cells were plated in the chosen plate format and returned to the incubator. The precursors began to adhere over the next day and by day 3 clear microglial morphology could be seen. Cells received a 50% media change with fresh microglia media on day 7 and were used for functional assays on day 10. Occasionally, if low adherence was observed for a specific clone, plates were pre-coated with fibronectin solution.

Table 2.4: Media components for microglia differentiation. All ingredients include final concentration in the media. For 2xEB media after seeding the final concentration is half of the values here. All cytokines supplied from Peprotech.

2X EB media	Factory media	Microglia media
E8 flex (Gibco)	XVIVO15 (Lonza)	DMEM/F12 (Gibco)
BMP4 100ng/ml	GlutaMAX 1X	GlutaMAX 1X
VEGF 100ng/ml	Pen/Strep 1X	Pen/Strep 1X
SCF 40ng/ml	2-mercaptoethanol 50uM	M-CSF 25ng/ml
	M-CSF 100ng/ml	TGF-β1 50ng/ml
	IL-3 25ng/ml	IL-34 100ng/ml
		GM-CSF 10ng/ml

2.4 Functional assays

2.4.1 Phagocytosis

2.4.1.1 MOP cells

MOP cells were differentiated as previously described in 6-well plates. On day 3 of the differentiation when macrophages were already present, media was aspirated from the wells. The monolayer was carefully washed with DPBS and around 1 mL of Accumax was added to each well and the plate was incubated at 37^{o}C for 5 minutes. Cells were then detached carefully by pipetting or using scraper and the suspension was centrifuged at 350 x g for 5 minutes. After this, the cells were resuspended in fresh media and counted using Muse. Cells were plated at 3-4x10^{4} cells per well in 200µL of media containing M-CSF in µClear black plates (Greiner). When re-plating cells it was aimed to have enough cells in each well but not a completely confluent monolayer as this made analysis less accurate due to overlap of cells and their borders. Plates were left overnight in cell culture incubator to allow for cells to attach properly. M-CSF was kept in the assay media at 10ng/mL during the duration of the whole experiment.

2.4.1.2 iPS derived microglia

For iPS derived microglia-like cells no replating was required as these were already plated in the appropriate format and density for the assay when harvesting precursors as explained in section 2.7.3.1.3. Usually, 7x10^{3} cells per well were plated for 384-well and 3x10^{4} cells per well for 96-well.

2.4.1.3 Zymosan preparation

Zymosan particles derived from *S. Cerevisiae* were conjugated to pHrodo™ red dye. The lyophilised particles were resuspended in 8mL Live imaging solution and sonicated using sonicator on ice for 15 cycles of 30 seconds at 50% amplitude which allowed complete separation of the particles. The stock was aliquoted at 3mL in 15mL plastic Falcon tubes and stored at -20^{o}C. Before use, aliquots were left to thaw at room temperature and then the solution was briefly vortexed to ensure proper resuspension. Particle concentration in each batch was quantified by counting on the Muse.

2.4.1.4 Assay

On the day of the assay, media from the experimental plate was aspirated and changed with fresh media appropriate to the specific cell type containing 5µM Cytochalasin D (CytoD) or DMSO as negative control. The cells were incubated for 45 minutes at 37^{o}C.

Following the incubation media was aspirated. Cell mask green (1:1000), 2 drops/mL NucBlue Hoechst, and CytoD or DMSO at the same concentration were resuspended in Live imaging solution and 100µL per well were added for 96-well format and 50µL for 384-well plates. The stains were incubated for 10 minutes. The plate was then carefully washed two times with Live imaging solution and 50 or 100µL were added per well. Next, baseline images were taken on the Opera Phenix, allowing for calibration of individual channels.

When calibration was complete, the plate was taken back, and media was aspirated. It was replaced by 100µL of Live imaging solution containing pH-Rodo zymosan particles and CytoD or DMSO. Negative control wells were left with only live imaging solution and no zymosan particles. The plate was loaded back into the machine and measurements were taken every 20 or 25 minutes for 6 timepoints.

2.4.2 Seahorse

All Seahorse experiments were conducted using the Seahorse XFe96 Analyser (Agilent) using the Seahorse XF Real-Time ATP Rate Assay Kit (Agilent) according to instructions. Cells were plated a day before the experiment at $3x10^4$ (this density was estimated to be optimal for the experiment from pilot tests, data not shown) per well of 96-well Seahorse plate. Some wells were stimulated with LPS (100ng/mL) or LPS (100ng/mL) and IFN-γ (20ng/mL) added to the media overnight (~18 hours). After cell plating, the cartridge was hydrated with 200µL of

Seahorse calibrant solution (Agilent) and left in 37°C incubator with no CO_2. On the day of the assay, the supernatant from each well was collected (later used for Legendplex cytokine analysis) and replaced with 180µL of Seahorse media containing 10mM glucose, 1mM pyruvate and 2mM glutamine. The cells were returned for around 1 hour in an incubator set at 37°C with no CO_2. In the meantime, the provided drugs for the test were prepared as indicated in table 2.5 and loaded to the cartridge. Once cartridge was ready it was loaded into the Seahorse instrument which was pre-warmed to 37°C and calibration was initialized. Following calibration, the plate containing cells was inserted and the assay started. After the test was complete and readings were acquired, the plate was imaged using Celigo Imaging Cell Cytometer (Nexcelom Biosciences) to obtain cell counts for normalization.

Table 2.5: Drugs used for Seahorse ATP assay.

Compound	Volume to resuspended in	Final concentration	Port	Loading volume
Oligomycin	420uL	150uM	A	20uL
Rotenone/Antimycin A	540uL	50uM	B	22uL

2.4.3 Legendplex

The concentration of various cytokines and chemokines in cell culture was detected using the 13-plex macrophage/microglia panel (Biolegend). A detailed list of cytokines included in the panel can be seen in Table 2.6. Cell cultures of choice were stimulated with LPS (100ng/mL) or LPS and IFN-γ (20ng/mL). All assays were performed in 96-well V-bottom plate format. The desired stimulation timepoint was collected by aspirating the medium from the wells and transferring to a new U-bottom 96-well plate and immediately stored at -80°C until the assay day.

On the day of the assay, plates containing supernatant were thawed on ice and 25µL of medium was used for the experiment. The assay was run in accordance with manufacturer's instructions. In brief, 7 standards were prepared by 1:4 serial dilution and 25µL was added from each one to the plate. Both sample and standard wells contained 25µL of assay buffer and everything was run in duplicate vertically. Finally, 25µL of premixed beads was added and the plate was sealed with foil film and incubated for 2 hours at room temperature with 800rpm shaking. Following this, the plate was washed twice with wash buffer, 25µL of detection antibodies added to each well and incubated additional 1 hour with the same

settings. Immediately after incubation, 25µL of RA-PE antibodies were added and the plate was incubated additional 30 minutes. This was followed by 2 washes and final resuspension with 150µL of wash buffer. The plate was run on Attune NxT flow cytometer using the CytKick platform. Flow cytometer set up details are available in section 2.18.6.

Table 2.6: List of all 13 cytokines included in the human/mouse kit of the assay. Differences between the two kits are highlighted in red.

Mouse cytokine panel	Human cytokine panel
CXCL1 (KC)	Arginase
TGF-β1	IL-1RA
IL-18	IL-4
IL-23	IL-23
CCL22(MDC)	IP-10
IL-10	IL-10
IL-12p70	IL-12p70
IL-6	IL-6
TNF-α	TNF-α
G-CSF	IFN-γ
CCL17 (TARC)	TARC
IL-12p40	IL-12p40
IL-1β	IL-1β

2.4.4 Endocytosis assay

Cell subjected to endocytosis assay were prepared similarly as phagocytosis plates. Microglia-like cells were directly plated in 384-well plate format ready on the experimental day.

2.4.4.1 Dextran preparation

pH Rodo Green Dextran was prepared by diluting 1 vial of lyophilised stock with 500µL of Live imaging solution and vortexed well. Stock solution was kept in -20°C.

2.4.4.2 Assay

Media was aspirated from cells and replaced with media containing 50µM Dynasore (Abcam) which supresses both clathrin-dependent and independent endocytosis or DMSO.

Cells were incubated for 30 minutes at 37°C after which media was removed from the plate. Live imaging solution containing NucBlue Hoechst (2drops/mL), Cell Mask Red (1:1000) and Dynasore (50µM) or DMSO was added to each well and incubated for further 10 minutes. Cells were subsequently washed twice with DPBS, live imaging solution was added to each well and calibration images were taken using the Opera Phenix (Perkin Elmer). Following this media was aspirated again and replaced with live imaging solution containing dextran (40µg/mL) with Dynasore (50µM) or DMSO. Negative control wells received only live imaging solution. Images were taken using the Opera Phenix every 20 minutes during 5 timepoints.

2.5 Cloning

All cloning steps are individually described below, and a summary of the whole process can be seen in Figure 2.2. DNA concentrations for every step were measured using the Nanodrop™ (Thermofischer).

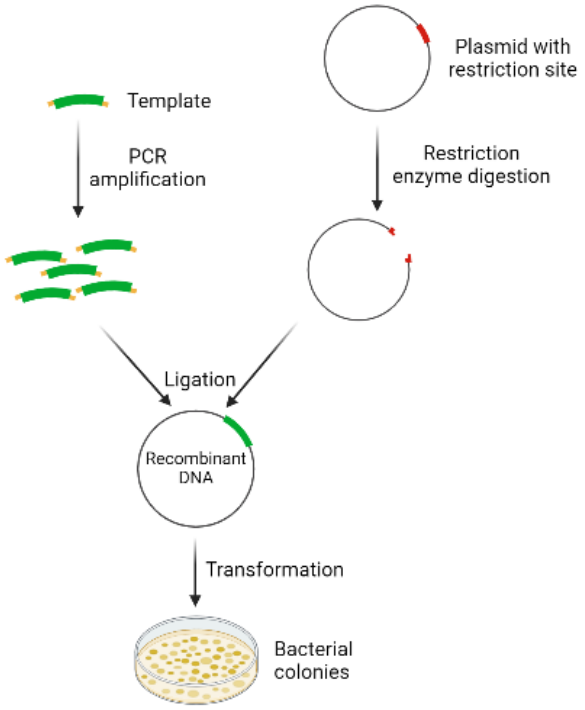

Figure 2.2: Cloning process summary. First the desired insert was amplified through PCR using specific primers usually from another vector or directly from cDNA. The vector of choice which contained a restriction site was digested via restriction enzyme creating a "break" in the circular DNA. The amplified template and the vector are then combined, and ligation occurs creating the new recombinant DNA which contains the insert of choice. The newly generated vector is

transformed into bacteria which are grown, and individual colonies are screened via PCR. Image generated with BioRender.

2.5.1 Vectors

Two vectors were utilized in this thesis. The ampicillin resistant pLSW-IRES-Puromycin (SIPW) vector (10,154bp) contained a puromycin resistance and was developed in house by Dr. Luke Davies, adapted from (247). The second vector, pFB-Neo (6572bp) was also ampicillin resistant and contained a neomycin resistance sequence. A detailed vector map of pFB-Neo sequence can be found in Appendix.

2.5.2 Preparation of plasmid stock

For each genotype, a falcon tube was filled with 5mL of Luria-Bertani (LB) broth and supplemented with 5µL of Ampicillin (100µg/mL) for final concentration of 5µg/mL. Sterile pipette tip was used to scrape the pre-existing glycerol stock and was inserted into the appropriate tube. Subsequently, the prepared samples were incubated for 6 hours at 37^{o}C with 150rpm. Meanwhile, autoclaved flasks were filled with 100mL of LB broth and supplemented with 100µL of Ampicillin. Following the incubation, the contents of the falcon tubes were emptied into the flask and were further incubated at 37^{o}C with 225rpm overnight. Amplified plasmids were purified on the following day using Qiagen Maxi Prep kit as per manufacturer's instructions (Invitrogen). The final plasmid was eluted in nuclease-free water and stored in -20^{o}C until further required.

2.5.3 Preparation of insert

Inserts were amplified from plasmid stocks. Infusion primers were first designed with 15bp overhangs between the target insert and the vector as per manufacturer's instructions (Takara).

As the full length PILRa sequence was amplified from the SIPW vector and it was already preceded by a Kozak sequence (CCACC) upstream of the start codon to improve translation, it did not need to be altered. The Phusion primer sequences can be seen in Table 2.7.

Table 2.7: Phusion primer sequences used to amplify target templates.

Direction (5'-3')	Target	Sequence
Forward	CD99	GGATCCCGGGCTCGATCGAGCCACCATGGCGCG
Reverse	CD99	TACCAGGCCTCTCGACTACACGGGGGCGGAGCC
Forward	PILRa	AATTCGGATCCTCGACCACCATGGGTCGGCCCC

Reverse	PILRa	ATCGCGGCCGCTCGAGTTAGGCCTTTAAGACAGAGTACAG

Multiple PCR reactions were performed to amplify the insert using high-fidelity Taq Phusion™ polymerase as per manufacturer recommendation (NEB). The correct temperature to achieve the best amplification conditions for the PCR reaction was optimised by performing gradient PCR with increasing temperature and the brightest band was identified. Once the correct conditions were identified and the insert was amplified and electrophoresed, the gel was placed under a UV transilluminator. The band with the correct size was excised using a scalpel and purified with NucleoSpin™ PCR clean-up kit (Macherey-Nagel). The resulting DNA was resuspended in nuclease-free water.

2.5.4 Vector linearisation

The required vector was linearised by using 3µg of the chosen plasmid and addition of the correct volume of restriction enzyme, *Xho I*, indicated by the manufacturer (NEB). Additionally, Cut Smart buffer was used to adjust the final reaction volume to 50µL in 0.2mL PCR tubes. To allow linearisation, the reaction was heated to 37^{o}C and incubated for at least 1 hour, followed by heating to 65^{o}C for 15 minutes to deactivate the enzyme using the Mastercycler Nexus Gradient PCR machine (Eppendorf). Reaction details can be seen in table 2.8.

Table 2.8: Vector linearisation reaction volumes. The reaction volume and individual reagents volume is indicated. Negative control undigested reaction was run in parallel.

Reagent	Digested	Undigested
Vector	3µg	3µg
10x Buffer (CutSmart NEB)	5µL	5µL
Restriction enzyme (*Xho I*)	5µL	0µL
H_2O	Adjust to total 50µL	Adjust to total 5µL

To ensure successful linearisation, the reaction product was compared to the circular template by running then on 1% agarose gel which is previously described in section X. The linearised vector was further purified using the NucleoSpin™ PCR clean-up kit (Macherey-Nagel). The resulting product was resuspended in nuclease-free water and stored at -20^{o}C.

2.5.5 Transformation

The vector and insert were combined according to the Infusion cloning kit. 200ng of linearised vector and insert equivalent to 3:1 molar ratio was added, followed by 2ul of Infusion enzyme mix in a PCR tube. The reaction was complete to final volume of 10µl with nuclease-free water. The resulting mix was incubated for 15 minutes at 50°C, then cooled on ice and stored in -20°C until further use. The newly generated plasmid was transformed into NEB 10-β Competent *Escherichia coli* (*E. coli*;10-β) cell as advised by the manufacturer. Aliquot of cells (50µl) was gently thawed on ice and 1µL of the cloning reaction mix was added. The mix was incubated on ice for 30 minutes, followed by heat shock at 42°C for 30 seconds and returned on ice for another 5 minutes. Once cooled, 950µL of stable outgrowth media (NEB) was added and the mix was incubated for 1 hour at 37°C with shaking at 250rpm. Serial dilutions were prepared from the transformed 10-β cell using LB broth. Pre-warmed LB agar plates containing 100µg/mL Ampicillin were used to spread 100µL of cell suspension with a plastic spreader. Plates were incubated for 20 minutes at 37°C and then inverted for overnight incubation. The formed bacterial colonies were screened via colony PCR.

2.5.6 Colony PCR

Master mix was prepared using GoTaq PCR mix (Promega) and primers designed to target either side of the insert (Table 2.9). Colonies were picked with individual clean pipette tips and added to the master mix. A minimum of 10 colonies were screened per transformation. The resulting PCR product was electrophoresed on a 2% agarose gel. Any colonies which produced a band of the expected size, and therefore contained the insert were selected again with a clean tip and incubated in 10mL of LB broth containing 100µg/mL Ampicillin overnight with shaking at 225rpm at 37°C in X incubator (Sigma Aldrich). If on the following day bacteria had successfully grown, LB broth would appear cloudy, glycerol stock was prepared. In a cryovial 600µL of autoclaved glycerol was added and mixed with 400µL of the cloudy LB broth and stored in -80°C until required. The remaining broth was used to purify the plasmid using Miniprep Kit (Thermofischer Scientific) following manufacturer's instructions. The final plasmid was eluted in nuclease-free water and sample was sent for Sanger sequencing (Eurofins genomics). Sequences were checked against the predicted

template and if confirmed, plasmids were prepared for further applications as detailed in section 2.5.7.

Table 2.9: Primers used for colony PCR. Direction of each primer and the target are indicated.

Direction (5'-3')	Target	Sequence
Forward	pFB-Neo x PILRa	CCATCCTCTAGACTGCCGGA
Reverse		GGTGGAAAATAACCGGATCGC
Forward	SIPW x CD99	GGGCTGGCTTAACTATGCGG
Reverse		GCTCGCTTGGATCCGAATTC

2.5.7 Sample preparation for sequencing

All sequencing was completed using Sanger sequencing by Eurofins Genomics (Wolverhampton, UK). The samples were sent as a premixed solution of 15µL plasmid DNA (50-100ng/µL) and 2µL primer (10pmol/µL). Additional primers used to sequence lentiviral vectors are listed in Table 2.10. The resulting sequences were checked for the guanine to arginine base pair substitution at position 78.

Table 2.10: List of primers used for sequencing different PILRa variants.

Primer target	Direction (5'→ 3')	Sequence
PILRA-FL-G78	Forward	CTCCGACAGACTGAGTC
	Reverse	GGAAGCATAGACGATGC
PILRA-FL-R78	Forward	AGCCTAGTGGCTCCAC
	Reverse	GGAAGCATAGACGATGC
PILRA-CD3z-G78	Forward	AGCCTAGTGGCTCCAC
	Reverse	AGTGCATTGTATACGCC
PILRA-CD3z-R78	Forward	CTCCGACAGACTGAGTC
	Reverse	AGTGCATTGTATACGCC

2.6 Virus production

2.6.1 Lentivirus

All lentiviral work was conducted in accordance with the local safety regulations and risk assessment procedures were followed. Category II laminar flow hood was used, and all waste was bleached as required per safety requirements.

2.6.1.1 Transfection

Appropriate number of flasks were seeded with $9x10^6$ HEK293T cells a day before the transfection from a pre-existing culture. The cells were detached using trypsin and counted as previously described after which they were plated in complete DMEM media and mixed

thoroughly to ensure good spread of cells across the flask surface. Flasks were incubated at 37°C overnight.

Following the incubation, the cell layer was washed with DPBS, where caution was taken not to detach the cells. The DPBS solution was aspirated, and fresh media was added, after which cells were placed at 37°C. The lentiviral components were mixed as shown in table 2.11. All volumes provided were used in T175 flask and Effectene transfection reagent (Qiagen) was used. The volume was made up to 600µL with Buffer EC and 36µL of enhancer was added. The mix was incubated for 5 minutes at RT. Following this, 120µL of Effectene was added and the mix was further incubated for 10 minutes. In the meantime, flasks were filled with 20mL of fresh media. Following the incubation 5.2mL of media was added into the lentiviral solution and mixed well with Pasteur pipette. The solution was added dropwise directly onto the cells in a manner that did not disturb the layer and the flask was swirled delicately to assure good spread. Cells were incubated for 48 hours at 37°C.

Table 2.11: Amount of plasmid required for the Effectene transfection kit.

Plasmid	Volume (µg)
pCMVd8.91 packaging plasmid	1.5
pCMVMD2G envelope plasmid	1
Lentiviral plasmid (e.g., SEW)	2

2.6.1.2 Collection

Media from the flasks was transferred into appropriately labelled falcon tubes. For an optional collection after 12 hours, the flasks were filled with fresh media and incubated at 37◦C.

2.6.1.3 Sucrose Purification

Supernatant was filtered through 0.45µm sterile filter into 50mL tube. Beckman ultracentrifuge conical tubes were layered with 3mL autoclaved 20% sucrose solution. The filtered media was carefully overlaid on top, forming two distinguishable layers. The conical tubes were inserted into the buckets and appropriate balance was created using sucrose or media. Buckets were placed on the rotor and the ultracentrifuge was run at 26,000rpm for 90 minutes at 4◦C. Following this, the sucrose and media layers were removed by tipping into bleach and the tubes were inverted for 10 minutes on a paper towel. Excess media was dried, and the virus pellet was resuspended in 1mL of fresh media and left for 20 minutes at

RT. During the optional second collection only 0.5mL were used to resuspend the pellet to adjust for the virus titer. The virus was aliquoted at 200µL in cryotubes and kept at -80◦C for long term storage.

2.6.1.4 Lentivirus Titration

In order to assess the efficiency of each batch of virus, Jurkat cells were infected by adding a small amount of the virus. Cells were counted as previously described and $2x10^5$ cells were seeded to each well in a 24-well plate and standard RPMI media was added to a final volume of 200µL. Lentiviral stock was aliquoted into 1.5mL tubes at 0.5µL, 1µL, 2.5µL, 5µL and 10µL per well. The volume was topped up with media to 100µL. After gently mixing, the virus was added directly into the appropriate wells by slowly dripping and ensuring good spread within the well. One well per plate was not infected with virus to provide a baseline control. Plates were incubated for 3 hours and then the total volume was made up to 500µL with media. Following this, further incubation for 48 hours at 37°C was carried out before assessing GFP infection levels with flow cytometry. Example of this can be seen in section 3.2.4.

2.6.2 Retrovirus

Ecopack cells were counted as previously described and seeded at $1x10^6$ cells per well in a 6-well plate. Plates were returned to the incubator and left overnight at 37°C. The following day media was replaced with 2ml of fresh DMEM per well. In a sterile Eppendorf 100ul of DMEM (no FBS) were mixed with 6ul ViaFect™ transfection reagent (Promega) per well and incubated at room temperature for 5 minutes. After this, 1ug of DNA per well was added, mixed, and incubated for further 15-20 minutes. Following the incubation, the mix was directly added to the cell culture wells and the plates were returned at 37°C. The next day, plates were transferred to 32°C and left overnight. Supernatant was harvested and polybrene was added to final concentration of 5µg/mL and subsequently filtered through a 0.45µm filter. The viral stock was aliquoted into 1mL cryovials and stored at -80°C for up to 3 months without any freeze/thaw cycles.

2.6.2.1 Spin infection

MOP cells were counted and aresuspended with MOP media at $5x10^5$ cells/mL. 250µL of cell suspension was added to each well of a 12-well plate. 850µL of viral supernatant, thawed in advance, was added to each well directly. The plate was then centrifuged at 1500rpm for 90

minutes at 25°C. Immediately after the spin, 2 to 3 mL of fresh MOP media was added to each well and the plate was returned to 37°C for 48-72h.

2.7 Flow Cytometry

All samples were run on Attune NxT flow cytometer (Thermofischer Scientific). Photo multiplier tube (PMT) voltage settings were kept constant between experiments where possible.

Table 2.12: Summary table for antibodies and dyes used in this thesis for flow cytometry experiments, including species, final concentration and fluorochrome.

Target	Host species	Target species	Clone	Concentration/ Dilution	Fluorochrome	Supplier
PILRa	Rabbit	Human	2175D	1µg/10^6 cells	AF488	R&D Systems
CD11b	Rat	Mouse	M1/70	2.5µg/mL	AF700	BioLegend
CD11b	Rat	Mouse	M1/70	2.5µg/mL	AF700	Invitrogen
CD45	Rat	Mouse	30-F11	0.5 µg/mL	eFluor450	Invitrogen
Syk	Mouse	Mouse	5F5	1µg/mL	R-PE	BioLegend
Propidium Iodide	N/A	N/A	N/A	1 drop/1mL	N/A	Thermofischer
Rabbit IgG Control	Rabbit	Human	60024B	0.5µg/10^6 cells	AF488	R&D Systems
TruStain FcX PLUS (CD16/32)	Rat	Mouse	S17011E	0.4µg/mL	N/A	Biolegend
AffiniPure F(ab')$_2$ Fragment IgG	Donkey/Goat	Human	Polyclonal	1:500	APC	Jackson ImmunoResearch

2.7.1 Unstained Sample Preparation

Cells of the chosen type were counted as previously described and aliquoted into 15mL falcon tubes. 2% v/v formaldehyde (PFA) was added at equal volume to reach the final concentration of 1%. Cells were incubated for 20 minutes on ice. Following this, the tubes were centrifuged for 5 minutes at 350 x g. Supernatant was removed and the pellet was resuspended in 200µL of FACS buffer.

2.7.2 Cell surface marker staining

M-CSF differentiated MOP cells in 6-well plate were washed twice with sterile PBS solution carefully so that the cell layer is not disturbed. Following this, lidocaine solution was added, and the plate was incubated for 10-15 minutes at 37°C. Cells were gently detached by pipetting slowly and were transferred into falcon tubes. Alternatively, iPS microglia-like cells

were detached using Accutase for 10 minutes at 37°C. The cell suspension was centrifuges and cell pallets were resuspended in fresh media, following which cells were fixed. Fixation was achieved using 2-4% PFA for 20 minutes at room temperature. $4x10^5$ cells were added to a 96-well U-bottom plate, centrifuged and resuspended in 50µL FACS block. The plate was incubated for 20 minutes at RT. Meanwhile, antibodies were diluted at 2x concentration in 50µL FACS buffer and added to each well. The samples were then incubated for 30 minutes on ice under foil. Following incubation, cells were washed 3 times with FACS buffer using centrifugation. On the last wash, cells were resuspended in 200µL FACS buffer and transferred to appropriate tubes for flow cytometry analysis.

2.7.3 Intracellular marker staining

Staining for any intracellular markers required permeabilization. As for cell surface staining, each cell type was lifter as described before. Once cells were fixed, they were resuspended in 90% ice-cold methanol, vortexed and left on ice for 30 minutes. Following incubation, the methanol was removed carefully due to the pellet being vulnerable and it was proceeded with staining as described above. Another permeabilization method involved using 0.3% Triton X-100 for 10 minutes on ice, following which cells were blocked and stained as per the standard protocol.

2.8 Generation of conditionally immortalized MOP cell line

2.8.1 Isolation and CD117-magnetic labelling of bone marrow cells

PLCG2 WT and KI mice were sacrificed, and the femurs were collected. The bone marrow from the femurs was collected by flushing the bone using MACS buffer and subsequent filtering with a 40µm strainer. Following this the cells were resuspended in MACS block at $40x10^6$ cells/mL and left to incubate for 10 minutes at 4°C. After, CD117-biotin was added at equal volume to reach a final concentration of 1 in 100. Cells were further incubated for 15 minutes at 4°C and spun at 350xg for 5 minutes. Supernatant was removed and cells were resuspended in 10mL MACS buffer and spun again. This was repeated twice more. After the last centrifugation, 90mL MACS buffer and 10mL MACS beads were added per $1x10^7$ cells and incubated for 15 minutes on ice. Following the incubation, 10mL MACS buffer was added, the cell suspension was spun again, and cells were resuspended in MACS buffer. Meanwhile, the LS column was prepared by running 3mL of MACS buffer. The cell suspension was added and after running through, an additional 3mL of MACS buffer was

added and let to fully run. MACS buffer was added two more times, and the flow was kept for safety until ensuring that there are cells on the column. The column was detached and washed through in a clean 50mL falcon tube with 5mL MACS buffer after which cell count was recorded.

2.8.2 Pre-stimulation of precursor cells

The collected cells were resuspended in pre-stimulation media at 10^6 cells/mL. Cells were incubated for 2-3 days in that medium before proceeding to the next steps.

2.8.3 Spin infection of expanded precursors

Pre-stimulated cells were harvested and resuspended in 2mL of standard MOP media. 250µL of cells were added to each well of a 12-well plate and a further 850µL viral supernatant was put into each replicate. The cells were centrifuged at 1500xg for 90 minutes at 25^{o}C. After spinning was complete, 3mL fresh MOP media was added to each well and the cells were incubated for 2 days at 37^{o}C.

2.8.4 Antibiotic Selection

Cells were supplied with 1.5µg/mL of puromycin and transferred to a larger culture vessel. Media was replaced every 2 to 3 days, cytokines were appropriately added and puromycin selection was continued. Around day 10, if enough viable cells were present, early passage stocks were frozen for future use. By day 14 puromycin addition was discontinued and more cells were frozen as previously described.

2.9 CRISPR-Cas9

Cells were grown in 6-well plate format until around 80% confluent on the day of CRISPR.

Table 2.13: Sequence of oligos used in PILRa iPSC CRISPR.

Oligo type	Sequence (in reverse)
CRISPR guide 1 (crRNA)	CUCCAGGAUAUUCUCACGUC
CRISPR guide 2 (crRNA)	AGAAGGACUGCCUGUGGAAG
HDR oligo (ssDNA template)	G*T* CCA GTT CAG AAA GAG CCG GTT CAC ATA ATC CTT GTG AAT GGA AGG CGG CCT TGT GCT GTA GAA GGA CTG TCC ATG GAA ATG CCC CCG TCT CCA TGA AAT CCT TAC ATC CGG AGC TGT GGC TAA CTC CCA GGG GTA ATA GAA GGA GAA GGG GAT TTC CAC AGA GCC ACC CAT* G*G

2.9.1 Preparing the RNP complex

Lyophilized oligos were resuspended in IDTE buffer at 200µM. The guide (crRNA - sequence in table 2.13) was resuspended in 10 µL buffer and fluorescent ATTO500 tracrRNA was resuspended with 100µL buffer. Equal volumes 1.7 of crRNA, tracrRNA and duplex buffer were mixed together and heated to 95^{o}C for 2 minutes to allow for annealing of the oligos. The mix was cooled at room temperature before addition of 5µL Cas9 complex and incubated for 20 minutes at room temperature. Immediately before electroporation 100pmol repair template was added.

2.9.2 Nucleofection

Cells were pre-treated for 30-60 minutes with RI prior to the procedure. Media was aspirated and cells were washed with DPBS. After this, pre-warmed Accutase was added directly to the cell monolayer, cells were incubated at 37^{o}C and periodically monitored under light microscope until fully detached. The dissociated cell suspension was transferred to a 15ml falcon and pelleted by centrifugation for 3 minutes at 1000rpm. Cells were resuspended in PBS and counted. Approximately 1x10^{6} cells were used per transfection. The required number of cells were aliquoted, pelleted and resuspended in 100µL of nucleofection solution containing 78µL Lonza buffer P3 and 22µL supplement. The previously made complex was added to the solution. The cell suspension was transferred to the nucleofection cuvette and nucleofected using the Amaxa 4D system, programme CA137. Cells were allowed to recover for around 10 minutes in the incubator before addition of any media. Following this, cells were added to a pre-coated culture dish containing E8 media, RI (1:1000), Pen/Strap and 1µM SCR7 and returned to the incubator overnight.

2.9.3 FACS sorting

On the following day, media from the nucleofected cells was aspirated. The cell monolayer was washed with PBS once and then Accutase was added. After cell dissociation, the suspension was pelleted and resuspended in 500µL media containing RI and Pen/Strap and transferred to a suitable FACS tube. In addition, an Eppendorf was prepared for collection of sorted cells containing media. Everything was kept on ice for the duration of the FACS sort. The top 10,000 cells were collected. Sorted cells were seeded aiming at a single-cell suspension into pre-coated with Geltrex 10cm dish containing E8 media, RI and Pen/Strap.

Cells were incubated overnight at 37°C. The following day, media was replaced to remove the RI.

2.9.4 Colony selection

FACS sorted cells were grown until formation of defined colonies around the culture vessel. Individual colonies were picked manually and seeded into 96-well plate. The cells were left to grow until fully confluent and then split in 1:2 ratio into identical 96-well plate which was used for screening of successful CRISPR clones.

2.9.5 Screening

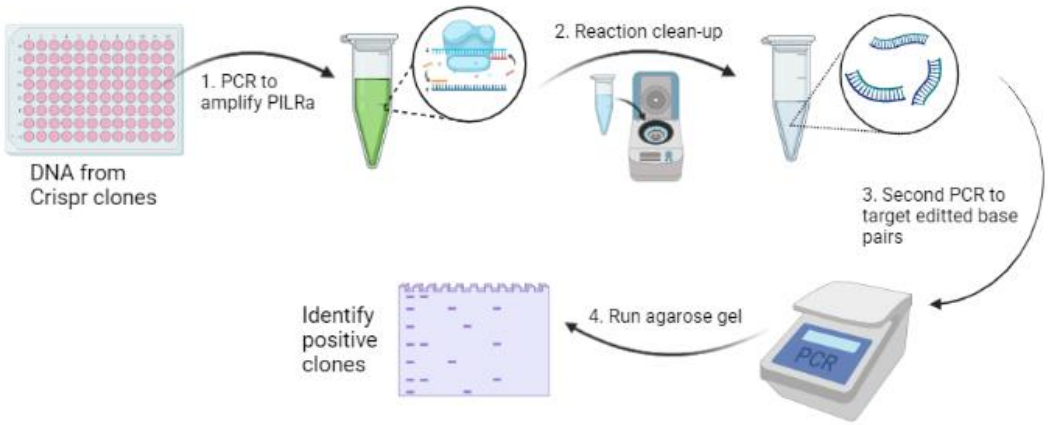

Figure 2.3: Summary of the screening process used to identify positive PILRa CRISPR targeted clones.

2.9.5.1 DNA extraction

Fully confluent 96-well plate was processed simultaneously by treating each well in parallel. All media was aspirated from the plate, and it was washed with PBS once. Then to the cell monolayer 50µL of cell mammalian lysis buffer was added. The plate was wrapped tightly in film and incubated at 50°C in humidified incubator for 3 hours or overnight at 37°C. The plate was removed from the incubator and allowed to cool at room temperature. To ensure successful lysis wells could be checked under a microscope where no cells should be visible. Following lysis, 100µL of ice-cold NaCl-ethanol solution was added directly to each well. The plate was allowed to sit still for at least 1 hour at room temperature. After this a network of genomic DNA was visible as white fibrils at the bottom of the well. All subsequent washes were done with extra caution because DNA can be easily detached and lost. The plate was gently inverted over paper towels to remove supernatant being careful not to cross-contaminate different wells. Next, 200µL of 70% ethanol was added to each well and again

the plate was inverted onto a paper towel. This wash step was repeated two more times. Alternatively, ethanol can be aspirated using a multi-channel pipette, but extra care should be taken not to touch the bottom of the plate and disturb the DNA. Following the last wash, the plate should be left at room temperature for around 30 minutes to allow for any ethanol residues to dry and evaporate. After making sure the wells are completely dry, 50µL of TE buffer (1X) were added to each well and mixed to resuspend the DNA. The plate was stored at 4°C or -20°C for long term storage. The DNA concentration from each well was quantified using NanoDrop™ (Thermo Fischer Scientific). Any wells where the DNA was too concentrated further dilutions were made.

Alternatively, when generating more clones, a commercially available DNA extraction method was used. Quick Extract (Lucigen) solution was applied to each well after removing media and washing the colonies gently with DPBS. 50µL of Quick Extract was applied to each well and the end of the tip was used to disrupt the colonies by scraping the bottom of the well. The plate was left at room temperature for 5 minutes to ensure complete lysis. The solution was transferred into 96-well PCR plate, sealed, and ran in a thermal cycler as per manufacturer's instructions. The resulting DNA was kept at -20°C until screening.

Standard 25µL PCR reactions were prepared using SYBR Green and 1µl of genomic DNA from each 96-well. The settings used can be seen in Figure 2.4.

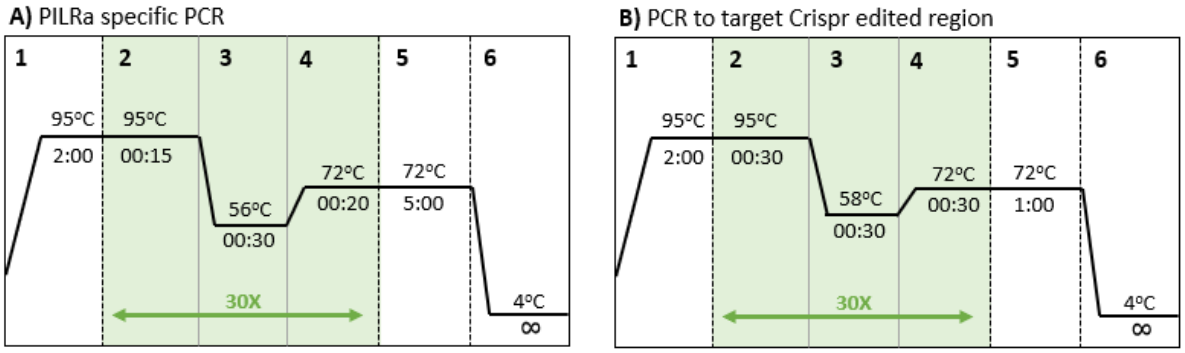

Figure 2.4: PCR cycle conditions required for screening positive CRISPR clones. (A) Schematic of the PCR cycle conditions used to amplify PILRa specific region containing the base pairs of interest. **(B)** Cycle conditions used for the second PCR used to screen for the specific PILRa variant change and identify positive clones.

2.9.5.2 Reaction clean-up

All PCR reactions were cooled on ice and then 25µL of DNA-se free water was added to each well to produce 50µL final volume per well. The reactions were then cleared using Macherey-Nagel kit per manufacturer's instructions. In short, each 50µL PCR reaction was mixed with 2 volumes or 100µL of buffer NTI and then transferred to a NucleoSpin column placed in 2ml collection tube to allow for DNA binding. Tubes were spun for 30s at 11,000 x g. Following this, 700µL of buffer NT3 was added to the column and tubes were centrifuged again at the same setting. This wash step was repeated once more. Finally, tubes were centrifuged for 1 minute at 11,000 x g so that the column membrane could dry. Each column was transferred into a clean 1.5ml Eppendorf and 20µL of DNA-se free water was added directly onto the membrane and incubated at room temperature for 1 minute. Tubes were subsequently spun at 11,000 x g for 1 minute. The resulting cleared product was used for the second PCR reaction.

As previously described 25µL reactions were prepared using 1µL from the first PCR clean-up. The reactions were incubated using programme outlined in Figure 2.4B and then ran on 2% agarose gels.

Table 2.14: Primer pairs used for CRISPR screening and subsequent off-target check.

Primer name	Sequence (5'-3')	Product size (bp)
PILRa specific Forward	GGCTCTCCTCACTCACCTCAA	986bp
PILRa specific Reverse	GGTCGTCAGAAGAAGTGGGG	
G78 CRISPR Forward	AGACGGGGGCATTTCCATGGA	340bp
G78 CRISPR Reverse	CAGAAGAAGTGGGGTCTGAGGTG	
PILRb Forward	AGCATTTCTGCAGCCTGGT	861bp
PILRb Reverse	ATGGAAGGGGTAGCAAGGTG	

2.9.5.3 Sequencing

All clones which produced a band with the correct size on the agarose gel were identified and sent for sequencing as previously described in section 2.5.7 to confirm the R78G nucleotide change (Eurofins Genomics).

2.10 Quantitative (qPCR)

2.10.1 Genotyping

2.10.1.1 DNA Extraction

Cells from each genotype were centrifuged at 350xg for 5 minutes and counted. $1x10^6$ cells from each line were taken and resuspended in 50µL mammalian cell lysis buffer with proteinase K (5µL/mL). Cells were heat-blocked for 30 minutes at 60°C and then for further 15 minutes at 72°C. Following this, 400µL nuclease free water was added to each sample and they were stored at 4°C or at -20°C for prolonged use.

2.10.1.2 Sample Preparation

TaqMan fast protocol was used for genotyping. Master mix containing 0.5µL primer and 5µL master mix solution was made up per each sample and added to the wells of a 96-well plate. 4.5µL of the appropriate DNA sample was added and the plate was sealed. All samples were run in triplicate.

2.10.2 Comparative C_T

2.10.2.1 RNA extraction

Depending on the starting material different extraction kits and lysis buffers were used. Once lysed samples were usually stored at -80°C for a couple of days before proceeding with extraction. Samples were thawed on ice and processed per instructions specific to each kit, all requiring column extraction (Qiagen). Finally, RNA was eluted in nuclease water and stored at -80°C for long-term purposes or further converted to cDNA. Concentration of extracted RNA was measured using the Nanodrop 2000 (Thermofischer Scientific). When very low quantities of RNA were expected or to obtain more accurate readings, the DeNovix kit was used to measure the concentration as instructed by the manufacturer.

Table 2.15: Summary of RNA extraction kits used based on different starting material.

Starting material	Kit used	Lysis reagent	Final elution volume
Immortalized cell lines	RNeasy® Mini	RLT buffer	30-50 µL
Microglia-like cells	miRNeasy®	Qiazol	14µL
Mouse primary microglia	miRNeasy®	Qiazol	14µL
iPS cells	RNeasy® Micro	RLT buffer	14µL
Microglia precursors	RNeasy® Micro	RLT buffer	14µL

2.10.2.2 cDNA synthesis

Conversion of RNA to cDNA was performed using the High capacity cDNA Reverse Transcription kit (Thermofischer) as per manufacturer's instructions. All kit components were fully thawed on ice before use. Final reaction of 20µL was composed, using 10µL RNA and 10µL of master mix. Amount of RNA, in ng, was kept consistent between experiments. The reaction was incubated 10 minutes at 25^{o}C, 120 minutes at 37^{o}C and finally 5 minutes at 85^{o}C and then cooled on ice. Once cooled, 60µL of nuclease-free water was added to each reaction, resulting in final volume of 80µL cDNA. This volume was adjusted for preps where lower cDNA yield was expected. Samples were stored in -20^{o}C until further use.

2.10.2.3 qPCR reaction

All qPCR reactions were performed using FAST qPCR Master Mix (with SYBR) according to instructions (Promega). In brief, 5µL of master mix was combined with 300nM of forward and reverse primers and combined with nuclease-free water to final volume of 8µL. Finally, 2µL of cDNA was added to each reaction for final volume of 10ul which was loaded to one well of 0.1ml MicroAmp Fast Optical 96-well or 384-well reaction plate (Applied Biosystems). A list of the most commonly primers used in this thesis can be seen in Table 2.16. Additional primer pairs can be found in the specific corresponding chapter.

Table 2.16: Primer sequences used for qPCR analysis in the thesis.

Target	Species	Forward primer (5'-3')	Reverse primer (5'-3')
PILRa	Human	GCTGTCACTGTGCTCGGAAT	TTAGTCCGCTGCTGACCTTT
Syk	Mouse	TGCCTTCTCTCCATTGCAGC	TGTATGGAGAAGTACCTTCCTGT
Ywhaz	Mouse	TTGAGCAGAAGACGGAAGGT	GAAGCATTGGGGATCAAGAA
GAPDH	Human	GCCACATCGCTCAGACAC	TGACTCCGACCTTCACCTTC
Nanog	Human	GATGGGAGGAGGGGAGAGGA	TTTGGAAGCTGCTGGGGAAG
Sox2	Human	TACCTCTTCCTCCCACTCCA	GGTAGTGCTGGGACATGTGA
Oct4	Human	CTCACCCTGGGGGTTCTATT	CTCCAGGTTGCCTCTCACTC
Fam222a	Mouse	GGGCCTTTCTCCAGCAATCTT	CCGCAGCAGGAATCCGTA
Cstb	Mouse	CGACTACTGCTGCCAAGATGA	GCTGGGACTTCACCTGGTCG
Rfxap	Mouse	ACGTCAAACTGGAGGAAAGCA	TAGGTCTTGCAGGGCGATCA
Gdp1	Mouse	GACGACCATCGGCTGCAA	GTGATGCGAAAGTTGGGTGT

Reactions were run in triplicate as standard, and in duplicate where this was not possible. In each qPCR plate primers targeting the endogenous control gene were also included. Ywhaz and GAPDH were the most used, and this will be specifically indicated in respective figure legends. Control samples not containing cDNA were also included on each plate. Complete

plates were sealed with an adhesive PCR plate seal (Thermo Fischer Scientific) and spun at 350 x g for 3 minutes. All experiments were run on version Quant Studio Real-Time PCR System 6 (Applied Biosystems) using the delta Ct method. Cycle details are illustrated in Table 2.17. For specific targets, an additional extension step was added to this cycle at 72°C.

Table 2.17: Temperature and cycling conditions used to generate qPCR data.

Step	Time	Temperature	Cycle number
Enzyme Activation	2 minutes	95°C	N/A
Denaturation	5 seconds	95 °C	X 40
Data Collection	20 seconds	60 °C	X 40
Melt Curve	15 seconds	95 °C	N/A
	1 minute	60 °C	
	15 seconds	95 °C	

2.11 PANP ligand interactions

2. 11.1 Preparation

PILRa associated neural protein (PANP) was conjugated to Fc portion (R&D Systems). The lyophilised product was resuspended with PBS at 500µg/m and aliquoted at small volumes (5-10µL). Aliquots were stored at -20°C for up to 3 month and repeated freeze-thaw cycles were avoided as per manufacturers recommendations.

2.11.2 Multimerising

Individual PANP-Fc aliquots were thawed before use on ice. Once thawed, the solution was mixed with anti-human secondary antibody conjugated to APC at 1:4 ratio (Jackson Laboratories). To allow for multimerising of the Fc domains the mix was left on ice for approximately 30 minutes.

During the incubation, cells of choice were prepared for flow cytometry as previously described. Once detached and counted, the correct number of cells were aliquoted into U-bottom 96 well plate. The cells were pelleted by centrifuging at 350 x g for 5 minutes.

After the incubation was done, the pelleted cells were resuspended in the pre-mixed PANP-Fc x secondary antibody complex. Cells were left on ice for 30 minutes to allow binding.

2.12 Luciferase Assay

2.12.1 NFAT Induction

Jurkat Lucia cells were centrifuged and resuspended at $2x10^6$cells/mL in fresh RPMI media. Following this, 20µL of the cell stimulant of choice was added to a 96-flat bottom well plate.

Combination of PMA (50ng/mL) and ionomycin (3µg/mL) was used as a positive control and ddH_20 or DPBS was added as a negative control. 180µL of cell suspension was added in each well and the cells were incubated for 18-24h at 37◦C.

2.12.2 Bioluminescence Measurement

The following day 20µL of cell suspension from each well was transferred to a 96-black or white well plate. The QUANTI-Luc™ (Invivogen) solution was prepared as indicated by the manufacturer and aliquoted for future use. FLUOstar Omega plate reader (BMG LabTech) was set with the following parameters: 50µL injection, end-point measurement with a 4 second start time and 0.1 second reading time. Prior to obtaining a reading, the injectors were primed with QUANTI-Luc™ solution. The prepared plate was placed in the plate reader and readings were obtained.

2.13 Mice

All animals used for this thesis were maintained at Cardiff University JBIOS facility in accordance with the 1986 Animals Act (Scientific Procedures) Guidelines. All experiments were conducted under the UK Home Office license (P92CA01DA). Mice were culled with approved schedule 1 methods, either by asphyxiation through slow increasing concentration of CO_2 or overdose of anaesthetic and further confirmed via cervical dislocation. Experimental animals were matched by age and gender whenever possible. Majority of experiments contained a mix of male and female mice between 8 and 26 weeks of age. The details of number, age and sex of mice used in each individual experiment can be found in the appropriate figure legends.

Small pilot experiments were performed usually using 1-2 animals per group to provide better idea of the biological effect and dosage of the substances used and to serve as justification for larger follow-up studies. All animals were housed together according to genotypes either in conventional cages or scantainers, receiving individual ventilation to each cage, and were provided with water and chow *ad libitum*. An exception from this were mice injected with tamoxifen, which for the duration of the injections received daily food pellets mixed with water to form “mush” which was added directly into the cage for easy access of the animals.

The transgenic mice strains which were used in this thesis were all purchased from Jax Laboratories and bred inhouse, details can be found in Table 2.18. All strains were produced on C57BL/6 and C57BL/6J background.

Table 2.18: Mouse strains used in this thesis and their abbreviations.

Official strain name	Thesis Abbreviation
B6.129P2-Syk$^{tm1.2Tara}$/J x APP$^{NL-G-F/NL-G-F}$	Syk$^{fl/fl}$ x APP
B6.129P2-Syk$^{tm1.2Tara}$/J x B6.129P2(C)-Cx3cr1$^{tm2.1(Cre/ERT2)\ Jung}$/J	Syk$^{fl/fl}$ x Cx3Cr1- Cre-ERT

2.13.1 APP mice

Male and female APP^{NL-G-F} mice were maintained as homozygous and were further crossed to floxed Syk mice to obtain Syk x APP experimental line used as a control. To generate the APP-KI mice Swedish mutation was introduced into exon 16 and Iberian and Arctic mutations were introduced in exon 17 of humanized Aβ, combined with pgk-neo gene cassette lox/FRT sequence utilized for positive selection (175).

2.13.2 Syk x Cre-ERT floxed mice

Mice were obtained from the Jackson Laboratory. In B6.129P2-*Syk$^{tm1.2Tara}$*/J animals exon 1 of the Syk gene has been flanked by two LoxP sites (248). Floxed homozygous Syk animals are viable and fertile. The strain was crossed with a conditional Cre-ERT expressing mice (B6.129P2(C)-*Cx3cr1$^{tm2.1(cre/ERT2)Jung}$*/J) which contain tamoxifen inducible Cre-recombinase transgene in the Cx3cr1 locus, to allow Cre-mediated deletion of the floxed sequences (249). Cx3cr1 expression is restricted to the myeloid lineage therefore allowing for microglia specificity (250). Only heterozygous Cre-ERT mice were used for experimental purposes.

Syk x Cre-ERT animals were bred to homozygous APP mice to produce Syk x APP x Cre-ERT animals.

2.13.3 Genotyping

Genomic DNA (gDNA) was isolated from single ear-punch biopsies collected by JBIOS staff. Mammalian lysis buffer containing 100 µg/mL of proteinase K (Sigma) was added at 50µL to digest the tissue in 1.5mL Eppendorf tubes and heated at 52°C for 1 hour being shaken at 1200rpm. Following this, proteinase K was deactivated by heating for 30 minutes at 72°C. Samples were cooled at room temperature and 400µL of water was added and briefly vortexed. The Go Taq® (Promega) master mix was used per manufacturer's instructions for

genotyping. Volumes for each PCR reaction are summarised in Table 2.19. Reactions were placed in 0.2mL tubes or 96-well plates and 1µL gDNA was added to each tube. Everything was transferred to the Mastercycler® Nexus Gradient (Eppendorf) and ran on the PCR programme detailed bellow in Figure 2.5.

Table 2.19: Standard genotyping PCR reaction volumes.

Reagent	Volume (µL)
Go Taq Green Master mix	12.5
Forward primer (10µM)	0.125
Reverse primer (10µM)	0.125
Nuclease free water	11.25
Total reaction volume	24

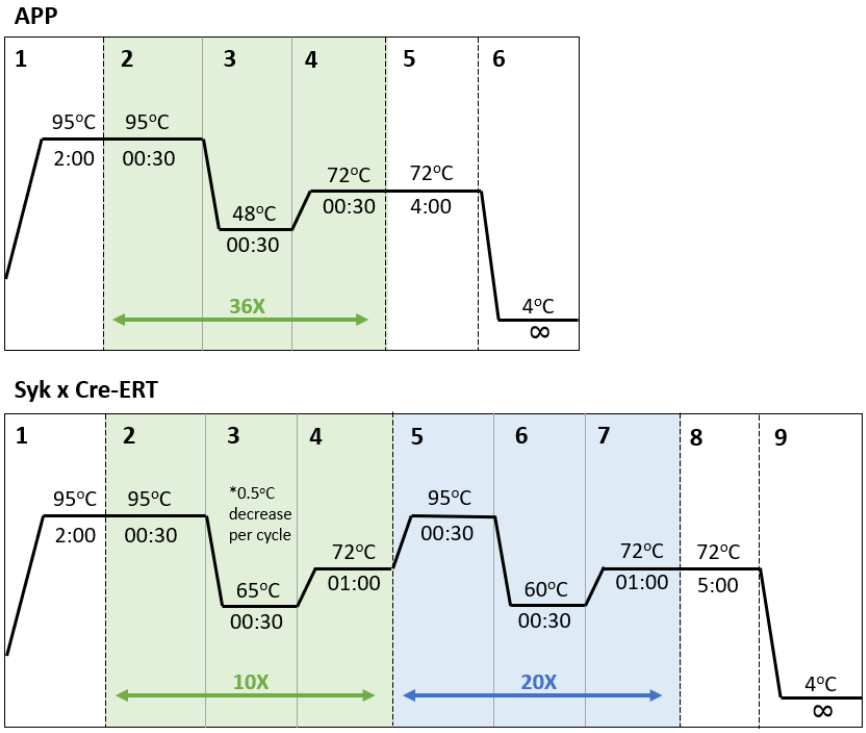

Figure 2.5: PCR programmes used for genotyping the mouse strains used in this thesis.

All primers used are shown in Table 2.20 and were supplied through Sigma. The PCR reactions were electrophoresed on a 2% agarose gel. The gel was made in 1X TAE buffer by dissolving appropriate amount of agarose powder (Thermofischer) and heating the solution. After the powder was completely dissolved by gentle mixing, SYBR safe was added at 1:10,000 dilution and mixed again before pouring the ready solution into the appropriate gel mould. Comb with the preferred size was inserted so that individual wells can be formed when the gel sets. As standard 10µL of sample was loaded alongside 100bp ladder

(Promega) and ran at constant voltage of 100V between 30 and 45 minutes using the Fischer brand™ gel system (Thermofischer).

Table 2.20: Primer sequences used for genotyping and the expected product size.

Mouse		Forward primer (5' to 3')	Reverse primer (3' to 5')	Product size(bp)
Syk cKO	Wild type	GCCCGTTCTGTGCCTACTGG	AGCTAACCAAACCCACGGC	234
	Mutant	GCCCGTTCTGTGCCTACTGG	AGCTAACCAAACCCACGGC	349
APP	Wild type	ATCTCGGAAGTGAAGATG	TGTAGATGAGAACTTAAC	700
	Mutant	ATCTCGGAAGTGAATCTA	CGTATAATGTATGCTATACGAAG	400
Cx3Cr1 ERT	Wild type	AGCTCACGACTGCCTTCTTC	ACGCCCAGACTAATGGTGAC	150
	Mutant	GAAGTGCAAGAACGTGGTGC	ACGCCCAGACTAATGGTGAC	800

2.14 *In vivo* intraperitoneal (I.P.) injection

All intraperitoneal (I.P) injections were performed in the lower right quadrant at 45^{o} angle. When more than one injection was delivered, the right and left quadrants were altered, to allow for better recovery of the injected site of the animal.

2.14.1 Tamoxifen

4-hydroxytamoxifen (OHT) or tamoxifen from here onwards, was prepared fresh from stock solution prior to every new experiment and was stored at 4^{o}C for no longer than 7 days. Tamoxifen (Sigma) was supplied as 1000mg powder. The initial stock was resuspended in 5mL of pre-warmed 100% ethanol (Sigma) and aliquoted at 500µL into cryovials. This step was done as quickly as possible and if crystal formation appeared the solution was returned at 70^{o}C to warm again. Aliquots were stored at -20^{o}C long term.

Before experiment, an aliquot was heated at 70^{o}C for at least 30 minutes or until no crystals were visible. Simultaneously 10mL of corn oil (Sigma) and 1mL filter tips were heated as well. The tamoxifen stock solution was mixed into the warm corn oil (Sigma) and the prepared solution was returned at 70^{o}C for further 30 minutes or until completely dissolved and inverted before use to ensure no crystallisation was present. The warm tamoxifen with final concentration 10mg/mL or 1mg/100µL was kept in a polystyrene box containing pre-warmed water packs so that the solution was maintained warm until all injections were completed. In case where crystals did appear, the tamoxifen was returned at 70^{o}C until completely warm and dissolved. The prepared solution was kept at 4^{o}C and reused for the following injection days after warming up to 70^{o}C again. Tamoxifen solution was kept for a maximum of 7 days at 4^{o}C.

Corn oil (Sigma) to match tamoxifen injections was used as a control in some experiments.

2.14.1.1 Weighing and welfare monitoring

Tamoxifen resuspended in corn oil was administered at 100mg/kg. To estimate the required volume for injections animals were weighted before the initial injection and the same volume was maintained for repeated injections. Scale was provided in the JBIOS facility. Animals were transferred to a small plastic see through pre-weighed box with lid and balanced on the scale until they remained still for the weight to be recorded.

Due to the potential harmful effects of tamoxifen and I.P injections, extra monitoring was required to ensure the wellbeing of experimental animals. During the days where animals were injected, monitoring was performed twice daily at 12h intervals which included weighing of animals and scoring of appearance, provoked and natural behaviour. The score for each of the components varied between 0 (natural behaviour) and 4 and was combined to form an overall welfare score for that particular check for each animal. One additional daily visual check between the two weightings was also performed.

2.15 Murine microglia isolation

Mice were culled before brains were collected and kept in 1mL of DPBS without Ca^{2+} and Mg^{2+} (Gibco) with 1g/L glucose on ice. When tissue was harvested for Sc-sequencing experiments mice were perfused with 25mL of RT DPBS before brain collection. Brains were further digested using the Neural Tissue Digest Kit P (NTDK; Miltenyi Biotec) as per manufacturer's instructions. After estimating brains weight, the correct volume of enzymes was calculated. In brief, GentleMACS™ C-tubes were labelled and buffer X and enzyme P were added. Brains were roughly chopped with scalpels and transferred to the tubes with minimal DPBS carryover, followed by buffer Y and enzyme A. C-tubes were securely locked and loaded onto the GentleMACS™ OctoDissociator (Miltenyi) and ran at programme 37C_ABDK, which included heating to 37^{o}C at 840rpm for 30 minutes.

2.15.1 Demyelination

After the dissociation was complete the resulting suspension was passed through a moist 70µM strained directly into 50mL falcon tube containing 10mL of ice-cold DPBS with Ca^{2+} and Mg^{2+}. The tubes were further centrifuged at 300 x g for 7 minutes at 4^{o}C. The supernatant was carefully removed, and the pellet was resuspended in 3100µL of ice-cold

DPBS with Ca^{2+} and Mg^{2+} and it was transferred to cooled 15mL falcon tubes. This was followed by addition of 900µL debris removal solution per sample and mixing by inversion of the tube to allow solution to spread on the side of the tube. Next, 4mL of ice-cold DPBS was carefully overlaid by slowly adding it to the tube and formation of 2 separate layers was present. The tubes were centrifuged for 10 minutes at 4°C at 3000 x g. After the spin, 3 layers were present in the tube, top clear one, intermediate myelin pluck and bottom cloudy one (can insert picture here). The top phase and the myelin pluck were carefully removed by pipetting. Around 1mL of the bottom phase was left with the bottom pellet undisturbed. Tubes were filled up to 15mL of ice-cold DPBS and mixed, following which centrifuged for 10 minutes at 1000 x g at 4°C. The resulting pellet contained microglia and other cells.

2.15.2 Red blood cell lysis

Red blood cell lysis was optional and performed only for certain protocols when perfusion was not performed before tissue collection. The resulting pellet from the previous step was resuspended and red blood cell lysis solution 10X (Miltenyi) was added and the solution was incubated for 2 minutes. The solution was then centrifuged for 10 minutes at 300 x g at room temperature. Following this the supernatant was removed and the cell pellet was resuspended in fresh DPBS.

2.15.3 Counts and live-dead staining

Cells were pelleted and counted using the MUSE as previously described. The pellets were resuspended in DPBS and PI was added for 20 minutes whole on ice. Samples were then washed twice and processed for the next stage.

2.15.4 Methanol fixation and rehydration

Cleared cell suspension was centrifuged again at 300 x g for 7 minutes at 4°C. The pellet was resuspended in 200µL of ice-cold DPBS containing 0.1% BSA. Next, 800µL of biological grade methanol kept at -20°C were slowly added dropwise to achieve final concentration of 80% methanol, while keeping the tube on slow speed vortex for constant mixing. The suspension was kept on ice for 20 minutes before transferring to -80°C.

Once fixed before use cells were taken from -80°C to 4°C and kept on ice during the whole procedure. Once thawed, the cells were pelleted at 1000 x g for 5 minutes at 4°C and then

resuspended in DPBS with 0.01%BSA. This wash step was repeated once more after which cells were resuspended in DPBS with 0.01%BSA and used for staining.

2.15.5 Staining for FACS

Cells were first blocked for 20 minutes on ice in the dark by resuspending the pellets in 200µl of block solution. Following this 200µl of 2X antibody solution was added directly to each tube. Anti-CD11b antibody, anti-CD45 and live/dead stain were used. The antibodies were incubated for 30 minutes in the dark. After this, cells were spun for 7 minutes at 300 x g. The pellet was resuspended in DPBS with 0.5% BSA and 5mM EDTA and transferred to FACS tubes. The samples were kept on ice for the whole time during the sort.

2.15.6 iCell8 chip

2.15.6.1 Positive and negative control

The supplied K-562 RNA (1µg/µL) was serially diluted 1:20 with nuclease free water to generate aliquots of 10ng/µL which were used as a positive control. 1X DPBS was used as a negative control. 25µL of positive and negative control were loaded onto each chip.

2.15.6.2 Cell preparation

Samples were sorted for maximum of 20 minutes or until minimum of $3x10^4$ cells were collected. Cells were collected in 5mL FACS tubes already containing 1mL of iCell8 buffer and 2 drops of Hoechst die. Sorted cells were spun down for 7 minutes at 300 x g. As much liquid as possible was removed while being careful not to aspirate the cells as there was no visible pellet. Cells were resuspended in 100µL of DPBS, and aliquot taken for counting.

Cells were aliquoted at the appropriate dilution and DPBS was added to a final volume of 80µL. Cell suspensions were loaded to the corresponding wells of the 384-well loading plate as per manufacturer's instructions.

Both the loading plate and the chip were carefully placed into the iCell8 machine and using the software as per instructions, cells were dispensed onto the chip. Following dispense, the chip was spun and imaged, then carefully placed on pre-frozen chip holders and kept in -80^{o}C until further processing.

2.15.6.3 Library preparation

Each chip was manually triaged following dispensing allowing for more precise selection of candidates and maximising the number of wells utilised. To generate complete libraries, manufacturer's instructions were followed for processing the chip. In brief, 5 subsequent dispenses were completed. These allow for generation of cDNA, amplification, tagmentation and addition of forward and reverse indexing primers. In this thesis, 2 different versions of the kit were used, the SMART-Seq® ICELL8 Application kit (Takara) and the SMART-Seq® Pro ICELL8 Application kit (Takara). The detailed instructions for each dispense condition can be found in the corresponding manual. After completion of all dispense steps, the generated library was extracted in 2mL tube and stored at -20^{o}C.

2.15.6.4 Clean up

Each newly generated library was processed using bead clean-up. The NucleoMag NGS Clean-up and Size Select (Takara) was used following manufacturer's instructions. Half of the library total volume was processed. The library target DNA was bound to the beads, following which 2 washes with 80% ethanol were completed. The bead pellet was left to dry at room temperature and was eluted using elution buffer.

2.15.6.5 Quantification

The purified library was quantified using Qubit dsDNA HS Assay Kit (Thermofischer) as per manufacturer's instructions.

2.15.6.6 Fragment analysis

Newly generated and purified libraries were run on 5200 Fragment Analyzer (Agilent) prior to sequencing to determine the quality, distribution and the exact concentration of the library. All libraries were diluted to 0.5ng/µL based on Qubit measurements and 1µL was loaded for fragment analysis. The NGS-HS workflow was used and smear analysis determining the average fragment size was obtained.

2.15.6.7 Sequencing

Libraries were diluted to the required concentration and sequenced using 150 cycles and 8 cycles for the index reads with the NovaSeq6000 platform.

2.16 Immunocytochemistry (ICC) staining

Cells for ICC staining were plated in 96-well µClear (Greiner) plates. On the day of staining, media was removed, and cells were washed once with DPBS. Following this, 4% paraformaldehyde (PFA) was added to each well and the plate was incubated at room temperature for 20 minutes. After the incubation, PFA was removed, and cells were washed three times with DPBS. Block solution was added to each well for 60 minutes at room temperature. Following this primary antibody was applied once diluted in antibody dilution buffer and cells were incubated at 4^{o}C overnight in dark. The next day, primary antibody was washed 3 times with DPBS and followed by secondary antibody for 1 hour at room temperature in dark. Cells were further washed 2 times with DPBS after which Hoechst nuclei staining solution (Thermofischer Scientific) and CellMask Green (Thermofischer Scientific) were added for 10 minutes at 37^{o}C. The plate was washed 2 more times and placed in the Opera Phenix (Perkin Elmer) for imaging. On each plate, isotype control and secondary antibody control were included. Cells were plated in 3 technical replicate wells and images were acquired from each well.

Table 2.21: Antibodies used for ICC staining in this thesis.

Antibody target	Dilution	Host species	Secondary antibody fluorophore	Supplier
Nanog	**1:100**	**Rabbit**	**AF647**	**Cell Signalling Technologies**
Sox2	**1:100**	**Rabbit**	**AF647**	**Cell Signalling Technologies**
Oct4	**1:100**	**Rabbit**	**AF647**	**Cell Signalling Technologies**
Iba1	**1:100**	**Goat**	**AF594**	**Abcam**
Tmem119	**1:100**	**Rabbit**	**AF647**	**Abcam**

2.17 Histology

2.17.1 Tissue sectioning and preparation

Tissue sections were prepared with Leica VT1200S Vibratome (Leica) cutting at 50µm thickness using 0.6mm/s speed and 1.3mm amplitude. Free-floating sections were kept sealed in 24-well plates containing PBS + 0.1% sodium azide at 4^{o}C for long-term storage. All subsequent staining was completed in 48-well plates.

2.17.2 Antigen retrieval

Citrate solution was prepared by 1:100 dilution in water and heated in a glass beaker for around 30 seconds in a microwave until boiling. PBS was aspirated from tissue and citrate buffer was applied to the sections. The plate was sealed, covered with aluminum foil and

kept over a heat block set to 95°C for 1 hour. After antigen retrieval solution was removed, sections were washed once with 1% Triton X-100 for 5 minutes, followed by two washes with PBS, after which it was proceeded with staining.

2.17.3 Iba1 and GFAP staining

2.17.3.1 Blocking

Blocking solution was prepared in 0.05% Tween and 200µL was applied to each well. The plate was incubated for 1 hour at room temperature while shaking.

2.17.3.2 Staining

Blocking solution was removed and immediately 200µL of antibodies prepared in 0.05% Tween was added. The plate was incubated for 72 hours at 4°C while shaking. After the antibody solution was removed, sections were washed with 1% Triton X-100 for 5 minutes, followed by two washes with 0.05% Tween. After this, tissue was transferred to a new plate containing PBS. The PBS was aspirated, and secondary antibody dilutions prepared in 0.05% Tween were applied. The tissue was incubated for 2 hours at room temperature while shaking. After secondary antibody staining was completed, the tissue was washed with 0.05% Tween and kept in PBS until additional staining.

2.17.4 Amylo-Glo staining

Amylo-Glo® RTD™ amyloid plaque stain reagent (Biosensis) solution was prepared in 0.9% saline solution using 1:100 dilution. PBS was aspirated from the tissue and 70% ethanol was applied for 5 minutes. This was followed by 2 minutes rehydration with distilled water. Then, 200µL Amylo-Glo® staining solution was added to each well and incubated for 15 minutes while shaking. After staining, the sections were rinsed with 0.9% saline solution for 5 minutes, followed by distilled water. Finally, the tissue was washed with PBS and kept in the plate until mounting. Each tissue section was mounted on a cover slip using VectaShield® Vibrance® Antifade Mounting Media (Vector Labs). Complete slides were kept in the dark at room temperature for around an hour to allow for setting of the tissue. Finished slides were stored at 4°C in slide holders.

2.17.5 Thioflavin S staining

Thioflavin S (Sigma) solution was prepared by dissolving a small amount of powder in 70% ethanol until reaching bright yellow colour and then sterile filtered before applied to

sections. After 15-minute incubation at room temperature, sections were washed twice with 50% ethanol followed by 2 minutes rehydration with water. Sections were transferred to PBS and then mounted on slides. Brain slices were left on the slide until completely dry after which FluorSave™ mounting reagent (Merck) was added dropwise and each slide was covered by a coverslip. Ready slides were stored at 4°C.

Table 2.22: Summary table for antibodies used for histology staining in this thesis.

Antibody target	Host species	Dilution	Supplier	Fluorophore
Iba1	Rabbit	1:1000	Wako	N/A
GFAP	Chicken	1:2000	Abcam	N/A
Anti-Rabbit	Goat	1:500	Invitrogen	594
Anti-Chicken	Goat	1:500	Abcam	FITC

2.18 Statistical Analysis and Graphs

2.18.1 Flow Cytometry

All flow cytometry data was analyzed using FlowJo software version 10.9.0.

2.18.2 Histology

Histology data was collected using Leica SP8 confocal microscope, data was transferred and analyzed using Imaris imaging software.

2.18.3 qPCR Data

Data for qPCR assays was collected using QuantStudio™ Real-Time PCR software (version 1.3; Thermofisher Scientific).

2.18.4 Seahorse data

Data generated using the Seahorse XFe96 Analyser was further processed using the Agilent online cloud platform.

2.18.5 Opera Phenix data

Data was acquired using the Perkin Elmer Opera Phenix platform and directly transferred to the Columbus server for further analysis. Data was analyzed using the Harmony software and results were extracted as Excel files containing the necessary values. Representative images from individual wells were saved.

2.18.6 Legendplex data

Data from the Legendplex 13-plex macrophage/microglia kit was acquired using the Attune NxT and set up as per manufacturers instructions, capturing both bead populations A and B (Figure 2.6). The data was further analyzed by using the available online software where fcs. files can be input to complete the necessary gating and convert the flow cytometry readings into quantitative ones. Example standard curves can be seen in the Appendix.

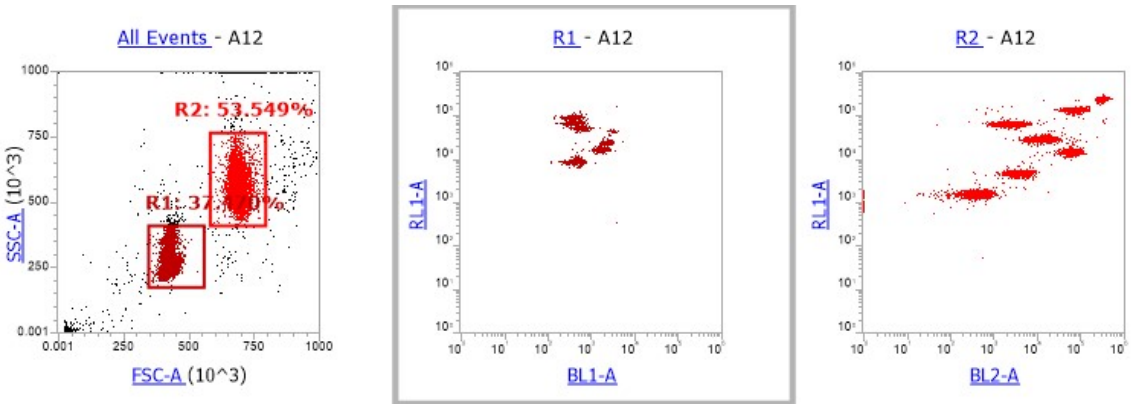

Figure 2.6: FSC/SSC of bead set-up on Attune. Gates are positioned so that they capture both bead populations.

2.18.7 Sc-RNA sequencing data

All sequencing data in this thesis was processed using scripts developed by Dr. Ruth Jones and utilized by Dr. Mateus Harrington and Dr. Carolina Toste to produce the final differential expression list of targets. The data was analyzed using Cogent NGS Analysis Pipeline v2.0.1. Further analysis was performed with R version 4.3.0 using DESeq2 package (251). The differential expression gene (DEG) list was further examined using IPA software (Qiagen).

2.18.8 Statistics and graphs

Most statistical analysis was performed using GraphPad Prism (GraphPad Software, version 9) or R (version 4.0.0). Appropriate statistical tests were selected based on the data. Power calculations were used to estimate the sample size for all animal studies using G Power software. In addition, animals were randomised when processing, so each group included 1 animal per genotype and sex in each experiment. Furthermore, all experiments were blinded when processing and obtaining images. For all assays p-value over 0.05 was taken as non-significant (ns.), $p<0.05$ was used as a significance threshold. Annotations are as follows

*p<0.05, **p<0.01, ***p<0.001, ****p<0.0001. Figures and diagrams in this thesis were made using BioRender or PowerPoint.

Chapter 3 : Establishing models to study PILRα function in vitro

3.1 Introduction

The main aim of this chapter was to establish a suitable cellular model to study the function of different coding variants of the gene for paired immunoglobulin-like type 2 receptor (PILR) alpha (*PILRA)*. As previously reported SNP (rs1476679, P value = 5.6 x 10^{-10}) associated with *PILRA* (35), leads to reduced risk of Alzheimer's disease (AD) development. Unpublished evidence from the group of Escott-Price suggests that the protection associated with the PILRa variant combined with the protection associated with the PLCg2 gene is greater than the additive risk of the individual variants. This increased protection when both variants are present could result from a functional link between the genes. PILRa and PLCg2 could potentially co-regulate relevant AD functions, therefore studying how different genetic variants of one gene impact the function of another, could provide an important insight for AD treatment. Exploring relevant macrophage functions might reveal what role PILRa has in cell signalling and in regulating some of these processes.

Research shows that PILRa modulates important immune response functions, including infiltration of neutrophils to the site of infection (192), recruitment of monocytes (193) and activation of NK cells (194). In terms of its involvement in AD development, there is limited evidence on how the receptor impacts microglia functionally. The common missense variant of PILRa, causing glycine (GGG) to arginine (AGG) substitution at position 78 alters the ligand binding properties of the receptor. The amino acid change leads to reduced ligand binding to both endogenous and exogenous ligands and activation. Consequently, this caused decrease in intracellular inhibition and signalling pathway activation (201) which could potentially modulate the microglia response in AD.

The molecular functions of the interaction between PILRa and its ligands are not well understood, however one of the conditions for PILRa binding is the presence of sialylated O-linked carbohydrates on the ligand. Some of the existing identified ligands for the receptor include PILR-associating neural protein (PANP), glycoprotein B (gB) and mouse CD99. Mouse CD99 is a single chain surface glycoprotein which has diverse functions within the immune system, including the migration of leukocytes through endothelial junctions (252). It associates both with PILRa and PILRβ and two sialylated O-linked glycans (Thr-45 and Thr-50) are critical for the interaction. The physiological consequence of the interaction, however, is not fully understood. Interestingly, human PILRa does not interact with human

CD99. The reason for that potentially is low sequence identity between human and mouse CD99 or differential glycosylation patterns. In comparison to the two O-linked glycans in mouse CD99, human CD99 contains only one (Thr-41). It is possible that other motifs have also diverged between human and mouse CD99 (253). Similarly, to CD99 interaction, evidence shows that specific *O*-glycosylation sites on PANP, primarily threonine residue at position 136 is required for PILRa interaction (254).

In all existing evidence relating to the role of PILRα in dementia, the functional properties of the receptor have not yet been explored in an appropriate model. Overexpression of the receptor in a cell culture system might provide an important insight into its importance for microglia and potentially how the different identified genetic variants might regulate AD relevant functions such as phagocytosis and Aβ uptake.

Lentiviruses are a type of retrovirus (RNA containing) which can successfully infect a variety of cell lines including, non-dividing cells (255). Lentiviral vectors (LV) have been used widely to establish stable cell lines efficiently independent of the tissue of choice. They are often derived from the genome of HIV-1 and have unique characteristics such as the ability to hold multiple different promoters or the resistance to transcriptional silencing (256). In addition, in comparison to transient transfections, viral approaches often achieve long term protein expression in the desired system. LV are usually used either to knock-down (through using shRNA) or overexpress (through using ORF) a target gene in the cell culture system of choice. Using viral vectors allows for creating stable cell lines within two weeks in a very safe and efficient way. The flexibility of viral approaches allows the functions of PILRα and PLCg2 to be studied in parallel *in vitro*. In this thesis, a viral approach was utilized to deliver the gene of interest contained in a plasmid. Using packaging helper-free cell lines which express the necessary components to package the vector, such as Gag-Pol and Env, it eliminates the need to deliver these by separate plasmids.

Luciferase reporter assays have been widely used to determine activation/inhibition of a target gene. The luciferase approach allows a direct functional connection to be established between the presence of a protein of interest and the quantity of gene product that is generated (257). These high-throughput screening assays use the expression of luciferase, a bioluminescent enzyme found naturally in many organisms. The addition of substrate produces a chemical reaction where bioluminescence is a biproduct. Therefore, luciferase

assays provide a fast and accessible way to determine whether a protein of interest controls a gene at transcriptional level (258).

In summary, this chapter will focus on developing a cell culture model combining various coding variants from the gene of interest in this thesis enabling the study of PILRα in more detail. To investigate the relevant AD functions of PILRα in conjunction with PLCg2 a lentiviral approach was initially utilized. Throughout these investigations, however this was determined to be unsuitable for the planned experiments and a switch was made to an MMLV- based retroviral vector. In addition, to study how PILRα activation might impact microglia responses, a successful stimulant for the receptor was also sought.

The main chapter aims were:

- Creating PLCg2 MOP cell lines
- Producing and characterizing MOP cell lines with stable PILRa expression
- Assessing any functional differences in G78 and R78 PILRa expressing M-MOPs
- Developing methods and optimizing assays to screen for successful PILRa stimulants

3.2 Results

3.2.1. PLCg2 MOP cell lines

Conditionally immortalized macrophage precursor (MOP) cells were derived from bone marrow precursors through enrichment of $CD117^{+}$ cells (details in methods). The cell lines were derived from P522 or R522 PLCg2 mouse strains. All newly derived precursors were validated through genotyping and differentiation to macrophages (M-MOP) with macrophage colony stimulating factor (M-CSF) (details in methods) (Figure 3.1).

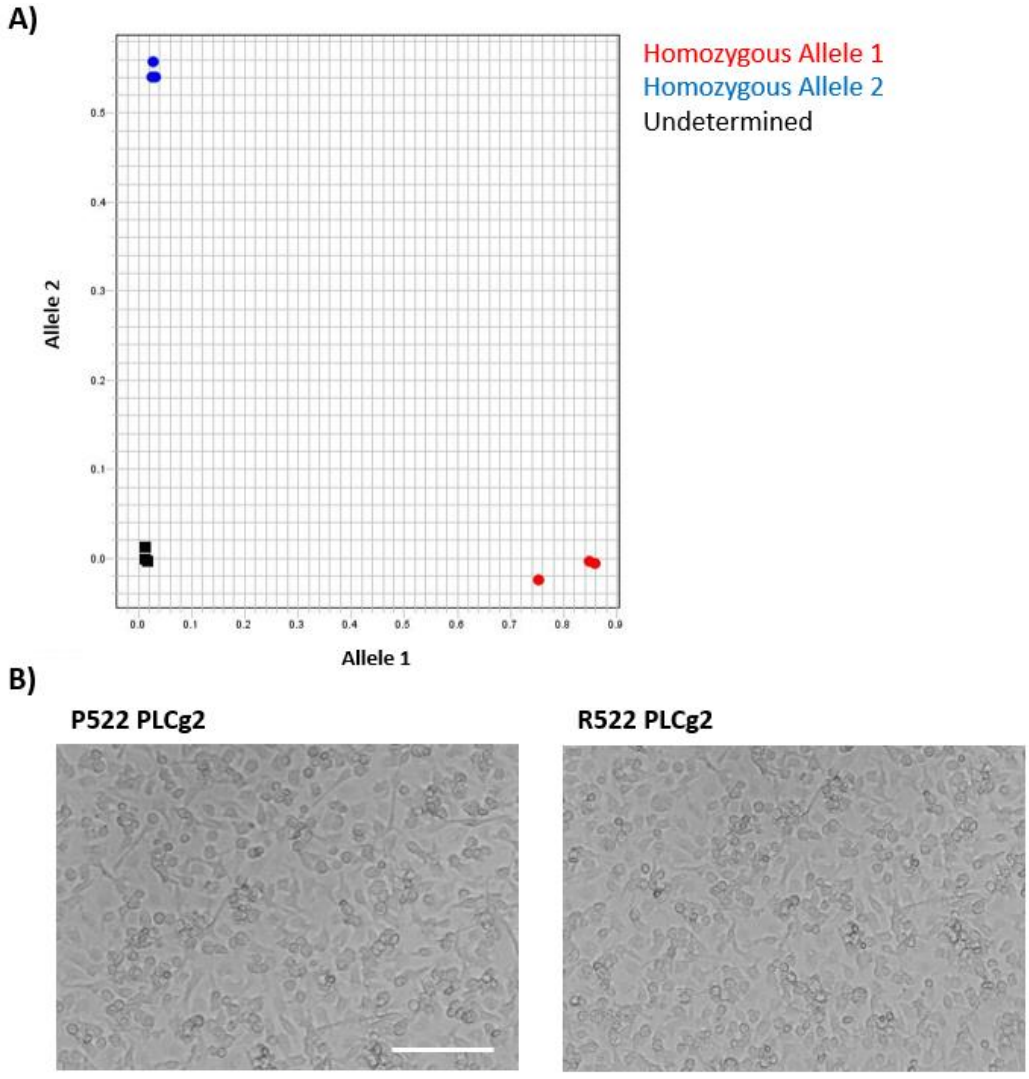

Figure 3.1: Validation of PLCg2 MOP cell lines. (A) Allelic discrimination plot of end-point genotyping qPCR. Cell lines were tested for both risk (P522) and protective (R522) variants of PLCG2. All samples were run in triplicate and the black squares represent a non-template control. **(B)** Light microscope images using the 10x objective of differentiated macrophages from MOP cells. P522 and R522 PLCg2 MOP cells were differentiated in 20ng/mL M-CSF for 4 days. Scale bar = 200µm.

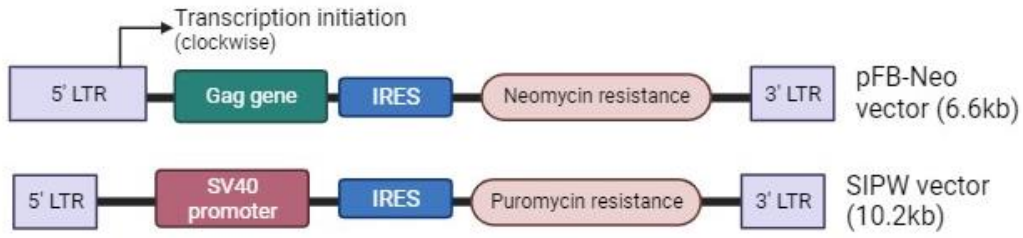

Figure 3.2: Linear diagram of vectors used in this chapter. Main features of the vectors, including antibiotic resistance and size are indicated.

3.2.2. Validation of lentiviral vectors for the expression of PILRα

The effectiveness of the full length *G78/R78 PILRA* SIPW virus was first tested in the human T-lymphocyte Jurkat cell line, which normally expresses low levels of PILRα. Figure 3.3 shows the results from Jurkat cells after infection with *G78 PILRA* SIPW or *R78 PILRA* SIPW viruses. RNA extracted from those cells 4 days post-infection underwent gene expression analysis. The qPCR analysis of the RNA indicates that *PILRA* mRNA expression is increased in the infected cells for both variants of the gene. The mRNA expression of *R78 PILRA* was higher compared to *G78 PILRA*.

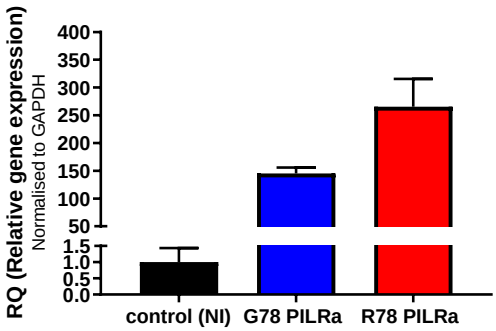

Figure 3.3: Increased mRNA expression of PILRα variants in Jurkat cells. Jurkat cells infected with *full length G78/R78 PILRA SIPW* lentivirus show an increase in mRNA levels of G78 and R78 PILRα in comparison to non-infected (NI) cells. The results are from a single experiment, where GAPDH was used as an endogenous control.

Having demonstrated the viral vectors were functional, the full length *PILRA* SIPW lentivirus was next introduced to PLCg2 MOP cells. P522 and R522 PLCg2 MOP cells were infected with G78 and R78 PILRα virus. The flow plots in Figure 3.3A show an increase in PILRα cell surface expression compared to control in P522 PLCg2 cells. PILRα expression was also

assessed by qPCR and the results (Figure 3.4B) reflect the protein expression changes. Similarly, the flow diagrams in Figure 16C show an increased expression of PILRα in R522 PLCg2 MOP cells. As reflected by the qPCR analysis of mRNA from those cells changes in PILRα expression correspond to the increase in protein expression. The cells infected with *R78 PILRA* SIPW virus show higher expression compared to cells infected with *G78 PILRA* SIPW cells independent of the background MOP cell line. Overall, there was an increase in expression in all 4 samples, although the proportion of positive cells through the population was small. These results were reproducible through multiple infections.

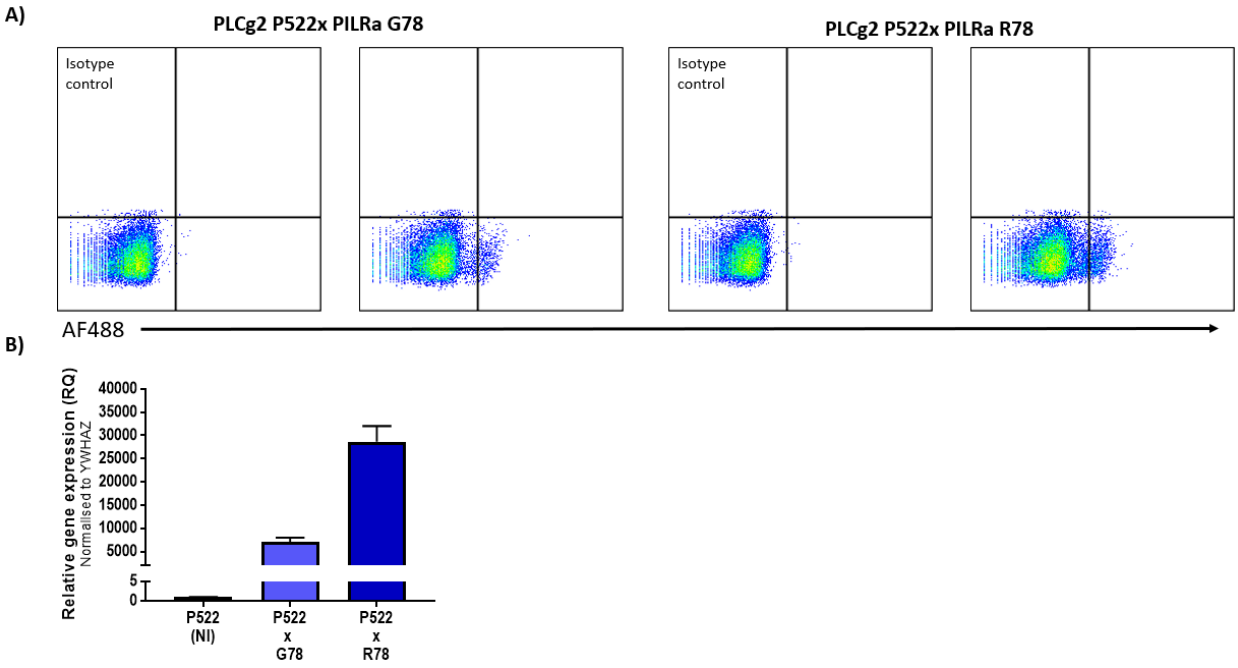

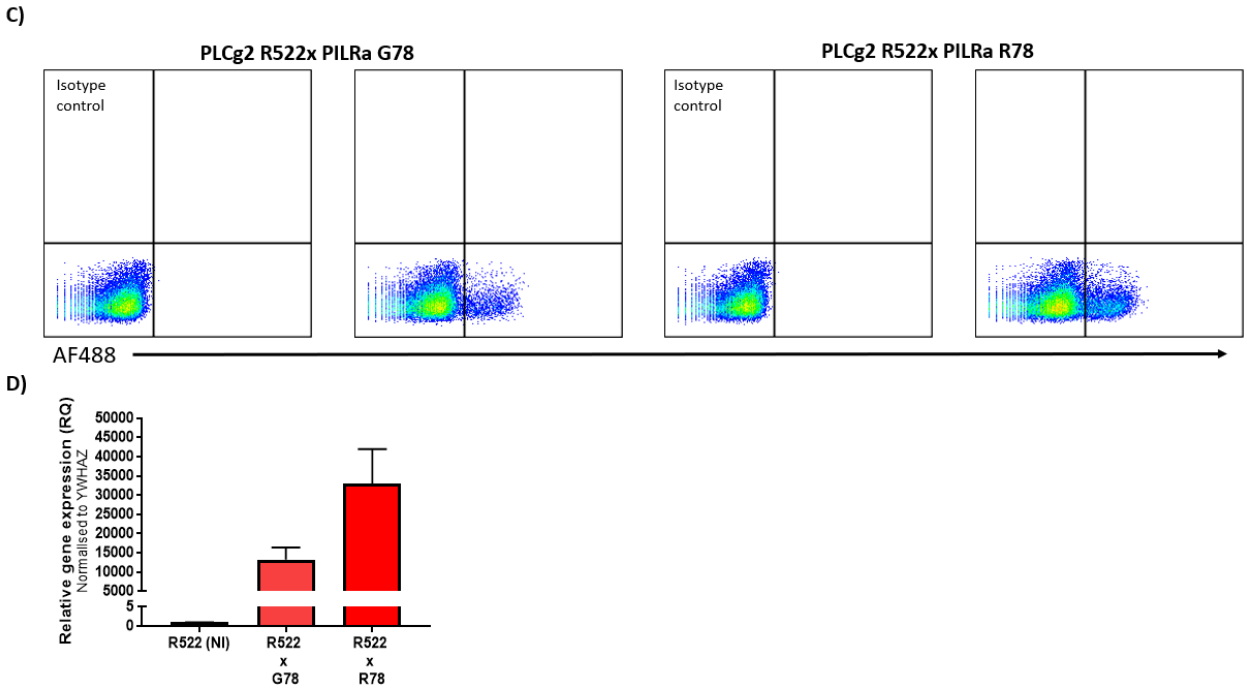

Figure 3.4: Increased PILRa expression in PLCg2 MOP cells. (A) Infected P522 PLCg2 MOP cells were fixed, blocked and stained with Alexa Fluor (AF)-488 conjugated anti-PILRa antibody or isotype control. The panels represent flow cytometry analysis showing altered PILRa expression in those cells. As expected, the infected cells show an increase in surface expression of G78/R78 PILRα. **(B)** mRNA of G78 and R78 PILRa is increased following lentivirus infection with full length *G78/R78 PILRA* SIPW. P522 PLCg2 MOP cells were used as a non-infected (NI) control. Results presented are from a single experiment, where YWHAZ was used as an endogenous control. Bars represent mean ± SEM (n=3 technical replicate wells). **(C**) R522 PLCg2 MOP cells which were infected with PILRa expressing lentivirus were fixed, blocked and stained with AF-488 conjugated anti-PILRa antibody or isotype control. The panels represent flow cytometry analysis showing altered PILRa expression in those cells. The infected cell population has an increase in surface expression of G78/R78 PILRa. **(D)** qPCR analysis shows that mRNA of G78 and R78 PILRa is increased following lentivirus infection with full length *G78/R78 PILRA* SIPW. R522 PLCg2 MOP cells were used as a non-infected (NI) control. Results presented are from a single experiment, where YWHAZ was used as an endogenous control. Bars represent mean ± SEM (n=3 technical replicate wells).

Following the increased PILRa expression in different variants of PLCg2 MOP cells infected with *PILRA* SIPW lentivirus, the cells were stained with anti-PILRα antibody. Samples were enriched by cell sorting using the FACS Aria Fusion sorter to detect positive populations and cells were kept on ice throughout sorting to minimise cell death. Positive cells were recovered and expression of PILRα was reassessed in those populations. In addition, mRNA

was extracted from the recovered cells to analyze gene expression using qPCR. Figure 3.5A shows cell surface expression of PILRα in P522 PLCg2 MOP cells. The flow plots show that although there was a shift in the cell population towards increased PILRα expression in the recovered cells, a large proportion of the cells were still not positive for PILRα expression. The mRNA analysis of those cells (Figure 3.5B) shows that gene expression of PILRα variants is increased overall after cell sorting in comparison to unsorted cells infected with full length *PILRA* SIPW lentivirus which were not positively selected for PILRα. The flow diagrams in Figure 3.5C show PILRα cell surface staining in FACS sorted R522 PLCg2 MOP cells around a week later. Although an increase like what is present in Figure 3.5A is seen, the cell population here is heterogenous, with around half of the cells expressing PILRα and half not. Gene expression of PILRα in those cells analyzed by qPCR shown in Figure 3.5D demonstrates that in both FACS selected cell groups PILRa expression is increased in comparison to infected cells which were not FACS sorted. In addition, R522 PLCg2 MOP cells infected with *R78 PILRA* SIPW lentivirus show the highest mRNA expression of PILRα which is also reflected on the histograms with highest proportion positive cells.

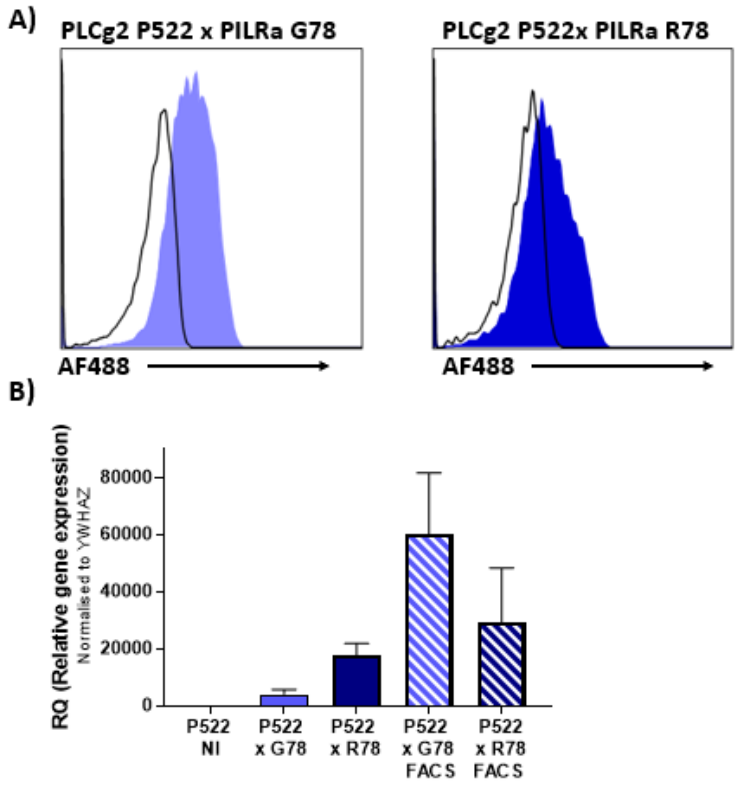

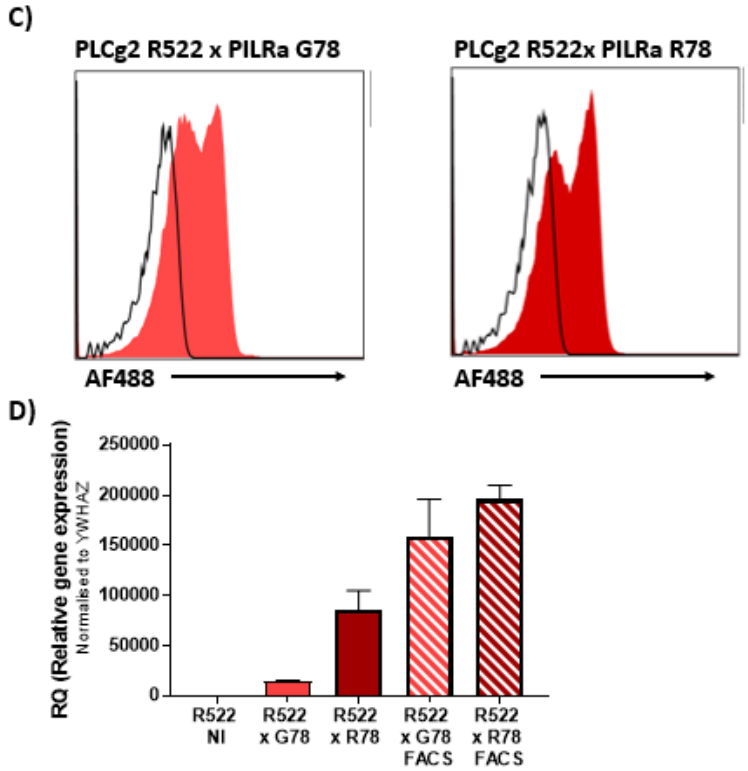

Figure 3.5: PILRα expression increases after FACS of lentivirus infected PLCg2 MOP cells. (A) P522 PLCg2 MOP cells were infected with full length *G78/R78 PILRA* SIPW lentiviral vector. The cells were then stained and FACS sorted according to AF-488 expression. After recovery of the sorted populations in culture and expansion, cells were fixed, blocked and stained with AF-488 conjugated anti-PILRa antibody (solid histogram) or isotype control (bold line). The histograms represent flow cytometry analysis showing altered PILRα expression in those cells. Although cells show an increase in surface expression of G78/R78 PILRα, most of the population still contains cells which are not positive for PILRα. **(B)** RNA was extracted from the cells and analyzed with qPCR. The mRNA of G78 and R78 PILRα is increased following FACS sorting compared to non-sorted cells. P522 PLCg2 MOP cells were used as a non-infected (NI) control. Results presented are from a single experiment, where YWHAZ was used as an endogenous control. Error bars represent mean ± SEM (n=3). **(C)** FACS sorted R522 PLCg2 MOP cells were fixed, blocked and stained with AF-488 conjugated anti-PILRα antibody or isotype control. The flow cytometry analysis shows altered PILRα expression in those cells. The FACS sorted population of cells appear to have an increase in surface expression of G78/R78 PILRα. However as seen from the histograms, there are two separate cell populations. **(D)** qPCR analysis of those cells shows that mRNA of G78/R78 PILRα is increased following FACS sorting of lentivirus infected cells. R522 PLCg2 MOP cells were used as a non-infected (NI) control. Results presented are from a single experiment, where YWHAZ was used as an endogenous control. Error bars represent mean ± SEM (n=3).

Cells which were sorted by FACS and harvested were subjected to a second FACS sorting to increase PILRα expression further and eliminate the heterogeneity of the cell culture. The cells were maintained in culture between the two cell sorting procedures for around a period of 7 to 10 days. P522 and R522 PLCg2 MOP cells expressing G78 and R78 PILRα variants were stained with PILRα antibody to select positive cells as previously described. Figure 3.6 represents the flow plots from the day when the sorting was performed. As seen from the histograms all cell populations excluding P522 PLCg2 x G78 PILRα MOPs, which were kept in culture for a shorter period, expressed very low amount of surface PILRα staining.

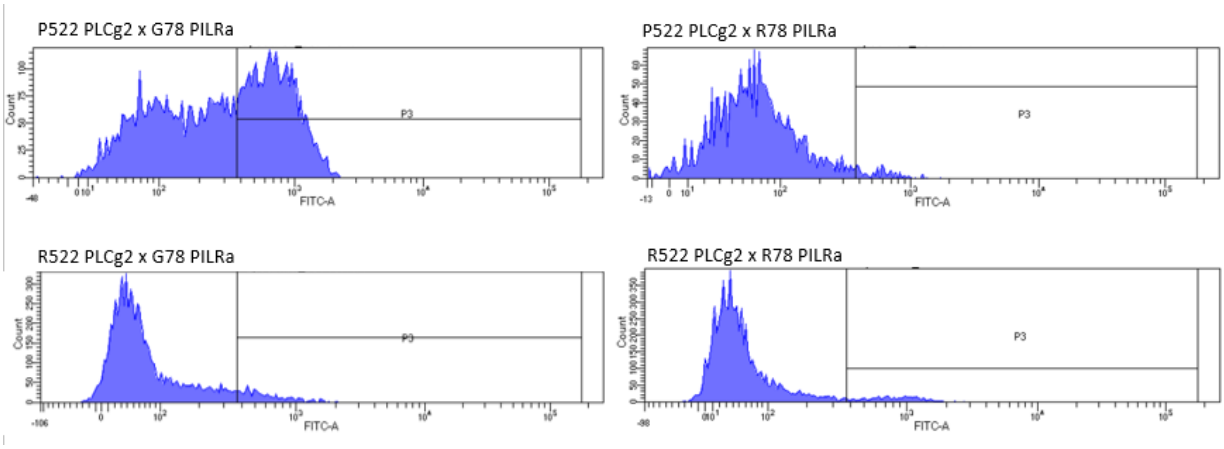

Figure 3.6: PILRα signal in cells during FACS sorting of MOP cells. Cells were stained with anti-PILRα antibody (R&D Systems) and kept on ice during the whole protocol. Histograms show the cell population and gate P3 represents the proportion of positive cells found in the samples during sorting.

Cell populations from the second FACS sorting were maintained in culture and regrown, excluding P522 PLCg2 x R78 PILRα MOP cells which did not recover after the sort. Cells were subjected to flow cytometry analysis of PILRa cell surface expression. Figure 3.7 represents the histograms from the PILRa staining. All plots show a slight shift in PILRα expression however, a large proportion of the cell population remains negative for PILRα expression. This does not show further increase in expression compared to cells after the initial sorting. When these cells were kept in culture for additional passages the PILRα expression decreases further (not shown).

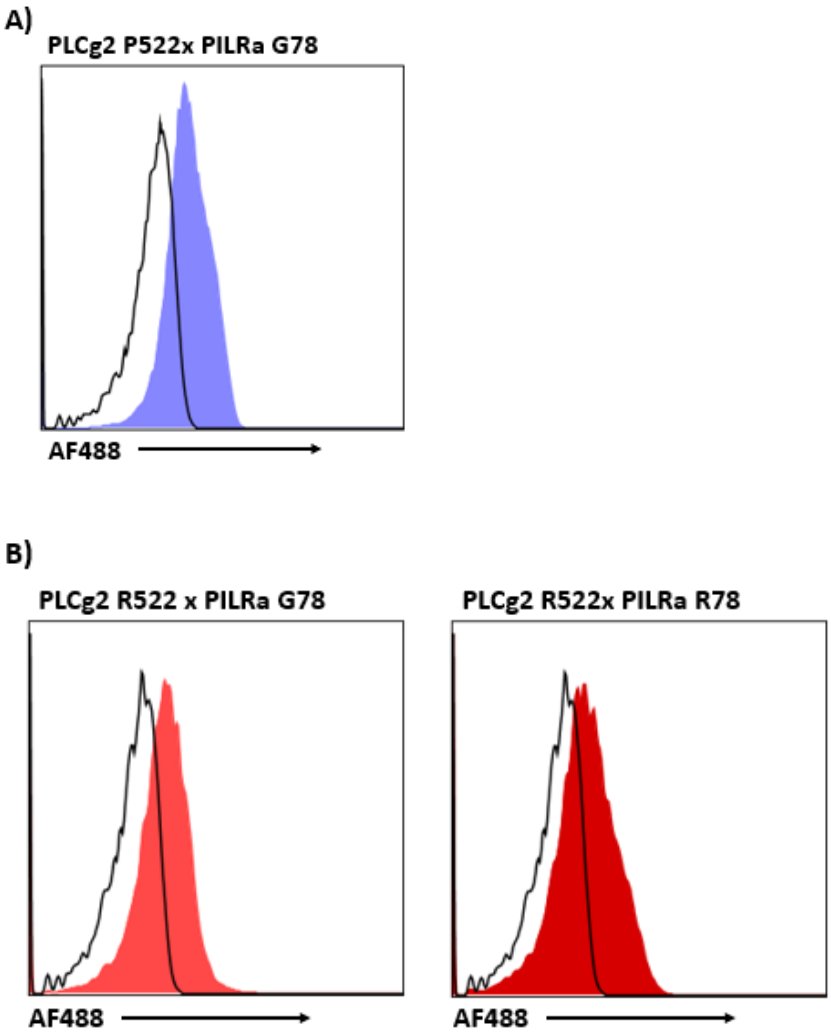

Figure 3.7: PILRα expression does not increase further after second FACS. Cells were FACS sorted for a second time by using anti-PILRα antibody. The recovered population of cells were fixed, blocked and stained with anti-PILRα antibody for flow cytometry analysis. **(A)** The histogram represents P522 PLCg2 MOP cells infected with *G78 PILRA* SIPW lentiviral vector and sorted twice. The flow cytometry analysis shows that although there are positive cells (filled plot), some of the cells do not express PILRα compared to the isotype control (black line). **(B)** The histograms represent R522 PLCg2 MOP cells infected with *G78/R78 PILRA* SIPW lentiviral vector and sorted twice. The flow cytometry analysis shows the presence of some positive cells (filled plots), however around half of the cell population does not express PILRα compared to the isotype control (black line).

Overall, these results indicate that full length *G78/R78 PILRA* SIPW lentivirus does not lead to stable overexpression of PILRα in PLCg2 MOP cells. Due to loss of expression in these cell lines over culture passages, an alternative expression system was required to deliver stable expression of full length PILRα variants in MOP cultures. A retroviral approach using

neomycin resistance driven by an internal ribosomal entry site (IRES) sequence downstream of *PILRA* was selected.

3.2.3. Use of an MMVL- based retroviral vector for the expression of PILRα

3.2.3.1 Cloning pFB-Neo retroviral vector

The full length PILRα sequence from the lentiviral SIPW vector (previously developed in the lab) was cloned to the pFB-Neo retroviral vector. This vector contains neomycin resistance gene driven by an internal ribosomal entry site (IRES). An example of vector linearization is shown in Figure 3.8A, where the linearized vector was electrophoresed faster. To optimize the temperature at which the primer annealing was most efficient, a temperature gradient PCR was performed using Phusion high-fidelity DNA polymerase (NEB) (Figure 3.8B). From the image of the gel 58^{o}C was determined as the optimal annealing temperature. After transformation individual bacterial colonies were screened via PCR using primers designed around the *XhoI* insert site as seen in Figure 3.8C (further details in methods). Retroviral plasmids were extracted after selected positive colonies were taken and grown overnight in LB media containing 100mg/mL Ampicillin. A selection of purified plasmids was sent for sequencing to confirm successful insertion of the full length PILRα and its variants (Eurofins Genomics).

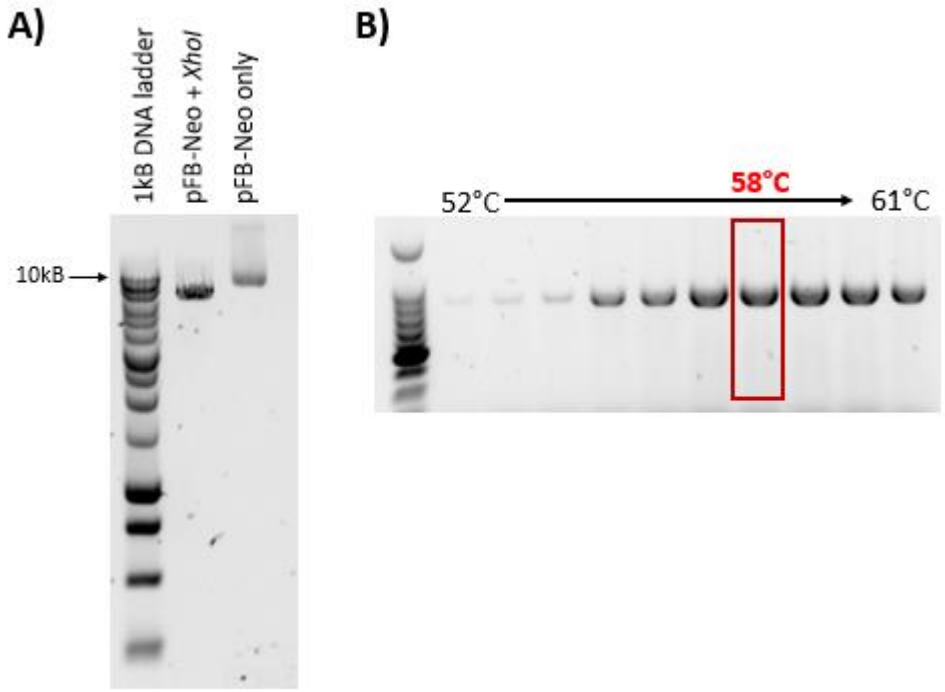

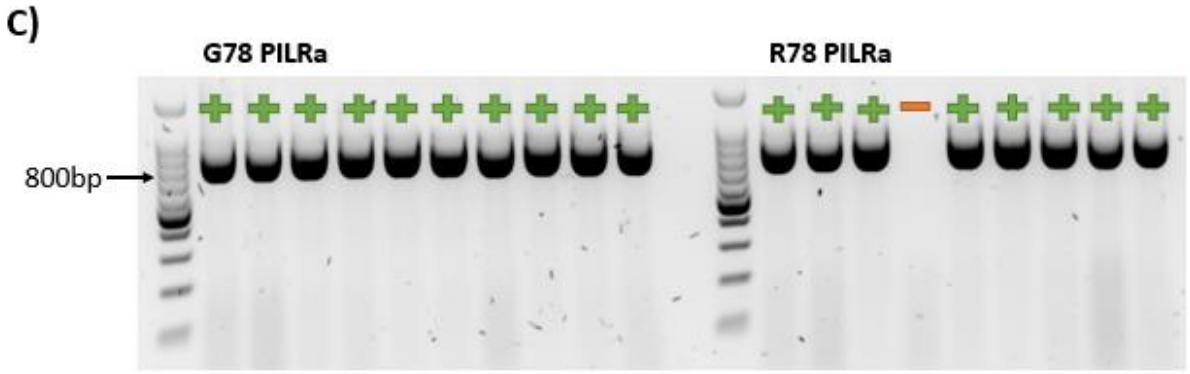

Figure 3.8: Cloning pFB-Neo retroviral vector. (A) Linearized pFB-Neo vector. pFB-Neo retroviral vector was cleaved by addition of *XhoI* enzyme. Linearization of the vector was confirmed on 1% agarose gel, where the linear form migrates quicker through the gel in comparison to the circular. **(B)** Temperature gradient PCR for PILRα insert. The temperature of the reaction was optimized to achieve a strong clear band of the correct size for PILRα (954bp). From the gel it was estimated that this temperature was 58 degrees. **(C)** Colony PCR for G78 and R78 PILRα pFB-Neo. Bacterial colonies were screened using specific primers designed to bind both sides of the insert in the desired orientation. The expected band size of positive colonies was 830bp (labelled with +) and negative colonies with no band (labelled with -), based on 100bp ladder (Promega).

3.2.3.2. Validation of PILRa expression in MOP cells

The derived retroviral vector was used to infect P522 and R522 PLCg2 MOP cells via spin infection. The generated cells were subject to selection with 0.5 mg/mL G418 (neomycin) for 10 days and expression of PILRα was subsequently analyzed. Uninfected control cells successfully died during selection. Cells were tested for gene expression of PILRα using RNA extracted following selection. Cell surface expression of the receptor was further validated through flow cytometry (Figure 3.9). G418 selection was maintained in cultures after transduction and completion of the initial selection period. Since PILRα variants are expressed upstream of an IRES-driven neomycin resistance cassette as part of a bicistronic transcript it was believed that this approach will result in sustained PILRα expression as it has done in other projects in the laboratory.

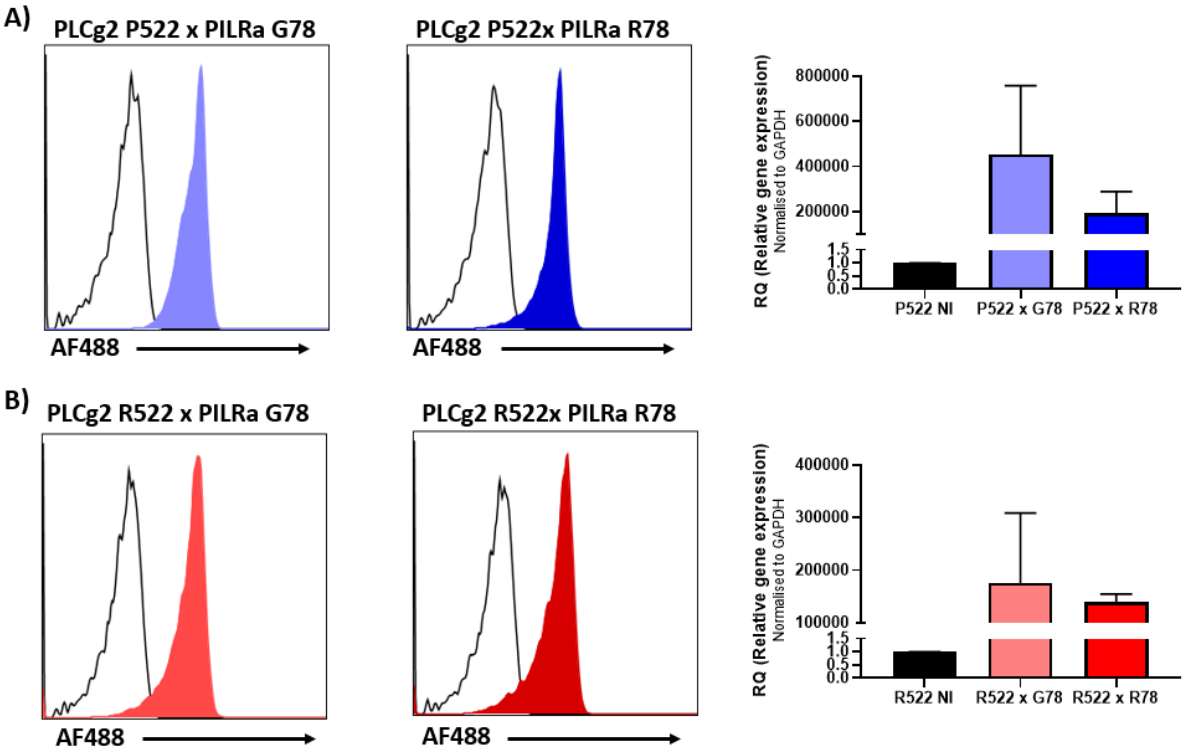

Figure 3.9: PILRα expression is increased in PLCG2 MOP cells infected with pFB-Neo containing PILRα vector. (A) Infected P522 PLCg2 MOP cells were fixed, blocked and stained with Alexa Fluor (AF)-488 conjugated anti-PILRα antibody or isotype control. The panels represent flow cytometry analysis showing increased cell surface PILRα expression (coloured histogram) in those cells compared to control (black line). In addition, mRNA of G78 and R78 PILRα is increased following retrovirus infection with full length *G78/R78 PILRA* pFB-Neo. P522 PLCg2 MOP cells were used as a non-infected (NI) control. Results presented are from a single experiment, where GAPDH was used as an endogenous control. **(B)** R522 PLCg2 MOP cells which were infected with PILRα expressing lentivirus were fixed, blocked and stained with AF-488 conjugated anti-PILRα antibody or isotype control. The panels represent flow cytometry analysis showing altered cell surface PILRa expression in those cells. The infected cell population has an increase in protein levels of G78/R78 PILRα. Further qPCR analysis shows that mRNA of G78 and R78 PILRα is increased following lentivirus infection with full length *G78/R78 PILRA* pFB-Neo. R522 PLCg2 MOP cells were used as a non-infected (NI) control. Flow cytometry histograms presented are from a single experiment. The mRNA analysis data represents 3 biological replicates, with n=3 technical replicate wells, where GAPDH was used as an endogenous control. Bars represent mean ± SEM.

After initial validation, MOP cells were differentiated using 20ng/mL of M-CSF as described in section 2.3.5.1. The resulting macrophage cultures were also assessed for PILRa expression through flow cytometry. As the results in figure 3.10 indicate, PILRa expression is

detected in all 4 newly generated lines. However, as opposed to the complete shift seen in the MOP cells, which indicates very high expression levels, here lower levels of expression are observed. Differences in the expression levels between the four lines can also be seen. For example, Plcg2 P522 x PILRa G78 cells show higher PILRa levels than Plcg2 R522 x PILRa R78 M-MOPs. This could potentially be due to changes occurring during the differentiation process which lead to loss or silencing of the vector in part of the cell population, which would further be considered in the chapter's discussion.

Additionally, a small trial was carried out to assess if selection with G418 during differentiation will increase the expression levels seen in M-MOPs. The flow cytometry results shown in Figure 3.11 indicate that antibiotic pressure does not seem to aid retention of PILRa expression. Therefore, cells were differentiated without G418 selection in following experiments. Furthermore, during multiple assays and additional experiments it was observed that the PILRa expression between differentiations can vary (data not shown), which might have functional implications.

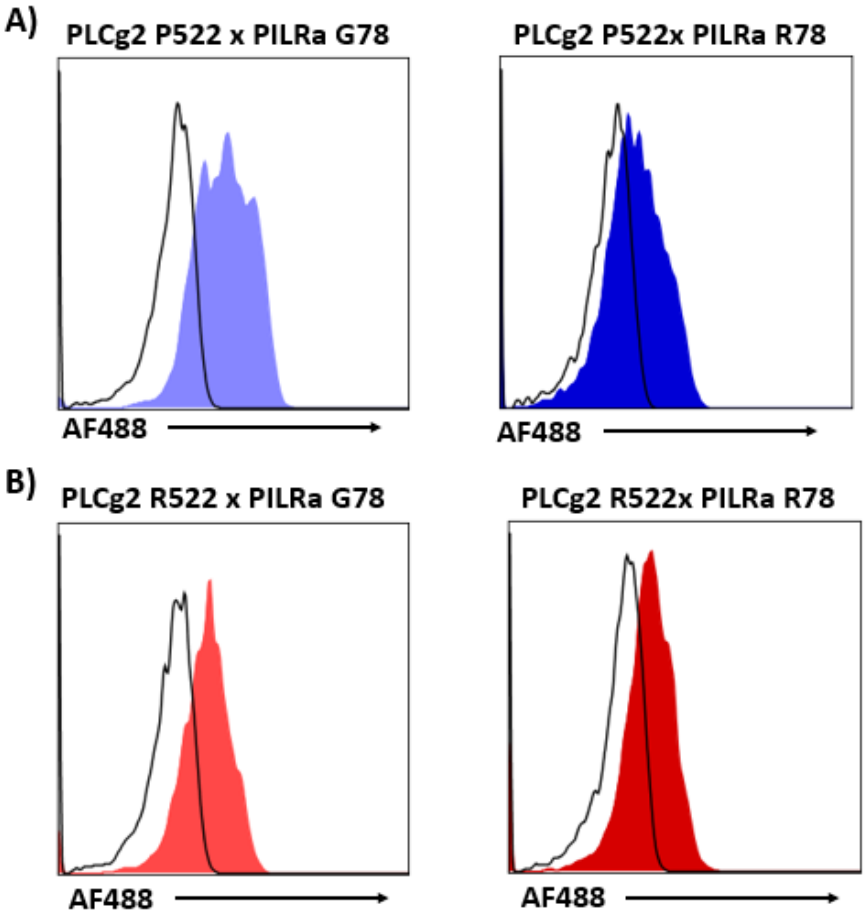

Figure 3.10: PILRa expression in M-CSF differentiated PLCg2 MOP cells. MOP cells were differentiated for 4 days in M-CSF and PILRα cell surface expression was analyzed with flow cytometry. Infected P522 PLCg2 MOP cells were fixed, blocked, and stained with Alexa Fluor (AF)-488 conjugated anti-PILRα antibody or isotype control. The panels represent flow cytometry analysis showing altered PILRα expression in those cells. As expected, the infected cells show an increase in surface expression of G78/R78 PILRα.

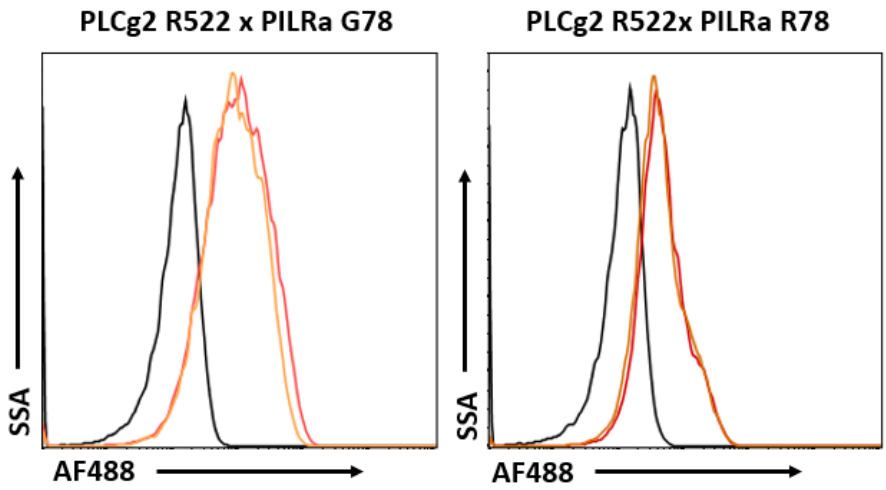

Figure 3.11: PILRa expression of M-CSF differentiated macrophage cells with or without presence of G418 antibiotic selection. Cells were cultured for 4 days with 20ng/mL of M-CSF. Differentiated cultures were detached, fixed and stained with AF488 conjugated anti-PILRa antibody or appropriate isotype control (R&D Systems) and analyzed using flow cytometry. Cells differentiated without G418 (yellow line) were compared to cells differentiated with G418 (red line).

3.2.4. Luciferase reporter assay for PILRa ligands

NFAT Jurkat Lucia cells (Invivogen) were derived from human Jurkat T-lymphocytes through a stable integration of NFAT-inducible luciferase reporter construct. Upon activation of a coelenterazine-utilizing luciferase, Lucia is secreted into the supernatant where it could be easily measured. NFAT cells were tested for luciferase activity after stimulation with ionomycin. The results are shown in Figure 3.12A. As the graph shows, cells stimulated with ionomycin for 18-24h. demonstrate a significant increase in luciferase signal. The ionomycin treated cells exhibit around 90-fold higher luciferase in comparison to the non-treated control (Figure 3.12B). In addition, stimulated cells present with a different morphology compared to non-treated cells. The cells which were subjected to ionomycin addition appear as large clumps in the culture media rather than a monolayer which indicates activation of NFAT. An example of this could be seen in Figure 3.12C.

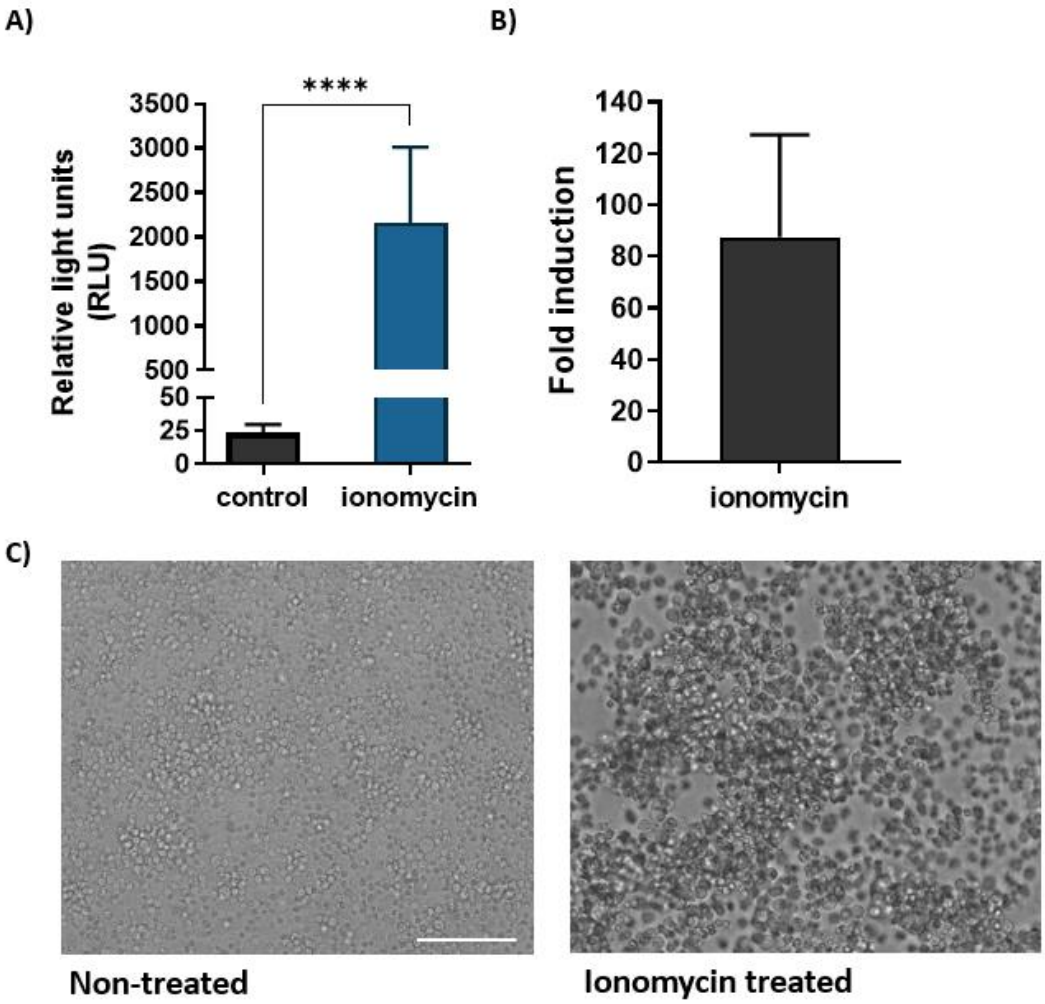

Figure 3.12: Jurkat Lucia NFAT cells respond to ionomycin. (A) Cells were treated with ionomycin (10ug/ml) and incubated for 18-24h. After treatment, 20ul of cell suspension was mixed with 50ul Quanti-Luc (Lucia luciferase detection agent) and the expression of luciferase in the culture was measured by a plate reader. Two-tailed unpaired t-test ($p<0.0001$) shows luciferase is significantly increased in the treated sample. **(B)** Fold change in luciferase expression of ionomycin treated cells. **(C)** Light microscopy image of NFAT Jurkat Lucia cells obtained on Evos (Thermofischer Scientific). Cells were either not treated or incubated for 18-24h. with ionomycin. Scale bar = 200µm.

Following confirmation of activation of the NFAT Jurkat Lucia cell line, the cells were infected with *G78/R78 PILRA-ECD-CD3ζ* SIPW lentiviral constructs. The appropriate lentiviral titer was estimated in advance using GFP control virus (Figure 3.13). The PILRα fusion protein contains an extracellular domain (ECD) paired with CD3ζ which mediates signalling through immunoreceptor tyrosine-based activation (ITAM) motifs which are stimulated through phosphorylation and play a key role in mediating T-cell activation (259). After positive selection with puromycin (0.5ug/ml) for 10 days, the expression of PILRα in the new

cell lines was assessed. As demonstrated on Figure 3.14, PILRα cell surface expression was analyzed using a flow cytometry approach. The histograms clearly represent an increase of both G78 and R78 PILRα-ECD-CD3ζ in infected cells as compared to appropriate isotype control and non-infected (NI) controls. Cell cultures were kept in puromycin to retain the selection pressure and expression was reassessed following few passages. The expression of PILRα in the NFAT Lucia Jurkat cells remained high and was sustained through the whole cell population.

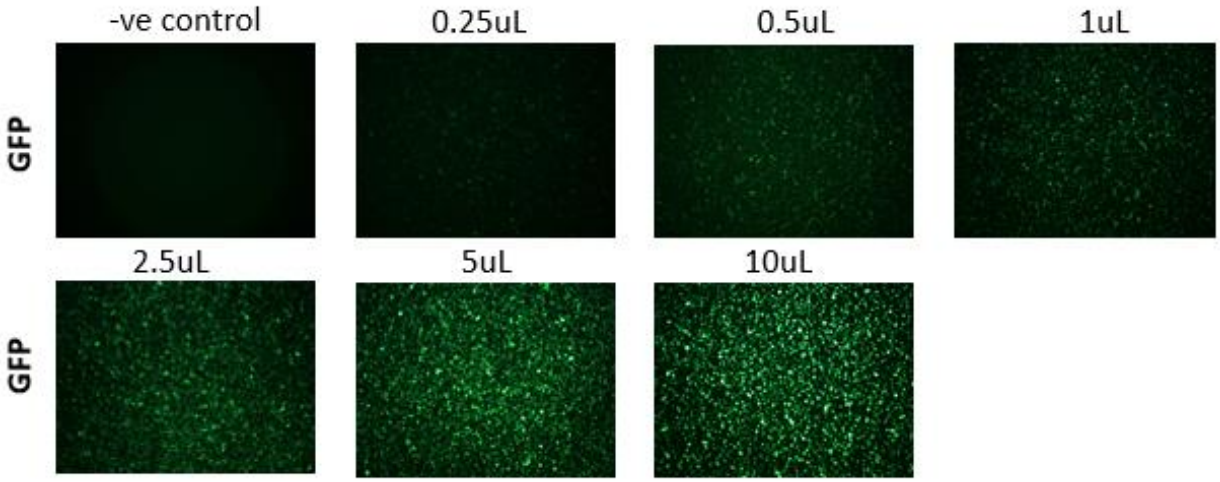

Figure 3.13: Fluorescent images of Jurkat cells 72h. post infection with various doses of GFP expressing lentivirus. Images were acquired using the 10X objective on the Evos (Thermofischer Scientific).

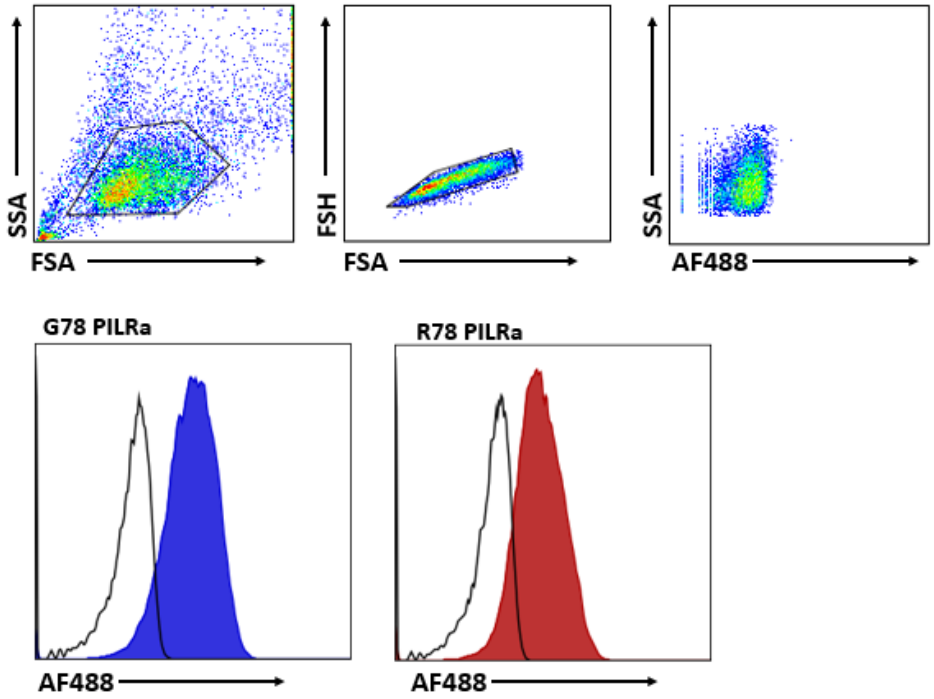

Figure 3.14: PILRa-ECD-CD3ζ shows increased cell surface expression in NFAT Jurkat Lucia cells. NFAT Jurkat Lucia cells (Invivogen) were infected with *G78/R78 PILRA-ECD-CD3ζ* SIPW lentiviral vector. After puromycin selection, cells were fixed, blocked and stained with anti-PILRα AF-488 conjugated antibody or isotype control. Unstained cells were used to gate on the correct population and eliminate doublets. The histograms show an increase in G78/R78 PILRα expression compared to the isotype control**.**

Infected Jurkat Lucia cells were stimulated with ionomycin to confirm that the line retains its properties in terms of luciferase expression. As previously described, cells were stimulated using ionomycin and incubated for 18-24h. Luciferase expression was significantly increased in both cell lines as expected (Figure 3.15).

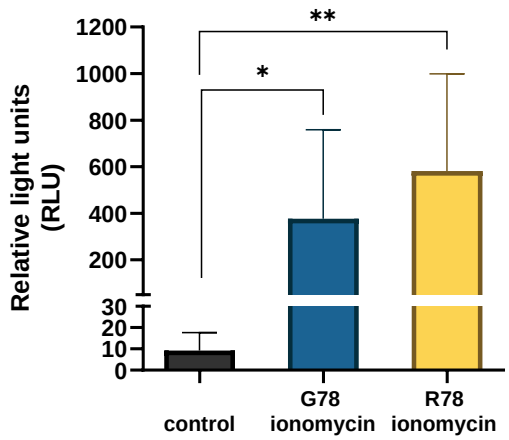

Figure 3.15: G78 and R78 PILRα NFAT Jurkat Lucia cells show an increase in luciferase signal when stimulated with ionomycin. Expression of luciferase was measured following ionomycin (10ug/mL) exposure. All samples were run in triplicate. One-way ANOVA test was carried out to determine significant differences in luciferase activity (p =0.0043), followed by a Dunnett's test for multiple comparison.

Overall, *G78* and *R78 PILRα-ECD-CD3ζ* SIPW lentivirus was stably integrated in NFAT Jurkat Lucia cells. The expression of the PILRα construct was sustained and cells showed positive response to ionomycin stimulation resulting in increase of luciferase signal. This chapter then moves onto developing a cell model appropriate for successful stimulation of the PILRα expressed on the NFAT Jurkat Lucia cell lines utilizing the luciferase assay approach.

3.2.5. Cloning and validating CD99 lentiviral plasmid

The full-length mouse CD99 (mCD99) sequence from the pEX-a128 vector was cloned into SIPW lentiviral vector. mCD99 was synthesized commercially in the pEX-a128 vector and supplied by Eurofins Genomics. The CD99 construct was amplified from the host vector using primers designed to bind either side of the insert containing a 15bp overhang required for the subsequent In-Fusion reaction. An example of vector linearization is shown in Figure 3.16B, where the linearized vector was electrophoresed faster. After transformation individual bacterial colonies were screened via PCR using primers designed around the *XhoI* insert site as seen in Figure 3.16C (further details in methods). Lentiviral plasmids were extracted after selected positive colonies were taken and grown-up. The purified plasmids were sent for sequencing to ensure successful insertion of CD99.

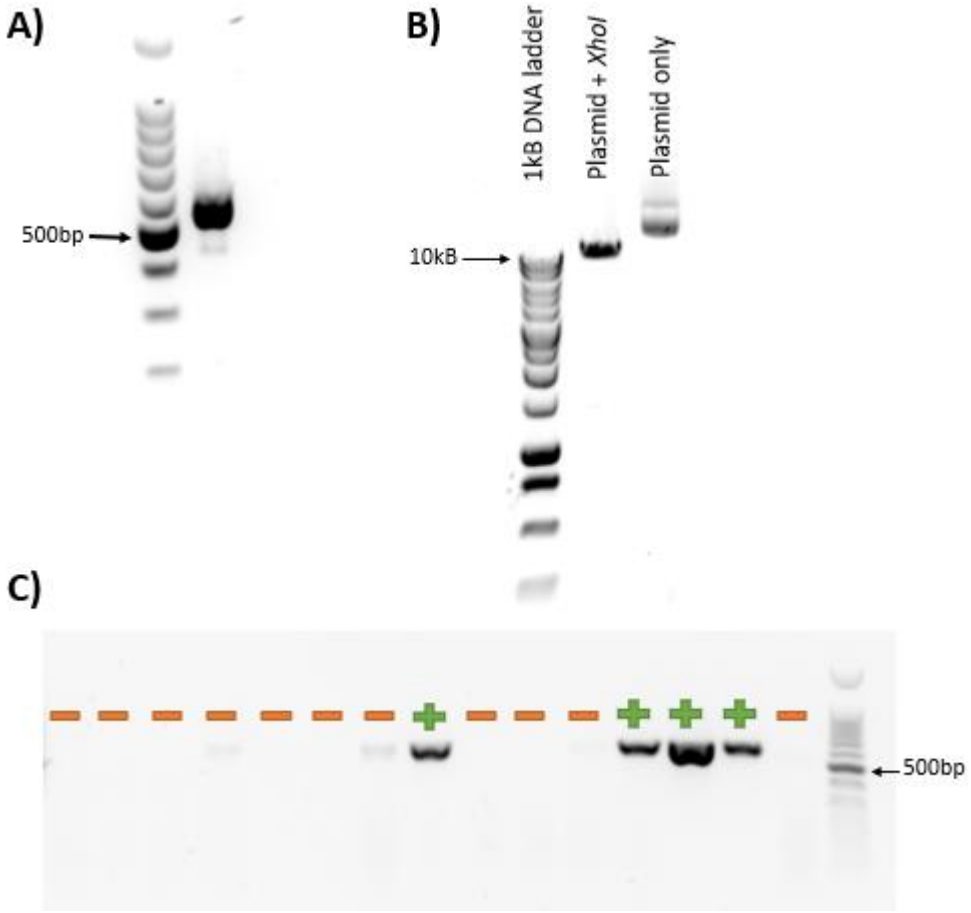

Figure 3.16: Cloning lentivirus to manipulate CD99 expression. (A) Amplification of the CD99 insert from pEX-a128 vector. Specifically designed primers to bind both sides of the insert were used. The desired product (545bp) was extracted from the agarose gel and purified. **(B)** Linearized SIPW vector. SIPW lentiviral vector was cleaved by addition of *XhoI* enzyme. Linearization of the vector was confirmed on 1% agarose gel, where the linear vector migrates quicker through the gel in comparison to the circular. **(C)** Colony PCR for CD99 SIPW. 15 bacterial colonies were screened using specific primers designed to bind both sides of the insert in the desired orientation. The expected band size of positive colonies was 605bp (labelled with +) and negative colonies with no band (labelled with -), based on 100bp ladder (Promega).

The newly cloned *mCD99* SIPW lentiviral vector was first subjected to validation in the mouse pro-B cell Ba/F3 cell line, because mCD99 has previously shown to be appropriately glycosylated to serve as a ligand for PILRa when expressed in Ba/F3 cells (254). To establish the best lentiviral dose for infecting those cells a titration using SEW (GFP expressing) lentivirus was performed. The results are shown in Figure 3.17, with 25uL of viral supernatant producing 90% positive GFP expressing cells.

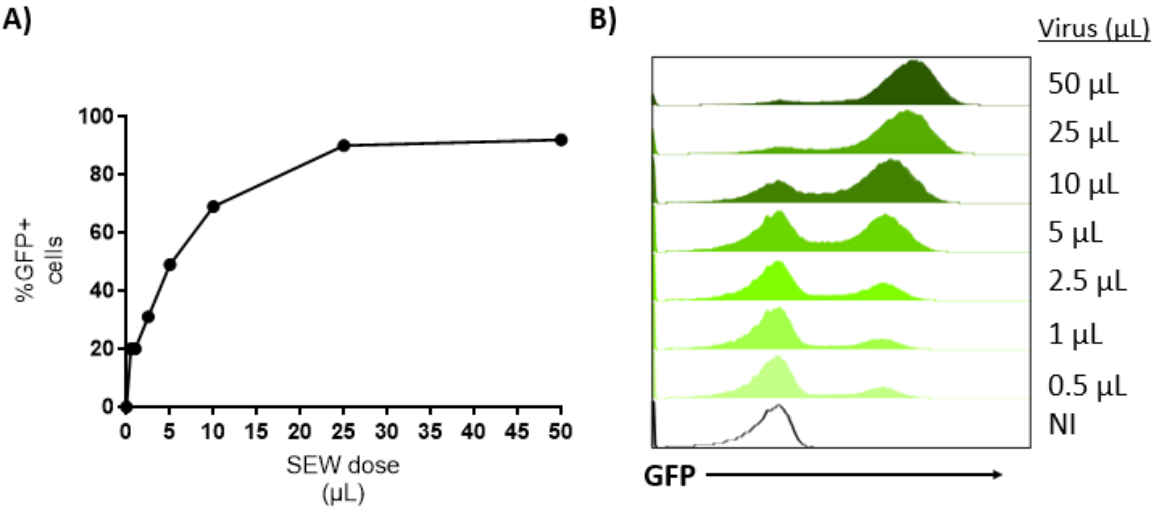

Figure 3.17: Titer validation of SEW lentivirus. Ba/F3 cells were infected with different doses of *SEW* (GFP expressing) lentiviral vector and expression of GFP was assessed 72h post-infection. **(A)** Percentage of GFP+ cells. **(B)** Cells were fixed and analyzed with flow cytometry 3 days post-infection. The GFP signal from cells is shown in the histogram.

Ba/F3 cells were infected with *mCD99* SIPW lentivirus. The infected cells were subjected to puromycin selection (2ug/ml) for 10 days, after which the expression of mCD99 in those cells was analyzed using flow cytometry. Uninfected cells treated with puromycin in parallel died. Cell surface expression of mCD99 was quantified by using an anti-CD99 staining. The histograms in Figure 3.18 clearly represent a shift in mCD99 expression, with infected cells showing a homogenous population of positive cells compared to non-infected (NI) cells. The positive cells were retained in puromycin so that selection pressure could be maintained. The expression of mCD99 remained high even after a few passages of the cell culture, pointing at a stable integration of the mCD99 construct.

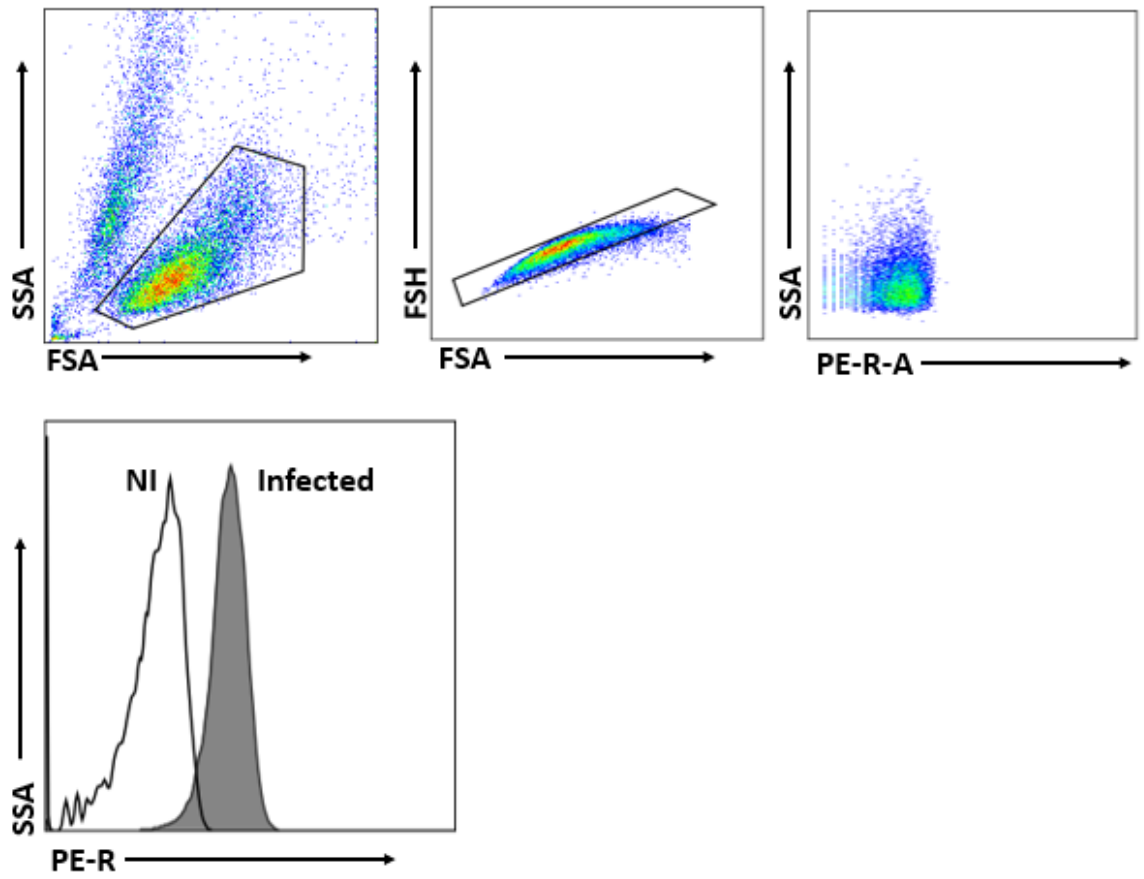

Figure 3.18: CD99 shows increased expression in Ba/F3 cells. Ba/F3 cells were infected with *mCD99* SIPW lentiviral vector. Cells were then subjected to puromycin selection (2ug/ml) for 10 days. Subsequently, cells were stained with goat anti-CD99 PE conjugated antibody. Non-infected (NI) Ba/F3 cells were used as a control (black area). The relevant cell population was gated, doublets were excluded and expression of mCD99 is shown.

3.2.6. Stimulation of human PILRα with mCD99

NFAT Jurkat Lucia cells stably expressing G78 or R78 PILRA-ECD-CD3ζ were stimulated through co-culture with Ba/F3 cells expressing mCD99 to confirm physical interaction and validate PILRa activation. Cells from both cultures were mixed and incubated for 18-24 hours prior to obtaining luciferase readings. In parallel, cells were stimulated with ionomycin which acts as a positive control indicating cell stimulation has occurred. The results in Figure 3.19 indicate that co-culture with the Ba/F3 cells did not successfully induce luciferase expression in the PILRa expressing cells. This indicates that PILRa and CD99 most likely do not interact functionally in the selected cell lines.

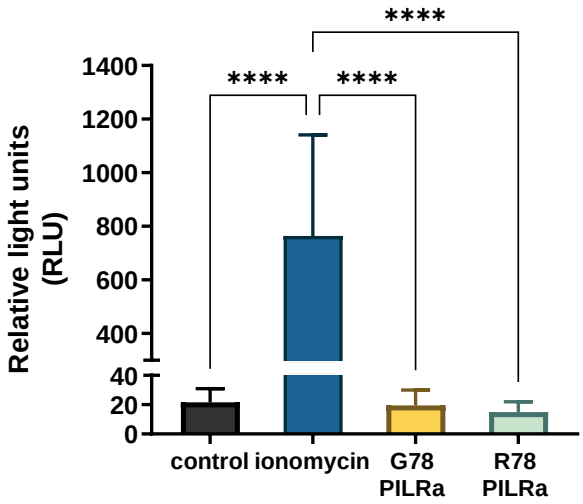

Figure 3.19: mCD99 expressed on Ba/F3 cells does not stimulate Jurkat Lucia cells expressing the PILRα-ECD-CD3ζ chimera. NFAT Jurkat Lucia cells expressing G78/R78 PILRα-ECD-CD3ζ were mixed in co-culture with mCD99 Ba/F3 cells for 18-24h. Cells treated with ionomycin were used as a positive control and water was used as a negative. All cells were plated in triplicate, n=2 biological replicates. Bars represent mean ± SD. One-way ANOVA was carried out to determine any significant differences in luciferase signal, followed by Tukey's multiple comparisons test.

3.2.7. Using PANP as a stimulant of PILRα

The potential to use previously identified PANP protein as a functional stimulant for PILRa was explored. Recombinant human PANP-Fc chimera protein (commercially available) was selected to initially validate the functional interaction. The PANP protein was utilized instead of a primary antibody and a secondary antibody was used to bind to the Fc portion of the protein and aid detection (Figure 3.20). To increase the detection of this interaction further the PANP-Fc chimera protein was incubated with secondary antibody before being applied to the cells which results in multimerizing of the Fc domains (Figure 3.21).

This was first trialed in the Jurkat Lucia cells expressing both PILRa variants. As demonstrated from the flow cytometry data in Figure 3.22A, a visible increase in secondary APC signal is detected. Interestingly, the G78 expressing cells exhibit a higher proportion of binding compared to R78 cells. This was further carried out in the PILRa expressing M-MOP cells since this was the main line of interest for future experiments. Surprisingly the observed increase was not reproduced in this cell line (Figure 3.22B). No PILRa-PANP binding was detected using the same protocol and dose of the Fc chimera protein. Based on this result the PANP-Fc chimera was deemed unsuitable for being used as PILRa ligand in further

functional assays including M-MOP cells. Finally, the protein was utilized on human iPS derived microglia-like cells. The Kolf2 line showed successful detection of PANP with increase compared to the negative control (Figure 3.22C). The contradictory findings presented here and the potential underlying reasons for them are further explored in the chapter discussion. Additional data for the use of PANP-Fc on iPS derived microglia-like cells can be found in the next chapter which explores this model in more detail.

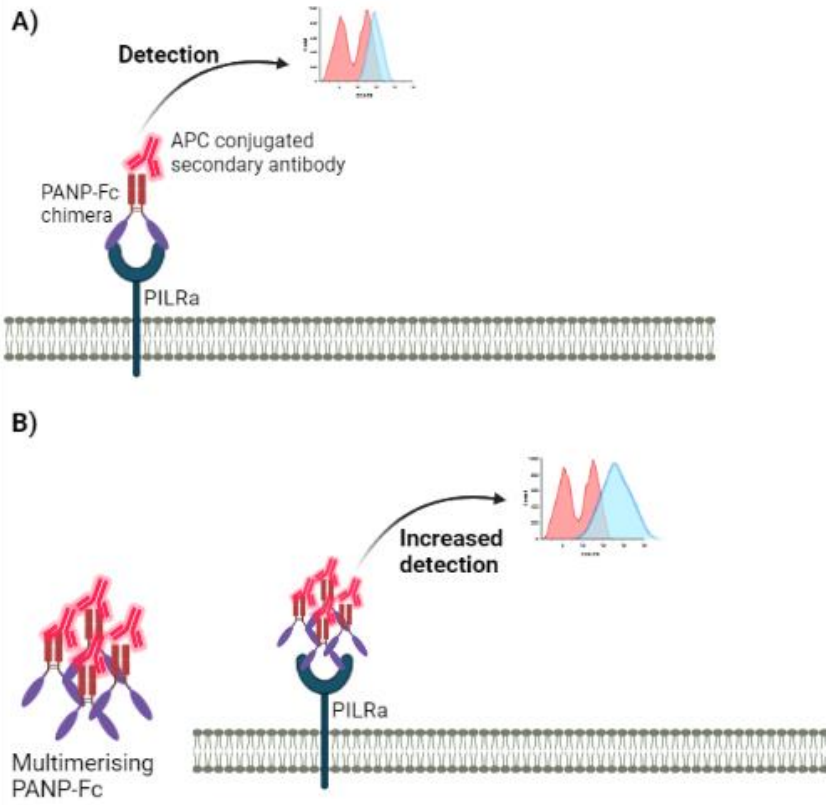

Figure 3.20: Using PANP-Fc as ligand for PILRa. (A) PANP-Fc is a chimera protein which contains PANP conjugated to human Fc. If PILRa is present on the cell surface, PANP will bind and then detected using secondary antibody which targets the Fc portion. The fluorescent antibody will be detected through flow cytometry. **(B)** To aid detection of PILRa-PANP binding, the protein was initially cross-linked with anti-Fc antibody which increases avidity, and the subsequent detection signal is higher.

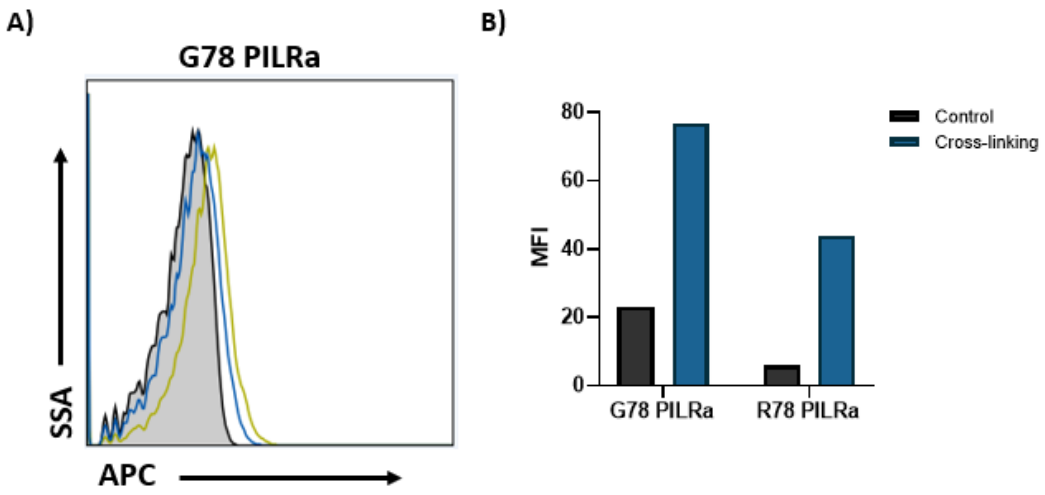

Figure 3.21: PANP binding to Jurkat Lucia cells with and without cross-linking. (A) Representative histogram demonstrates APC signal detected in cells treated with PANP. Cells were incubated with 50ng/ml PANP (blue line) or PANP crosslinked with secondary antibody in 1:4 ratio (yellow line). Secondary only control was used (black line). **(B)** APC MFI of Jurkat cells. Bars represent values from a single experiment.

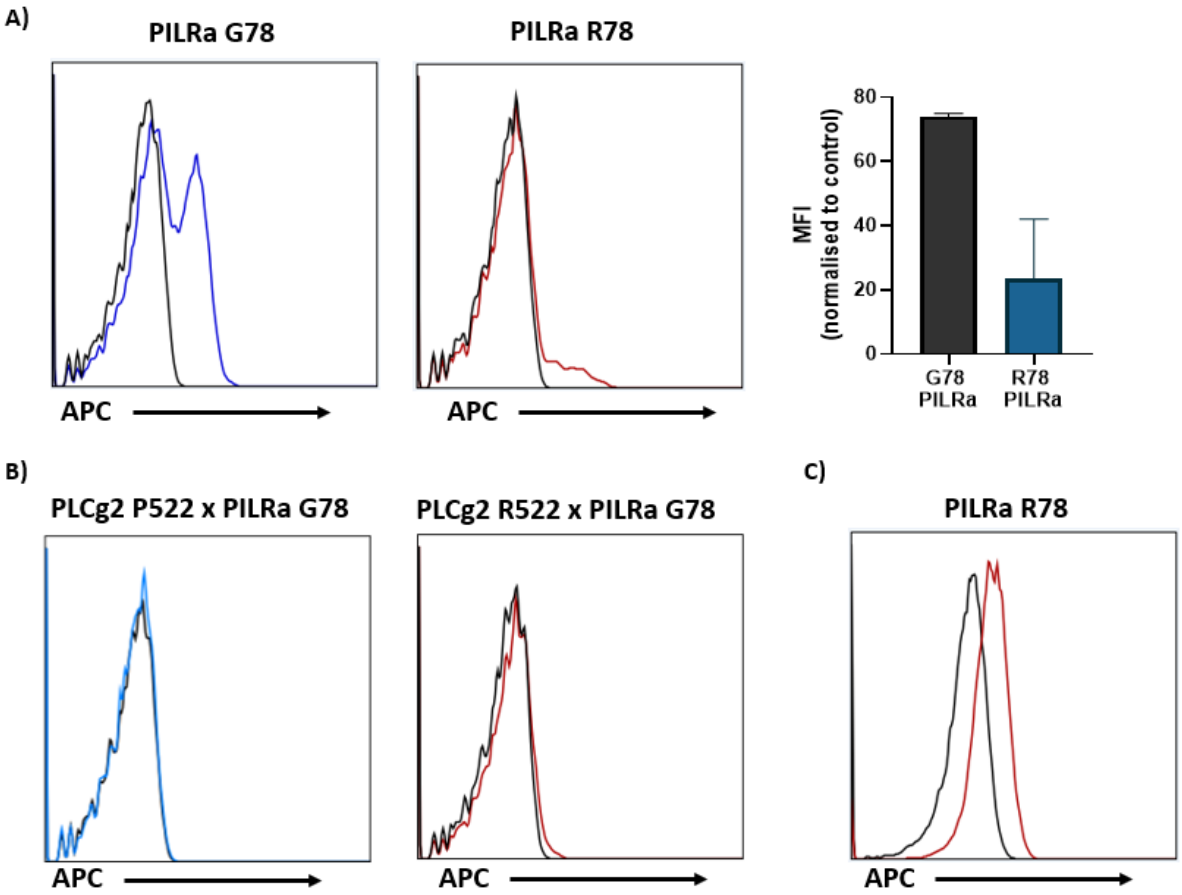

Figure 3.22: PANP-Fc chimera activity in different cell lines. Cells were incubated with PANP-Fc (50ug/ml, R&D systems) and stained with secondary antibody (anti-human) conjugated to APC (1:200 dilution, Jax Immunoresearch). Samples were run on Attune NxT to detect binding. The black line represents a secondary only control. The coloured histogram indicates the PANP-Fc treated samples. **(A)** Jurkat Lucia cells expressing PILRa interact with PANP-Fc chimera. Bars represent mean ± SD (n=2). MFI is normalized to secondary only control. **(B)** Level of PANP-Fc in M-MOP cells demonstrates no difference compared to control (black line) **(C)** Kolf2 derived iPS microglia-like cells show increase in APC signal representing PANP-Fc binding.

3.2.7. Exploring functional differences between PILRa variants

The following assays were used to observe macrophage relevant functions and detect any differences induced by the presence of different PILRa variants. A variety of assays were selected which cover core functions of these cells but also additional cell functions which might reveal a more detailed picture about the role of the PILRa receptor in cell functions. Due to issues with differentiation of some of the previously generated and characterized PILRa lines in this chapter, the following assays were performed only on macrophages differentiated on the R522 Plcg2 background line. The utilized lines were created using the

pFB-Neo vector and undergone G418 selection method as previously described. All assays contain a control line, which expresses no PILRa but contains the same vector backbone.

3.2.7.1. PILRa expressing cells do not have altered phagocytosis

Phagocytosis is one of the key macrophage functions, therefore it was initially tested to observe any PILRa relevant differences. The differentiated lines were subjected to a time course measuring the uptake of pH-Rodo conjugated zymosan particles. The results on Figure 35 demonstrate that overall signal increases during the time course of the assay. No significant changes are reported related to genotype, although a trend towards decreased phagocytosis can be seen in the PILRa expressing cells compared to control. In addition, no uptake is recorded with the Cytochalasin D control which provides a positive control for the assay. Representative images in Figure 3.23A demonstrate the difference between the assay conditions. Due to time constraint this experiment was not further followed in these cells although it would have been interesting to observe the response to other particles such as E. coli, synaptoneurosomes or apoptotic cells, which might have provided a better insight into the overall uptake properties of the cultures.

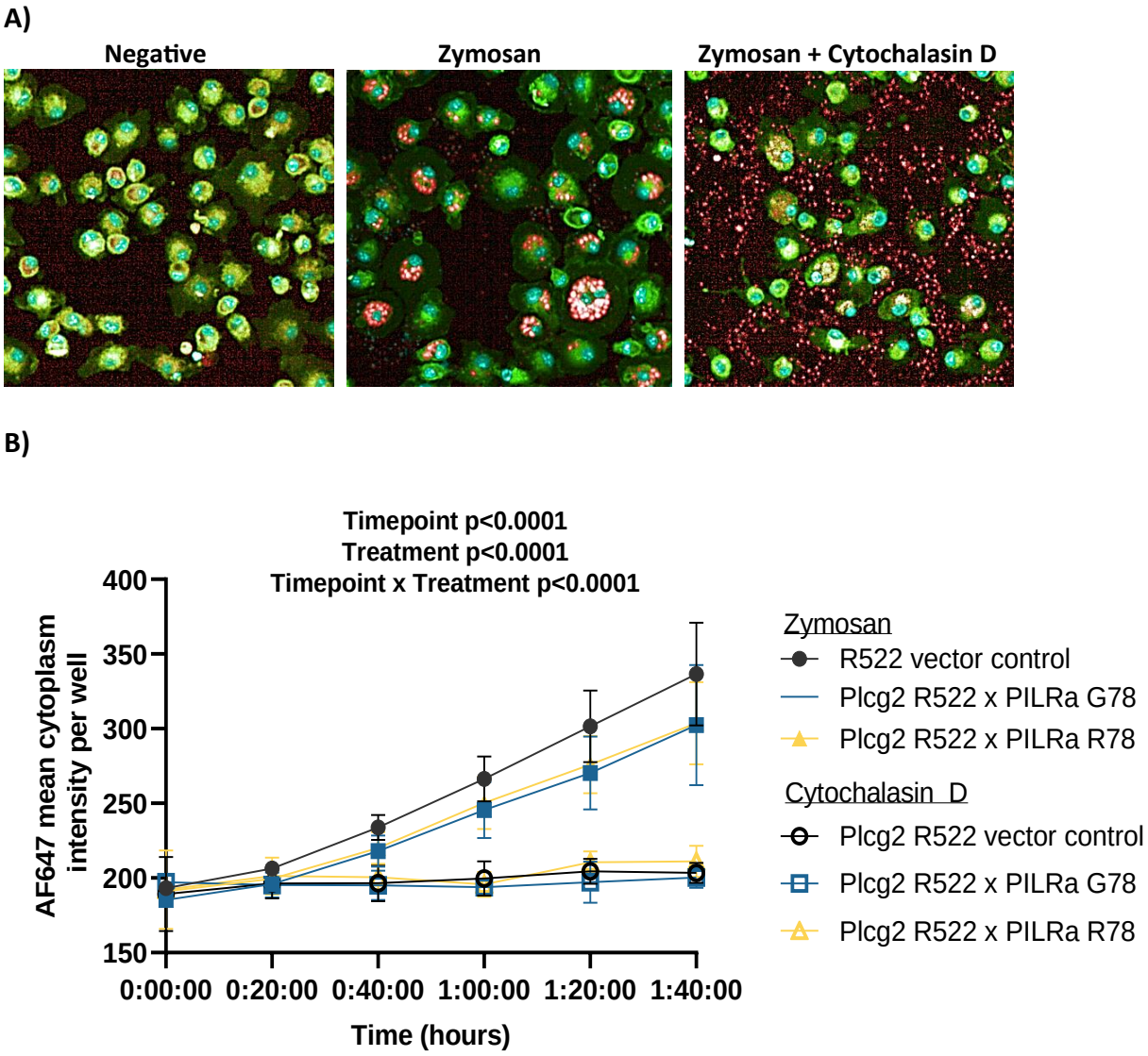

Figure 3.23: Live pH-Rodo zymosan phagocytosis in PILRa expressing M-MOP cells. M-MOPs were incubated with pH-Rodo zymosan beads and images were acquired every 20 minutes for 5 timepoints using the Opera Phenix (Perkin Elmer). Vector control line was used as a control for PILRa variants. **(A)** 20X water objective representative images of wells containing no zymosan, zymosan without treatment or zymosan and CytoD treated. Scale bar = µm **(B)** Average AF647 cytoplasmic intensity per well. Each time point represents mean ± SD, triplicate replicate wells (n=3 biological repeat plates). Data was analysed using two and three-way ANOVA followed by Tukey's multiple comparisons test. Only significant interactions are reported above the graph.

3.2.7.2. The metabolic response of PILRa expressing cells

To investigate the effect of PILRa and any differences between the two variants on cell metabolism, a Seahorse Real-time ATP assay (Agilent) was performed. The assay measures in real-time the production of adenosine triphosphate (ATP) simultaneously from glycolysis

and mitochondrial respiration. The assay depends on the output of two main parameters, the oxygen consumption rate (OCR) and the extracellular acidification rate (ECAR) allowing measurement of oxidative stress and glycolysis. Differentiated M-MOP cells replated as previously described on day 4 were used for the assay. The assay involves addition of two compounds, oligomycin and rotenone, which block variable complexes of the electron transport chain and change the metabolic state of cells. Figure 3.24A shows the OCR trace during the assay and the points at which compounds are added. The cells respond in the expected way, therefore providing a positive control for the assay efficiency. In addition, analyzing the ratio between oxidative phosphorylation and glycolysis (XF ATP index) shown in figure 3.24B it can be estimated which metabolic pathway cells are primarily using. As seen from the results, the only significant change based on genotype differences is that in the unstimulated group. Cells expressing G78 PILRa have significantly lower ATP index, meaning these cells demonstrate higher levels of glycolysis. As reported by two-way ANOVA, G78 PILRa cells produce significantly more ATP utilizing glycolysis than oxidative phosphorylation compared to control ($p=0.0018$) and R78 PILRa cells ($p=0.0039$) pointing at a shift in the metabolic state. However, this result is not reflected in the other parameters analyzed such as OCR and ECAR.

In addition, most of the observed changes are related to stimulating the cells with LPS or LPS and IFN-γ instead. Interestingly, LPS stimulation seems to push cells towards a more glycolytic state. This is seen in the OCR trace, where compound treatment does not impact the levels of oxygen produced. However, LPS and IFN-γ treatment would be expected to shift this response even further and show high levels of glycolysis. What is observed in the data here shows the opposite trend. The stimulation seems to reverse some of the effects observed with LPS and seems to respond to the compound treatment meaning cells were relying more on oxidative phosphorylation.

A)

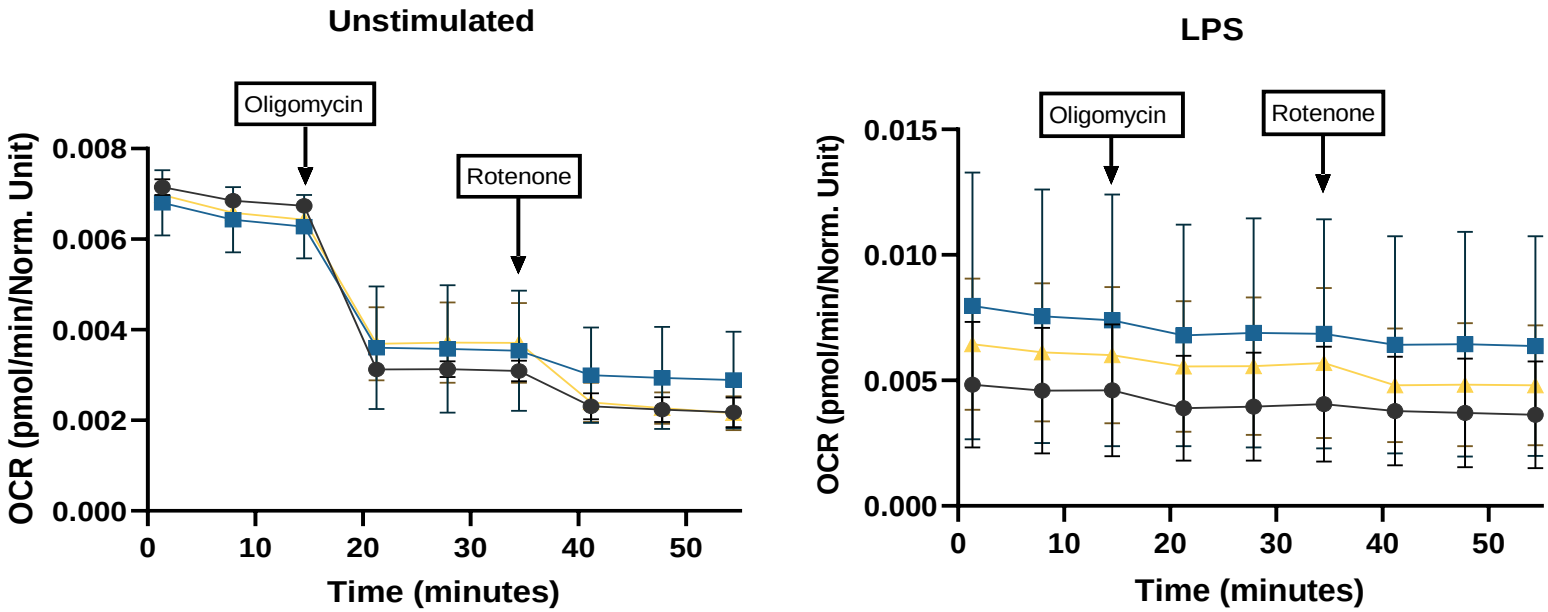
Unstimulated
Oligomycin
Rotenone
OCR (pmol/min/Norm. Unit)
0.008
0.006
0.004
0.002
0.000
0
10
20
30
40
50
Time (minutes)
LPS
Oligomycin
Rotenone
OCR (pmol/min/Norm. Unit)
0.015
0.010
0.005
0.000
0
10
20
30
40
50
Time (minutes)

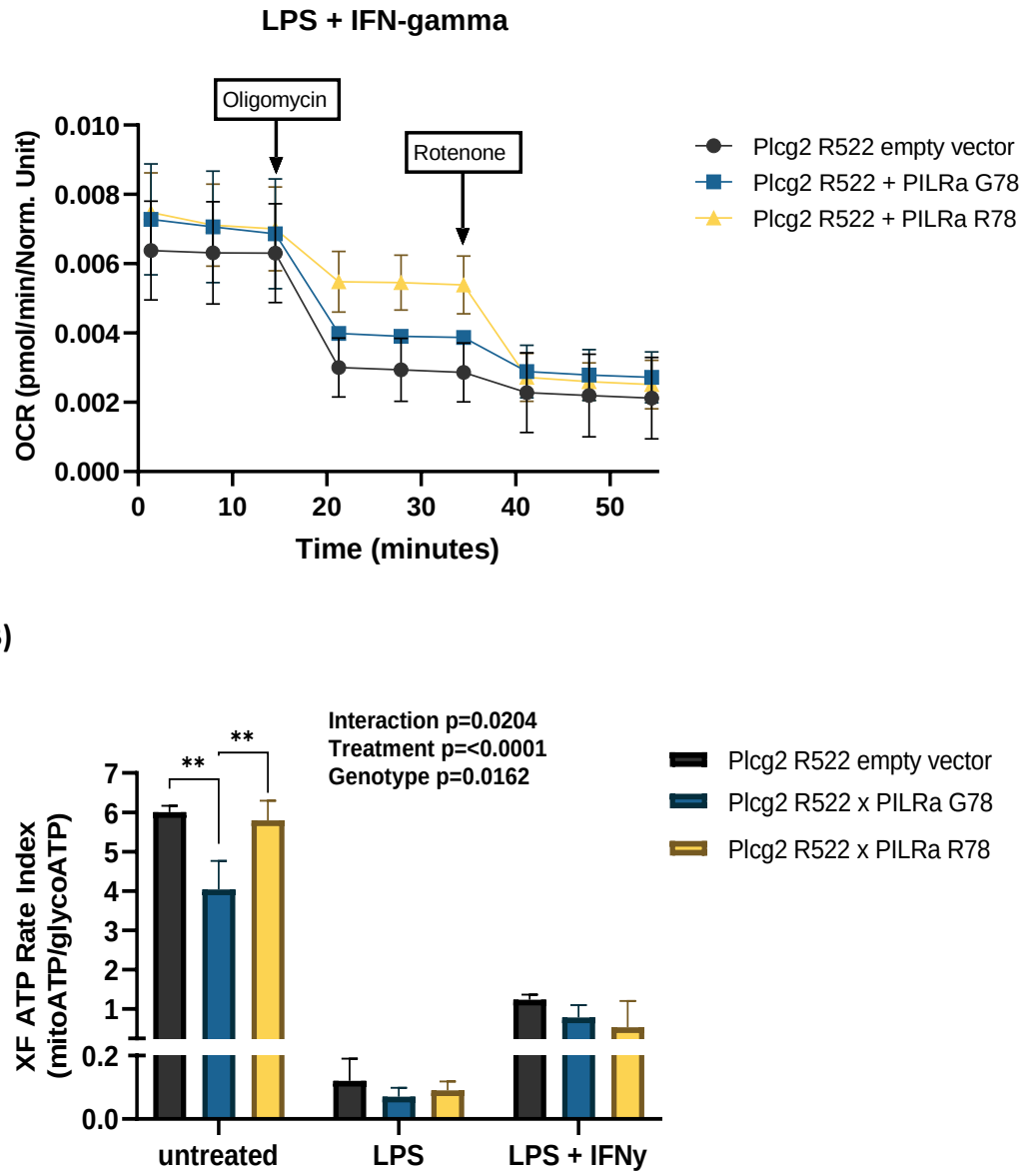

Figure 3.24: Seahorse Real Time ATP rate assay using differentiated M-MOP cells. Cells were treated with LPS (100ng/mL) or LPS (100ng/mL) and IFN-γ (20ng/mL) overnight and supernatants were collected for analysis. **(A)** Oxygen rate trace measured during the experiment. Traces of unstimulated, LPS treated and LPS and IFN-γ cells

presented. Compounds added and the timepoint of addition is indicated with the black arrows. Individual points represent mean ± SD. **(B)** XF ATP rate index representing the ratio between oxidative phosphorylation and glycolysis. Bars represent mean ± SD. Data was analysed using two-way ANOVA, followed by Tukey's multiple comparisons test (**p<0.001). For all experimental plates, cells were plated in triplicate, n = 3 biological replicate plates. Data was normalised to cell count per well obtained with Celigo Imaging Cell Cytometer (Nexcelom Biosciences).

3.2.7.3 PILRa M-MOPs exhibit altered cytokine release upon stimulation

To explore the cytokine response seen in PILRa lines, cell supernatant was collected from cultures stimulated with LPS (100ng/ml) or LPS (100ng/ml) and IFN-γ(20ng/ml) overnight. The levels of secreted cytokines were evaluated with the LEGENDplex Mouse macrophage/microglia panel (Biolegend) assay which allows simultaneously to measure 13 cytokines relevant to macrophage and microglia functions. Only results for cytokines where a response was detected are shown (complete list can be found in Methods). In Figure 3.25 the concentrations of different cytokines are shown. Overall, what is clear from the presented data is that LPS or LPS combined with IFN-γ induces a significant increase of various cytokines (analyzed by two-way ANOVA and individual values above each graph). With most cytokine responses, LPS combined with IFN-γ shows a more acute, stronger response than what LPS stimulation alone can induce. In addition, no significant interactions are reported in the non-stimulated group at baseline.

When looking at individual cytokine responses in more detail, PILRa expressing cells, irrespective of the variant, show minimal concentrations of IL-10 compared to control cells (Figure 3.25C). A marked increase is observed in vector only control cells, however that response is minimal in PILRa cells. This response is significant both in LPS treated cells and with the more acute stimulation including IFN-γ. This points to a mechanism through which PILRa might be downregulating critical cytokines and controlling other macrophage relevant responses. IL-10 acts in a feedback loop with IL-6 and TNF-α and increase in IL-10 actively downregulates expression through the Jak-STAT pathway (260). Increase in TNF- α levels can be observed in PILRa expressing cells stimulated with LPS compared to control. Similar response is seen with IL-6 expression. This can potentially be explained by the low levels of IL-10 observed. This trend does not seem to be replicated in cells stimulated with LPS and IFN-γ, which might be related to the IFN-γ response but also by the bigger variation in the response between replicates. The responses towards IL-10, IL-6 and TNF- α seem to be universal irrespective of the PILRa variant and no significant differences were reported between G78 and R78 expressing cells.

In addition, interestingly one of the cytokines where a difference between PILRa variants is observed in the cells is IL12-p40. Cells expressing PILRa G78, the risk variant of the receptor, show significant increase in the cytokine levels compared to control after LPS stimulation. In

addition, the group stimulated with LPS and IFN- γ demonstrates the same result including significant increase compared to the R78 variant. This might indicate that under acute inflammatory conditions, cells expressing G78 PILRa respond in a different way and lead to activation of alternative pathways. Interestingly, IL12-p40 is a subunit for IL-23, however no increase in IL-23 was detected. The role of IL-12p40 and its impact on microglia will be further explored in the chapter discussion.

Apart from cytokines the response of 2 different chemokines was also detected. When stimulated, with LPS alone and LPS with IFN- γ, the levels of both CCL22 and CXCL1 were increased significantly compared to non-stimulated cells. The response to CCL22 in LPS stimulated cells demonstrates a significant increase in G78 PILRa cells. In the presence of IFN- γ, the same response is seen. In addition, it is observed that R78 PILRa expressing cells fail to increase production of CCL22 in the presence of IFN-γ and show significantly lower levels compared to control and to G78 PILRa macrophages. Interestingly, the opposite effect is observed with CXCL1, where upregulation is observed in R78 PILRa cells treated both with LPS and LPS with IFN-γ. In the IFN-γ treated group, G78 PILRa macrophages show significantly reduced levels of this chemokine. Both CCL22 and CXCL1 are classified as pro-inflammatory chemokines and it is expected to see them increased in the presence of stimuli such as LPS. The variance in the reaction based on the PILRa variants however is interesting and might point at a difference in the functional response of macrophages based on the PILRa variant expressed. Depending on the PILRa variant present in cells, different cytokines are expressed therefore the pathways initiated by those might vary and result in a different cell response during inflammatory conditions.

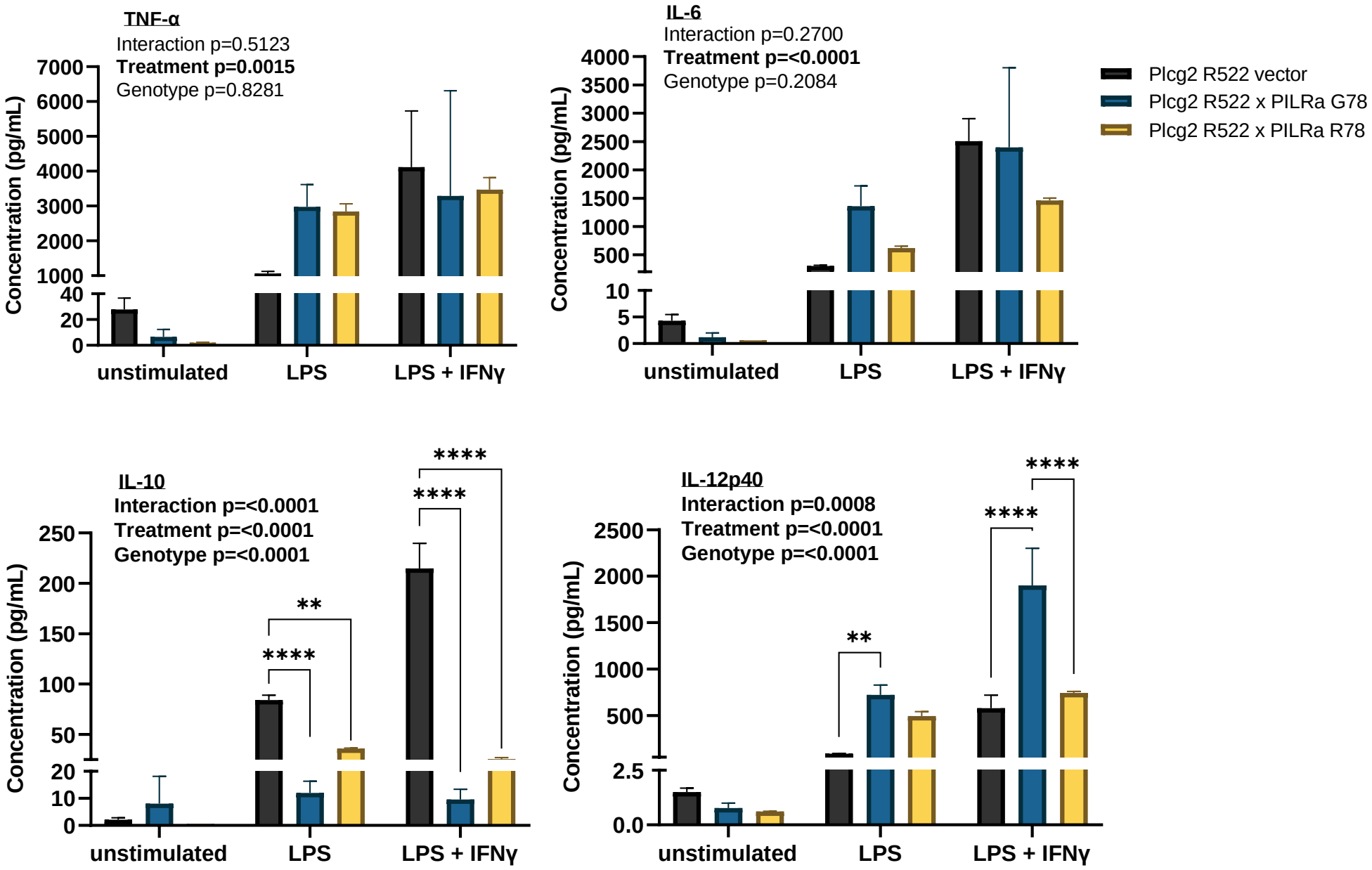
TNF-α
Interaction p=0.5123
Treatment p=0.0015
Genotype p=0.8281
Concentration (pg/mL)
7000
6000
5000
4000
3000
2000
1000
40
20
0
unstimulated
LPS
LPS + IFNγ
IL-6
Interaction p=0.2700
Treatment p=<0.0001
Genotype p=0.2084
4000
3500
3000
2500
2000
1500
1000
500
10
5
0
Plcg2 R522 vector
Plcg2 R522 x PILRa G78
Plcg2 R522 x PILRa R78
IL-10
Interaction p=<0.0001
Treatment p=<0.0001
Genotype p=<0.0001
250
200
150
100
50
20
10
0
**
****
****
****
IL-12p40
Interaction p=0.0008
Treatment p=<0.0001
Genotype p=<0.0001
2500
2000
1500
1000
500
2.5
0.0
**
****
****

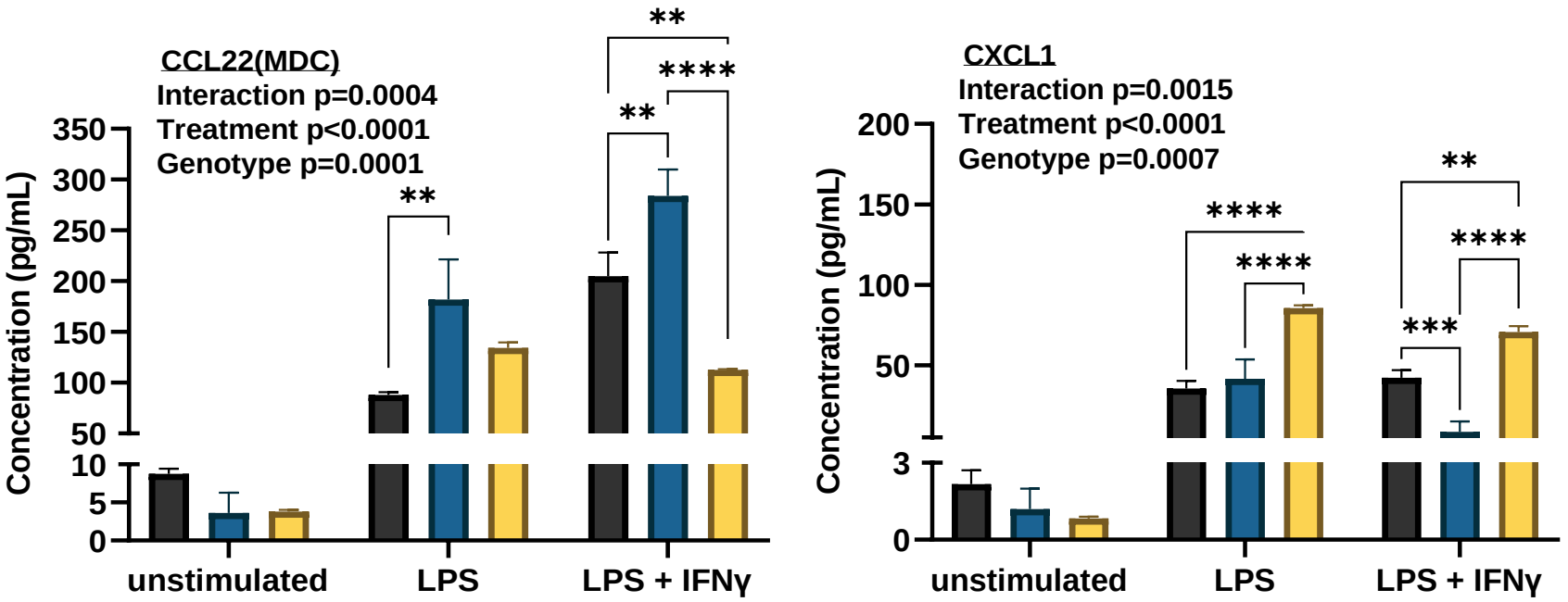

Figure 3.25: Cytokine expression in PILRa expressing M-MOP cells. Differentiated M-MOP cells were treated with LPS (100ng/mL) or LPS (100ng/mL) and IFN-γ (20ng/mL) overnight. Lysates were stored at -80°C and analyzed using the Legendplex flow-based assay (Biolegend). Bars represent mean ± SD (n=2 replicate wells, n=3 biological replicate plates, pooled). Data was analyzed with two-way ANOVA presented above each graph (significant values showed in bold) and followed by Tukey's multiple comparison test. Only significant interactions are plotted on each graph.

3.3. Discussion

The current chapter aimed to develop appropriate *in vitro* models to better understand PILRα's cellular role and its genetic variants through manipulating its expression in cell culture and exploring key macrophage functions. In addition, it aimed to find an appropriate stimulant for PILRα to represent more appropriately how activation of the receptor might impact the cell response in functional assays.

3.3.1. Summary of main findings

In summary, the results showed that whilst lentiviral vectors effectively transduced M-MOP cells, the PILRa expression was not long-lasting. Full length PILRα expression was stably achieved by retrovirus in PLCg2 MOP cells instead. In addition, other lentiviral vectors, *PILRA-ECD-CD3ζ* SIPW and *mCD99* SIPW were successfully integrated in different cell lines, maintaining high expression when kept under antibiotic selection, to explore potential activation of PILRα.

The first set of experiments clearly demonstrates the transient expression of PILRα lentiviral variants in MOP cells. Full length *PILRA* SIPW viruses were not able to achieve stable overexpression of PILRα. Although an increase in gene expression was observed through qPCR analysis, the cell surface expression of PILRα was low. The loss of expression in those cells is potentially caused by silencing of the transgene by epigenetic regulation. DNA methylation and chromatin changes are the two main epigenetic modifications contributing to transgene silencing (261). Stable gene expression is usually driven by a small proportion of vectors which integrate stably into the genome. As previously proposed, there are two types of gene silencing following infection with HIV-1 based vector constructs (262). The first one occurs initially after integration, and it affects most vectors which could explain the initial low amount of PILRα expressing cells (Figure 3.4). However, once fully integrated, the vector activity remained stable for a long period of time. In the case of PILRα transduced MOP cells studied here, due to lack of selection pressure, the vector most likely did not integrate stably into the host genome, therefore was silenced over time.

In addition, another explanation for the loss of expression in MOP cells could be the generation of episomal circles by lentiviruses (263). During the process of lentivirus integration into the host genome, DNA episomes are generated. The linear episome will be integrated into the genome, also known as the provirus. However, two types of circular

episomes are also generated (264). These episomal circles do not integrate within the host genome but do have intact viral coding sequences, therefore can successfully express proteins. Episomes will not persist in dividing cells as they are not integrated and lack an origin of replication (Ori). Studies have determined that these episomes are diluted through cell replication where the estimated half-life correlates with the division rate of the specific cell line used (265). Therefore, the use of selection pressure might be beneficial to reduce transient integration in cell culture models and eliminate expression increased by the presence of episomal circles. Whilst the SIPW vector does express the puromycin selection cassette as part of a bicistronic transcript, driven by an IRES sequence, puromycin selection could not be used in MOP cells, as they are already puromycin resistant. For these reasons, the full length *PILRA* coding regions were moved to an MMLV-based vector that utilized neomycin resistance.

The next set of experiments demonstrates that full length PILRa construct was cloned on the retroviral vector of choice and that stable expression under antibiotic selection can be achieved, tested at mRNA level and at protein cell surface expression. Interestingly, validation of PILRa expression after differentiation of MOP cells to M-MOPs shows that cell surface levels are lower independent of the presence of selection marker. There could be multiple reasons explaining this effect, most likely a result of silencing during the differentiation process. The transition which cells undergo is dependent on induction of multiple transcription factors which in turn may regulate other pathways. Cellular differentiation leads to a cell gaining a specialized function and the process is associated with changes in size, shape and energy demand of the cells. In addition, during differentiation, specific subset of genetic information is expressed selectively. Potentially very high PILRa expression might not be favorable for cell survival/ function, therefore it does get decreased intrinsically. The variation of PILRa expression observed between differentiations could potentially explain some of the differences seen in functional assays later in the chapter and should be taken into consideration.

Another finding from this study is that stimulation of PILRα was not achieved directly by the introduction of mCD99 expressing cells. The co-culture system used did not show an increase in luciferase signal (Figure 3.19). Although there might have been some interaction between those cells, it was not enough to produce a response equal to that seen with

ionomycin stimulation. Closer observation of the culture showed that the characteristic clumping of cells present with NFAT activation was not evident. During the undertaken work it was also evident that higher doses of ionomycin than what was recommended by the supplier were required to induce the luciferase activity. This means that even if some interaction occurred between PILRa and mCD99 it might have been insufficient to induce the luciferase response. Some previous studies validating PILRa ligands used GFP reporter lines (254), which might have provided a better approach for the studies in this thesis. Additionally, titering and using different cell to cell concentrations might have been beneficial to explore.

Previous studies which identified PILRa ligands use proteins expressed on or purified from 293T HEK cells (253). This indicates that HEK derived ligands must have the correct glycosylation pattern for PILRa activation. Therefore, using commercially available stimulants like human PANP-Fc chimera protein which is HEK derived provided an alternative when investigating stimulation of PILRα. Interestingly the presented data shows conflicting results. It seems that when PANP-Fc chimera is applied to human cells there is binding occurring, however the same cannot be detected in differentiated M-MOPs. The human data from Jurkat cell lines suggests being in line with what has already been reported in the literature and points that R78 PILRa has decreased binding compared to G78 PILRa. This is further replicated in human iPSC lines which points at the fact that there is something intrinsically present in the mouse lines which limits this interaction between PILRa and PANP. One potential reason would be the expression of a commonly conserved ligand which is expressed by mouse macrophages. This could lead to the receptor binding site being already engaged, therefore preventing binding of PANP. Data from Wang et al. shows that a similar issue was observed in neutrophils (192). Endogenous ligands were present and therefore blocked binding of additional stimulants. Further investigating this might be through the addition of sialidase A, an enzyme which cleaves sialic acid residues, which would disturb the interaction and free the binding site, allowing binding of the desired ligand.

3.3.2 PILRa functional responses in M-MOPs

Macrophage lines developed in this chapter using pFB-Neo retroviral vector were subjected to several assays to assess basic macrophage relevant functions and to investigate the potential effect which PILRa and its variants might have on these responses.

3.3.2.1 Phagocytic response

Firstly, the data demonstrates that PILRa expressing cells can successfully phagocytose and although not significant, demonstrate a trend towards reduced phagocytosis compared to control. Using different varieties of phagocytic particles, such as *E.Coli* might be interesting to see if similar results are observed or if there are differences between the endocytic mechanisms.

3.3.2.2 Metabolic response

The data demonstrates how M-MOP cells respond metabolically to different stimulants. Interestingly, G78 PILRa cells show significantly lower XF ATP rate index compared to control and R78 cells. This indicates that G78 PILRa cells present with higher levels of glycolysis at the time of the assay which might be linked to some of the cytokine responses discussed later. Macrophages tend to switch their energy production towards glycolysis upon stimulation in inflammatory conditions, leading to higher glucose concentrations and increase in inflammatory activity (266). The data from PILRa expressing M-MOPs suggests that under no stimulation G78 PILRa cells produce more glucose and might be already more prone to inducing inflammatory responses than R78 macrophages. No differences between the variants are reported under stimulation, therefore suggesting that in healthy conditions G78 expressing cells might influence the microenvironment differently and potentially induce inflammation, therefore leading to a harmful phenotype.

Additionally, irrespective of the cell line, cells do not respond to IFN-γ treatment as expected which should be leading to further increase in glycolysis. This data was collected in parallel with the cytokine data where we see an IFN-γ mediated cytokine release, therefore the reagent did stimulate cells successfully and rules out any technical mistakes. This also points towards the unreliable use of M-MOPs and suggests that the observed responses should be reviewed with caution.

3.3.2.3 Cytokine response

M-MOPs cells were subjected to stimulation with LPS or LPS with IFN-γ and interestingly showed some alterations in cytokine production. Overall, macrophages seem to respond as expected under inflammatory conditions, leading to an increase in TNF-alpha and IL-6. This is further correlated to IL-10 production. In relation to PILRa expression and variants, the first main finding demonstrates that PILRa expressing cells show no increase in IL-10 upon stimulation. This result is irrespective of the variant and might be linked to the PILRa overexpression instead. In the literature, activation of ITIM receptors usually leads to an increase in IL-10 production. Several studies demonstrate that in relation to various Siglec receptors (267). Most of these studies, however, use a direct stimulant of the receptor rather than an inflammatory mediator such as LPS which does not target PILRa directly. Therefore, here we observe the response of PILRa in inflammatory conditions. In addition, PILRa knock out macrophages demonstrate increased production of cytokines such as IL-6, IL-1b and MCP-1 (195). Interestingly, knock-out models of Siglecs demonstrate abolished response with LPS stimulation which is like what was demonstrated here. Siglec E knock-out mice show significant reduction in IL-10 production upon LPS stimulation (268). Further research in cell lines and human derived PBMCs demonstrates that overexpression of Siglec-7 for example inhibits the NF-kB pathway and reduces the production of pro-inflammatory cytokines such as IL-6 (269). Overall, different work on Siglecs demonstrates that these receptors have a very versatile function and play an important role in mediating the inflammatory response. We can assume that maybe at an earlier timepoint IL-10 concentration in PILRa expressing cells was higher but then that was downregulated and at the timepoint of the assay we observe a decrease. Interestingly, studies on CD33, an ITIM receptor resembling PILRa, show that upon LPS the receptor is downregulated which might affect the cytokine response observed (270). Although not investigated here, potentially a similar mechanism exists for PILRa.

The data suggests that there is a difference in IL-12p40 secretion based on PILRa variant expression. G78 PILRa expressing macrophages secrete significantly more IL-12p40 compared to controls when stimulated with LPS, and significantly more compared to R78 PILRa cells when stimulated with LPS and IFN-γ. IL-12p40 is a subunit of 2 other cytokines, IL-12 and IL-23, which no differences in were reported from the assay. It has been

recognized that IL-12p40 can have an independent activity as chemoattractant for macrophages and also to provide negative feedback loop by binding to the IL-12 receptor (271). Studies demonstrate that IL-12p40 has an important role in macrophages and microglia and can induce other inflammatory mediators such as TNF-alpha. The role of the G78 PILRa variant in relation to IL-12p40 will be further discussed in the next chapter and in the main discussion.

Interestingly, differences based on the PILRa variant are shown with two different chemokines, CCL22 and CXCL1. CCL22 also known as MDC, is a chemokine secreted by macrophages which has various roles, mainly linked to T-cell function. The results here demonstrate that G78 PILRa expressing M-MOPs produce significantly higher levels of CCL22 upon stimulation compared to control and R78 M-MOPs. Some evidence suggests that CCL22 might play an important role in regulating Th-1 and Th-2 responses in the CNS. Study by Columba-Cabezas demonstrates that in mouse experimental autoimmune encephalomyelitis (EAE) microglia expresses MDC and actively secrete it, regulating inflammation (272). If microglia contain a variant such as G78 PILRa, which is hyperactive and produces higher levels of certain cytokines, this can impact the overall response towards pathology. Further studies reported that MDC increases the phagocytic activities of peritoneal macrophages (273). Since here no difference in the phagocytic response was detected between PILRa variants, it is not excluded that under inflammatory conditions these cells will respond differently. Therefore, treating cells with LPS prior might provide some answers on how these cytokines might influence cell functions.

CXCL1 in comparison is significantly elevated in R78 PILRa cells. This is particularly interesting since this variant is considered hypoactive, due to the decreased binding demonstrated previously by other papers, but also functionally seen here in PILRa expressing Jurkat Lucia cells. CXCL1 which is a pro-inflammatory factor has been shown to induce the NF-kB pathway in macrophages (274). In addition, some transcriptomic data suggests that CXCL1 might have an important role in mediating microglia inflammatory responses following LPS stimulation (275). Different variants of PILRa might impact the cytokine release which in turn will lead to activation of various pathways and these subtle changes might dictate the overall functional response which in turn will impact the tissue microenvironment.

Overall, the results here possess a limitation since we demonstrate cytokine levels from a single timepoint and combine multiple plates from different biological replicates. A future approach to investigate in more detail the inflammatory response in these cells will involve running a time course including earlier point which might reveal the full response. Additionally, stimulating the cells with PILRa specific ligand might provide a better insight into the role of the specific variants. The data suggests some intriguing differences between cells expressing PILRa variants, but further validation is required to explore this in more detail. Seeming from multiple publications, investigating the impact of cytokines on other cellular functions might reveal additional differences between the variants investigated here. Finally, it is important to consider that most published PILRa work is based on knock out mouse models. Taking into consideration the homology difference between human and mouse PILRa it might be hard to compare those responses and derive a conclusion about the role of PILRa in human macrophages.

3.3.3 M-MOPs as a model of neurodegeneration

The primary cell culture model used in this chapter are macrophages (M-MOPs) differentiated from macrophage precursor (MOP) lines generated and established previously in the lab. The reason for selecting this cell model lies in its time efficiency compared to other culture models and also the parallel that could be drawn between macrophages and microglia, part of the same lineage and sharing many overlapping cellular functions. Therefore, it was deemed suitable to use macrophages for some of the preliminary work and optimization when investigating PILRa cellular function.

On the other hand, the lines proved difficult to work with, including multiple failed attempts to differentiate properly and the occurrence of additional population through culturing. Increasing passages showed that cells decrease in size and become less viable.

Throughout the project we planned to use four different lines, combining various Plcg2 and PILRa genetic variants. All lines were created and validated in parallel using the same batch of virus to eliminate any variation. Even though initially the lines were successfully infected and undergone antibiotic selection, during further use the cells expressing P522 Plcg2 and R78 PILRa failed multiple differentiation attempts. When successful the number and health of cells looked poor. Due to the issues working with this line and time constraints to repeat the viral transfection, it was excluded for future experiments.

In addition, all the utilized models in this chapter were created using a viral transduction method, therefore creating an overexpression model. Although useful, overexpression of PILRa may not resemble the natural levels seen in patients. The overexpression of PILRa might be masking some more minor effects caused by the variant therefore a better model to research this is required. In addition, the MOP cells are derived from mice whereas the PILRa variants introduced are human. This raises questions about the importance of the genetic background and potential interactions between mouse and human.

Interestingly, the results demonstrate that PANP-Fc chimera can successfully bind to both Jurkat and iPS-derived microglia cells. However, this is not reproduced in the M-MOP cell lines. Both Jurkat and iPS cultures are human-derived whereas M-MOPs have murine background. There could potentially be a common ligand expressed by mouse macrophages which is able to interact with the human PILRa receptor, therefore blocking the interaction with PANP. More research is required to understand better how much of PILRa's functions are conserved between human and mouse and what domains are responsible for receptor-ligand interactions.

3.3.2. Summary

The current study aims to develop an *in vitro* model for studying the function of PILRα. Although the use of MOP cells is subject to some criticism, this system provides an accessible way to obtain some preliminary data on the role of PILRα variants in cellular context. The use of MOP cells provides a more rapid technical model for validating the reagents to be used. Although the initial stimulation of PILRα with mCD99 using co-culture system did not produce the desired outcome, the stable line expressing PILRα-ECD-CD3ζ was used to explore further options. The use of recombinant human PANP-Fc chimera protein was utilized and showed some promising results in human cells. Its use in functional work will be further explored in the next chapter.

In conclusion, these investigations suggest that the selected lentivirus was not suitable for stable expression of PILRα *in vitro*, therefore a retroviral approach including selection pressure would be more appropriate. The current study provides some additional information on the interaction between PILRα and PANP. The cell culture models developed here were used to investigate core macrophage functions and provided an insight into the role of PILRa in macrophages and some intriguing differences between its variants.

Therefore, the next chapter will move onto providing more insight on PILRα's function in AD on more disease relevant model.

Chapter 4 The role of human PILRα G78R variant in iPSC derived microglia-like cells

4.1 Introduction

Increasing evidence suggests the G78R variant of PILRa has a role in Alzheimer's disease (AD) however, to date no information about its impact on microglia function has been reported in the literature (197, 201, 206). To better investigate the role of the PILRa gene in AD, a relevant model had to be employed. PILRa is predominantly expressed on microglia cells within the brain, although some expression is detected in neurons. Therefore, to study how it can regulate microglia relevant functions, an appropriate model in the context of human AD was required.

Studying genes which are not well conserved between human and mouse, or which might have evolved to have different functions represents a challenge. Although mice are evolutionary closer to humans that other genetic model systems, some crucial differences in protein function, signalling and cell-cell interactions exist between the two (276). As an example, the PILRa gene shares only around 40% homology between human and mouse, therefore the study of mouse PILRa variants may be less relevant in the context of human disease development. In addition, working on genes expressed on microglia for example, which are hard to acquire due to their location within the CNS, represents a particular challenge. Even with advances in genetics allowing for humanised mouse models and cell culture technologies making culturing primary cells possible, there are still multiple drawbacks to each model. In the last couple of years, studies have raised a lot of questions about how the microglia transcriptome changes once they are removed from a physiological environment. In addition, when working with primary microglia, age and sex differences have to be experimentally considered, making culturing those cells more challenging for researchers (277). Some commercially available and established immortalised microglia cell lines exist, such as the BV2 line. These however also face criticism over critical differences in gene expression profiles compared to primary microglia, especially in inflammatory context (278), making them an undesirable model for research of neurodegenerative conditions. Combined, this evidence suggests that there is a need for a better and renewable models where complex diseases can be researched, and novel therapies can be applied in terms of human pathology.

Embryonic stem cells (ESC) are cell population derived from the inner cell mass of blastocysts (279). These cells are pluripotent and can remain undifferentiated for prolonged

periods. Pluripotency is a state regulated by complex network of transcription factors, allowing cells to differentiate into any cell type of all three germ layers: endoderm, ectoderm, and mesoderm (280). Some of the more important regulators of pluripotency include Oct4, Sox2 and Nanog which regulate multiple target genes, most of which involved in development and maintain undifferentiated state. This process involves a strongly autoregulated circuit which involves microRNAs and epigenetic modifications as well as a variety of transcription factors (281).

Initially, ESCs were derived from mouse blastocysts and were grown on feeder layers composed of embryonic fibroblasts, which maintained the pluripotency state (282). Since then, human ESCs were derived as well, which greatly advanced the field of stem cell research. The use of human pluripotent stem cells (hPSCs) derived from donor patient offers a lot of advantages to study disease relevant functions. Due to the ability to differentiate those cells into any specific cell type with the use of specific growth factors and cytokines, they allow development of more appropriate models which better mimic the brain environment.

Induced pluripotent stem (iPS) cells are pluripotent stem cells which were generated through reprogramming from adult cells. All newly derived lines undergo validation through the formation of embryoid bodies (EBs) which are stained with the corresponding markers for each germ layer. Alternatively, a teratoma formation test is carried out (283). The Yamanaka experiments showed that with the use of only 4 factors, Oct4, Klf4, Sox2 and c-Myc, reduced from 24 originally, fibroblasts can be reprogrammed into any desired cell specific type (181). These factors play an important role in inducing and maintaining pluripotency state of the reprogrammed lines. Interestingly, addition of Nanog, showed that it does not impact the reprogramming process, however, is required by cells to remain pluripotent (284). Through the use of integrating retroviruses, these elegant experiments showed that cells can be reverted to their pluripotent state. iPS cells, like embryonic stem cells can self-renew and grow continuously. This discovery entirely changed the field of stem cell research. In comparison to older methods for generating iPS cells where the percentage of off-target effects caused by insertional mutagenesis would be higher which in turn reduced the application of such cells in gene therapy for example, this method is widely available and easily applicable (285). iPS cells can be generated from virtually any starting

material, although skin cells and peripheral blood mononuclear cells (PBMCs) are the preferred source, due to their easy accessibility and sample collection simplicity (286). The source of iPS cells can have an effect on the reprogramming and differentiation efficiencies, due to differences in the endogenous expression of transcription factors(287). In addition, compared to the use of ESCs, there are less complex ethical issues accompanying the use of iPS cells in research.

Recent studies demonstrate that iPS cells can be a useful tool in terms of neurodegenerative disease research. Some promising results demonstrate that iPS cells represent a valid model for identification of drug targets (reviewed in (288)). In addition, AD-derived iPS neurons have been used to investigate *in vitro* further some of the hypothesized mechanisms behind amyloid pathology (289). Since the development of iPS derived microglia, multiple protocols have been created to optimise the process and validate those microglia-like cells. One of the most widely used was developed by Haenseler *et al*. (290). The main challenge to derive iPS microglia stems from their unique developmental origins (70). Murine studies on microglial origin and differentiation have been particularly useful to depict the necessary factors to mimic an environment close to that in the developing embryo (78). In addition, it remains unknown how closely iPS derived microglia-like cells resemble human microglia on transcriptional level. Most studies involving human samples are small scale and samples are collected at the end point of disease rather than early on, therefore drawing direct comparison with iPS cells might not be relevant (291).

Although overall a very attractive model for research, iPS cells have a few disadvantages. Generation and culturing of new lines is a long, expensive, and sometimes a very low efficiency process. In addition, during the reprogramming stage data shows that multiple oncogenes are induced. Cells which have undergone reprogramming also demonstrate high genetic instability rate (292) and random mutations occurring within the line during the culturing process (293). All of this need to be carefully considered when studying diseases where genetic factors are a driver of pathology development.

Studying disease risk in the context of the patient's genetic background has been one of the biggest advantages of iPSC as models, but it also constitutes one of the biggest challenges. Studies show that genetic background can significantly contribute to the heterogeneity of iPSC lines (294), therefore interpretation of results derived from different patient lines can

lead to the wrong conclusions. In the context of AD, which is highly polygenic, ideally multiple lines representing patient's genetics will be used simultaneously. However, this poses some experimental and technical challenges. To study the role of specific gene on a cell type, lines with identical genetic background can be utilised instead. This can be achieved through the generation and analysis of isogenic cell lines. Such lines are generated by introducing mutations via homologous recombination.

The development of the Clusters of Regularly Spaced Short Palindromic Regions (CRISPR)-Cas9 system made gene editing accessible and widely available to researchers allowing for single nucleotide polymorphisms (SNP)s to be generated in selected cell lines (295). In combination with the development of iPS cells, generation of custom isogenic lines became widespread in the field of neurodegenerative conditions. Combining the specific cell type with the necessary genetic factors made models for the study of those conditions more accessible. The CRISPR-Cas9 system is widely available in nature in bacteria and is used as a defence mechanism to foreign DNA, however, has been utilised in research to allow to target practically every genomic sequence (296). CRISPR-Cas9 is a type II CRISPR system where the Cas9 protein alone can successfully bind to the crRNA, a short sequence complementary to the target DNA and produce a cut in the target DNA site. Cas9 cleavage induces a double stranded break (DSB) in the DNA (297). The target recognition is based on two elements, the protospacer adjacent motif (PAM) and the crRNA. Studies show that PAM is crucial for initial binding to the DNA (298). The DSB break is either repaired through the non-homologous end joining (NHEJ) repair pathway or homology-directed repair (HDR). Mammalian cells preferentially employ the NHEJ repair pathway, as opposed to HDR (299). This is due to the first one being faster and active throughout the whole cell cycle, in comparison HDR is restricted to S/G2 interphase (300). In addition, NHEJ repair suppresses HDR. All of those in combination with the really low efficiency of HDR repair makes the process of gene-editing more challenging. In the past couple of years, a lot of efforts have gone into improving the precision and efficiency of CRISPR-Cas9 gene editing in cells. Although creating specific single nucleotide polymorphism (SNP) mutations has been improved, there are still many challenges that remain and usually the efficiency remains fairly low, especially for genes with very low transcriptional activity.

With advances in iPSC technologies and increasing evidence of the importance of genetic factors for development of AD, we aimed to investigate how PILRa, identified AD risk gene, can contribute to this process. Using iPS cells provides a suitable model to investigate this in microglia-like cells. In this chapter, isogenic lines were derived using the established Kolf2 iPS cell line.

Chapter aims:

1. Evaluate the expression of PILRa in Kolf2 microglia-like cells.
2. Using CRISPR-Cas9 method engineer Kolf2 iPS cells expressing G78 PILRa.
3. Characterise and validate PILRa Kolf2 microglia-like cells.
4. Validate potential PILRa ligands using generated microglia-like cells.
5. Explore functional differences between G78 and R78 PILRa expressing iPS microglia-like cells

4.2 Results

4.2.1 PILRa expression in Kolf2 iPSC microglia

To identify if differentiated microglia-like cells derived from iPS Kolf2 cells express PILRa, and if that expression is at a detectable level, a qPCR analysis and flow cytometry analysis were performed. This allowed to check expression of PILRa at both the mRNA and protein level. As seen from Figure 4.1, PILRa levels are high enough to be detected by qPCR. In addition, after staining microglia-like cells with AF488 conjugated anti-PILRa antibody (R&D Systems) surface expression of PILRa was analysed by flow cytometry and the histogram shows a shift compared to isotype control. This indicates that PILRa is detectable at the cell surface of Kolf2 derived microglia-like cells.

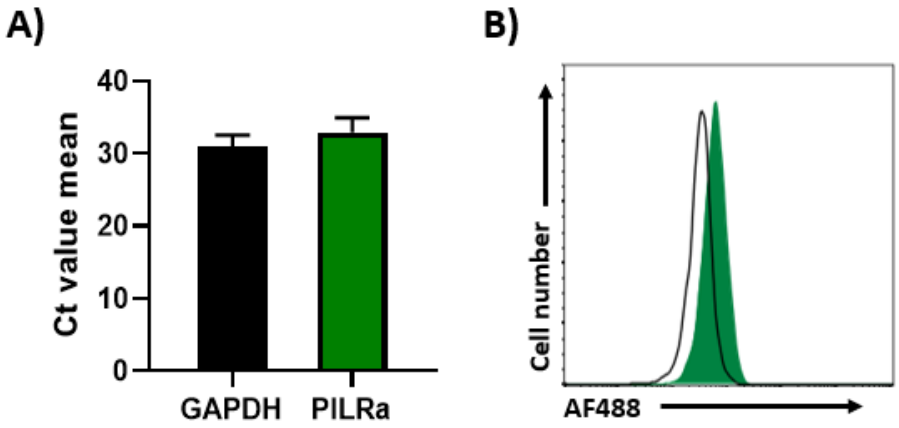

Figure 4.1: PILRa expression in microglia-like Kolf2 derived cells. (A) Analysis of PILRa mRNA expression in Kolf2 microglia. Bars represents mean ± SEM (n=2 independent repeats, 3 x replicate wells). GAPDH was used as a reference gene. **(B)** Histogram showing PILRa cell surface expression on Kolf2-derived microglia assessed through flow cytometry. Cells were stained with anti-human AF488 conjugated PILRa antibody (R&D systems, green histogram) or isotype control (black line).

4.2.2 CRISPR-Cas9 mediated PILRa R78G SNP

As identified in the previous section, the expression of PILRa in the microglia-like cells differentiated from Kolf2 was detectable at both mRNA and protein level. This indicated that overexpression through a lentivirus for example, of both G78 and R78 of PILRa would not be a suitable option and the endogenous levels of PILRa cannot be neglected. Next, which variant of PILRa is expressed in the Kolf2 cell line was identified. Through using the Sanger CRISPR tool, it was identified that Kolf2 cells contain PILRa which expresses arginine (R) at

position 78 encoded by AGG. Therefore, using CRISPR engineering it was aimed to introduce the guanine (G) encoded by GGA through using homology-directed repair (HDR). Using an HDR oligo, it was planned to induce a single nucleotide polymorphism within the edited cells. In addition, to allow for easier screening and to be able to identify positive clones where recombination has occurred, the HDR template was designed to contain silent mutations upstream of the target site (Figure 4.2A).

A single guide RNA (gRNA) was designed in close proximity to the target site based on predicted high efficiency and number of potential off-target effects. The gRNA was synthesised and coupled with 5' universal ATTO 550 labelled Alt-R Cas9 tracrRNA. This was further combined with Alt-R® S.p. HiFi Cas9 Nuclease V3 to form the ribonucleotide protein (RNP) complex. Finally, the single stranded donor template (ssODN) or the HDR oligo, was added. Kolf2 iPS cells were electroporated with the fluorescent RNP complex. The presence of the ATTO 550 fluorescent dye allows for cells to be FACS sorted based on their enrichment, therefore reducing the screening pool of colonies which need to be selected. Cells were incubated overnight after which they were detached and sorted using the BD FACS Aria Fusion flow cytometer. Non-transfected cells were used as a control. 10,000 cells from the top 10% with highest emission were selected (Figure 4.2C). Sorted cells were plated onto a 10cm dish, aiming at single cell suspension, and cultured for 4-6 days allowing for growth of individual colonies which were then picked and placed into a 96-well plate.

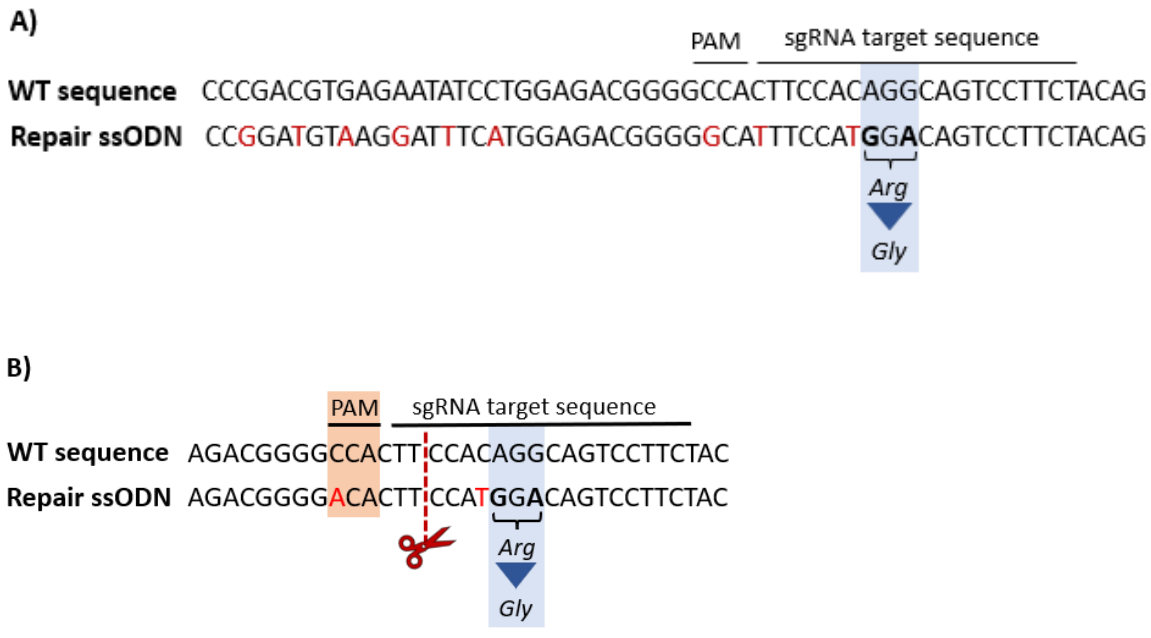

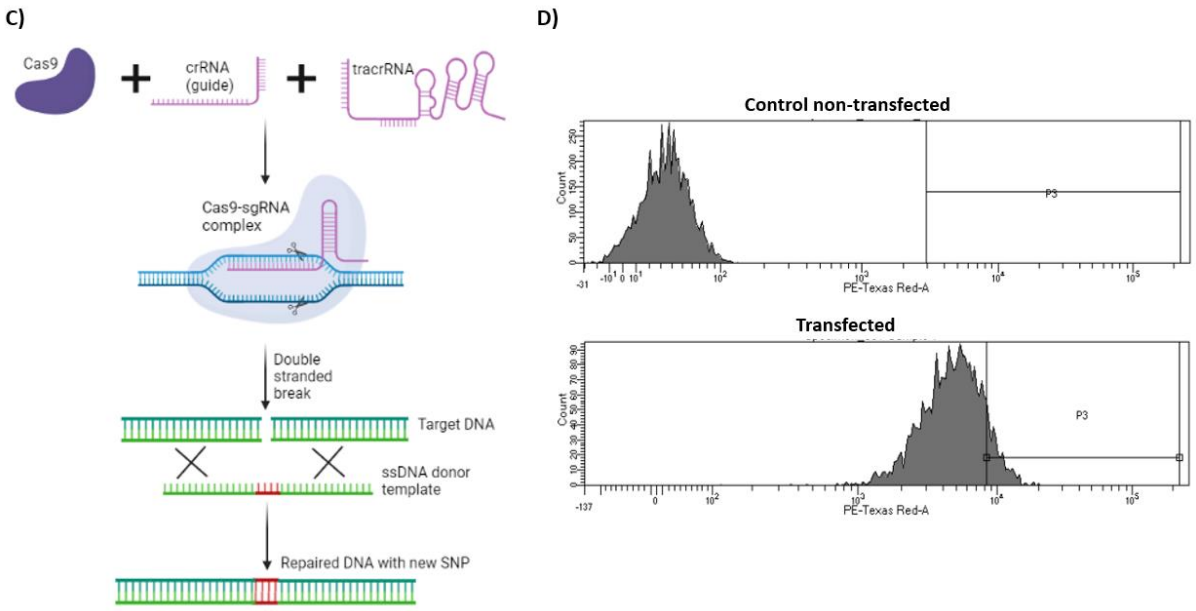

Figure 4.2: Generation of G78 PILRa iPS lines. (A) Schematic of the CRISPR design and guide sequence. The base pairs highlighted in red represent silent mutations inserted for screening purposes. The selected guide is designed to bind the lagging strand in 3' to 5' direction, followed by a PAM sequence. **(B)** Alternative CRISPR design used to generate additional clones. The designed template only contained single mutation at the PAM site and one additional mutation at the target site (shown in red). **(C)** Diagram of the CRISPR-Cas9 process. Reagents were combined to form the ribonucleotide complex (RNP). The donor DNA template is added right before nucleofection. If successful recombination occurs, the edited cells will contain the new base pair sequence. **(D)** Histograms from FACS around 24 hours post nucleofection. Gate P3 represents the population selected for sorting. 10,000 cells were sorted in total from the top 10% of cells with highest signal.

4.2.3 Screening for positive colonies

Following the CRISPR a successful screening strategy had to be employed to identify positive clones. As PILRa shares high homology with PILRb, another receptor from the same family, the screen had to specifically target PILRa. A two-step screen was designed. In the first part, primers specific for PILRa were used to amplify only the desired sequence containing the site targeted by the CRISPR. A gradient PCR was performed to estimate the best temperature for primer annealing and optimal amplification of PILRα. The temperature for the PCR was selected to be 56^{o}C, resulting in amplified product with size of 960bp (Figure 4.3B and C). All reactions were subjected to a clean-up (Macherey Nagel kit) and were used instead of a DNA template for the consecutive PCR reaction. The second PCR was run using primers designed to target the region of the base pair change. The forward primer contains

the same sequence at the 3' end as the predicted sequence after a successful addition of the HDR oligo. Only clones containing the edited sequence should produce a band with the correct size of 340bp. 96 colonies from the transfection were screened. As seen in Figure 4.3D, 10 potential positive clones were identified (10.4%). To confirm if the sequence is correct and whether the HDR oligo is successfully integrated within the sequence, the initial PCR product containing PILRa only was sent for further Sanger sequencing (Eurofins Genomics). From the identified clones, 2 were expressing two copies of G78 PILRα (2.1%), 3 were heterozygous (3.1%), 2 were negative, expressing the wild type PILRα (2.1%). The other 2 clones had incorrect sequences as a result from a potential frameshift or DNA repair damage and were not brought forward for further analysis.

A)

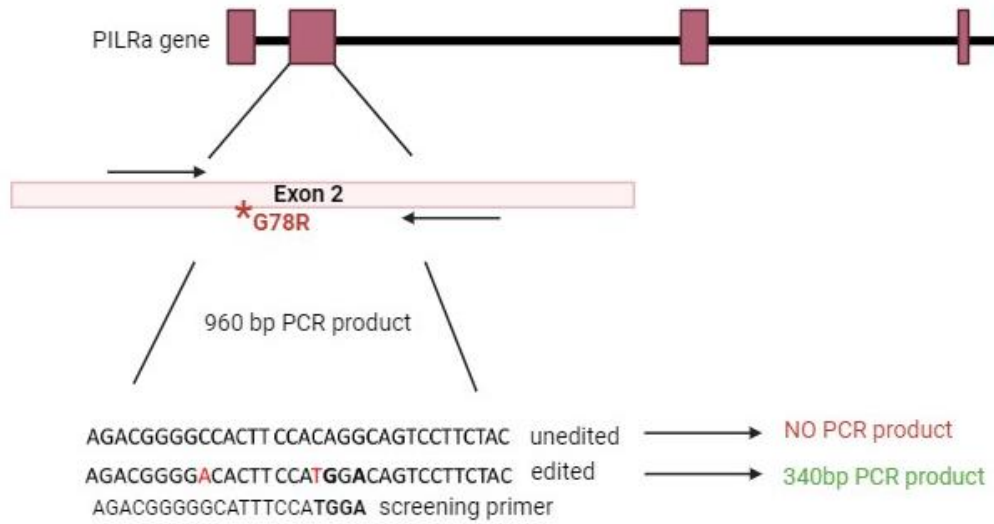

B)

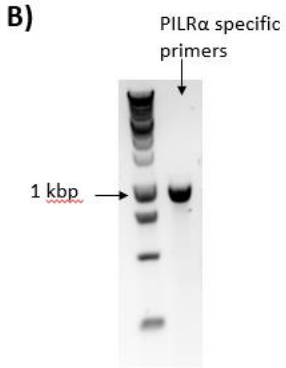

C)

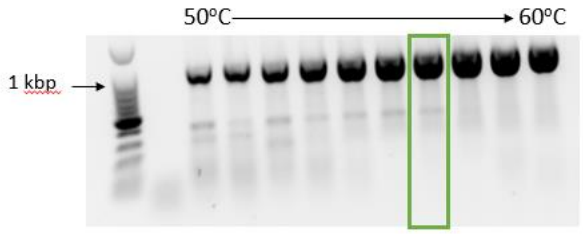

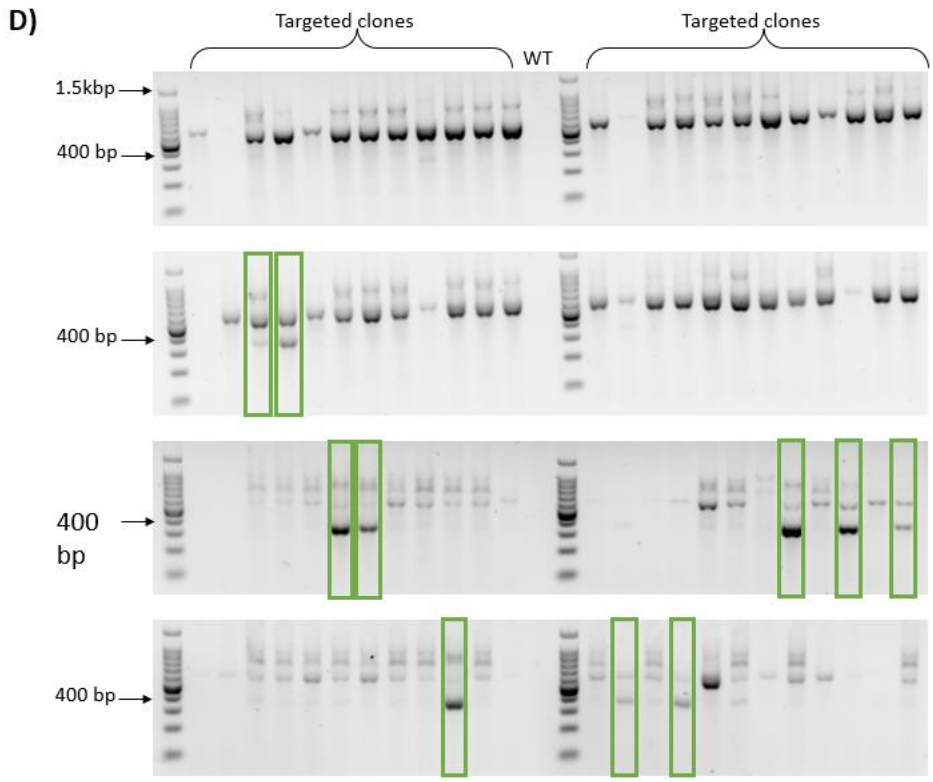

Figure 4.3: CRISPR screen optimisation and results. **(A)** Schematic of screening strategy with detailed PCR product sizes. **(B)** Primers designed to specifically amplify region of PILRa containing the base pairs of interest. Product was run on an agarose gel using 100bp DNA ladder. **(C)** Gradient PCR to choose the best annealing temperature for PILRa specific primers. Primers were run between 50°C and 60°C and the best temperature was selected at 56°C. **(D)** Gel images containing all 96 reactions screened for successful CRISPR clones. All reactions were run on an agarose gel using 100bp DNA ladder. Green boxes represent clones containing the correct band size.

Following Sanger sequencing the traces showing the region of interest were analysed. Representative images from some clones are shown in Figure 4.4. Interestingly, the identified positive clones did not show the initially predicted base pair change. Based on the CRISPR design, the original R78 PILRa, encoded by AGG, would be modified to G78 encoded by GGA. However, the base pairs detected in the positive clones showed AGG to GGG transition. GGG encodes for Glycine, which was the desired amino acid, meaning these clones were still compatible with the aims of the project.

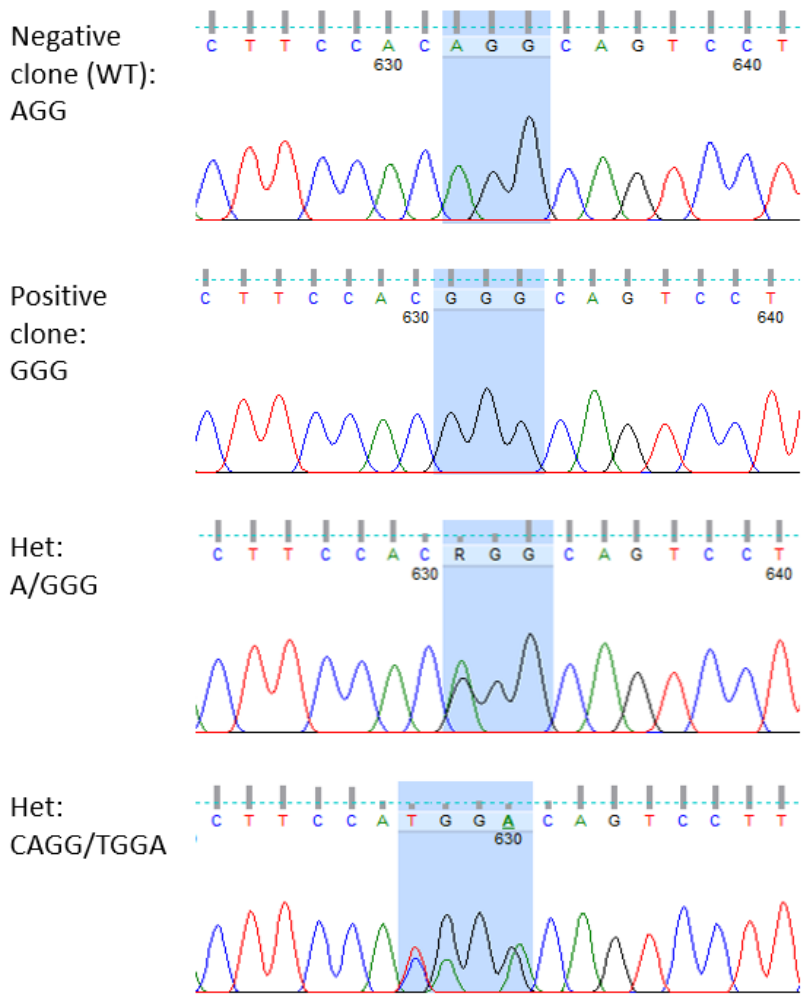

Figure 4.4: Sequencing traces of positive clones. The top trace represents a negative clone, containing the original PILRa sequence encoded by AGG. The second trace represents a positive homozygous clone, where arginine is encoded by GGG. The last trace shows a clone where both A and G are detected. This clone has one copy of G78 PILRa and one copy of R78 PILRa, making it heterozygous. Alternatively, some heterozygous clones contained the predicted sequence leading from AGG to GGA transition. The silent mutation placed before the knock-in target from C to T is also detected.

All identified positive clones, both homozygous and heterozygous were brough forward for further characterisation and validation (Table 4.1).

Table 4.1: Summary of clones generated by CRISPR.

Type of clone	Number
Negative (AGG)	**9**
Homozygous (GGG)	**2**
Heterozygous (A/GGG)	**7**

Table 4.2: Clone nomenclature. Newly derived lines were labelled using their corresponding clonal name and will be referred as such throughout the thesis. In this table each clone is presented with the corresponding genotype.

Clone Abbreviation	Corresponding genotype
C1	R78 homozygous
C2	R78 homozygous
C3	R78 homozygous
F10	R/G78 heterozygous
F12	R/G78 heterozygous
G10	R/G78 heterozygous
F8	G78 homozygous
C4	G78 homozygous

4.2.4 Characterisation of iPSC microglia

Clones which were derived through sequencing had to undergo additional characterisation and validation to ensure that no other changes on genetic or functional level have occurred within those cells during the CRISPR process. Apart from the identified homozygous and heterozygous clones, 3 negative clones which did not show any amplification during the screening PCR, were selected to act as a negative isogenic control lines.

4.2.4.1 Virtual karyotyping of G78 PILRa Kolf2

All selected clones, both positive and negative, were screened for any large insertions, deletions or duplications within the genome which allows the detection of any copy number variants (CNVs) created during the targeting process. Clones were genotyped using Illumina Global Screening Array v3.0 and compared to GRCh37 / hg19 as a reference genome. The assay was performed on Infinium Global Screening Array-24 BeadChip which has a coverage of 654,027 SNPs and creates a "virtual karyotype". The assay produces two intensity signals, one for each allele. These signals are further transformed into log scale ratio between the observed and the expected intensity, called log R ratio (LRR). The relative contribution of one of the alleles to the overall fluorescent signal is also reported through the B Allele frequency (BAF).

After quality control of the samples, 5 CNVs were detected across all samples (Table 4.3). The parental Kolf2 line was analysed to act as a control to the lines which have undergone CRISPR engineering. Deletions were detected at 3p13,6p22.3 and 9q33.1 (Figure 4.5A). In addition, duplication was reported at 3p14.2 and 18q22.1 (Figure 4.5B).

In comparison to other Kolf2 lines where duplication develops often at 20q11.21, none of the analysed clones contained this CNV. CNVs are of high importance and could have profound effect on cellular function. CNVs are considered a major source of variability in the human genome. However, since all detected CNVs were present in the Kolf2 line, it suggests that these were probably present in the donor rather than a consequence of the gene-editing process. In addition, these results are in accordance with what has been reported previously about the Kolf2 cell line.

Table 4.3: CNV analysis performed on clones genotyped with Infinium Global Screening Array. The analysis reveals deletion at 3p13, 6p22.3 and 9q33.1 in addition to duplication at 3p14.2 and 18q22.1 present across all samples. The length and approximate position of each CNV can be seen in the table.

CNV locus	**3p13**	**6p22.3**	**9q33.1**	**3p14.2**	**18q22.1**
Approx. position	chr3:72289657 -72424795	chr6:15499419 -15722102	chr9:119244642 -119374306	chr3:61136894 -61869264	chr18:62115075 -62264706
Status	Deletion	Deletion	Deletion	Duplication	Duplication
Length (bp)	135,138	222,683	129,364	732,370	149,631
Samples detected	All	All	All	All	All

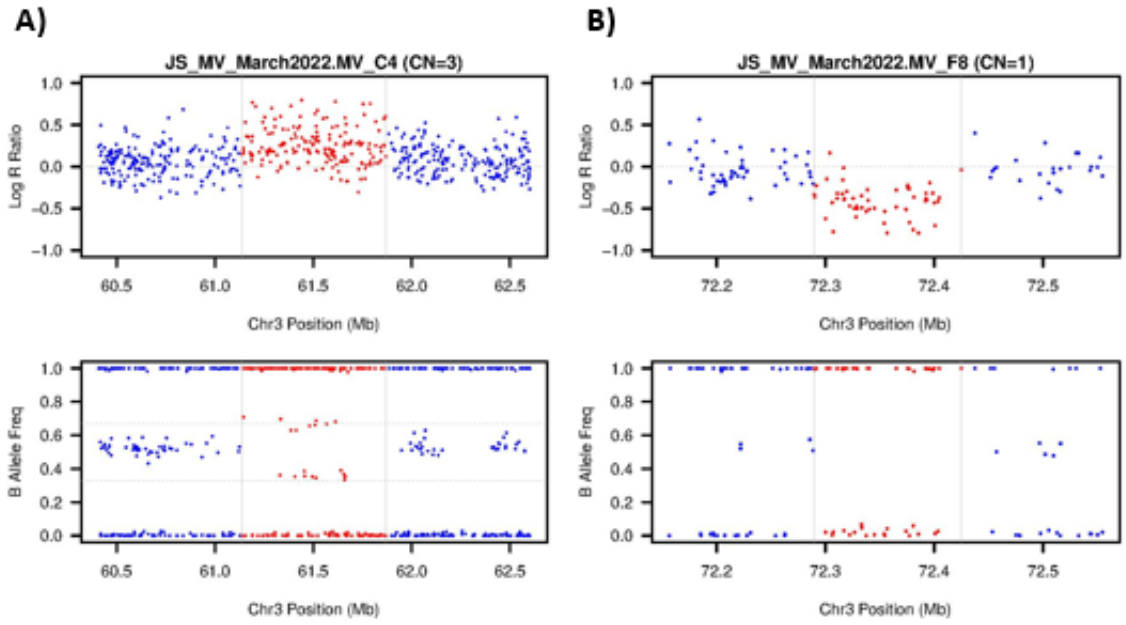

Figure 4.5: Representative SNP array plots of PILRa edited Kolf2 clones. All selected clones were run in parallel with Kolf2 unedited control line. **(A)** Duplication characterised by increase in the Log R ratio above 0 and presence of 2 groups in the B allele frequency plot around 0.4 and 0.6 showing the presence of 2 copies of the region. **(B)** Deletion characterised by decrease in the Log R ration below 0 and absence of SNPs around 0.5 in the B allele frequency.

4.2.4.2 Validation of potential off-target effects

Often during the gene-editing process off-target effects are detected due to the specificity of the chosen guide-RNA or the activity of the Cas9 enzyme. The guides used to create the G78 PILRa Kolf2 lines are no exception and although preferentially binding to the target region, they can also target other regions within the genome. To assess if any off targets occurred during the CRISPR process, a list of the top targets proposed by the guide design software was created. Since PILRa and PILRb show high similarity in their sequence, it was predicted that during the CRISPR, the guide RNA could also target PILRb. This is of particular importance because it has been demonstrated that Cas9 cleavage at genes with similar sequences can lead to gross chromosomal deletions (301). To evaluate if this has occurred in any of the positive clones, primers specific for PILRb were used. The amplified product which had predicted size of 860bp was ran on an agarose gel. As seen in Figure 4.6, all 8 clones exhibit the correct band size, and no other bands are present.

A more detailed and elaborate assessment of all potential off-target effects, predicted and not predicted, can be done via whole exome sequencing (WES).

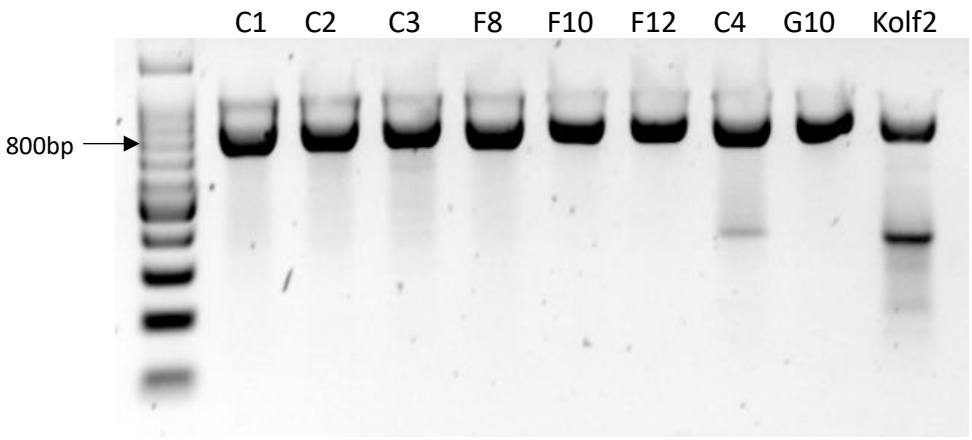

Figure 4.6: Agarose gel showing PILRb amplification in G78 PILRa Kolf2 cells. DNA from the positive clones was amplified using PILRb specific primers. The resulting product was run on an agarose gel using 100bp DNA ladder.

4.2.4.3 Pluripotency characterisation

Next, after validation of the cell lines and confirmation that no additional genetic changes occurred during the gene-editing process, the morphological properties of these cells were evaluated. Pluripotency is an important property of iPS cells and is required to allow experimental differentiation to the desired terminal cell type. To confirm that all selected clones still remained pluripotent, a panel of pluripotency markers was selected and expression in those cells was measured. Cells were subjected to both mRNA expression analysis and immunocytochemistry (ICC) staining.

In figure 4.7A brightfield images of all clones are present. Human iPS cells grow with a population doubling time of 24–48h in flat colonies. These present with distinct cell borders. Stem cells exhibit large nucleoli and a high nucleo-cytoplasmic ratio (279). The CRISPR-targeted cells retain iPS cell specific morphology and grow in flat colonies (Figure 4.7A). The colonies show smooth edges and no visible 3D structures, or spiky ends are present, which might be seen in spontaneously differentiating cells. PILRa targeted clones show uniform levels of mRNA expression of the pluripotency markers. All clones showed expression of Sox2, Oct4 and Nanog (Figure 4.7B). In addition, when stained with monoclonal rabbit antibodies against the same markers (Cell Signalling Technologies), followed by anti-rabbit AF647 secondary antibody, cells were positive

inside the nucleus (Figure 4.7C). This evidence therefore confirms the pluripotency of the CRISPR targeted clones. This is particularly important in terms of downstream differentiation towards specific cell type.

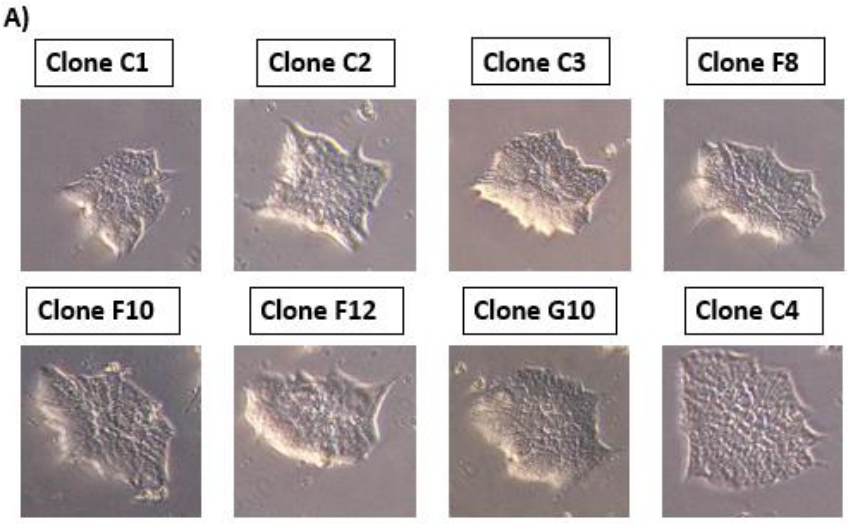

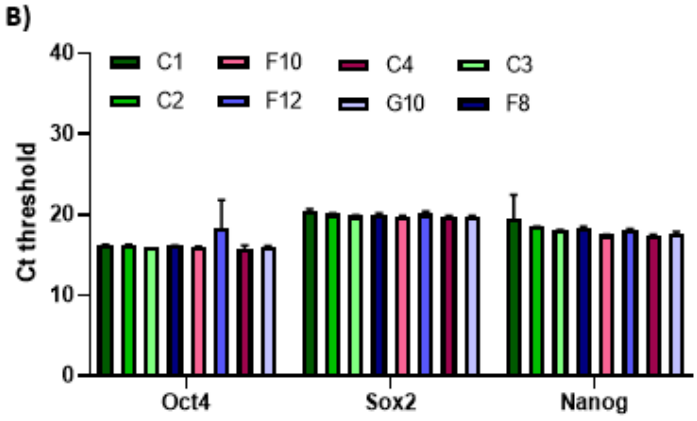

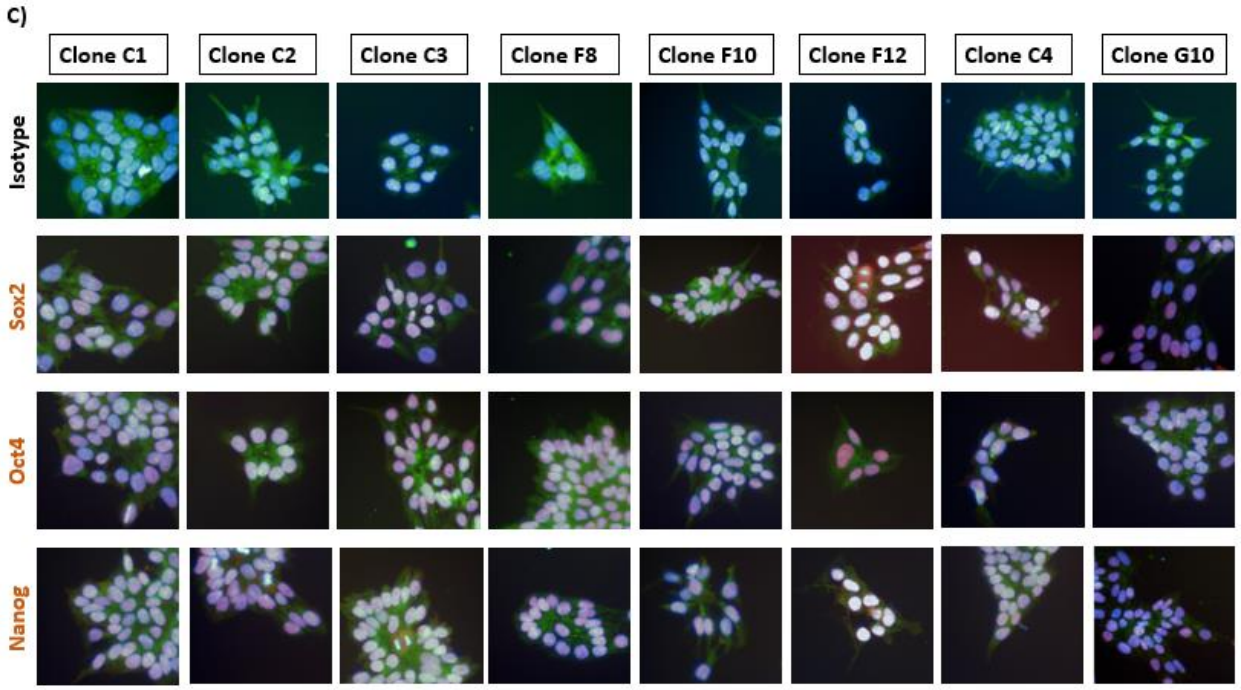

Figure 4.7: Validation of pluripotency in iPSC PILRa clones. (A) Phase contrast images of PILRa targeted iPS cells maintained in chemically defined xenofree medium on Geltrex coated plates. All cells show classic iPS morphology and form colonies successfully. **(B)** mRNA expression of Oct4, Sox2 and Nanog assessed through qPCR. Values presented show the Ct threshold for each sample since no reference sample is available. Each bar represents n=3 technical replicate wells, mean ± SEM. **(C)** ICC staining of iPSC colonies. Antibodies against Oct4, Sox2 and Nanog were used (Cell Signalling Technologies). Rabbit IgG was used as an isotype control (Cell Signalling Technologies). All cells were stained with secondary anti-rabbit AF647 antibody (Jackson ImmunoResearch). DAPI and Cell mask green were used to stain the nucleus and the cell membrane respectively, allowing for colonies to be identified. Cells were stained in 96-well clear bottom plate and imaged with the Opera Phenix (Perkin Elmer).

4.2.4 Microglia-like cell differentiation from G78 and R78 PILRa iPS cells

Clones which were successful for all quality-control steps were taken further through the differentiation process. 3 wildtype, 3 heterozygous and 2 homozygous were cultured in parallel and differentiated simultaneously. The different differentiation stages and some representative pictures can be found in Figure 4.8. All 8 clones were successfully carried through the differentiation process and were able to form microglia-like cells. Factories which usually produced cells 2-4 weeks after setting up were harvested weekly and microglia-like cells were utilised for further experimental purposes.

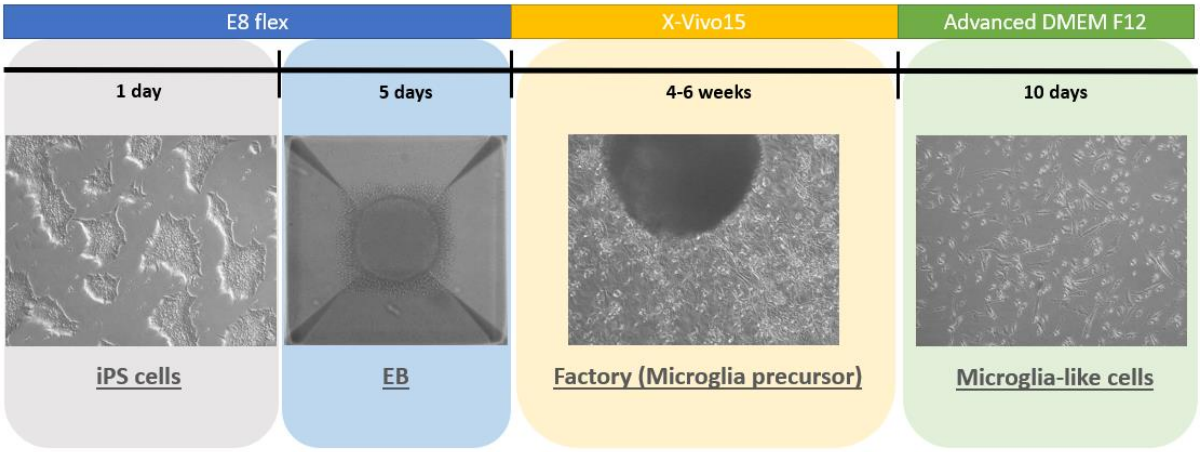

Figure 4.8: Diagram depicting the timeline of differentiation of microglia-like cells. The cells at each stage are indicated below the representative picture. The main media type used for a specific differentiation stage is colour coded. The full media components are available in Table 2.4 in the method chapter.

4.2.5 Characterisation of G78 and R78 PILRa microglia-like cells

All terminally differentiated microglia-like cells from monocyte precursors were further characterised. Cells were subjected to characterisation by validating expression of established cell surface microglia markers Iba1 and Tmem119 (Figure 4.9).

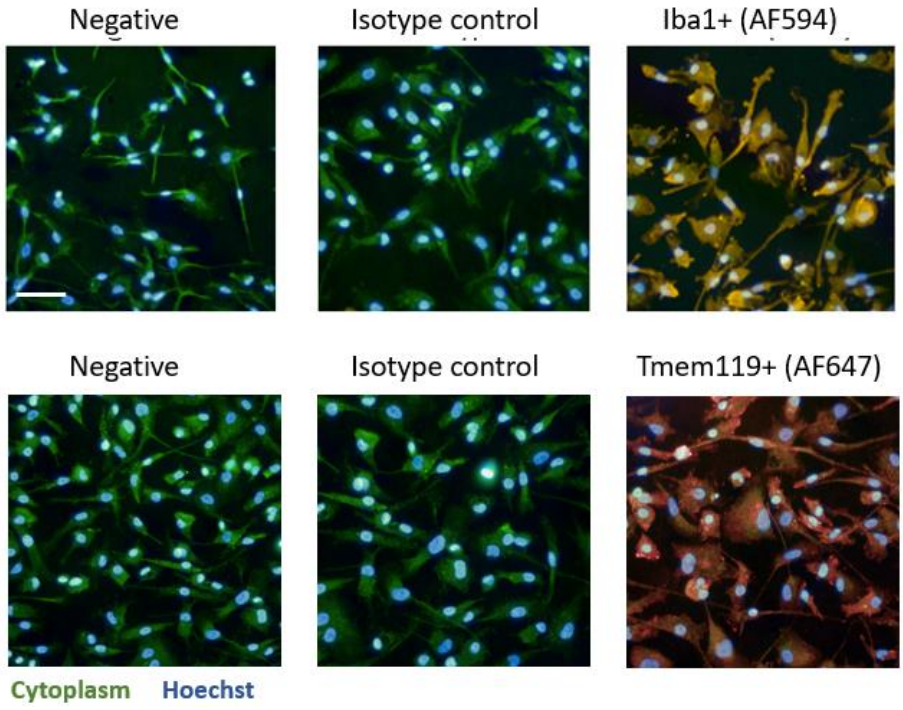

Figure 4.9: Microglia marker expression in iPS derived microglia-like cells. Representative images showing immunocytochemistry staining with Iba1 or Tmem119. Antibodies against Iba1

and Tmem119 were used. Secondary antibodies conjugated to AF594 and AF647 respectively were added, Hoechst was used for nuclear staining and Cell Mask Green was applied to stain the cytoplasm. Images were obtained using 20X water objective on the Opera Phenix (Perkin Elmer). Scale bar = 100µm.

In addition, the PILRa expression in microglia-like cells derived from all clones was tested. The mRNA levels were assessed both in microglia precursors and in terminally differentiated microglia-like cells. Figure 4.10 demonstrates that all clones express detectable *PILRa* mRNA confirming the CRISPR editing process have not impaired the ability of cells to express PILRa. In addition, the level of PILRa across genotypes and clones seem to be consistent with no significant increase or decrease in any of the generated lines. This seem to be reproduced in the microglia-like cells as well. Interestingly, there are no significant changes in PILRa expression resulting from the differentiation process to microglia-like cells. This experiment represents a single timepoint during the factory development therefore may not fully reveal any dynamic changes linked to PILRa expression.

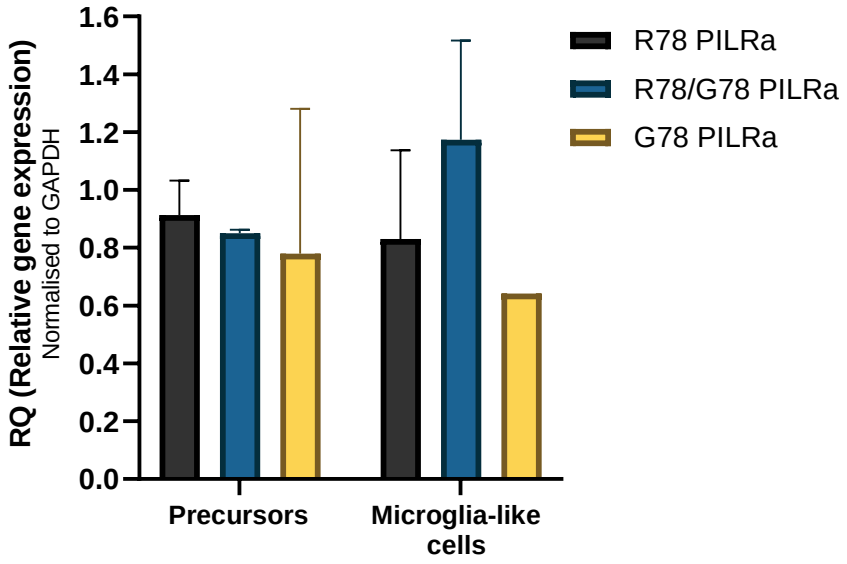

Figure 4.10: PILRa mRNA expression in microglia precursors and microglia-like cells. Bars represent mean ± SD (n=2, 3 x technical replicate wells). Each genotype contains 3 individual clones, apart from G78 PILRa which has 2 clones. GAPDH was used as endogenous control.

4.2.6 PANP as a ligand in microglia-like cells

Differentiated microglia-like cells were incubated with PANP-Fc as previously described on day 10 after harvesting. To assess the binding between different variants of PILRa in clones, cells were analysed using flow cytometry. The histograms on Figure 4.11A represent the detected binding in PANP treated cells. Overall, there are no big differences between any of the clones and they all seem to show around 10-15% of positive cells compared to cells treated with secondary only control antibody. In Figure 4.11B a more comprehensive analysis reveals that overall, there is a marked increase in binding in heterozygous clones compared to wild-type and homozygous clones. Homozygous clones show minimal average increase compared to wild-type cells.

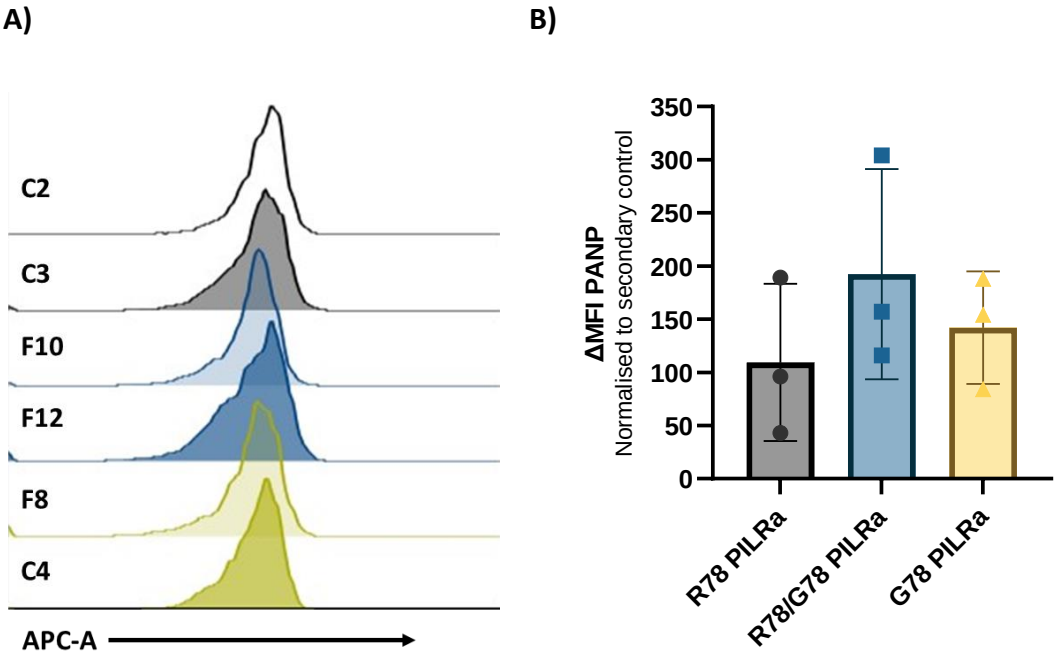

Figure 4.11: PANP binding between different clones in microglia-like cells. (A) Representative histograms of PANP binding on microglia-like cells expressing different PILRa variants. The coloured histograms represent the APC signal, the lines indicate secondary only control staining. **(B)** ΔMFI of PANP normalised to secondary only control. Bars represent mean ± SD and the individual symbols are representative of biological repeats (n=3). Each symbol indicates average of 2 x individual clones.

4.2.7 Functional analysis of PILRa variants in microglia-like cells

All confirmed clones were subjected to differentiation via generation of factories which produce monocyte precursors using an already established protocol (302). In

comparison to older versions, this utilised media containing TGF-β which produces microglial morphology and signature closer to that observed *in vivo*. The precursors were used to terminally differentiate to microglia-like cells. In order to explore what potential functional differences might arise in the PILRa edited clones, cells were applied to a variety of cell function assays. Microglia relevant functions which might contribute to and modulate AD pathology development were investigated.

4.2.7.1 G78 PILRa microglia-like cells exhibit altered phagocytic properties

Since one of the main microglia functions is phagocytosis, this was the first we onset to explore. Microglia-like cells were used on day 10 of the differentiation and pH-Rodo zymosan was used for the assay. Cells were imaged live at equal 25-minute intervals to produce a time course response. From Figure 4.12A which represent the last timepoint, cells clearly exhibit the characteristic microglia morphology. The images in the panel show different conditions applied during the assay which correspond to untreated and also inhibitor (cytochalasin D) treated cells. From the graph in Figure 4.12B which demonstrates the phagocytic response over the time course of each different genotype, it is clear that all lines are able to successfully uptake zymosan particles. In addition, the cytochalasin D treatment works efficiently, with treated cells demonstrating significantly less uptake and remaining entirely negative for pH-Rodo zymosan particles. No significant differences based on genotype are reported (Two-way ANOVA, Figure 4.12B).

A)

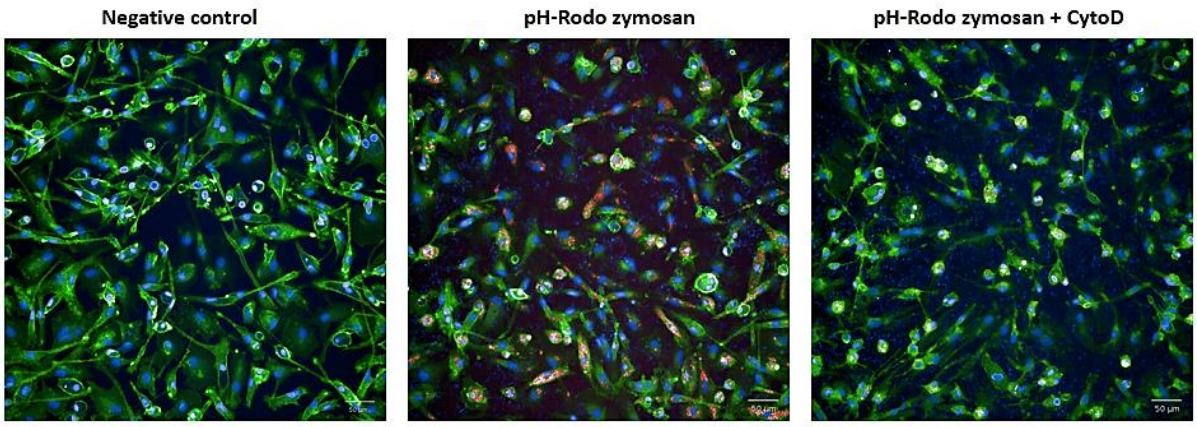

B)

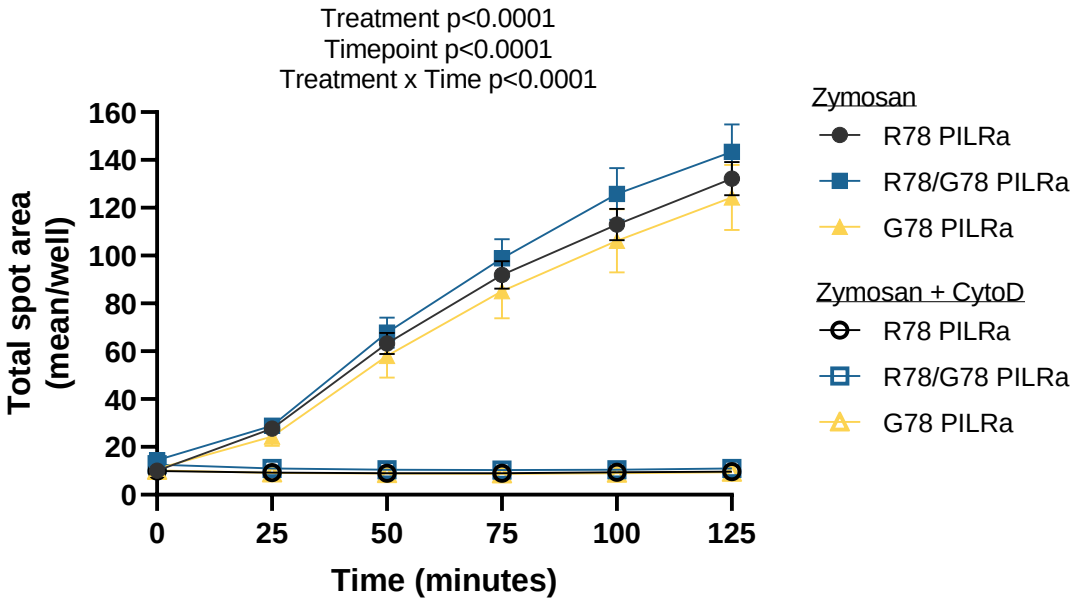

Figure 4.12: Phagocytosis of pH-Rodo zymosan in G78 and R78 PILRa microglia-like cells. Cells were differentiated in 384-well plates (Greiner) (n=5 technical replicate wells) and on day 10 incubated with pH-Rodo zymosan. Images were collected every 25 minutes with Opera Phenix (Perkin Elmer). **(A)** Representative images of microglia-like cells in the final timepoint of the assay. During the assay cells were either given LIS only, which served as a negative control, pH-Rodo zymosan particles or pH-Rodo zymosan and Cytochalasin D (CytoD). Scale bar =50µm. **(B)** Total spot area analysis of pH-Rodo zymosan phagocytosis. Data was analysed in Columbus (n= 5 biological replicate plates). CytoD D (2µM) was used as a control. Each point represent mean ±SD. Data was analysed with 2-way ANOVA comparing genotype and timepoint or treatment and timepoint, followed by Tukey's multiple comparisons test.

In addition to exploring the phagocytic properties of the microglia-like cells, PANP was applied to the cells as potential PILRa specific stimulant to investigate whether activation will produce a different response. The cultures were supplied with 50µg/mL of PANP added to live imaging solution prior to the assay and kept during the whole duration of the time series. The images in Figure 4.13A show that no visible morphological changes are induced by the addition of PANP assessing the last timepoint of the assay. Similarly, to the unstimulated phagocytosis response, all clones successfully uptake zymosan particles and show no uptake when CytoD is used verifying the efficiency of the assay. Based on the response recorder in Figure 4.13B, there is no significant difference between clones expressing different PILRa variants. If we compare the stimulated and

the unstimulated response, there is only a slight decrease in the heterozygous clones response upon stimulation with PANP compared to the unstimulated.

A)

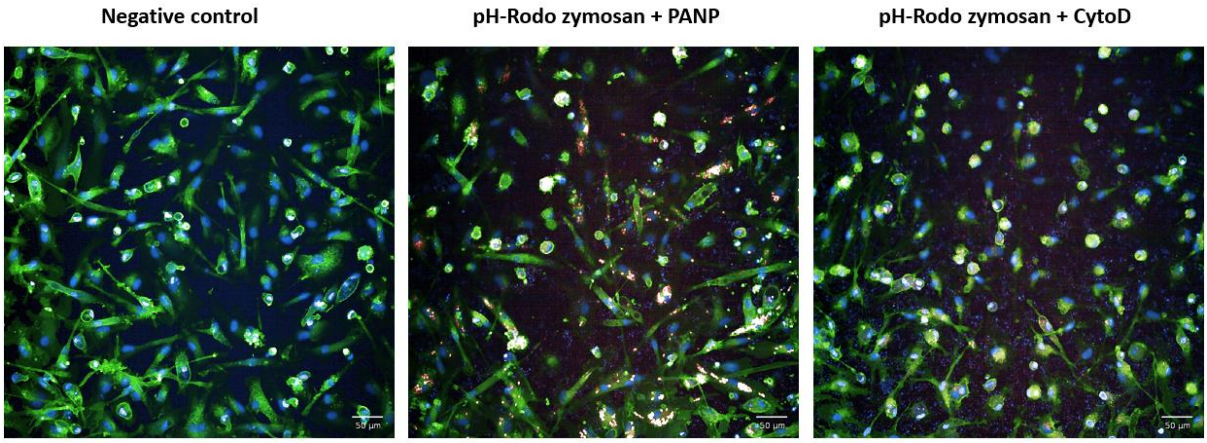

B)

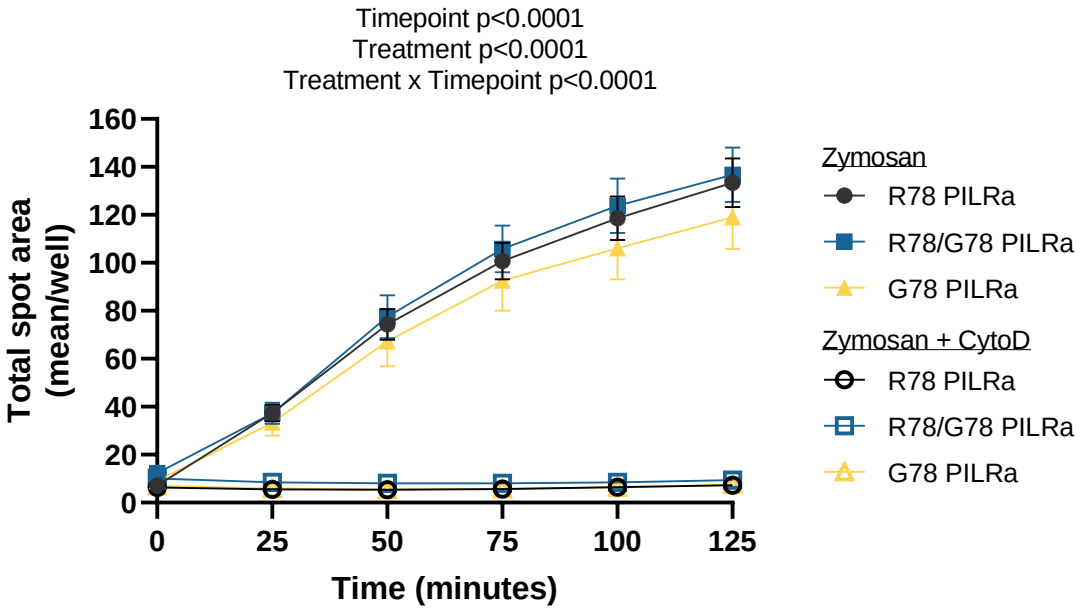

Figure 4.13: Phagocytosis of pH-Rodo zymosan by G78 and R78 PILRa microglia-like cells with 50µg/mL PANP. (A) Representative images of different experimental conditions collected at the last timepoint of the assay. Scale bar = 50µm **(B)** Total spot area analysis of zymosan phagocytosis. Cells were differentiated in 384-well plates (Greiner) (n=5 technical replicate wells) and on day 10 incubated with pH-Rodo zymosan particles and PANP (50ng/mL). Images were collected every 25 minutes with Opera Phenix (Perkin Elmer), and data was analysed in Columbus (n= 4 biological replicate plates). Cytochalasin D (conc.) was used as a control. Each

point represents mean ±SD (n=3 clones per genotype, 5 x technical replicate wells). Data was analysed with 2-way ANOVA and followed by Tukey's multiple comparisons test. Only significant interactions are plotted

The graph in Figure 4.14 demonstrates the individual clone response during the phagocytic assay compared to the overall genotype, which allows us to observe any cell line specific changes. The representative images exhibit the uptake of pH-Rodo zymosan cargo during the different assay timepoints (Figure 4.14A). As it is apparent from the graph in Figure 4.14B, clones do not cluster based on their PILRa variant expression and have varying responses. For example, some clones such as F12 show higher phagocytosis rate compared to all control clones. F12 is a heterozygous clone but seems to exhibit different functional response to the other 2 heterozygous clones, F10 and G10, which show lower or similar to control phagocytic uptake. Furthermore, two of the wild-type clones seem to produce a similar response, however the third clone, C2, regularly scores lower and is more consistent with some of the heterozygous clones. In addition, the two homozygous G78 PILRa clones, C4 and F8 behave very differently. The C4 clones shows consistently lower phagocytosis compared to controls, but this is not observed with clone F8. The responses seen from each clone seem to be reproducible and the trend remains similar from week to week, showing no impact of the factory age. However, the factory harvest does have a significant impact on the response (Two-way ANOVA, Figure 4.14B).

Furthermore, the individual clonal response of cells stimulated with PANP reveals further insight. Figure 4.14C demonstrates that compared to non-stimulated cells, there is not much difference observed in wild-type clones and the response remains similar. However, for example, clones F12 and F8 seem to produce a reduced pH-Rodo uptake when stimulated with PANP. Interestingly, clone C4 remains the clone demonstrating lowest phagocytic response. In contrast, clone F10 increases its response. Although none of these responses are significant, they might indicate a subtle trend or variation in response. Since only a SNP is investigated, there is no way to predict the power of any functional responses produced by the change. This means that the trends which are identified here might represent small functional changes which eventually in the correct conditions impact the overall microglia response.

A)

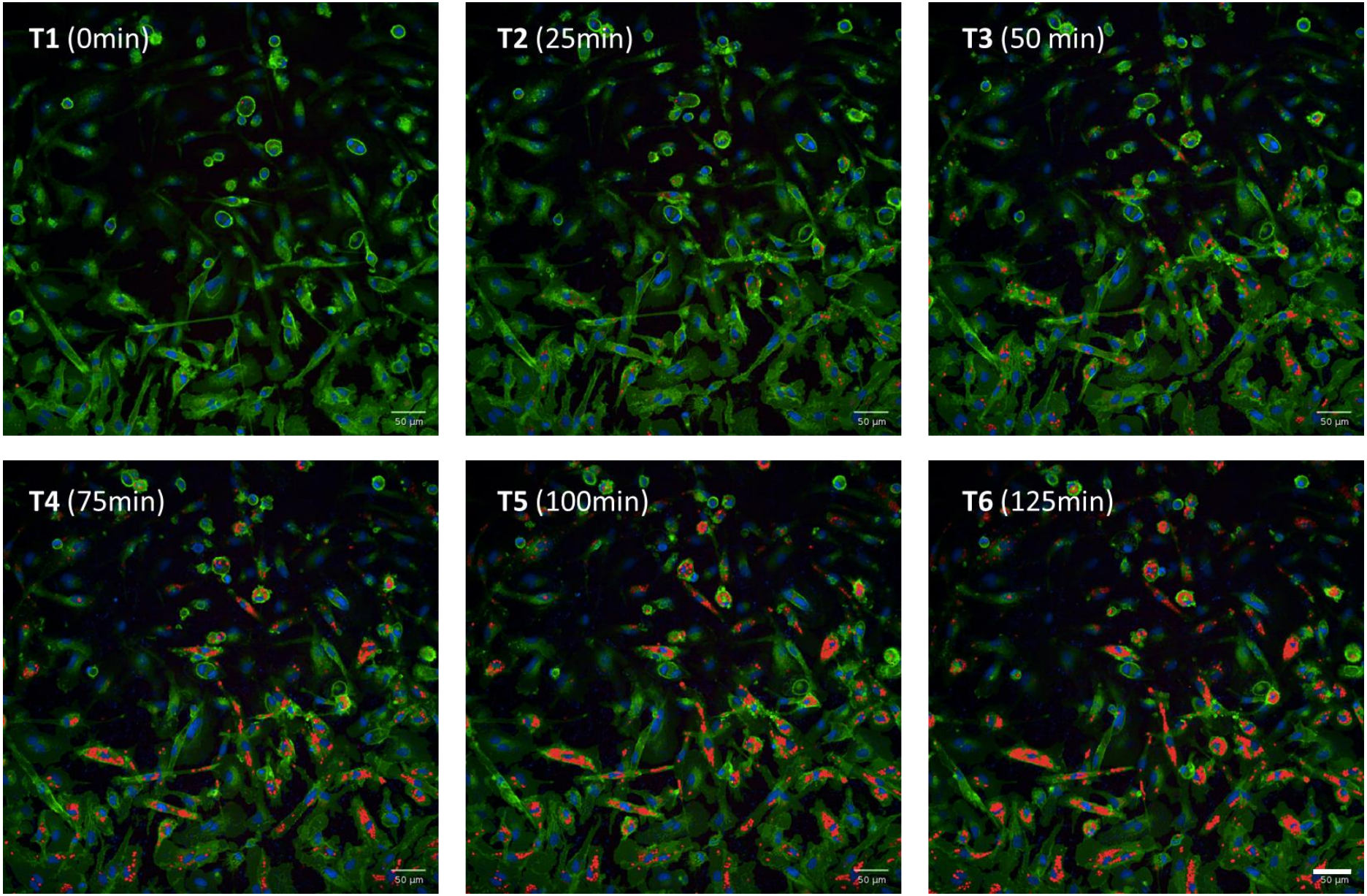

B)

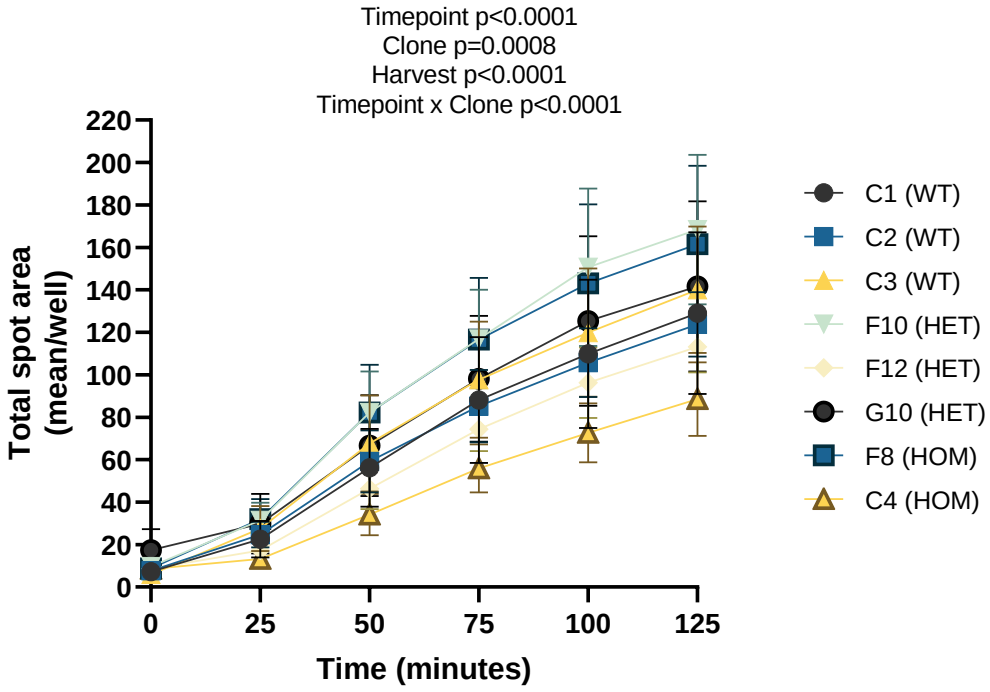

C)

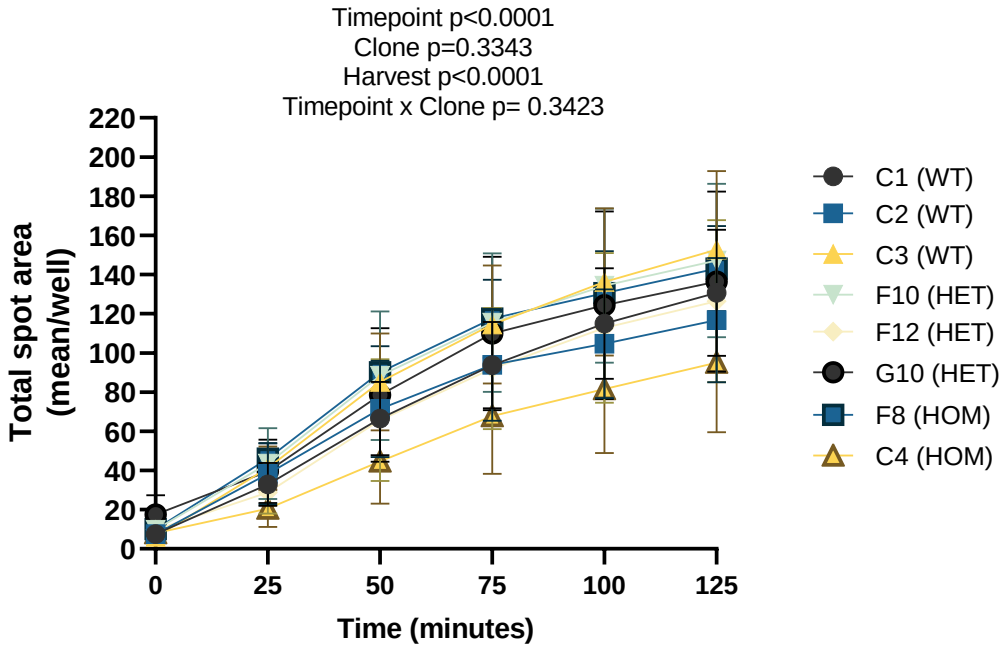

Figure 4.14: Phagocytosis of pH-Rodo zymosan in G78 and R78 PILRa microglia-like cells. (A) Representative images of microglia-like cells at each timepoint of the assay (T1-T6). Increase in zymosan within the cell bodies can be easily seen. Scale bar=50µm **(B)** Total spot area analysis of pH-Rodo zymosan phagocytosis. Cells were differentiated in 384-well plates (Greiner) (n=5 technical replicate wells) and on day 10 incubated with pH-Rodo zymosan particles. Images were

collected every 25 minutes with Opera Phenix (Perkin Elmer), and data was analysed in Columbus (n= 5 biological replicate plates). Each point represents mean ±SD. Data was analysed with 2-way ANOVA and followed by Tukey's multiple comparisons test. Only significant interactions are reported. **(C)** Total spot area analysis of pH-Rodo zymosan phagocytosis in microglia-like cells treated with 50µg/mL PANP. Cells were differentiated in 384-well plates (Greiner) (n=5 technical replicate wells) and on day 10 incubated with pH-Rodo zymosan particles. Images were collected every 25 minutes with Opera Phenix (Perkin Elmer), and data was analysed in Columbus (n= 4 biological replicate plates). Each point represents mean ±SD. Data was analysed with 2-way ANOVA and followed by Tukey's multiple comparisons test. Only significant interactions are reported.

4.2.7.2 G78 PILRa microglia-like cells show no difference in endocytic response

In addition to phagocytosis, it was important to explore the endocytic response in more detail. This included using cargo which is taken up by a different mechanism compared to phagocytosis. To do this, cargo smaller in size was utilised. pH-Rodo Dextran Green which is taken up by receptor mediated endocytosis was applied to differentiated microglia-like cells and the response was evaluated. The data on Figure 4.15A outlines all conditions included in the assay during the final timepoint of the experiment. Figure 52B demonstrates that all differentiated microglia-like cell lines are successfully able to uptake pH-Rodo Dextran Green. Cells treated with dynasore which was used as an inhibitor of endocytosis demonstrate significantly lower AF488 levels within cell boundaries. No statistical significance is reported between the cells expressing different PILRa variants. A trend towards decrease is observed with heterozygous clones which is even more prominent in homozygous clones.

A)

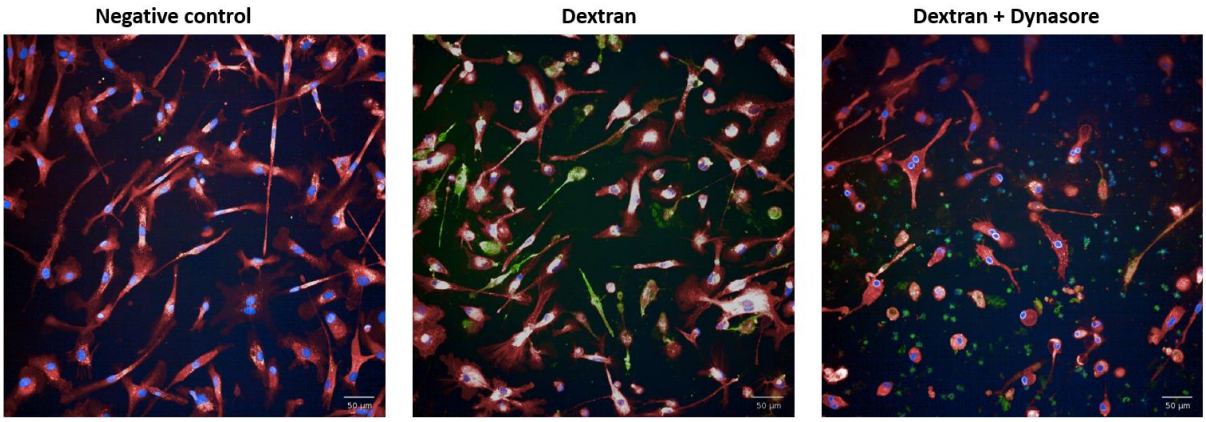

B)

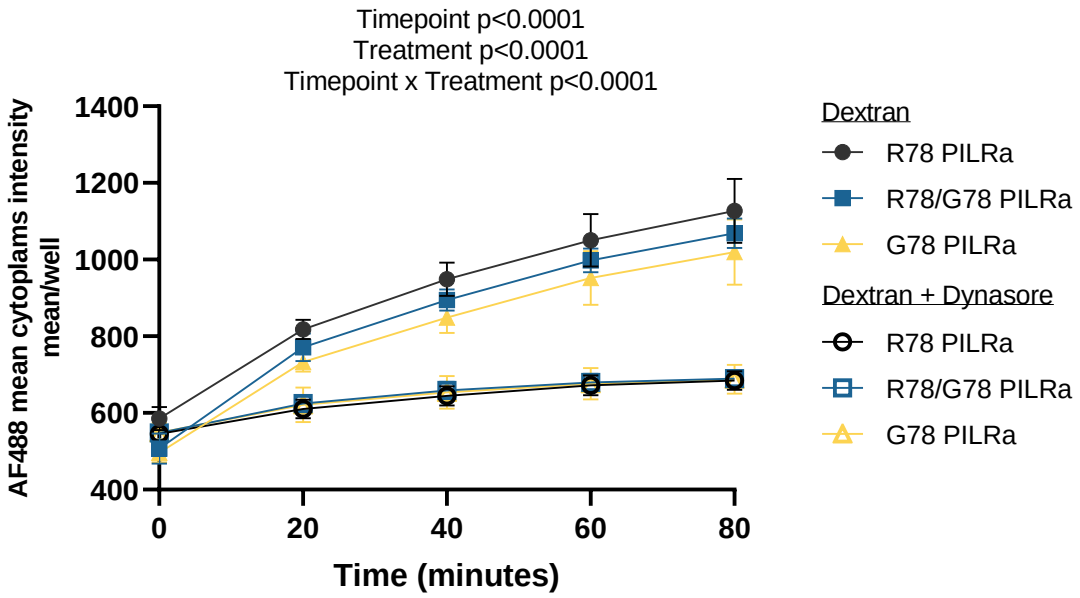

Figure 4.15: Endocytosis of G78 and R78 PILRa microglia-like cells.(A) Representative images of microglia-like cells subjected to the endocytosis assay. Cells were either incubated with Live imaging solution only, pH-Rodo Green Dextran or Dextran combined with Dynasore (50µM). The images were collected from the final timepoint of the assay. Hoechst was used as a nuclear dye and Cell Mask Red was used to stain the cell membrane. Scale bar =50µm. **(B)** AF488 mean intensity per well of dextran endocytosis. Cells were differentiated in 384-well plates (Greiner) and on day 10 incubated with dextran-green. Images were collected every 20 minutes using the Opera Phenix (Perkin Elmer), and data was analysed in Columbus (n= 4 biological replicate plates). Dynasore (conc.) was used as an inhibitor of endocytosis. Each point represent mean ±SD (n=2 or 3 lines per clone, 5 x technical replicate wells). Data was analysed with 2-way ANOVA, followed by Tukey's multiple comparisons test. Only significant interactions are shown.

4.2.7.3 G78 PILRa microglia-like cells demonstrate altered cytokine secretion

Another set of experiments included assessing the ability of microglia-like cells expressing different variants of PILRa to produce cytokines. Cytokine secretion was evaluated by collecting supernatant from cells stimulated with LPS (100ng/ml) or LPS and IFN-γ (20ng/ml). To provide a more detailed picture of the cellular response to these

stimulants, two different timepoints were used, 6 hour and 24-hour stimulation. Figure 4.16 demonstrates the different cytokines and their levels upon stimulation. All cytokines where a response was recorded are presented. Concentrations of all 13 cytokines and chemokines included in the experimental kit were successfully detected. IFN-gamma secretion is excluded as that was added to the media therefore the collected readings will not be accurate.

Overall, the data demonstrates that LPS and LPS combined with IFN-γ successfully stimulate microglia-like cells and all cultures are able to produce an array of cytokines in response to the inflammatory stimuli. Both expression of pro- and anti-inflammatory cytokines is detected.

Marked increase in IL-6 and TNF-α is observed which is in line with the LPS stimulation response. Interestingly, the anti-inflammatory IL-10 concentrations demonstrate that the response is higher with LPS stimulation alone compared to LPS combined with IFN-γ which is different than what was observed with most other cytokines where the response is more acute in the presence of IFN-γ.

An example of a cytokine where the later timepoint reveals a difference based on the cell genotype is IL-1β. Concentrations of this cytokine are elevated at 6-hours post stimulation, but no significant differences are observed. However, the data at 24 hours reveals even further increase in overall concentrations and demonstrates that heterozygous PILRa clones secrete significantly less IL-1β than R78 homozygous clones.

No significant differences are observed in respect to IL-4, Arginase and IP-10 concentrations secreted by different lines. These cytokines demonstrate an increase based on the stimulation alone but no change regarding the timepoint or the type of stimulant. In addition, IL-1RA concentrations demonstrate that this is expressed at higher levels in unstimulated cells than many other cytokines and the secretion is not impacted hugely by the addition of inflammatory stimuli in the culture medium.

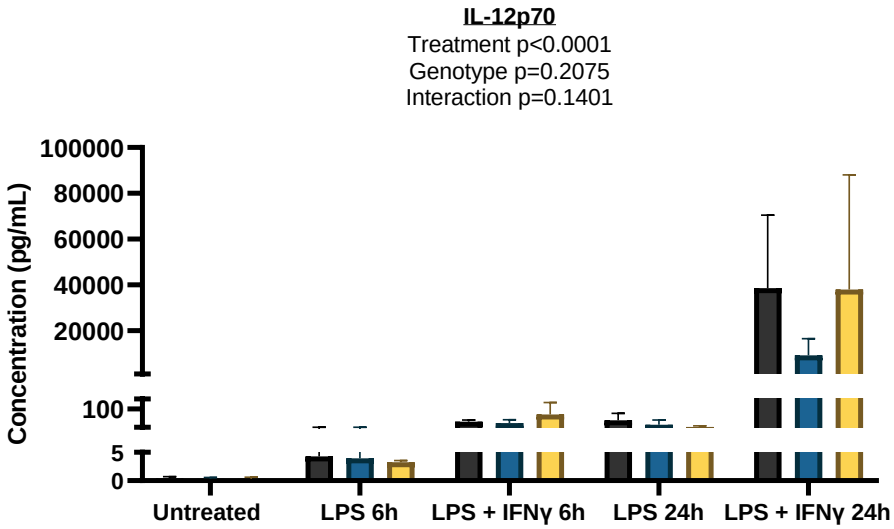
IL-12p70
Treatment p<0.0001
Genotype p=0.2075
Interaction p=0.1401
Concentration (pg/mL)
100000
80000
60000
40000
20000
100
5
0
Untreated
LPS 6h
LPS + IFNγ 6h
LPS 24h
LPS + IFNγ 24h

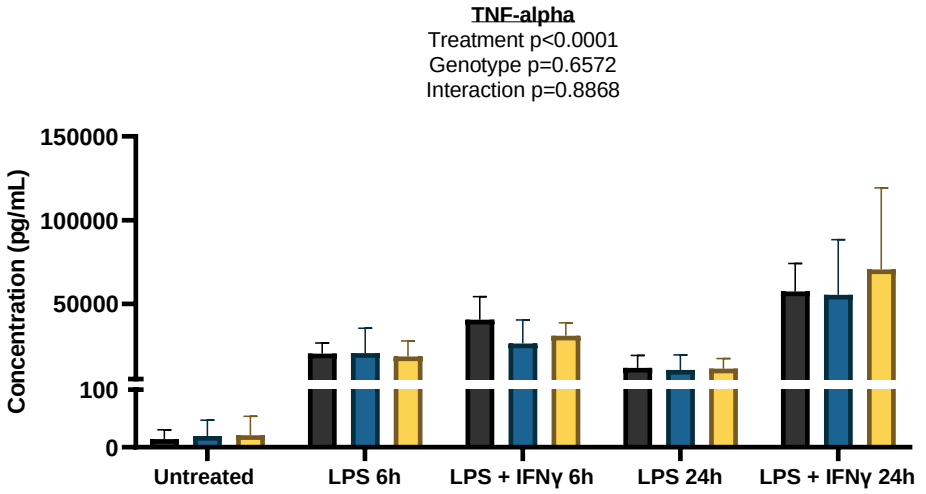
TNF-alpha
Treatment p<0.0001
Genotype p=0.6572
Interaction p=0.8868
Concentration (pg/mL)
150000
100000
50000
100
0
Untreated
LPS 6h
LPS + IFNγ 6h
LPS 24h
LPS + IFNγ 24h

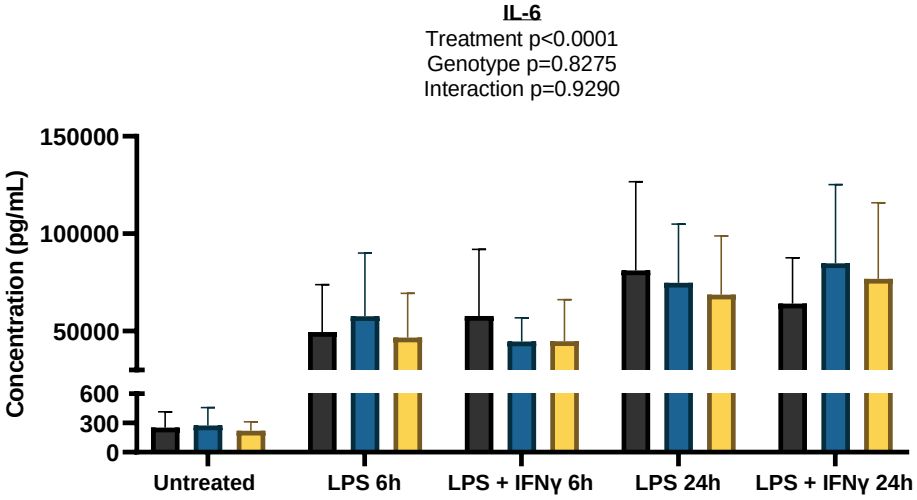
IL-6
Treatment p<0.0001
Genotype p=0.8275
Interaction p=0.9290
Concentration (pg/mL)
150000
100000
50000
600
300
0
Untreated
LPS 6h
LPS + IFNγ 6h
LPS 24h
LPS + IFNγ 24h

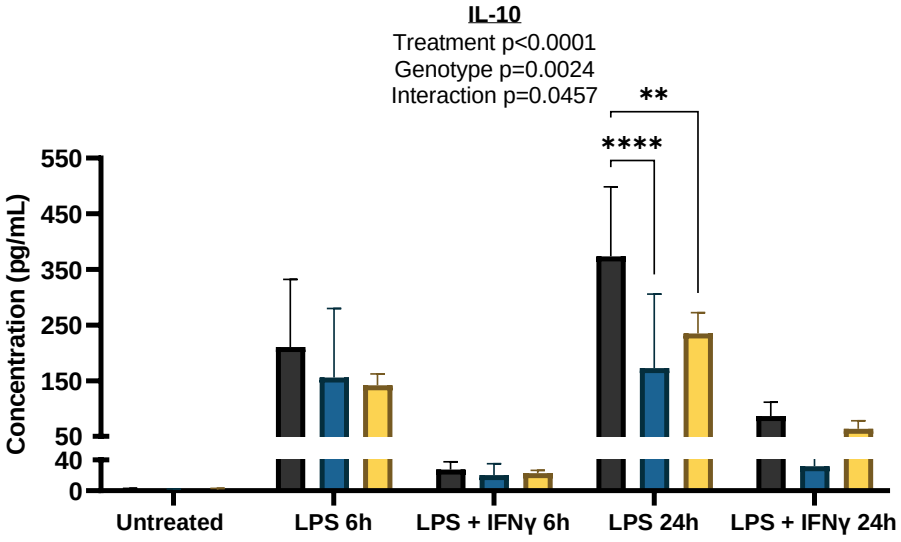
IL-10
Treatment p<0.0001
Genotype p=0.0024
Interaction p=0.0457
**
****
Concentration (pg/mL)
550
450
350
250
150
50
40
0
Untreated
LPS 6h
LPS + IFNγ 6h
LPS 24h
LPS + IFNγ 24h

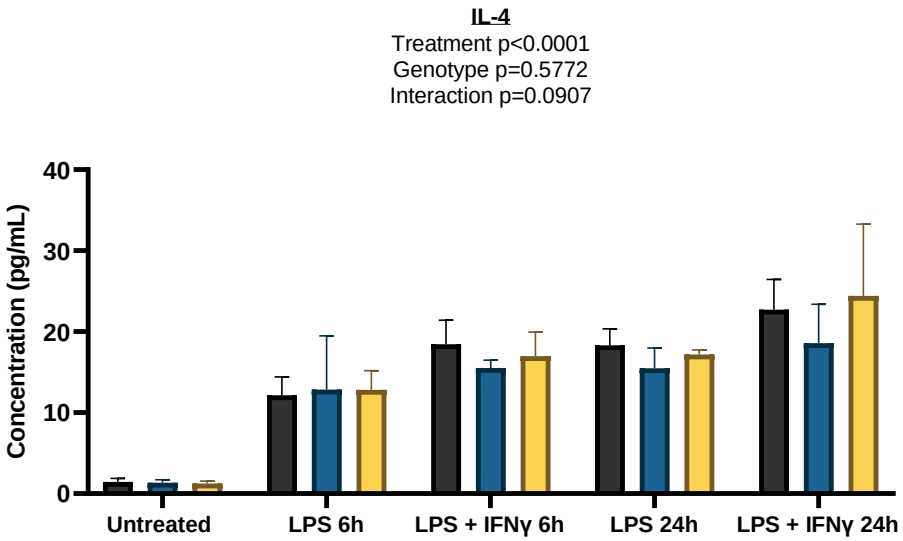
IL-4
Treatment p<0.0001
Genotype p=0.5772
Interaction p=0.0907
Concentration (pg/mL)
40
30
20
10
0
Untreated
LPS 6h
LPS + IFNγ 6h
LPS 24h
LPS + IFNγ 24h

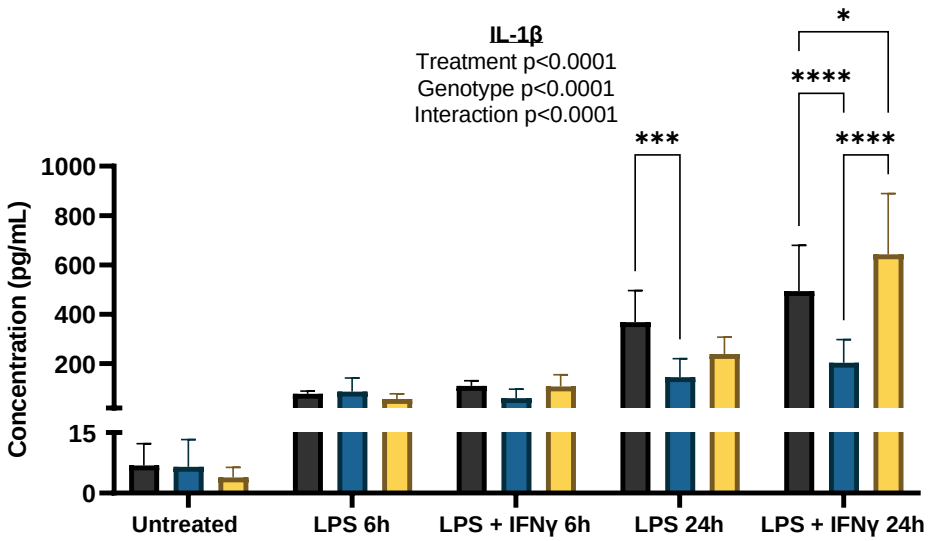
IL-1β
Treatment p<0.0001
Genotype p<0.0001
Interaction p<0.0001
Concentration (pg/mL)
1000
800
600
400
200
15
0
***
****
****
*
Untreated
LPS 6h
LPS + IFNγ 6h
LPS 24h
LPS + IFNγ 24h

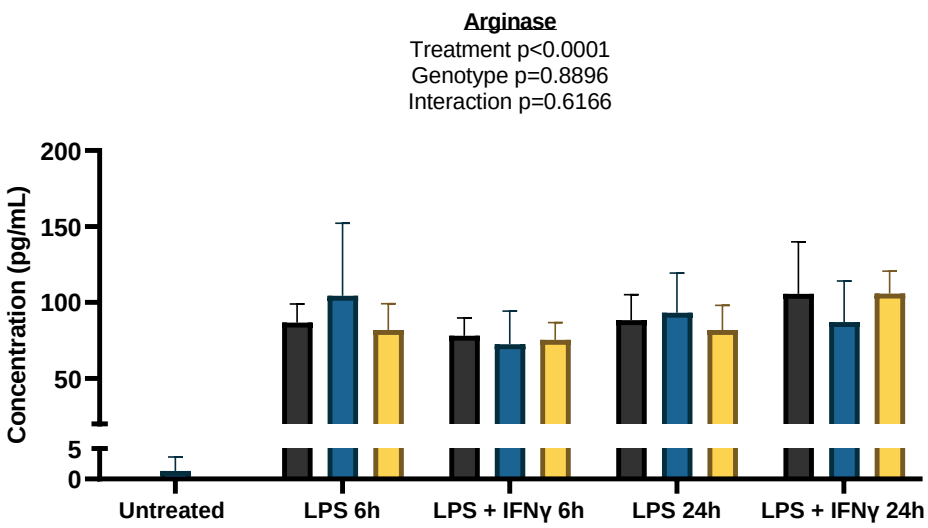
Arginase
Treatment p<0.0001
Genotype p=0.8896
Interaction p=0.6166
Concentration (pg/mL)
200
150
100
50
5
0
Untreated
LPS 6h
LPS + IFNγ 6h
LPS 24h
LPS + IFNγ 24h

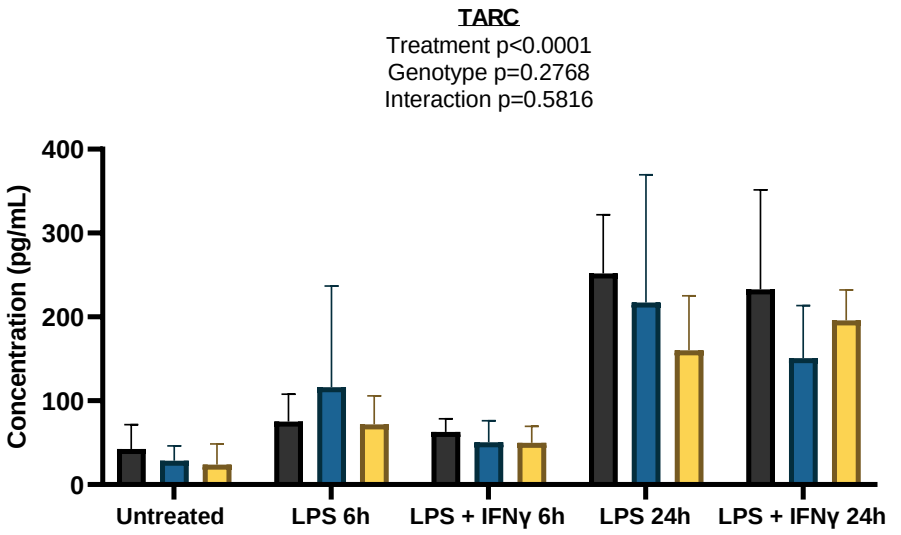
TARC
Treatment p<0.0001
Genotype p=0.2768
Interaction p=0.5816
Concentration (pg/mL)
400
300
200
100
0
Untreated
LPS 6h
LPS + IFNγ 6h
LPS 24h
LPS + IFNγ 24h

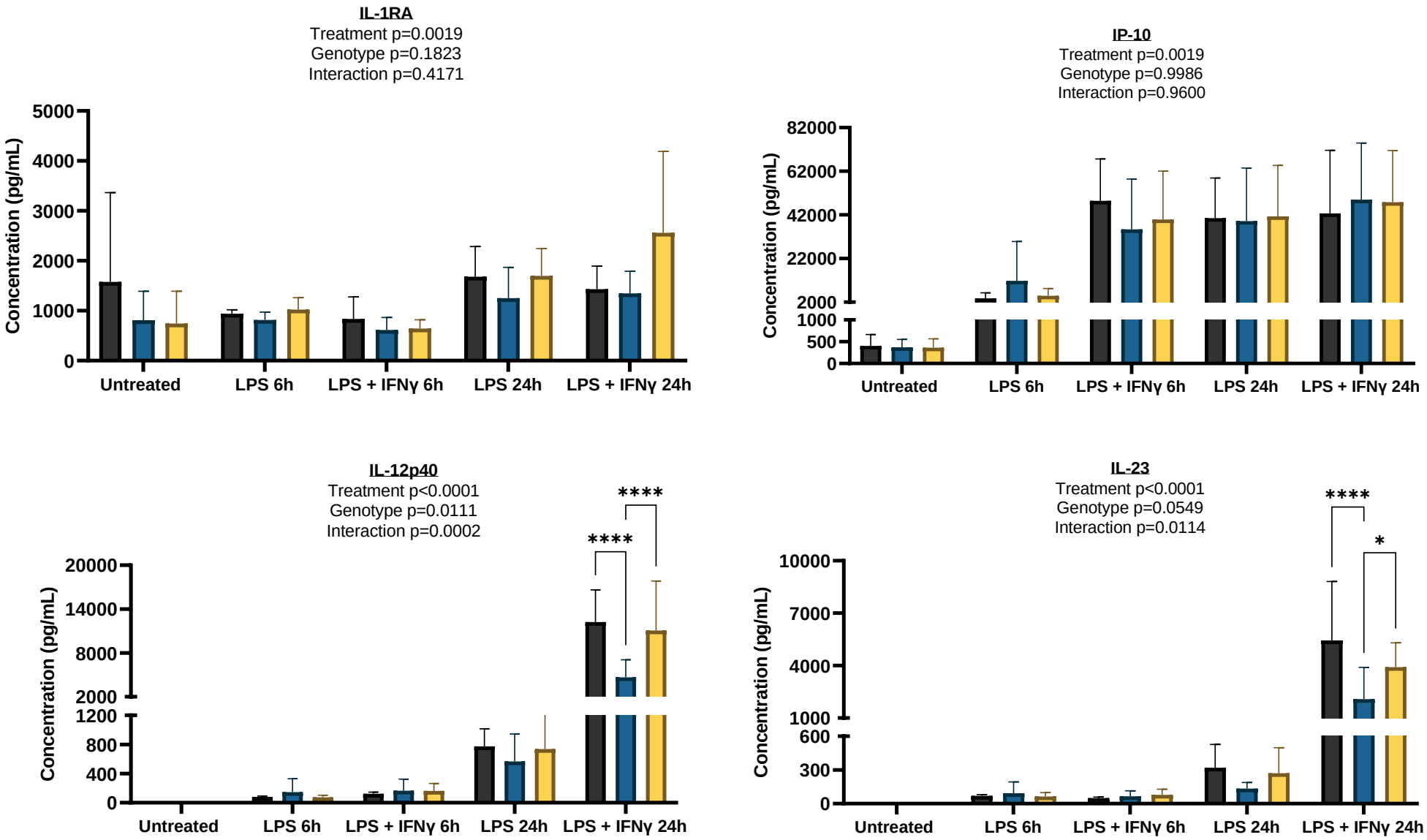

Figure 4.16: Cytokine production in iPS derived microglia-like cells. Following 10-day differentiation media was substituted with fresh microglia media containing LPS (100ng/ml) or LPS and IFN-gamma (20ng/ml). Cell supernatant was collected 6 hours and 24 hours post media change. Control cells were kept with microglia media

only. Bars represent mean ± SD (n=2 biological repeats, 2x technical replicate wells). Data was analysed using two-way ANOVA (reported above each graph), followed by Tukey's multiple comparison test (only significant values are plotted; *p<0.05, **p<0.01, ***p<0.0001). Dark grey bars indicate homozygous R78 PILRa, blue is heterozygous cells containing R78 and G78 PILRa and yellow bars correspond to G78 PILRa homozygous cells.

4.3 Discussion

4.3.1 Summary of main findings

In this chapter an appropriate model to study human PILRa using iPSC cells was developed. The chapter describes how PILRa G78 iPS lines were generated using CRISPR-Cas9. The different stages of the screen are presented, and the characterisation of the positive clones is shown. In summary, the derived isogenic lines and their controls seem to exhibit all required characteristics of iPSCs and could be used for downstream applications. Since no functional differences have been previously reported between G78 and R78 PILRa in microglia, these lines are critically important to investigate such effects *in vitro* in an AD relevant context.

4.3.2 DNA repair pathways and CRISPR mechanism

Within recent years the efficiency of CRISPR editing has significantly improved as seen from literature reports (303). However, due to the molecular complexity of HDR repair, the number of targeted cells remains significantly lower in comparison to knock-out models. Depending on the cell line and the transfection efficiency, efficiency of less than 1% has been reported for some low transcriptionally active genes (304). In here, targeting efficiency of around 10% was reported, which can be considered standard for this type of edit. There has been significant effort in the field to improve targeting efficiency. Multiple strategies from guide design and selection, nucleofection protocols and FACS can be employed to improve the number of edited cells. In addition to protocol changes, there has been an emerging tendency to use various chemical and genetic modulations to influence the cell decision over which gene repair method to use (305). Since cells overall use NHEJ as a preferred method to repair damaged DNA, there are compounds which can inhibit that pathway and push the equilibrium in favour of HDR. Some examples seen in the literature include SCR7 (Pyrazine). SCR7 is an inhibitor of ligase IV, important enzyme in NHEJ repair. Through blocking this part of the pathway, studies report increased CRISPR efficiency of up to 13-fold (306). In addition, timed delivery of the CRISPR-Cas9 system during specific time of the cell cycle can also aid the number of positive targets (307).

Following Sanger sequencing of the newly generated PILRa lines, it was revealed that although the cells encoded for glycine at position 78, the sequence did not match what

was predicted from the initial CRIPSR-Cas9 design. Interestingly within the traces, a sequence matching that of the HDR oligo present could not be identified, therefore predict that recombination did not occur successfully during the CRISPR process. Studies show that often off-target effects usually occur at sites bearing a PAM and complementary to the sequence of the guide (308). In the case of the edit here, the initial base pair sequence, AGG, represents a PAM site in itself and could have been potentially targeted by the Cas9. If DSB has occurred at the site, then it could have been repaired through NHEJ, which is more error prone, and coincidentally some cells resulted with the desired edit.

4.3.3 Genomic instability of iPS cells

To ensure that no large chromosomal rearrangements have occurred during the CRISPR process, a CNV analysis was performed.

It is important to take into consideration the genomic instability of iPS cells when analysing results especially in polygenic conditions such as AD where how individual genes influence the pathology is not known. Interpretation of the functional consequences of genetic variation needs to be carefully considered. It is hard to establish mutations which might be a driver of specific phenotype and their overall effect on cell function. A potential way to overcome those disadvantages experimentally might be to perform assays in parallel on different lines with different genetic background and their respective controls, to validate the role of individual genes.

Previous study performing whole genome sequencing (WGS) demonstrated that more than half of the CNVs detected in iPS cell lines originated from low frequency somatic mutations in the parental fibroblasts (309). Furthermore, other studies reveal that some CNVs can occur during the reprogramming process, where genes associated with survival and pluripotency are switched on (310). Some pre-existing mutations could potentially benefit the reprogramming and proliferation of iPS cells, therefore would be favourably propagated by selective advantage (311).

Another source of iPS instability is prolonged culture. Gore *et al*. demonstrated that point mutations spontaneously arise in late passage cells (293). Interestingly, one of the identified hot-spot regions of many iPS lines (312), including Kolf2, the chromosome

region 20q11.21 was not altered in the newly generated lines included in this chapter. This could however occur over time and might be seen in higher passages of cultured cells. To test this, cells can be kept in culture for longer and DNA can be collected at higher passage and analysed again for any new CNVs.

Advancement in array-based methods allow us to examine copy number variants (CNVs) with kilobase resolution across the whole genome. It is worth noting that those methods do not accurately identify balanced inversions and translocations (313). For comprehensive analysis more advanced methods which allow detection of genetic variation at single nucleotide resolution across the whole genome such as next generation sequencing (NGS) should be used. In addition, NGS allows for low frequency variations to be detected which can usually be missed with array-based detection methods, providing greater insight into the source of genomic instability in iPSCs (314).

To improve genomic instability in iPS cells the reprogramming methods need to be considered, including the delivery method and the reprogramming factors used. In addition, selecting the best starting material is important. Due to the higher predisposition of spontaneous mutations occurring in certain cell types, such as fibroblasts, due to environmental pressures, the field of stem cells is moving towards using more stable starting material such as PBMCs.

4.3.4 Functional response of microglia-like cells with different PILRa variants

To investigate how microglia-like cells which express G78 or R78 PILRa compare in their responses an array of phenotypic assays was used. Functions relevant to microglia and their role in AD were explored.

4.3.4.1 The endocytic response

Overall, the combination of endocytic assays used in this thesis suggest that the generated microglia-like cell lines respond to different cargo (zymosan and dextran) and do not show any impairment in activity. No significant differences are reported for either of the assays based on PILRa genotype. However, it is apparent that the response between individual clones is highly variable. Assessing the homozygous clones, clone C4 clearly appears to be hypofunctional in comparison to other clones, however clone F8 shows higher response than the average for the remaining clones.

This difference in the response represents a challenge in forming conclusions about the activity of G78 PILRa expressing microglia-like cells. It also highlights the importance of generating multiple clones with the same genotype as sometimes variation is present. Here only 2 homozygous clones were successfully generated and validated, therefore cannot confirm which of the 2 is representing the 'true' response and can only speculate.

If C4 is exhibiting the response which is expected in G78 PILRa then a marked decrease in both phagocytosis and receptor mediated endocytosis is seen, which might suggest that G78 cells are less active due to higher PILRa inhibitory function. In the context of AD, this can potentially result in decreased uptake of plaques and altered inflammatory response. Therefore, cells expressing R78 PILRa might show increased response which could confer protective effect.

On the other hand, if clone F8 is mimicking *in vivo* responses more accurately, an increase in phagocytosis is present and that seems to be altered by the addition of PANP. This shows that potentially microglia-like cells with G78 PILRa are less activated upon stimulation, potentially attributed to higher PILRa activation triggering inhibitory pathways, which leads to a decreased response. Most ITIM containing Siglec-family receptors are known for reducing phagocytic responses upon exposure to surface glycans (host or pathogen), a mechanism commonly used by bacteria to avoid host immune defence (315). This may suggest that in the presence of a stimulant clone F8 is responding more in accordance with predictions. However, this all remains speculative.

Additionally, it is interesting to consider the responses seen in the heterozygous clones. These lines demonstrate a certain variability between clones as well, however overall, there is a trend between all the different assays. Firstly, heterozygous clones exhibit slightly higher *PILRa* mRNA levels when differentiated to microglia-like cells than control clones. In addition, there is a trend towards increased PANP binding in clones expressing both G and R78 PILRa. This combined with the findings from the functional assays, increased phagocytosis compared to wild-type clones with and without stimulation and reduced endocytosis, suggest that these clones are not responding as predicted. Based on the conformational changes

occurring with the G78R mutation, there is no structural analysis which demonstrates how a heterozygous clone will respond. The proportion between G78 and R78 PILRa expressed on these cells could be varying and most likely one allele would be dominant. From the literature it is evident that majority of publications do not include heterozygous findings most likely due to no significance especially when studying SNP changes (163). In addition, majority of publications focus on studying knock-out lines rather than SNPs. This however limits the understanding of effects seen with heterozygous variants and decreases translating findings to patients.

Similarly, to the experiments in Chapter 3, stimulating the cultures with LPS prior to phagocytosis may have provided a better understanding of how the cells respond under inflammation. Additionally, using different cargo, such as *E.coli* or synaptoneurosomes and extending the duration of the time course might have provided additional information about the endocytic response in different PILRa variant expressing microglia-like cells.

4.3.4.2 Cytokine response

Some significant findings are reported with the stimulus-induced secretion of IL-10, IL-12p40, IL-23 and IL-1β.

The only cytokines where significant differences between wild-type and homozygous clones are reported are IL-10 and IL-1β. In homozygous IL-10 cells a marked reduction in IL-10 concentrations is reported when cells were stimulated with LPS for 24 hours. This potentially indicates that microglia-like cells containing G78 PILRa respond less to inflammatory stimuli and produce lower levels of anti-inflammatory cytokines. IL-10 concentrations are linked to IL-6 and TNF-α, therefore these cells may have more acute inflammatory response which can potentially be harmful.

In addition, G78 microglia-like cells demonstrate increase in IL-1β which is a pro-inflammatory cytokine. IL-1β signals through the NF-κB pathway and can induce a variety of cell responses (316). Microglia secrete cytokines and chemokines to regulate inflammatory responses mediated via communication with other cells. In AD, chronic neuroinflammation can lead to a self-propagating cycle of cytokine release, causing continued elevation of inflammatory signals such as IL-1β. If G78

PILRa cells demonstrate even higher levels if IL-1β upon stimulation this potentially can chronically lead to faster disease progression and detrimental impact on other cell types. Research demonstrates that IL-1β can mediate neuronal damage and injury (317), notably important in AD context.

The observed clonal variation in the other assays is apparent in the cytokine response of cells as well. For example, when quantifying the cytokine levels, some homozygous clones demonstrate the opposite response to that seen in heterozygous clones. Interestingly, concentrations of both IL-12p40 and IL-23 demonstrate significant decrease in heterozygous clones stimulated with LPS and IFN-γ for 24 hours compared to homozygous and wild-type lines. Although not significant the trend remains the same in only LPS stimulated cells. This provides another example of the variable phenotypic response documented in heterozygous clones. As discussed previously, this could be attributed to expression differences between the two alleles. During characterisation of those lines, no additional mutations were detected therefore it is unlikely all 3 clones would contain off-target effects impacting the functional outcome. In line with some published work, it is considered experimentally challenging to manipulate gene dosage in iPSC cultures. However, precise regulation of gene dosage and expression levels *in vivo* is what makes the brain environment so unique. There is a large amount of identified AD risk genes whose effect has been associated with gene dosage in knock-out models, including *ZCWPW1 (318).*

4.3.5 iPS microglia as a model of AD research

iPS cells represent an incomparable opportunity to study human genetic risk associated with neurodegenerative diseases. They, however, also have a major drawback, as it difficult to control for genetic variability. Furthermore, experimental differences and differentiation variability contributes to the challenges of research in the field. Although a variety of experimental protocols are now available (as reviewed in (319)), it remains to be determined to what extent *in vitro* differentiated microglia resemble *in situ* human microglia. The field requires a more standardised methods of culturing iPS cells and ways to characterise the terminally differentiated cells, so that parallels between studies can

be drawn correctly. This can greatly improve the identification of future drug targets and aid therapeutic advancements in the field of AD research.

Another important question of the field remains the 'age' of iPS derived microglia. During the reprogramming process when new lines are generated it is believed that the natural clock of cells is reset, therefore iPS microglia in culture resemble more closely early embryonic stages of development. This is of particular importance especially in neurodegenerative conditions like AD where age remains the leading factor for disease development.

The advantages and challenges of using iPS derived microglia-like cells as a model for neurodegenerative disease compared to other existing models will be discussed further in the overall discussion chapter of the thesis.

4.3.6 Future directions

Most of the functional assays used here, point towards a trend in the response of the different clones expressing PILRa variants but do not conclusively suggest there is a difference in that response. Due to the G78R variant being a single polymorphism change within the protein the impact such a mutation would cause on the functional response is not necessarily known. Therefore, a more radical approach will involve creating knock-out lines for PILRa which might directly reveal some responses where PILRa's function is essential. However, in terms of patient context this represents a less disease relevant model and will aid the understanding of PILRa's functions but not necessarily provide any understanding of the AD associated variant. Ideally, creating lines expressing both G78 and R78 PILRa using background lines with different AD genetic background can prove more useful to investigate the SNP role in conjunction with other AD relevant genes where the combinatorial effect might provide a stronger phenotypic response.

To further explore the function on PILRa in relation to AD and microglia, more complex models can be used. Advances in the field of stem cells, allows us to utilise co-culture systems and 3D organoids. In comparison to standard monoculture where the role of the individual mutation is depicted and unidirectional interactions, in this case the G78R variant of PILRa, using co-culture can predict potential cell-cell interactions and complex

processes which might have impact on the whole brain environment. In addition, microglia co-culture with neurons shows expression of important inflammatory markers, making it a more relevant model for studying of neurodegenerative diseases (320). To mimic more closely the brain environment, some protocols involve culturing iPSC microglia with conditioned medium from other cell types to provide some important factors. Apart from studying genes in isolation, it is important to start linking individual identified risk genes into whole pathways which might drive specific cellular changes and phenotypes. Identifying such potential mechanisms will provide new ways to target AD development.

In addition, the use of chimera models can be a useful approach in the case of PILRa studies. Since there is a significant difference between human and mouse PILRa and the gene is not very well conserved between species, it would be interesting to study how human PILRa behaves within *in vivo* environment. Chimeric models where human iPS cells have been differentiated and introduced directly into the mouse brain will be beneficial to study individual genetic impact during disease development. A potential model can include G78 and R78 PILRa microglia delivered into mouse model of AD such as the APP^{NL-G-F} model. This will allow to study PILRa in more physiologically and disease relevant context and to compare how each variant might impact disease progression through analysing plaque burden and microglia morphology for example.

4.3.7 Conclusions

This chapter describes the generation and characterisation of G78 PILRa expressing iPSC lines in an isogenic system. These lines have the potential to be a promising model to study the functions of the AD associated G78R variant of PILRa and to depict its role in microglia. iPSC derived microglia-like cells from the new lines represented a useful tool to utilise in an array of experiments aimed to investigate microglia relevant functions in the context of AD. The presented data suggests that the G78R variant might contribute to important microglia responses such as phagocytosis and cytokine production where certain trends are observed. The subtle differences seen here in microglia-like cells require further research to conclusively suggest what the role of the variant might be and if any significant responses are observed. When researching SNP changes significant differences might be hard to identify since it is unclear how the predicted genetic risk

transfers to phenotypic effects. More importantly, the cumulative work here highlights the multifaceted nature of the receptor and its related responses and clearly demonstrates the complexity and the challenges of the models used to study microglial functions *in vitro*.

Chapter 5 Validation of Syk cKO in APP^{NL-G-F} mouse model and associated early transcriptional changes

5.1 Introduction

SYK has a central role in immune signalling. A 72kDa nonreceptor kinase, SYK is rapidly phosphorylated upon activation of signalling pathways. SYK contains two SH2 domains and a kinase domain (321). The kinase contains multiple phosphorylation sites, some of which are located within the linker region and are subject to autophosphorylation. Usually in the resting state, the kinase domain is inactive and can be activated by binding to both SH2 domains by dual-phosphorylated ITAMs (210). This activation initiates a cascade of downstream signalling responses. In addition, apart from classic ITAM activation, SYK signalling was shown to be mediated via other receptor classes such as integrins and C-type lectins (322). Activation of SYK is counteracted by the presence of phosphatases and this balance between SYK and phosphatase activity is what determines the ultimate signalling output. This is a combination of multiple converging pathways which are regulated by upstream receptors driving kinase or phosphatase responses.

In terms of AD relevance, studies demonstrate that SYK is part of the same signalling pathway with important AD associated genes such as *TREM2* and *PLCG2*, potentially regulating key microglia functions (323). A study by Ghosh *et al*. demonstrated that in primary microglia SYK promotes the formation of stress granules which induce oxidative stress and reduce the phagocytic abilities of microglia (236). In addition, both human and mouse models demonstrate SYK hyperactivation recorded in activated microglia, neurons affected by Tau and dystrophic neurites around amyloid plaques (231). Schweig and colleagues showed that activation of SYK leads to Tau hyperphosphorylation and accumulation potentially due to defects associated with autophagic clearance (233).

Collectively this evidence suggests that SYK might play an important role in cellular responses to AD. Multiple SYK inhibitors are readily available (reviewed in (324)) which makes SYK an exciting potential drug target for AD treatment. However, to modulate SYK activation in AD, first there is a better need to understand what impact it has on the microglia response in neuroinflammatory conditions. Studies show that homozygous *Syk* knock-out (KO) mice suffer from haemorrhaging at embryonic stages and die at mid-gestation or perinatally due to vascular defects and hyperproliferation (325). This makes the study of *Syk* in animal models more challenging requiring additional genetic tools to be utilised.

The Cre-ERT system is a widely used tool in generating transgenic mice. This system allows researchers to have conditional control over gene expression. The Cre-ERT2 is a fusion protein generated from the Cre DNA recombinase and a mutant form of the ligand binding domain of the human oestrogen receptor (ER) (326). Cre recombinase, type I topoisomerase has the property to facilitate site-specific recombination between loxP sites. Depending on the orientation of the loxP sites, Cre recombination can result in deletion, insertion, translocation, or inversion of the target gene (reviewed in (327)). In physiological conditions, similarly to the human oestrogen receptor, Cre-ERT is kept inactive in the cytosol by heat shock proteins. Upon induction with different stimulants, this complex is disrupted and the Cre-ERT is released to translocate to the nucleus where it facilitates recombination of the floxed gene of interest.

This system has undergone several modifications since its initial development. Second generation of Cre-ERT lines also known as Cre-ERT2 is 10-fold more sensitive to tamoxifen and its metabolites than to oestrogen found in the circulation (328). Therefore, the system is not concerned with physiological levels of oestrogen which can be an issue particularly in female animals. In addition, the use of cell type specific promoters to drive Cre-ERT2 expression allows the study of gene expression in a tissue specific manner. In the case of the mice used in this thesis, Cre-ERT2 expression is driven by the microglia specific promoter Cx3Cr1 by replacing the first 390 base pairs of the gene (249). This allows us to look at the role of SYK expression in myeloid cells, including macrophages, and specifically for this study, microglia.

Cre-ERT2 can be induced by different sources, including tamoxifen. Tamoxifen is a selective oestrogen receptor modulator which has been widely used for the treatment of hormone breast cancer (329). The drug acts as an oestrogen receptor antagonist. Systemically the drug is rapidly metabolised by the cytochrome P450 and UDP enzymes. Tamoxifen is broken down to *N*-desmethyltamoxifen and active 4-hydroxy (OH)tamoxifen. Both metabolites can be further broken down into 4-hydroxy-*N*-desmethyltamoxifen, also known as endoxifen (330). Endoxifen is the most pharmacologically active metabolite and shows highest affinity for the oestrogen receptor.

There are multiple published protocols on the ways of administration, dosage and preparations of tamoxifen (331). This makes analysing how efficient induction is for existing

Cre lines challenging. Previous studies demonstrate that tamoxifen dosage has been modified based on animal age and target. Interestingly, older transgenic animals have demonstrated to require higher dosage and longer treatment to achieve suitable induction of Cre-ERT2 activity (332). Irrespective of the dose and administration method, tamoxifen concentrations are thought to peak 1 week after induction and then slowly decrease (333).

For the purpose of this thesis, the Cre-ERT2 system was combined with the APP^{NL-G-F} knock-in mouse model of AD. This model was created using C57BL/6 background mice and has 3 different mutations associated with familial forms of AD (334, 335). These include the Iberian, the Arctic, and the Swedish mutation all localised withing the APP construct which contains a humanized region of Aβ (175). In combination, these mutations drive the accumulation of Aβ. The Swedish (NL) mutation causes overall increase in Aβ production, the Iberian (F) promotes increase in Aβ42 which shifts the Aβ40/42 ratio, in favour of the more harmful species. Finally, the Arctic (G) mutation accelerates oligomerisation which promotes aggregation of Aβ. In combination, over time animals present with plaques (2-3 months), closely followed by gliosis. At a later stage synaptic loss is present and inevitably by 6-months of age behavioural deficits are present (138). In comparison to other AD mouse models, the APP^{NL-G-F} model is not an overexpression one and aims to mimic a more 'natural' way of disease development by maintaining physiological-relevant expression levels and sources of APP.

The Cre-ERT2 system offers a valuable way to investigate the role of *Syk* in microglia. In addition, expressing this system in an animal model of AD allows to study how inducing *Syk* knock-out at different ages impacts microglia and disease progression, both from gene expression perspective and functional changes.

Chapter Aims:

- Validate the safety and efficacy of tamoxifen in Syk x APP x Cre-ERT2 transgenic mice
- Establish an appropriate dosing regimen of tamoxifen achieving consistent high conditional knock-out (cKO) levels
- Determine if Syk-cKO in microglia is long-lasting when induced at different ages
- Understand how cKO of *Syk* impacts microglia transcriptional profile on a single cell level

5.2 Results

In this chapter, 2 mouse strains were used. All mice were bred on APP^{NL-G-F} background and were stable for floxed *Syk*, resulting in $Syk^{fl/fl}$ x APP^{NL-G-F} line which was utilised as control and from now on will be termed Syk x APP. Additionally, mice were crossed to Cre-ERT2 expressing animals, producing experimental heterozygotes, with regard to Cre-ERT2. This line will be referred as Syk x APP x Cre-ERT2.

5.2.1 Induction of *Syk* conditional KO (cKO) by I.P. tamoxifen (100mg/kg)

Initially, for initial investigation of tamoxifen, mice received 100mg/kg, which was chosen based on published literature, and expected to be safe and effective in the strain of interest. To evaluate the use of tamoxifen in the Syk x APP x Cre-ERT2 mouse model, animals were treated with 100mg/kg tamoxifen delivered using intraperitoneal (I.P.) injection. Animals received 3 injections on consecutive days of either tamoxifen or corn oil, used as a control. Brain tissue for analysis was collected 10 days after the last injection.

5.2.1.1 Tamoxifen effect on animal welfare

To determine the tolerability of tamoxifen in this strain and to ensure animal welfare, during the duration of the experiment animals were monitored at 12-hour intervals. At each check weight, appearance, natural and provoked behaviour was evaluated for each animal and overall welfare score recorded (Figure 5.1A). 20% weight loss was set as a humane endpoint for all tamoxifen experiments. Overall, the results indicate that animals tend to lose more weight in the initial 2 days of the experiment (Figure 5.1B and C). In addition, this seemed to be replicated in oil controls, meaning animals do not experience specific weight loss effect due to tamoxifen administration, but potentially linked to the injection itself.

(A)

Date	ID#	Genotype	Treatment	Ear	Original Weight	New Weight	Weight Change				Appearance				Natural Behaviour				Provoked Behaviour				Score
							Norm	<5%	<15%	>15%	Normal	Lack of Grooming	Discharge	Piloerection	Normal	Minor	Less Mobile	Vocalisation	Normal	Minor	Moderate	Violent/ Weak	
	104238	SAE, m	Tam	L0R1	29.20		/	27.74	24.82	23.36		/ *overgrooming, patches of s			/					/			2
	104239	SAE, m	Tam	L1R1	29.90		/	28.41	25.42	23.92	/				/					/			1
	104240	SAE, m	Tam	L2R0	28.5		/	27.08	24.23	22.80		/ *			/					/			2
	104247	SAE, f	Tam	L1R1	20.2		/	19.19	17.17	16.16	/					/			/				1
14.11.2021	104248	SAE, f	Tam	L2R0	19.2		/	18.24	16.32	15.36	/					/			/				1
4pm	104809	SA, m	Tam	L0R2	27.9		/	26.51	23.72	22.32		/ *			/					/			2
	104810	SA, f	Tam	L0R1	20.9		/	19.86	17.77	16.72	/					/			/				1
	104811	SA, f	Tam	L0R2	19.4		/	18.43	16.49	15.52	/					/			/				1
	104912	SA, f	Tam	L2R1	19		/	18.05	16.15	15.20	/					/			/				1
	104245	SAE, f	Tam	L1R0	20.8		/	19.76	17.68	16.64	/					/			/				1

(B)

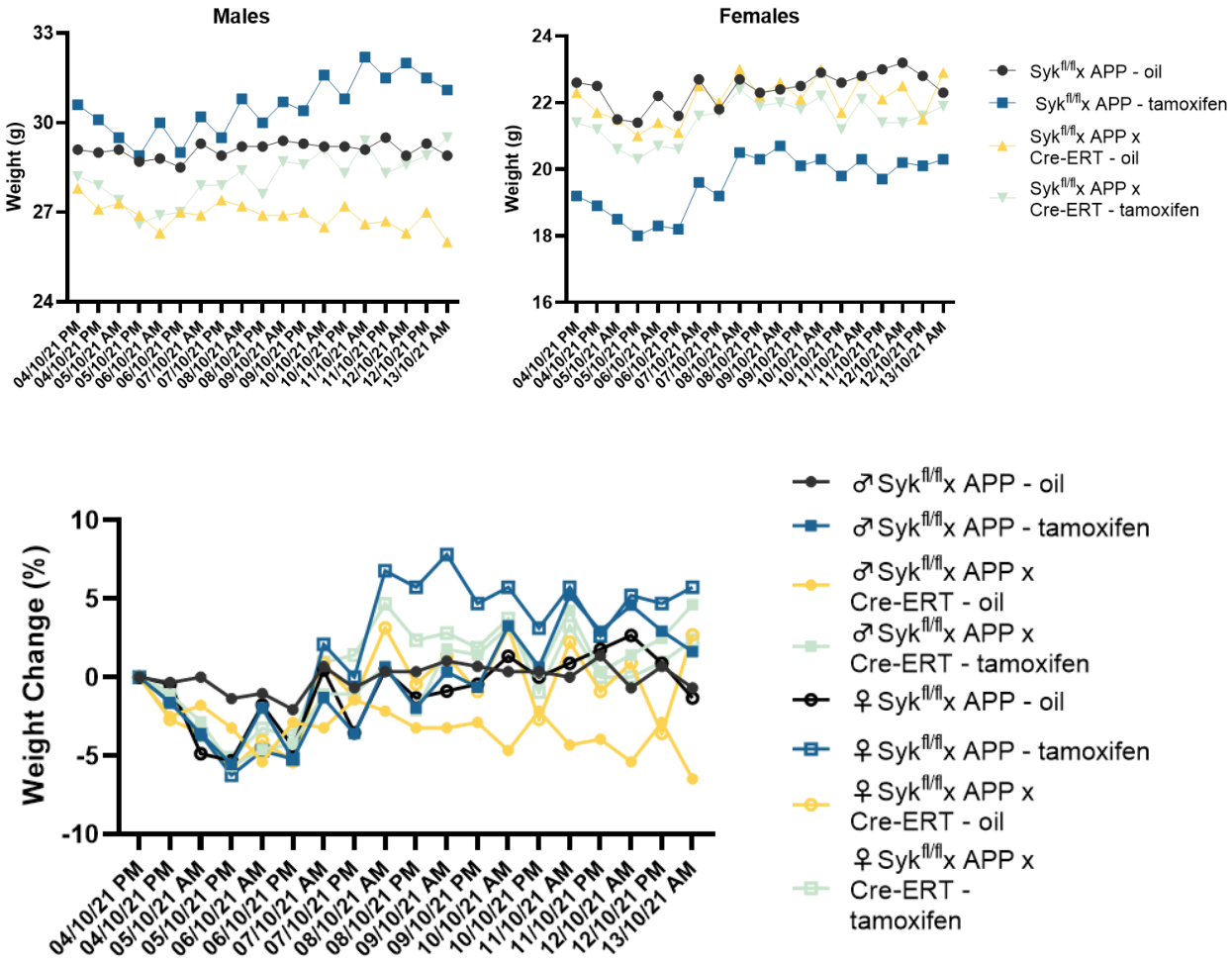

(C)

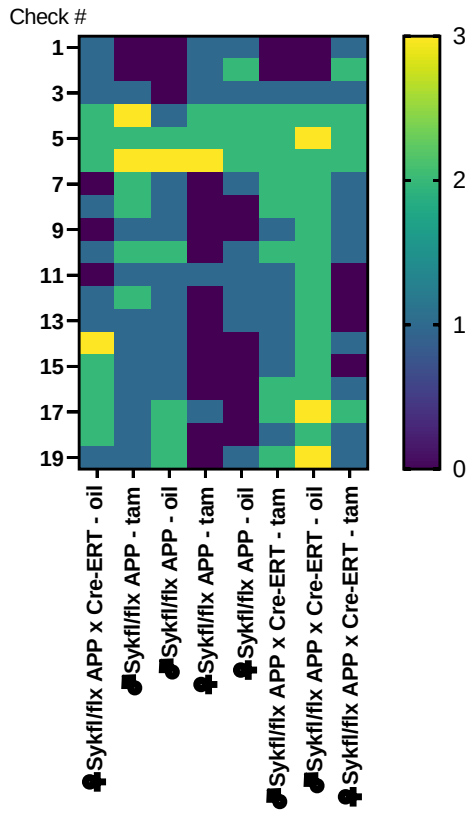

Figure 5.1: Welfare of tamoxifen treated mice. All animals received 3 injections on consecutive days with 100mg/kg tamoxifen or corn oil (n=2 male and female animals per genotype). **(A**) Example scoring sheet used during tamoxifen experiments. **(B)** Weight recorded in grams during the experiment for both female and male mice. In addition, the last graph represents the weight change in %. **(C)** Heatmap representing animals' overall welfare score.

5.2.1.2 Tamoxifen efficiency

Within the brain SYK expression is largely restricted to microglia and other brain macrophages, although neuronal expression can also be detected. To analyse *Syk* gene expression in microglia only, the cells had to be isolated (protocol in methods). Using flow-cytometric cell sorting, $CD11b^{high}$ and $CD45^{low}$ cells were selected (Figure 5.2A). *Syk* mRNA expression was analysed via qPCR. From the results on Figure 5.2B, decreased mRNA levels of *Syk* are present only in Syk x Cre-ERT2 animals treated with tamoxifen compared to control animals. Here a cKO of around 80% in male and 75% in female mice is reported.

We further evaluated the protein levels of SYK detected in the treated mice. Cells were stained using CD11b, CD45 to allow for microglia selection and anti-SYK antibody (all reagent details can be found in Methods). The results are presented in Figure 5.2C which

demonstrates a marked reduction in protein expression of SYK in the Cre-ERT2 mice treated with tamoxifen. This applies both to male and female mice.

A)

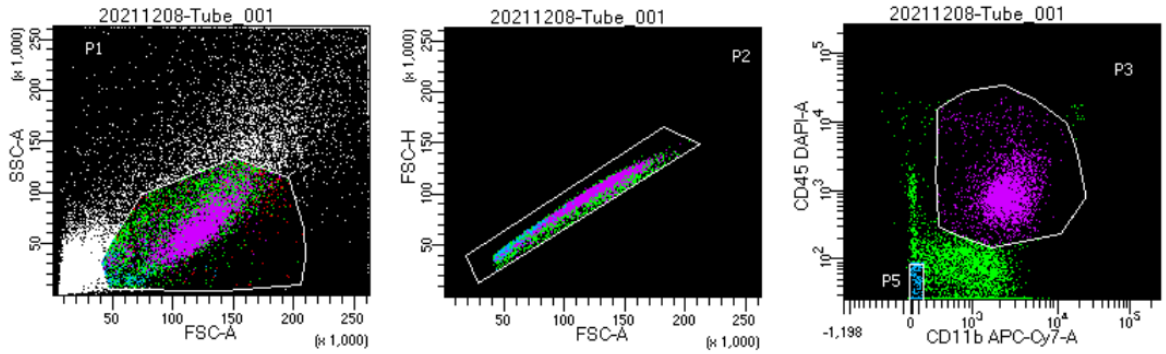

B)

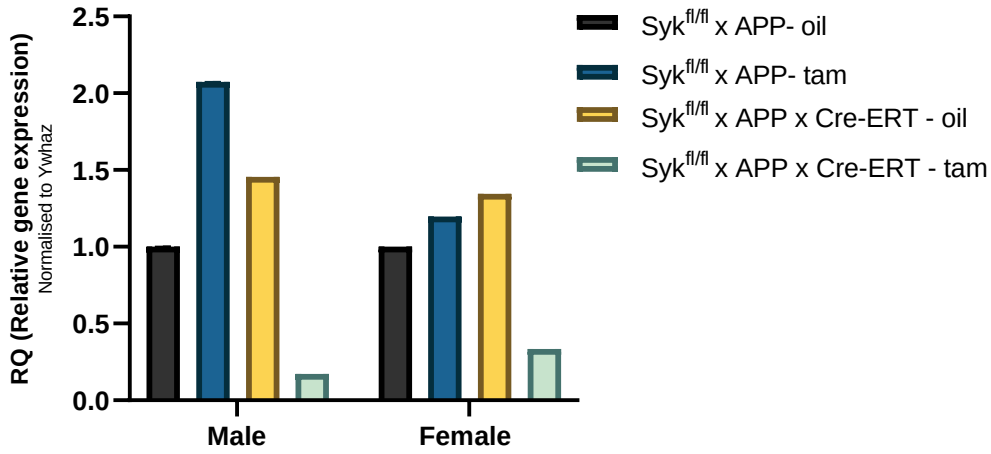

C)

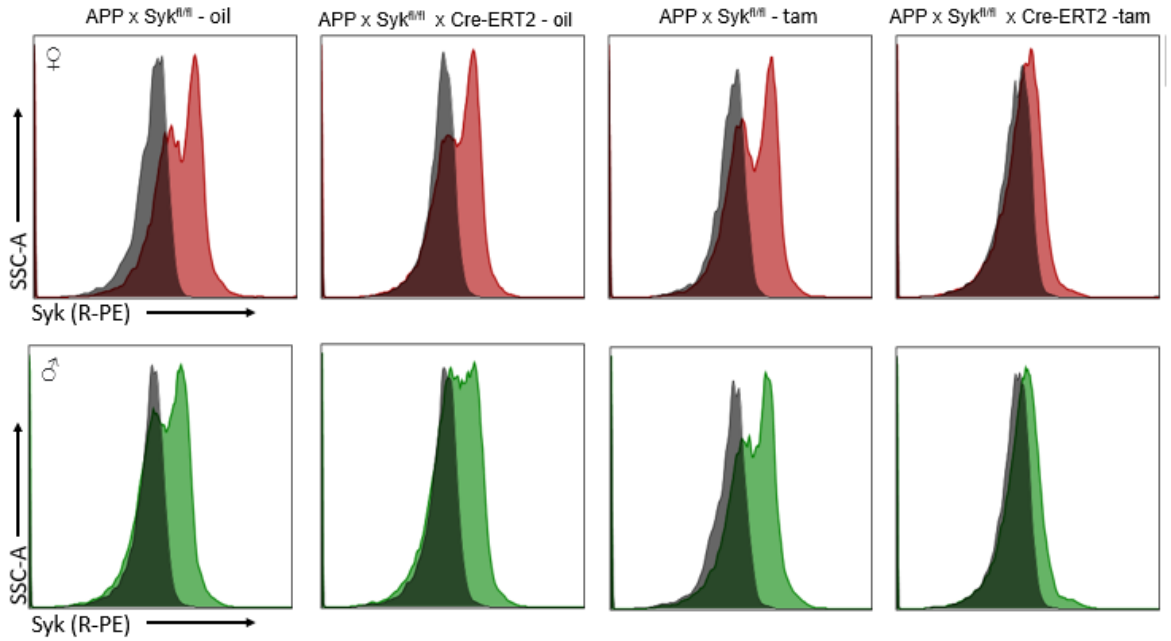

D)

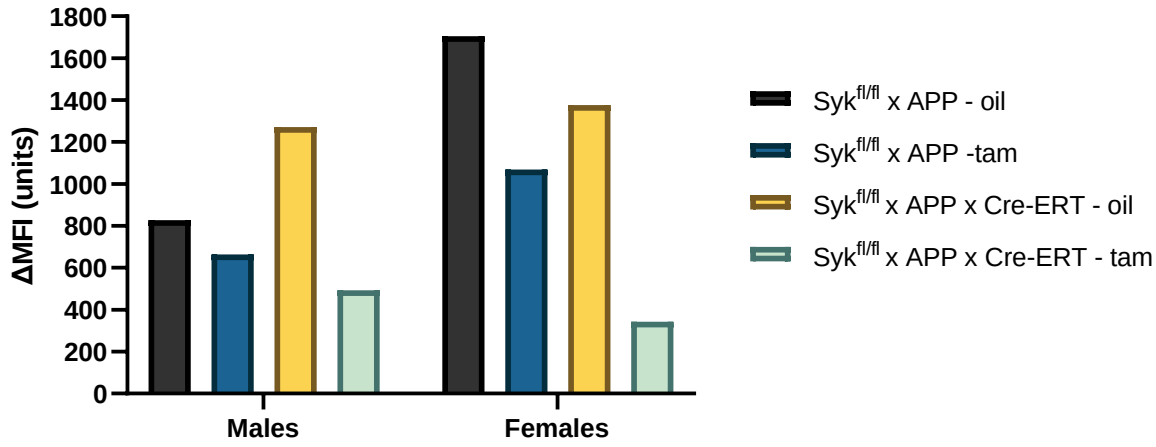

Figure 5.2: Validation of tamoxifen efficacy in APP^{NL-G-F} mice. (A) FACS gating strategy utilised to select microglia cells. Cell population was selected based on size, following which doublets were excluded. Microglia were selected specifically based on their CD11b^{+} and CD45^{+} expression. Cells which are CD11^{high} and CD45^{low} were sorted**. (B)** mRNA expression of *Syk* in microglia cells derived from animals treated with 100 mg/kg tamoxifen or oil controls for 3 consecutive days. Bars represent mean values (n=1 animal per group, 3 x technical replicate wells). **(C)** Flow cytometry histograms representing protein levels of SYK in microglia. The grey histograms show the isotype control and the coloured represent the SYK antibody staining. Top row of histograms indicates the female mice, whereas the bottom corresponds to the male. Above each histogram the corresponding genotype and treatment can be found. **(D)** Delta MFI levels of SYK in animals treated with tamoxifen or corn oil. Bars represent mean (n=1).

The data conclusively demonstrates that 100mg/kg tamoxifen induces significant decrease of *Syk* at mRNA level which does lead to reduced protein expression as well. No changes in expression are demonstrated in Syk x APP x Cre-ERT2 animals treated with corn oil which shows that no detectable Cre activity is present without stimulation. Based on these findings all further experiments were completed by administering tamoxifen alone and excluding corn oil control injections.

5.2.2 Estimating the optimal dose to achieve higher *Syk* cKO level

After the initial validation of the drug in this mouse strain, for all future experiments Syk x APP mice treated with 100mg/kg dose of tamoxifen delivered I.P. The initial pilot experiment demonstrated that 3 injections of tamoxifen deliver sufficient levels of mRNA reduction. However, to investigate if higher number of tamoxifen injections will deliver

more efficient cKO levels, another experiment was conducted. Syk x APP and Syk x APP x Cre-ERT2 male and female animals (n=1) were treated with either 3, 4 or 5 consecutive tamoxifen injections to compare the difference in *Syk* mRNA expression levels. The cohort was treated at 8 weeks of age and tissue was harvested 10 days following the last injection.

During the injection period animals' weight was monitored at 12-hour intervals to estimate if multiple doses of tamoxifen impact animal welfare differently. As seen by the weight changes shown in Figure 5.3A, both male and female mice tend to decline in weight during the first 2-3 days from the onset of injections. This result indicates that more than 3 doses of tamoxifen do not have additional impact on the weight changes in animals. What was observed showed that animals start to recover and even show increase in their weight by day 4 of the experiment. In addition, the welfare scores (Figure 5.3B) show that 4 and 5 injections were well tolerated in both sexes. It is important to point that we observed increase in provoked behavioural changes manifesting as anxiety and nervousness in the animals who received more than 3 doses of tamoxifen. This can be explained by the prolonged treatment period including more handling time and checks.

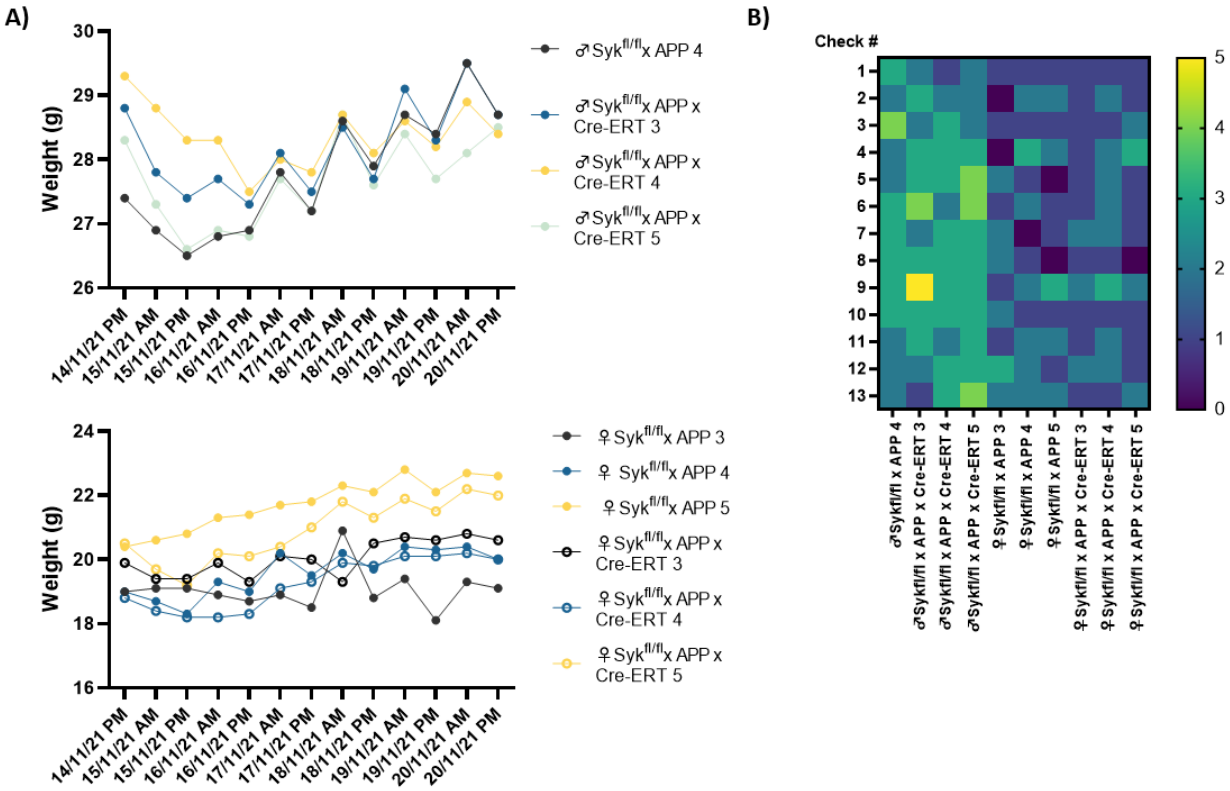

Figure 5.3: Tolerability of tamoxifen in APP^{NL-G-F} mice. (A) Chart with weight of mice during the experiment. The top graph shows the weight change in male mice (n=4). The bottom one represents

the weight in female mice (n=3 per genotype). All mice were weighed twice daily, AM and PM during injections days and followed for 2 days after the last injection. The figure legend indicates the number of injections received, shown by the number following the genotype. **(B)** Heatmap representing the welfare score based on individual check performed.

The results from the mRNA analysis of isolated microglia presented in Figure 5.4 show that receiving 5 consecutive tamoxifen injections leads to higher cKO levels compared to 3 consecutive injections overall. Figure 5.4A and B demonstrates the expression differences of *Syk* between the 3 different tamoxifen doses. Due to low mRNA levels, one of the female samples treated with 5 injections failed to amplify, therefore is missing from the analysis. In the male animals a very clear gradient between 3, 4 and 5 tamoxifen doses can be seen. Evaluating the overall percentage of cKO (Figure 5.4C) compared to 3 tamoxifen I.P injections (if considered at 100%) levels of further 70-80% reduction is present. Since the results in the male mice demonstrated conclusively that 5 I.P. injections achieve the highest cKO levels, while no adverse health effects were reported, it was decided that this protocol will be applied for all future experiments to achieve optimal cKO levels.

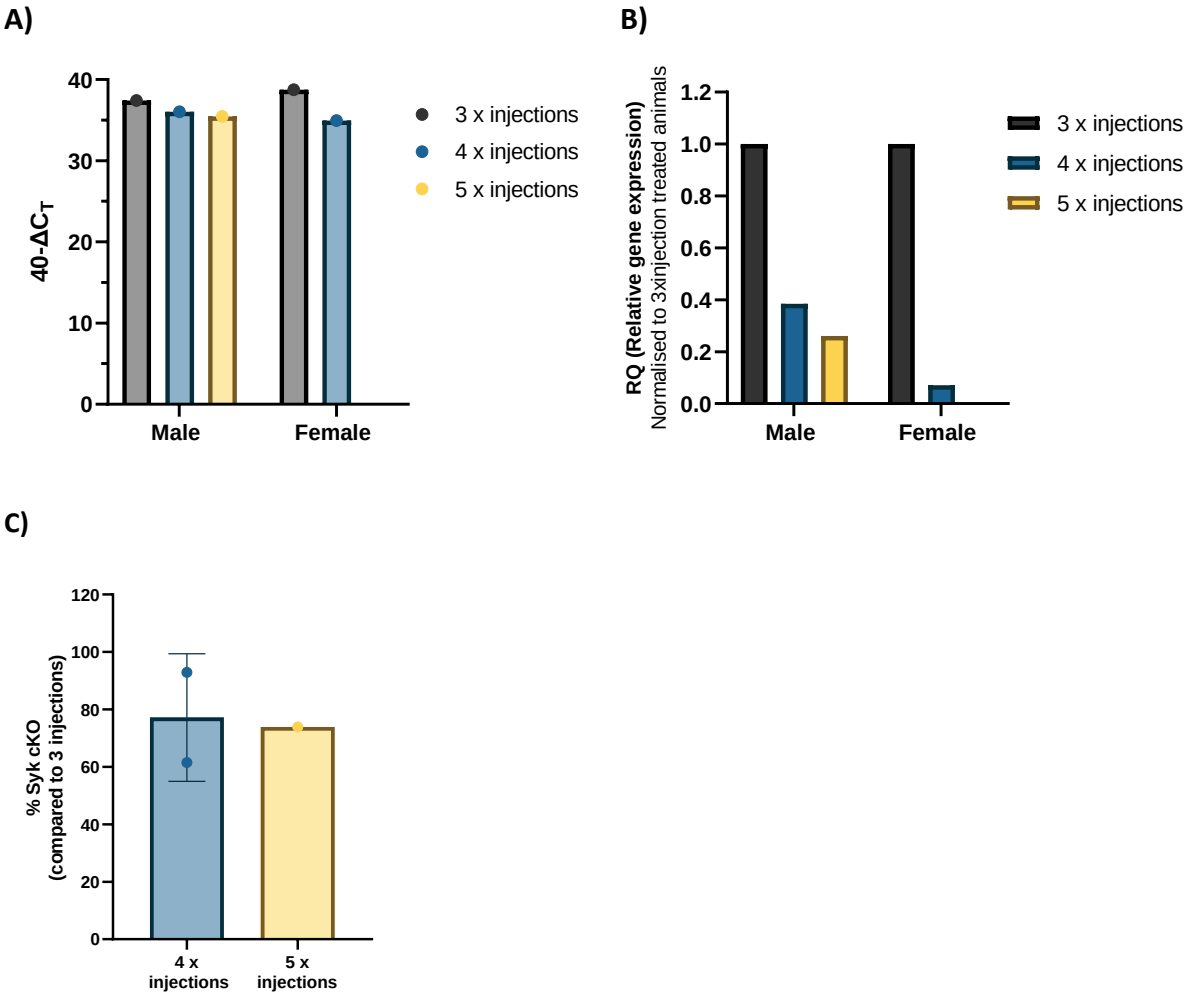

Figure 5.4: mRNA levels of Syk in mice treated with different tamoxifen doses. (A) 40-delta C_T values showing *Syk* mRNA expression between different tamoxifen doses. Bars represent mean values. **(B)** Relative gene expression normalised to animals treated with 3 doses of tamoxifen. **(C)** Overall percentage difference of *Syk* cKO levels in mice treated with 4 or 5 doses of 100mg/kg tamoxifen compared to reduction observed with 3 injections.

5.2.3 Tamoxifen induced *Syk* cKO lasts for at least 6 months

After establishing the appropriate dose of tamoxifen to achieve high and efficient cKO levels, the next aim was to validate the longevity and observe if the process is 'irreversible' in this strain. To complete this, Syk x APP and Syk x APP x Cre-ERT2 female mice (n=1) were utilised. Tamoxifen was delivered I.P. at 100mg/kg 5 consecutive days at different ages. The experimental design is outlined in Figure 58A. The cKO was induced at either 8 weeks or at 16 weeks, following which both groups of animals were aged until 25 weeks. Tamoxifen was well tolerated in both groups of mice long-term showing no additional behavioural changes

(Figure 5.5). No difference in the weight response to tamoxifen or other adverse effects were observed based on the age of induction.

Microglia cells were isolated from brain tissue as previously described and mRNA expression of *Syk* in microglia was analysed using qPCR. The results in Figure 5.6B demonstrate over 98% decrease in Syk expression at 25 weeks in both groups of animals. Interestingly, this treatment achieved higher cKO levels than in the previous experiments where tissue was harvested around 10 days following the last injection. This suggests that the induction of the Syk-cKO by the Cre-ERT2 is not reversible and longer period between induction and harvest might be recommended. In addition, it suggests that the microglia niche is not repopulated over this time either by turnover or recruitment of peripheral macrophages.

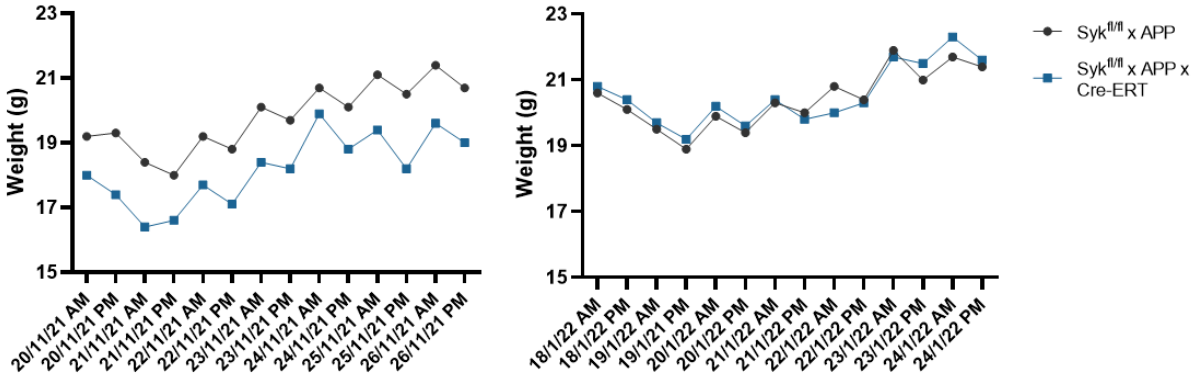

Figure 5.5: Weight changes in mice treated with tamoxifen at 8 weeks and 16 weeks. Both groups of animals received 5 consecutive tamoxifen 100mg/kg I.P. The plots represent the weight at each check (twice daily) for the duration of the experiment and two days following the last injection.

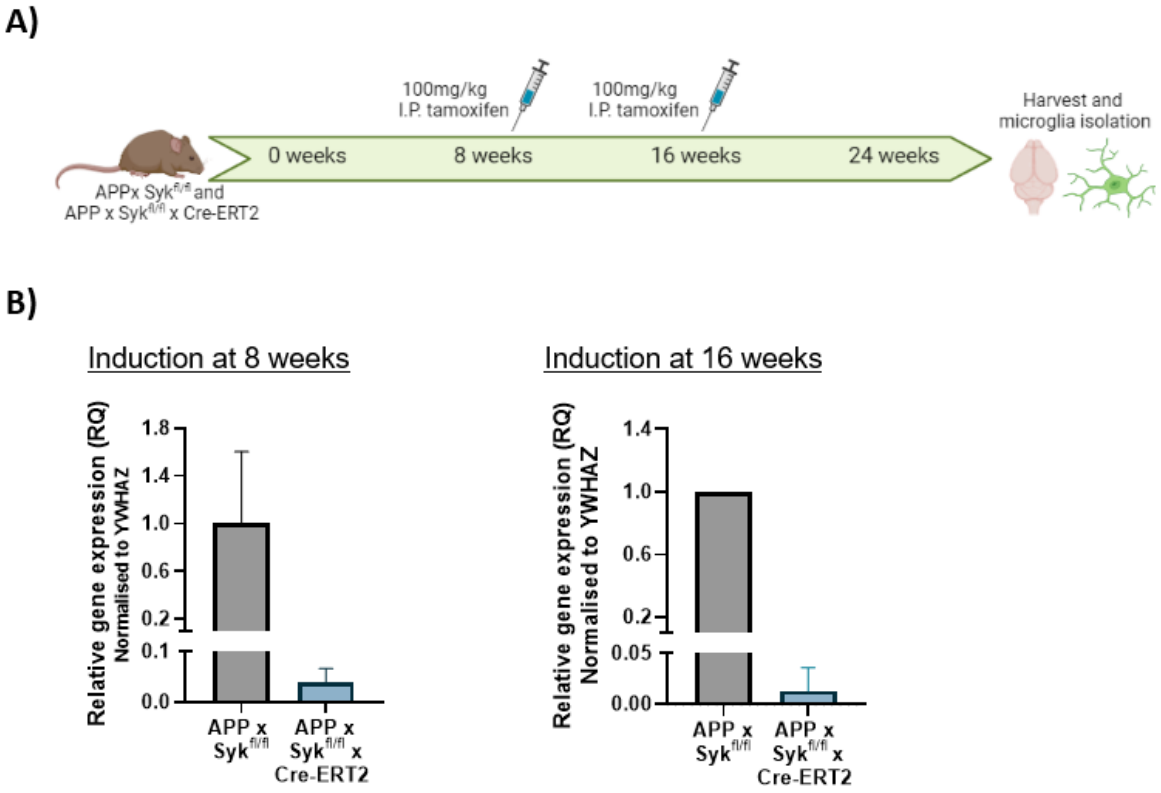

Figure 5.6: Validation of long-term cKO of Syk. (A) Experimental timeline. Two groups of animals were either treated with tamoxifen at 8-weeks of age or at 16-weeks of age and aged until 24-weeks. All tissue was harvested at 6-months. **(B)** *Syk* mRNA expression in microglia at 6 months derived from Syk x APP x Cre-ERT2 and Syk x APP control mice. Bars represent mean ± SEM (n=1 animal per group, 3 x technical replicate wells). YWHAZ was used as a reference gene control.

5.2.4 *Syk* cKO modulates the transcriptome of microglia early after induction

To better understand the role of *Syk* in microglia, transcriptomic analysis on a single-cell RNA level was performed. The first aim was to investigate the changes occurring short after induction of cKO by tamoxifen early in disease progression using 8-week-old mice. For the chosen AD model in this thesis, at 8-weeks early plaque formation is occurring but neither microgliosis or cognitive deficits are evident. Animals used in this experiment were treated 5 times I.P. with tamoxifen and sacrificed 10 days later when they were around 10 weeks old. Syk x APP and Syk x APP x Cre-ERT2 mice (n=3 males per group) which were cohoused from 21 days old were utilised for this experiment.

Microglia were isolated as previously described and processed using the iCell8 (Takara) platform. Cells were loaded on a chip, followed by library preparation and sequencing (Table

1). The generated library was quantified and subjected to quality control checks. The purified library was run on a bioanalyzer, and the trace generated by the library can be seen in Figure 5.7. This demonstrates the distribution of the library and the average fragment size. In the case of the generated library here, we can see that it is skewered towards smaller fragments with a bigger peak in the left corner of the histogram. However, the library was considered satisfactory based on the distribution and the average fragment size and was taken forward for sequencing.

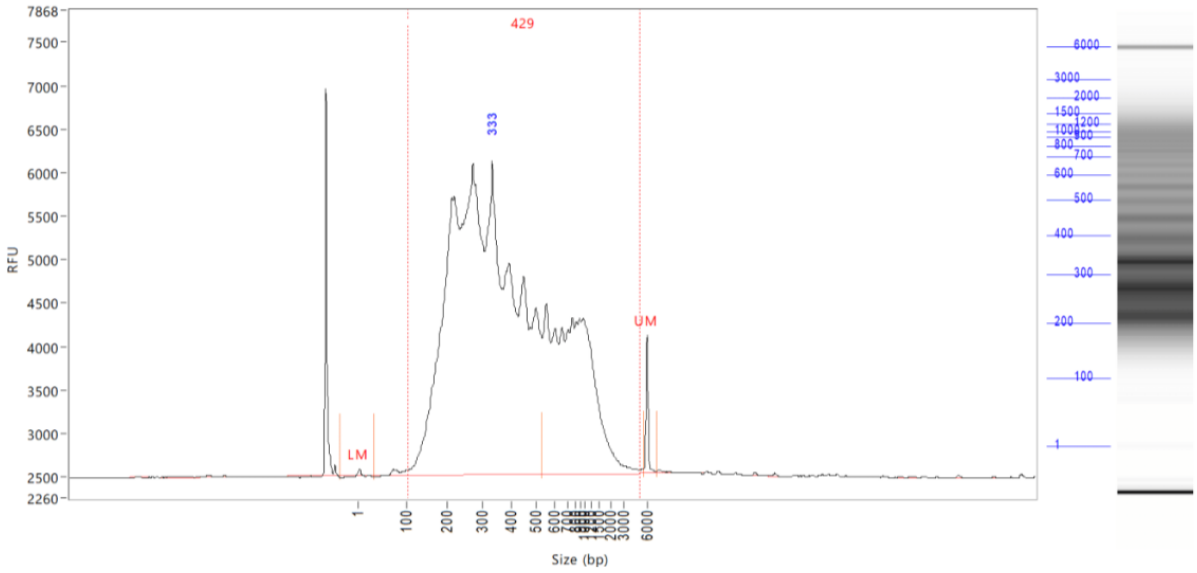

Figure 5.7: Bioanalyzer trace of generated and purified library. The newly created library was run on a bioanalyzer using 0.5µg/µL based on Qbit measurements. Smear analysis was performed between 100 and 5000bp indicated by the dotted lines. The average fragment size displayed at the top was determined to be 429bp. On the right-hand side, the ladder identifies different fragment sizes.

Following sequencing, the data was demultiplexed and analysed (details in Methods). An overall distribution of the library showing the number of reads for each candidate is presented in Figure 5.8. This demonstrates that for majority of the identified candidates over 10,000 gene reads are detected which illustrates the sensitivity and depth of the method. Clearly, 2 samples exhibit a large proportion of cells with very low or no detected reads. Additionally, although the distribution of the positive control is wide, the RNA utilised and provided from the supplier is human cell line derived, therefore is not completely representative of the samples used in this experiment.

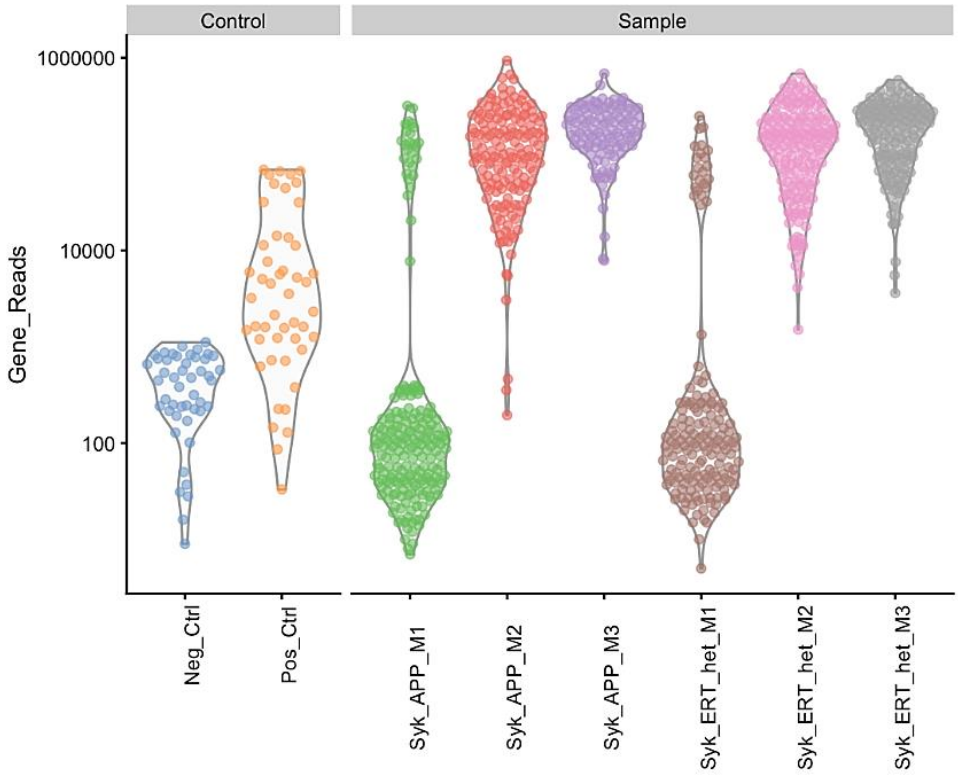

Figure 5.8: Sequencing library. The graph outlines the 6 samples and 2 controls and shows the gene read distribution. The negative control shows low reads as predicted. The positive control which is derived from a cell line shows a higher range in distribution. From the experimental group, there are 2 samples which present with low amount of reads in many of the candidate cells. The rest of the samples have over 1000 reads in majority of candidates.

Initially the data was assessed via quality control steps based on different inclusion criteria. Mitochondrial and ribosomal genes are a reliable indicator of cell health. A high percentage of mitochondrial gene expression indicates that cell is dead or dying. In 2 of the samples, high number of mitochondrial and ribosomal gene expression was identified, indicating for poor quality of the cells in these samples (Figure 5.9A and B). This can potentially be explained by some issues with the processing of these samples which may have caused high cell death at the time of loading. Therefore, these 2 samples, one experimental (Syk x APP x Cre-ERT2) and one control (Syk x APP), were removed from the subsequent analysis of the data to avoid bias. Exclusion of the cells expressing high mitochondrial genes was applied, however because of the overall low read umber detected in the samples, it was decided it was better to exclude the whole population because very few cells could be used for subsequent analysis.

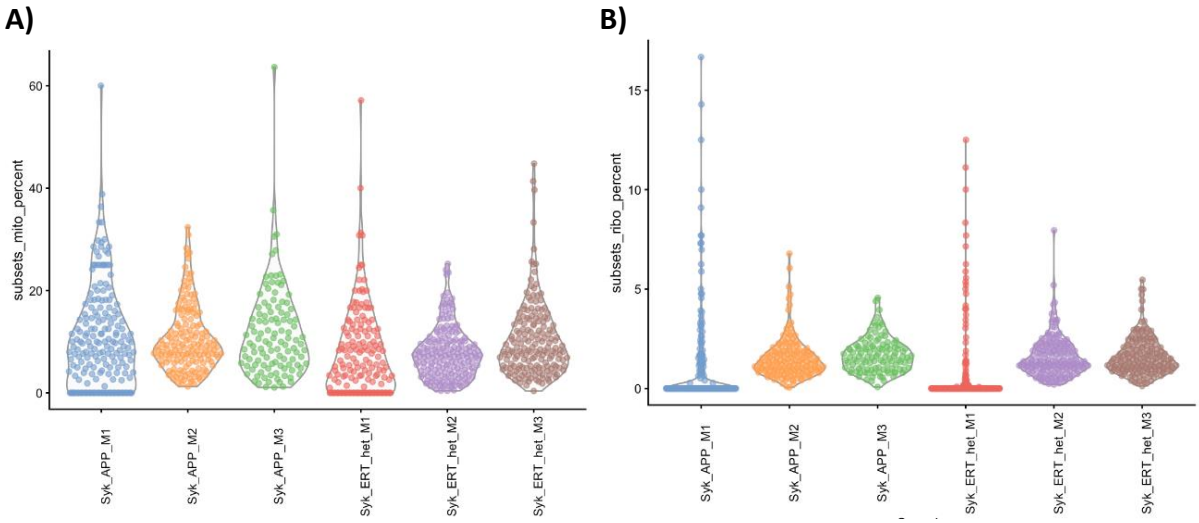

Figure 5.9: Quality control of ScRNA-sequencing library. (A) Expression of mitochondrial genes detected in all samples, 3 controls and 3 experimental. Samples 1 and 4 show altered distribution with higher proportion of cells expressing over 20% mitochondrial genes. **(B)** Expression of ribosomal genes detected in samples from the sequencing library. Samples 1 and 4 demonstrate very low number of reads and contain some candidate cells where over 10% ribosomal genes are detected.

The remaining results were derived from experimental (n=2) and control (n=2) animals. After exclusion of poor-quality cells, principal component analysis (PCA) was performed to investigate any variation observed between the samples. From the PC plot on Figure 5.10 there is a clear split between experimental and control samples based on PC2. This suggests that the second largest source of variation in the dataset is the genotype of the samples. Additionally, some separation is also seen based on PC1, however it is less clear what this variation is due to. The first two principal components account for only ~3% of the total variance between cells. The analysis was followed by pseudo bulk of samples according to genotype and completing differential expression analysis using the DeSeq2 package since individual cells are not independent biological replicates.

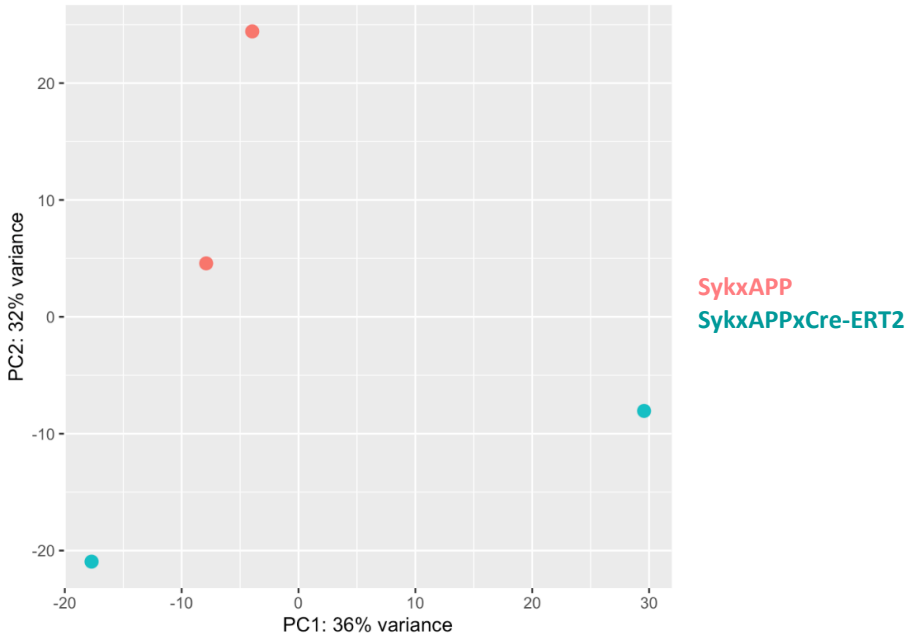

Figure 5.10: Principal component (PC) analysis of samples from the sequencing library. The plot identifies the top 2 principal components and the variance in them (%). Each dot represents an individual sample.

The differential expression analysis revealed 626 differentially expressed genes (DEGs) compared to controls (significance at log2 fold change >1). Overall, there is higher proportion of upregulated than downregulated genes (Figure 5.11). A comprehensive list of all DEGs can be found in the Appendix with corresponding p-values and log2 fold change difference.

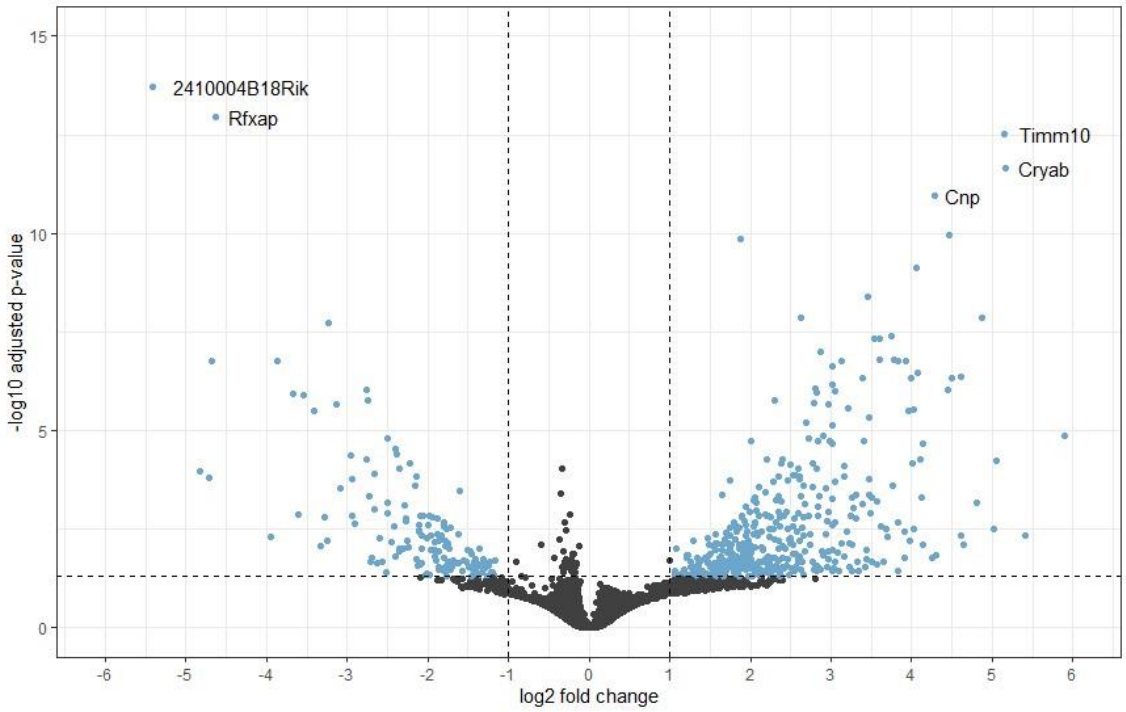

Figure 5.11: Volcano plot of differentially expressed genes detected in Syk-APP mice compared to Syk-APP-Cre mice. The blue dots represent genes which pass the significance threshold based on adjusted p-value and on log2 fold change (>1). Left side of the plot indicates downregulated genes, whereas right side of the plot indicates increase in expression. The top 5 genes based on p-value significance are labelled on the plot.

The top 20 genes by either p-value or log2 fold change are plotted in Figure 5.12. Interestingly the most significant genes based on p-value are mostly upregulated in the Syk x APP x Cre-ERT2 animals. However, when log2 fold change values are observed it appears that the biggest changes are observed in downregulated genes.

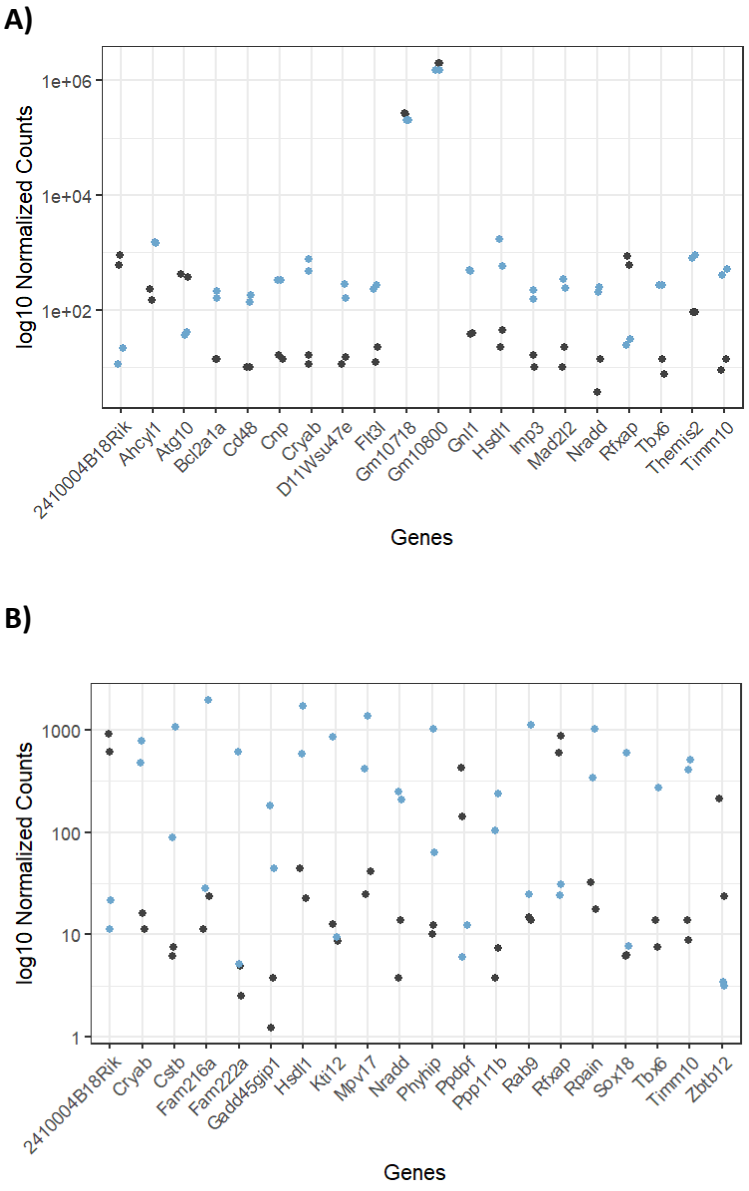

Figure 5.12: Summary of differentially expressed genes identified between Syk cKO mice and control. (A) Top 20 differentially expressed genes based on p-value (adjusted). **(B)** Top 20 differentially expressed genes based on log2 fold change. Analysis completed using DESeq2. Dark grey dots represent Syk x APP samples, blue dots represent Syk x APP x Cre-ERT samples.

Additionally, the distribution of different microglia subpopulations and clusters was evaluated. Figure 5.13A presents the UMAP plots identifying individual clusters and the distribution of microglia subpopulation according to cluster. A total of 4 clusters were identified and based on expression of marker genes they were annotated as homeostatic, transitioning, cycling and proliferating and MHC high. The diagram in Figure 5.13B demonstrates the proportion between different microglia subtypes identified in the

sequenced samples. Overall, this demonstrates that majority of sequenced microglia are homeostatic (>60%) with only small proportion of cells showing markers linked to other clusters. This also means that the results presented further in the chapter are obtained mostly from cells not yet impacted significantly by the amyloid pathology and the associated transcriptomic signature.

A)

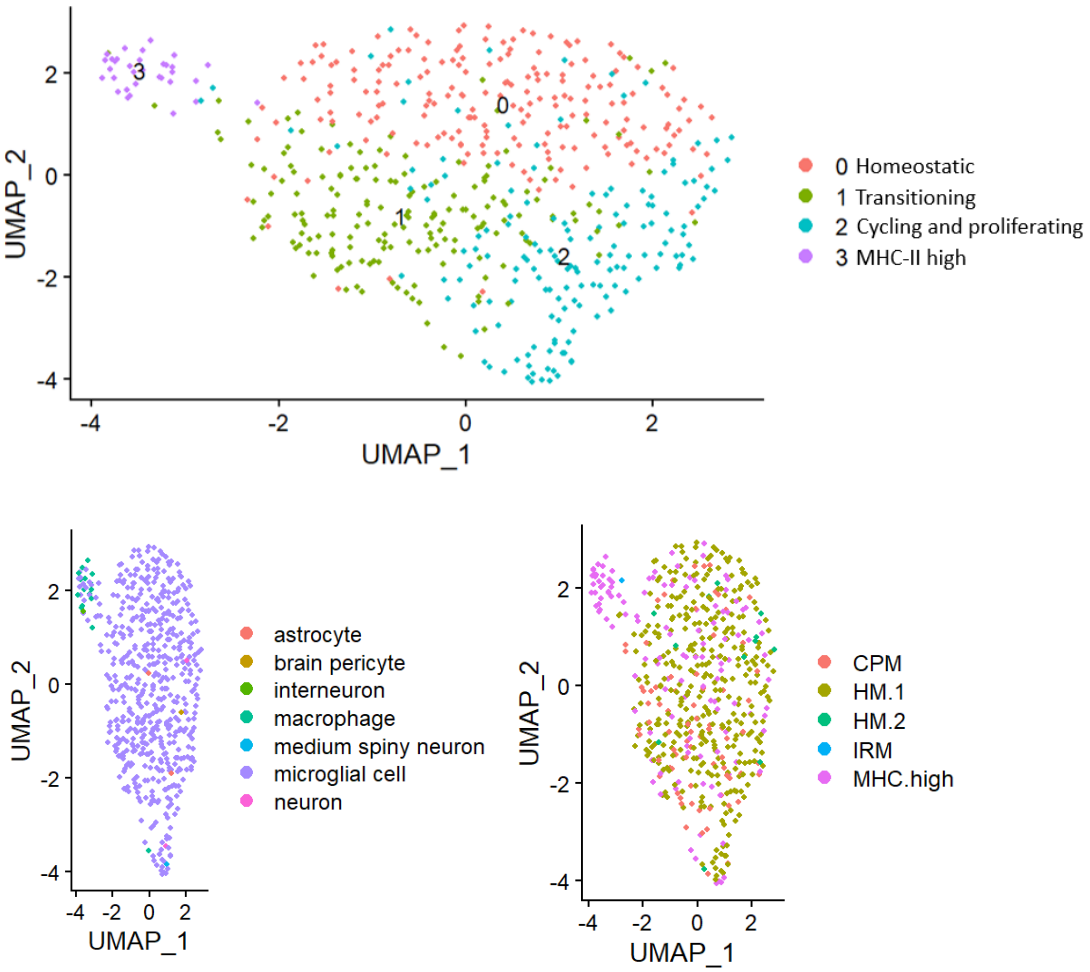

B)

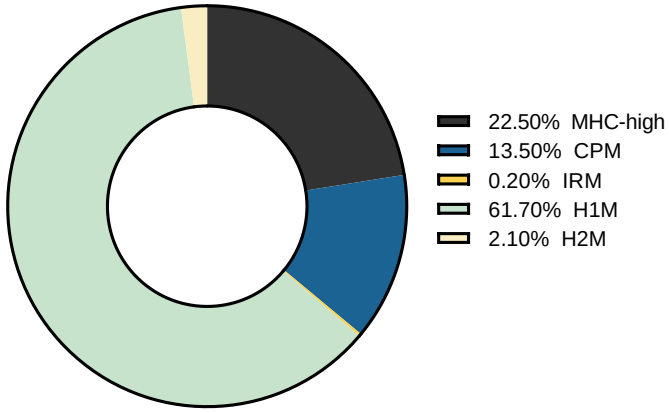

Figure 5.13: Distribution of microglia subpopulations in sequenced cells. (A) Uniform Manifold Approximation and Projection (UMAP) plot visualising sequenced microglia cells. Cells are coloured according to cluster identified using Seurat's k-nearest neighbours (kNN) approach. Microglia subpopulations are then defined using singleR. Based on marker expression microglia clusters (0-3) were labelled. A UMAP identifies the cell types in each cluster. **(B)** The overall percentage of each microglia subpopulation is identified in the figure legend. The microglia subsets are as following: homeostatic microglia 1 (HM1), homeostatic microglia 2 (HM2), cycling and proliferating microglia (CPM), MHC high microglia and interferon response microglia (IRM). Microglia cluster populations mapped to Sierksma *et al*. (336).

The identified DE genes were analysed using gene ontology (GO) terms. Figure 5.14 presents the top identified cellular components and biological processes identified. The generated list of differentially expressed genes was further used to complete more in-depth pathway analysis and gene ontology enrichment using the Qiagen IPA platform. First, the genes were compared to a list of already available canonical pathways and based on candidate overlap potential pathways where these molecules could be involved are generated. All identified significant canonical pathways can be seen in Figure 5.15A. From the graph it is apparent that there are activated (orange), inhibited (blue) or not impacted (white) pathways as well as pathways whose direction of response is unclear (grey). Overall, some of the top identified pathways are linked to cellular metabolism and regulation of important metabolic pathways such as oxidative phosphorylation. Additionally, Figure 5.15B identifies some of the link between the top 10 pathways and highlights how many of the candidate genes are shared between these pathways. This further highlights that metabolic and biosynthetic processes are affected, as well as the overlap in identified genes which contribute to each

pathway. For example, the response seen in one pathway such as the Sitruin will be linked to some of the other identified pathways and the direction in which they are regulated.

A)

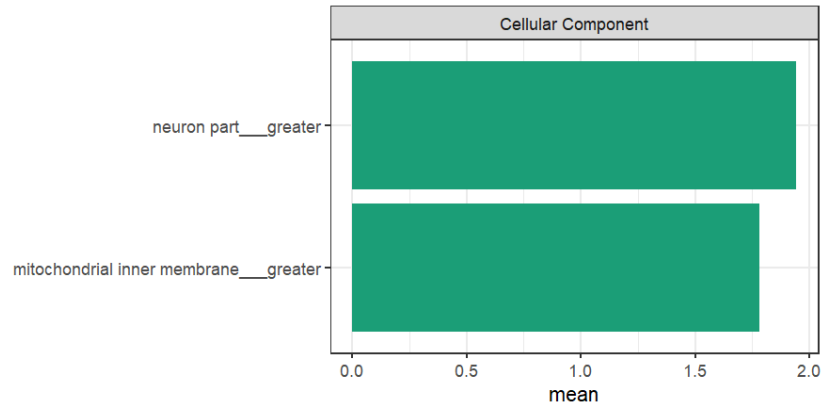

B)

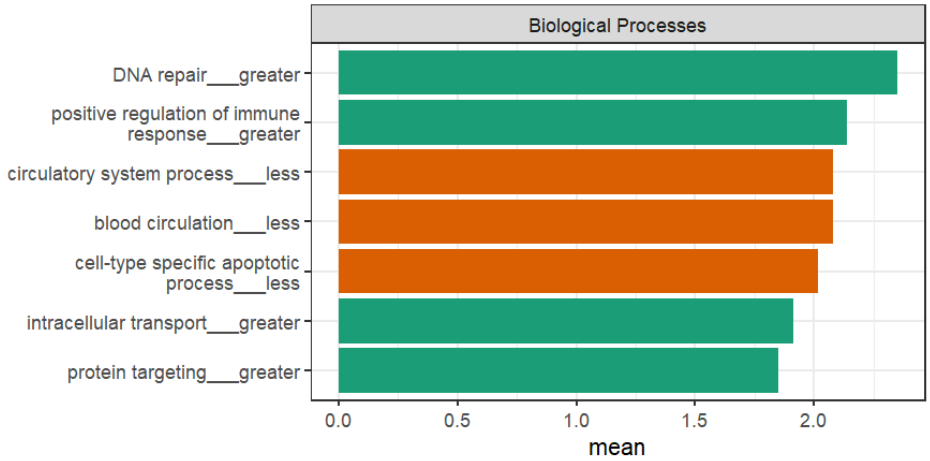

Figure 5.14: Gene ontology (GO) analysis of identified DE genes. (A) Top 10 significant cellular component (cc) pathways identified. **(B)** Top 10 significant biological processes (bp) identified. Green colour indicates increase, whereas orange represents decrease.

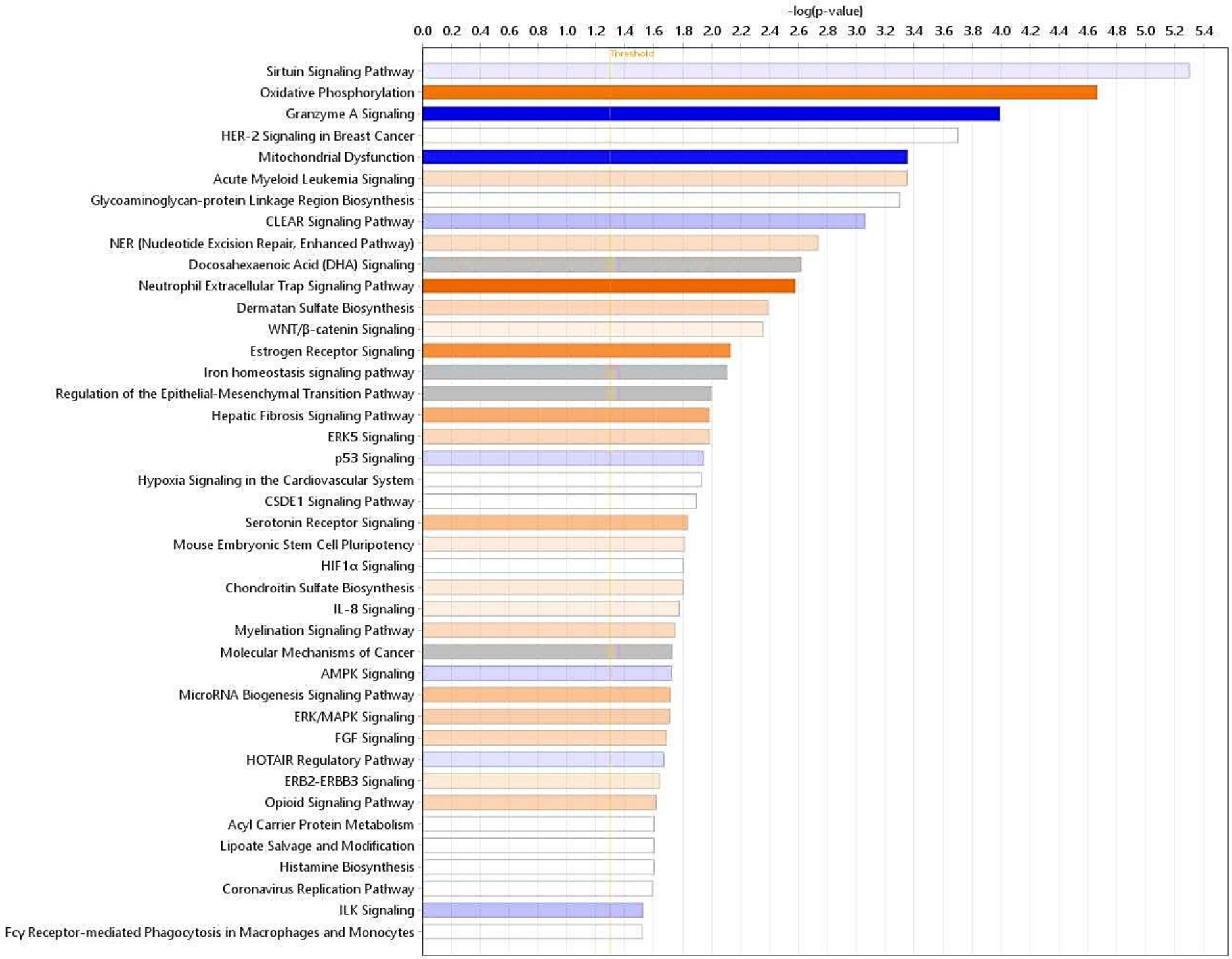
-log(p-value)
0.0 0.2 0.4 0.6 0.8 1.0 1.2 1.4 1.6 1.8 2.0 2.2 2.4 2.6 2.8 3.0 3.2 3.4 3.6 3.8 4.0 4.2 4.4 4.6 4.8 5.0 5.2 5.4
Threshold
Sirtuin Signaling Pathway
Oxidative Phosphorylation
Granzyme A Signaling
HER-2 Signaling in Breast Cancer
Mitochondrial Dysfunction
Acute Myeloid Leukemia Signaling
Glycoaminoglycan-protein Linkage Region Biosynthesis
CLEAR Signaling Pathway
NER (Nucleotide Excision Repair, Enhanced Pathway)
Docosahexaenoic Acid (DHA) Signaling
Neutrophil Extracellular Trap Signaling Pathway
Dermatan Sulfate Biosynthesis
WNT/β-catenin Signaling
Estrogen Receptor Signaling
Iron homeostasis signaling pathway
Regulation of the Epithelial-Mesenchymal Transition Pathway
Hepatic Fibrosis Signaling Pathway
ERK5 Signaling
p53 Signaling
Hypoxia Signaling in the Cardiovascular System
CSDE1 Signaling Pathway
Serotonin Receptor Signaling
Mouse Embryonic Stem Cell Pluripotency
HIF1α Signaling
Chondroitin Sulfate Biosynthesis
IL-8 Signaling
Myelination Signaling Pathway
Molecular Mechanisms of Cancer
AMPK Signaling
MicroRNA Biogenesis Signaling Pathway
ERK/MAPK Signaling
FGF Signaling
HOTAIR Regulatory Pathway
ERB2-ERBB3 Signaling
Opioid Signaling Pathway
Acyl Carrier Protein Metabolism
Lipoate Salvage and Modification
Histamine Biosynthesis
Coronavirus Replication Pathway
ILK Signaling
Fcγ Receptor-mediated Phagocytosis in Macrophages and Monocytes

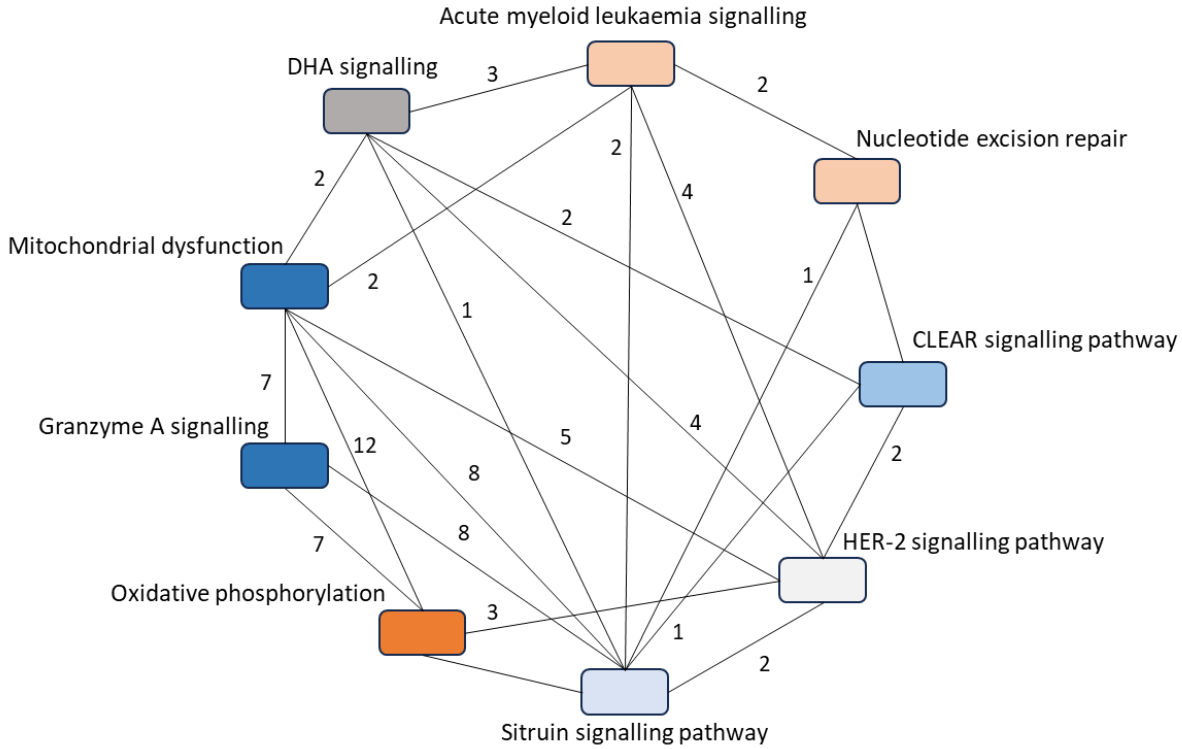

Figure 5.15: Pathway analysis of differentially expressed genes using IPA. (A) Identified significant canonical pathways. Qiagen IPA was used to generate a list of pathways regulated by the identified DEGs. The orange colour indicates activation, the blue represents inhibition, grey identifies unknown direction and white represents no change (z-score). The intensity of the colour corresponds to the number of targets in the DEG list overlapping with the canonical pathway. The p-value significance threshold is marked by the orange line ($p<0.05$). Analysed by Fisher's Exact test. **(B)** Causal link between the top 10 significant pathways. The numbers between each node identify the number of shared genes from the DEG list. Colours are as above.

More detailed analysis using the IPA software reveals a list of upstream regulators which might control the identified pathways and the direction in which they are modulated. The top regulatory molecules which are either upregulated or downregulated are summarised in Table 5.1. These regulators further highlight how the effects of *Syk* cKO can be manipulated and what associated molecules are involved. Interestingly a lot of the identified targets are transcription factors. In addition, the network of genes controlled by some of these upstream regulatory molecules can be explored. This reveals the connection each regulatory molecule has to the identified DEGs as well as other molecules which are likely to be linked and the predicted direction they will be affected. Overall, this highlights that Syk cKO can modify the inflammatory response through regulation of different transcription factors which in turn lead to induction of inflammatory responses. Additionally, this highlights that although *Syk* is not an identified genetic risk factor, its interaction with known AD risk genes can be particularly important.

Although the interaction network for each identified upstream regulator (761 total) cannot be displayed here, some highly significant and important targets are outlined in Figure 5.16. This demonstrates the downstream network of genes linked to each upstream regulator. The direction of the interaction and the state of the downstream molecule is predicted.

Table 5.1: Top upstream regulators with predicted direction identified by IPA.

Upstream regulator	Predicted direction	Function	z-score	p-value
XBP1	**Activated**	Transcription factor	2.186	0.00000229
LPS		Chemical drug	2.06	0.0000257
TCF4		Transcription factor	3.385	0.0000891
TFRC		Transporter	3.317	0.000174
TEAD1		Transcription factor	3.051	0.000182
HDL	**Inhibited**	Complex	-2.2	0.0106
CPT1B		Enzyme	-2.538	0.0159
TOX		Transcription factor	-2.219	0.0233
Phenylephrine		Chemical drug	-2.433	0.0282
EGLN		Group	-2.392	0.0445

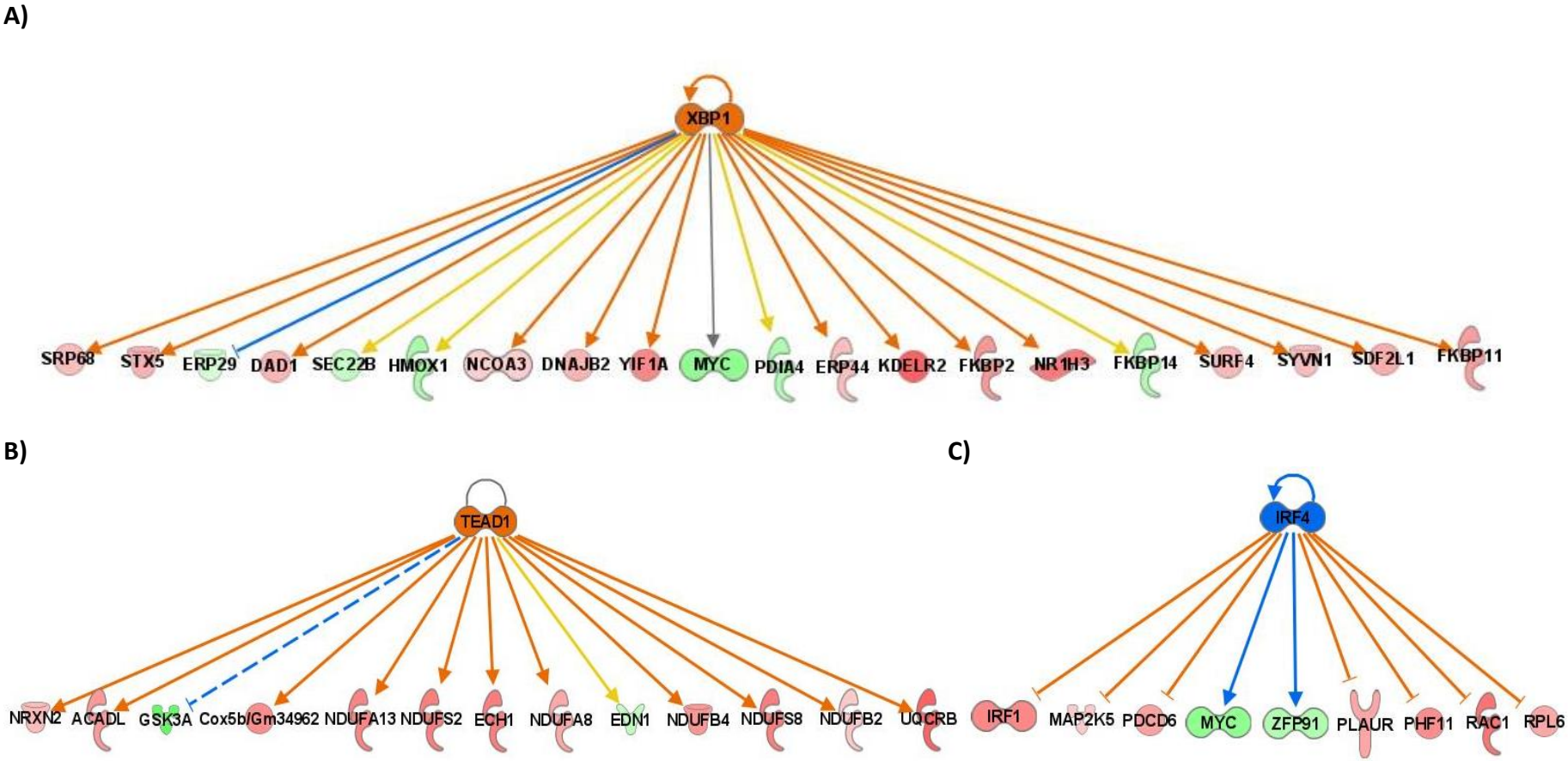

Figure 5.16: Interaction network associated with upstream regulatory molecules. (A) Predicted interaction network of XBP1, identified upstream regulator. **(B)** Predicted interaction network of TEAD1, upstream activated regulator. **(C)** Interaction network associated with predicted inhibited upstream regulator IRF4.Green colour represents downregulation in dataset, whereas red is upregulation of the target. Orange indicates predicted activation, blue predicts inhibition. The intensity of the colour indicates the strength of the change. Orange arrows indicate activation, blue inhibition, grey unpredicted

effect and yellow incompatibility based on the state of the upstream signal. Solid lines show direct interaction, whereas dashed identifies indirect link between the molecules.

5.2.5 Fixative impact on gene expression

Firstly, based on Figure 5.17 which represents a microglia sample during FACS sorting prior to loading on the iCell8 chip, 3 distinct live/dead populations can be identified using PI staining. Cells were stained with PI prior to methanol fixation (detailed protocol can be found in Methods). This clearly shows that most likely the fixation has impacted the cell membrane, which in turn impacts the autofluorescence levels detected. All the processed samples were counted prior to methanol fixation and demonstrated high viability and presence of only 2 populations eliminating anything related to the earlier processing stages. Additionally, the higher expressing PI population, but still showing values $<10^3$ seem to be corresponding to live cells based on the FSC and SSC distribution. This population also has a lot higher CD11b signal compared to what is detected in the lowest PI negative cells. Analysis of the sequenced data revealed that *Syk* expression cannot be detected or is low in all the samples, including controls. This effect was attributed to the use of methanol as a fixative and to check that other sequencing data available in the lab was also used. As seen in Figure 5.19 (data kindly provided by Dr Ruth Jones) different fixatives can impact the ability to detect certain genes and *Syk* expression specifically is very much impacted by methanol fixation. Compared to fresh and glyoxal treated cells, in the methanol sample very few cells have detectable *Syk* and most of these show high levels of expression.

Overall, the inability to detect *Syk* expression in majority of the samples possesses a certain experimental limitation, not allowing for bioinformatic validation of the cKO and comparison between cells potentially expressing different levels of *Syk*. As seen from Figure 5.17, some cells derived from Syk x APP x Cre-ERT2 still demonstrate moderate *Syk* levels although the proportion of these from the whole population would be very low.

Alternatively, other fixation methods might be required to detect *Syk* expression and might be more beneficial for these samples.

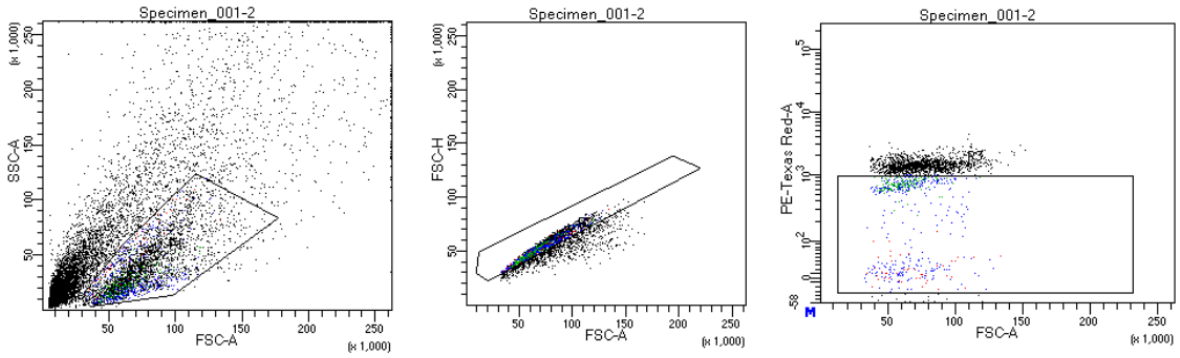

Figure 5.17: Representative gating used for FACS sorting of microglia for transcriptomic analysis. The first two gates represent the cell population and identify how doublets were excluded. Gate 3 shows the live/dead stain, in this case cells were treated with propidium iodide before fixation. The dot plot represents 3 distinct cell populations and identifies the gate from which cells were collected.

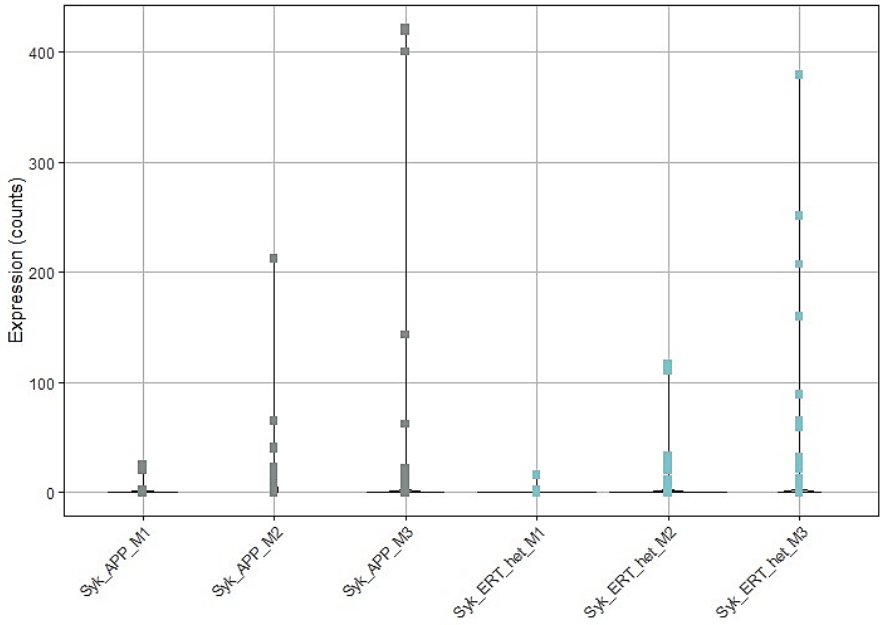

Figure 5.18: Syk expression in samples from the sequencing library. The plot demonstrates that expression of *Syk* (counts) is detected in very few of the cells from the generated library. Very few cells exhibit high levels of detectable *Syk* irrespective of the genotype.

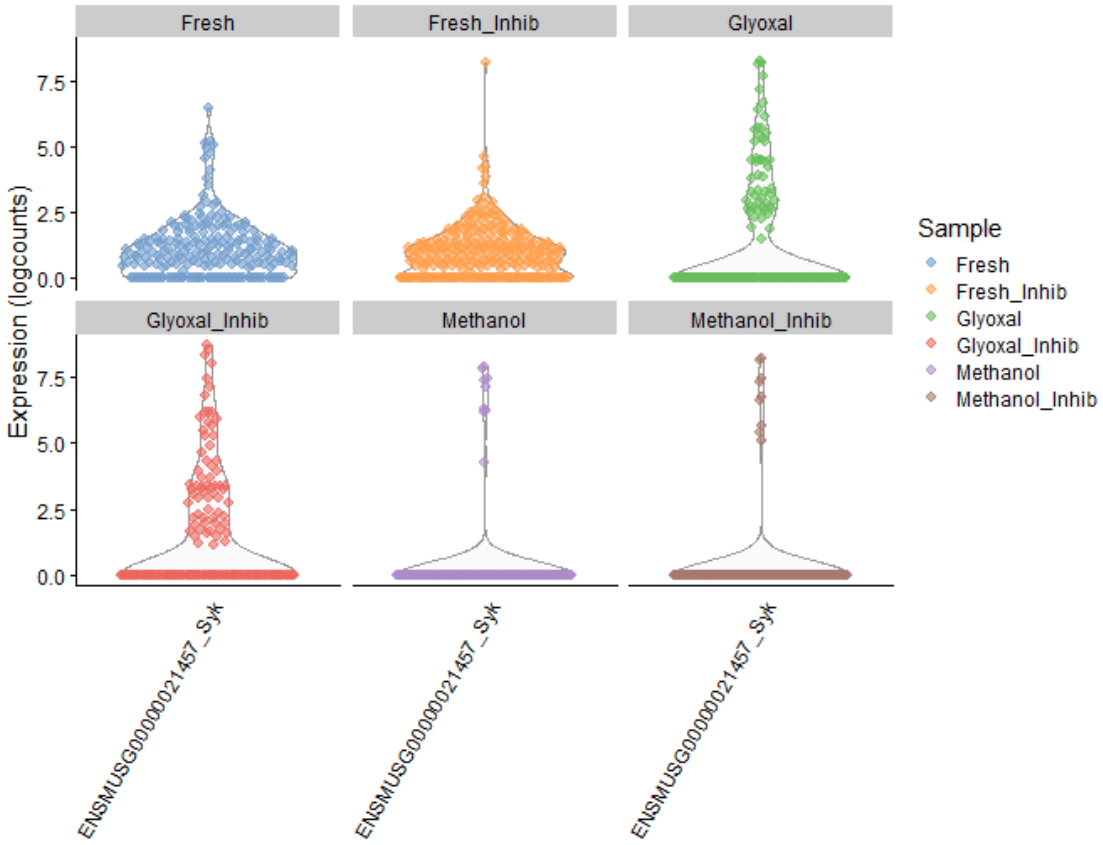

Figure 5.19: Expression of Syk in microglia from different fixation method. The graph shows expression levels of *Syk* in 6 different microglia samples which differ in the fixation method of the cells. The dot plots reveal that there are obvious differences between the way the sample was prepared. Fresh microglia exhibit large population of cells which have low to medium *Syk* expression. In contrast, glyoxal fixed samples demonstrate higher *Syk* expression. Lastly, methanol fixed cells show very few cells where expression is detected at all. Cells were further split into two groups, untreated or treated with RNA inhibitors during processing of the samples. Data provided by Dr Ruth Jones.

To ensure that *Syk* expression was reduced in the sequencing samples, mRNA from the remaining samples was extracted from the remainder of the FACS samples. The qPCR results demonstrated that *Syk* expression is significantly lower compared to controls in these samples (data not shown). The remaining cells are part of the sample subjected to FACS sorting therefore will contain a variety of cell types apart from microglia but still provide a useful validation for the *Syk* expression level, especially since *Syk* is primarily expressed on microglia within the CNS.

5.2.6 Validation of single cell RNA-sequencing

To validate the results observed from ScRNA-sequencing an independent cohort of samples was examined. Both male and female (n=3) mice at 8 weeks were treated with tamoxifen as previously described. Syk x APP mice were used as controls. Animals were harvested 10 days after the last injection and processed using the same protocol as for the iCell8 experiment. After FACS sorting cell pellets were lysed for RNA. The RNA was processed, and qPCR was performed to evaluate the expression of some candidate genes. Some of the top 5 up-regulated and down-regulated targets based on fold-change difference were selected to be examined.

First, *Syk* mRNA expression was evaluated to confirm the reproducibility of the model and validate the samples. The results on Figure 5.20 clearly show that *Syk* expression is significantly reduced in animals treated with tamoxifen irrespective of sex. This result demonstrates that what the pilot experiments showed is reproducible and consistent through different cohorts. Additionally, high variability was observed between individual animals which diminishes the overall response. Two upregulated (*Cstb* and *Fam222a*) and two downregulated (*Rxfap* and *Gdp1*) were examined. Overall, the trend in all samples is as predicted from the ScRNA-sequencing experiment although not significant with all selected genes. The reported gene expression changes are only around 2-3-fold in comparison to control samples. Male and female animals show a similar response which further validates the results and indicates there are no significant changes in the response of male and female mice in respect to these target genes. The expression differences seen here are very mild compared to what is reported on single cell level, however this is expected since these technologies allow more depth and precision. This highlights the benefit of ScRNA-sequencing and the importance of identifying subtle transcriptional changes which might not be detectable with other methods. Additionally, examining wider variety of identified DEGs and also genes with endogenous high microglia expression might be more favourable to detect differences via qPCR analysis. The selected genes here were picked based on their fold expression, however their expression detected in microglia overall is relatively low.

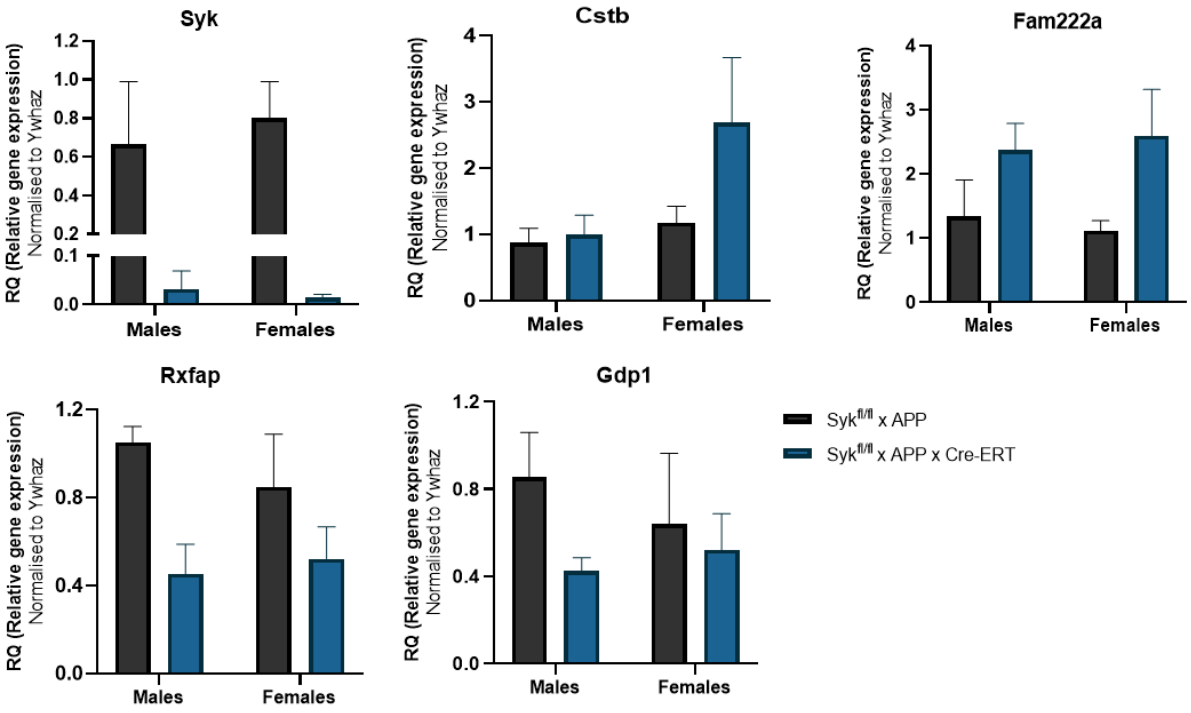

Figure 5.20: mRNA of various DEGs identified by ScRNA-sequencing in mouse microglia. Syk x APP and Syk x APP x Cre-ERT2 animals were treated with 100mg/kg I.P tamoxifen 5 times. Microglia were isolated 10 days following tamoxifen treatment and qPCR analysis was performed to evaluate *Syk, Cstb, Fam222a, Rxfap* and *Gdp1* expression. Each bar represents mean ± SD (n=3 animals per genotype per sex).

5.3 Discussion

5.3.1 Summary of main findings

In this chapter a conditional knock-out model of *Syk* in the APP^{NL-G-F} mouse model of AD was utilised to explore the role of *Syk* in microglia cells. We used an inducible Cre-ERT2 system to produce gene knock-out in these animals and to validate this approach in the APP^{NL-G-F} mice. The results conclusively demonstrate that tamoxifen used intraperitoneally can successfully induce significant and long-lasting *Syk* knock-out model. In addition, the RNA-sequencing work provides some useful insight into the role of *Syk* early in pathology and demonstrates some of the initial changes which cells undergo following *Syk* cKO.

The presented data clearly demonstrates that tamoxifen is effective in generating cKO of *Syk* in microglia. The majority of animals used in this chapter were treated at 8 weeks, therefore we cannot draw conclusions about the safety of tamoxifen in younger animals. The reduction in mRNA levels proved to be rapid, only 10 days after injection, over 80% KO is reported. These findings are translated to reduction in protein level as well. In addition, aging animals for longer showed that even higher levels of KO can be achieved, and it might be beneficial to allow longer periods of time between tamoxifen administration and harvest to allow KO levels to reach optimum capacity. In addition, comparing mice treated at 8 weeks versus 16 weeks, no significant differences in the mRNA levels were reported, therefore treating older animals produces just as efficient KO levels.

5.3.2 Limitations

One of the challenges in analysing gene expression from microglia is that these cells are low transcriptionally active. The amounts of RNA extracted from microglia from full brain are quite low. This therefore causes some issues with the downstream application of the extracted RNA. There are methods available to improve the quantity derived from the isolated microglia, including the use of more specialised kits such as the miRNeasy® (Qiagen), developed for low yield RNA extractions. In comparison to standard protocols, this method uses phenol and chloroform in the initial lysis step before proceeding with the column clean-up.

Although effective, the intraperitoneal route of administration of tamoxifen poses challenges to both animals and researchers. Multiple injections increase the risk of injury to animals as well as increasing anxiety due to the prolonged handling. Therefore, additional

routes of administration should be explored especially for experiments where prolonged tamoxifen administration is required. Most of the recent research points at using pre-mixed diet with gradually increasing levels of the drug to achieve knock-out in animals. Some criticism towards this approach might be that the exact time at which the gene expression is switched off might be harder to identify as well as ensuring same level of administration throughout the whole cohort. Therefore, it is best to consider the benefits and drawbacks of each approach in terms of the experimental question in place.

Additionally, although all the initial trials were completed both in male and female mice, later on the transcriptomic experiments were performed only in male mice, due to breeding issues and litter loss at the time of the experiments. This issue was further overcome by using female mice completing the validation experiments to try and compare any potential sex differences.

In addition, the clear impact of methanol fixation on the cell expression profile is evident. Due to the technical challenges encompassing these experiments, live cells cannot be used. Methanol fixation is well-established and widely used method, therefore it was selected for the transcriptomic experiments. However, due to the mechanism of methanol fixation, the membrane integrity and potentially the subsequently derived RNA is impacted. The data shows that *Syk* levels within the samples are undetectable in majority of cells irrespective of the genotype and this is further replicated in multiple independent datasets. The findings should be taken as an important consideration when analysing and interpreting ScRNA-sequencing data. There could be a subset of genes, which are impacted more than others by methanol fixation and changes in those might not be detected. A recent publication demonstrates that genes with higher GC content are impacted more by methanol fixation and gene length also has an influence (337).

5.3.3 Early transcriptomic response in microglia

The ScRNA-sequencing dataset which is presented here demonstrates some interesting initial findings about the function of *Syk* in microglia. The experiment was performed only around 10-days after onset of the cKO, therefore revealing the very early, initial transcriptomic changes which occur within microglia upon *Syk* deletion. Overall, these novel findings report that a high proportion of the identified genes are linked to metabolic responses and have a role in major metabolic pathways rather than immune ones, which

might have been the initial prediction when assessing *Syk* function. Interestingly this demonstrates that the metabolic state is key for microglia function and minor changes in metabolism might control and manifest as altered functional responses. The role of metabolism has been implicated in AD pathophysiology previously with many studies investigating mitochondria and its role in disease development. IPA analysis revealed a list of over 20 pathways which are influenced under *Syk* cKO. The first one, with highest p-value is the Sirtuin pathway, demonstrating very slight decrease in activation. Interestingly, the sirtuin family of proteins, which are regulators of metabolism and inflammation, has been implicated as a target in ageing. Studies show that sirtuins can modify the microenvironment by inhibiting secretion of various pro-inflammatory cytokines and chemokines which mediate inflammation (reviewed in (338)). Additionally, sirtuin activity has been linked to macrophage activation previously and KO models demonstrate increase in inflammation (339). Interestingly, SIRT3 which is located within the mitochondria demonstrates anti-inflammatory properties in mouse models, decreasing oxidative stress, inflammatory cytokines and inflammasome activity (340). Additionally, in more disease relevant context, just recently it has been demonstrated that SIRT3 has protective neuron properties and attenuates excitotoxicity (341). The role of SIRT3 is also recapitulated in a publication using the APP^{NL-G-F} model where neuronal hyperexcitability and synaptic plasticity deficits are reduced in SIRT3-dependent manner (342). Overall, the anti-inflammatory effects demonstrated by the sirtuin family are attributed to inhibition of the NF-kB pathway (343). Therefore, it can be speculated that in *Syk* cKO animals, the sirtuin pathway response is decreased, therefore microglia will exhibit more inflammatory properties. This can be particularly important in AD where chronic inflammation is known to contribute to pathology progression. This highlights the necessity for proper activation of *Syk* and downstream signalling.

Interestingly, an activation of oxidative phosphorylation (OXPHOS) is also predicted to occur in the absence of *Syk*. This is particularly intriguing because in AD downregulation of OXPHOS has been previously reported in patients (344). The direction at which this pathway is modulated is based on the energy demand of cells. Looking into more detail through the rest of the identified pathways, Nucleotide excision repair (NER) comes up as an activated pathway as well. There is evidence from publications that DNA repair is highly energy

demanding process and studies demonstrate that increase in OXPHOS is a way for cells to combat DNA damage (345). Although some of these studies have not been done in microglia or related cell types, some common mechanisms in cell responses most likely exist and useful parallels can be drawn from previous work. The differences in OXPHOS are most likely conducted by a cluster of DEGs involved in different complexes of the mitochondrial transport chain, including the NADH-Ubiquinone Oxidoreductase (NDUF) family and Cyclooxygenase (COX) enzyme family. This is most likely driven by the transcription factor TEAD1 which is identified as one of the top activated upstream regulators by IPA and is known to be key for mitochondrial function and homeostasis (346). Increase in the rate of the mitochondrial transport chain (MTC) can be responsible for altering the redox balance and leading to potentially increased production of reactive oxygen species (ROS) (347). ROS are in turn linked to oxidative stress and have been implicated in multiple diseases as a pathological hallmark. The role of *Syk* in regulating genes important for mitochondrial function is further enhanced by the identification of DNM1L as a DEG in the dataset. DNM1L is involved in mitochondrial fragmentations and mutations within the gene have been linked to encephalopathy, refractory epilepsy and cerebral atrophy (348).

The link between the top 2 identified pathways is further confirmed by some functional studies which demonstrate that in increased energy demand state, sitruin levels are decreased due to decrease in NAD^+ levels (349). Additionally, decrease in SIRT1 activity has been reported in response to oxidative stress and advancement of cellular senescence (350). Interestingly SIRT1 has been linked to APP processing and accumulation of amyloid plaques. SIRT1 deletion in mouse models was shown to cause increased plaque formation. SIRT1 activity was linked to enhancing the non-amyloidogenic APP processing pathway which most likely explains the reduction in overall plaque load (351, 352). This evidence implies that in the absence of *Syk* decrease sitruin pathway activity might be linked to increased Aβ deposition and implementing that microglia might have an active role in this process.

Furthermore, deletion of *Syk* causes a change in some important biosynthesis pathways at a transcriptional level which might also have an impact on cell functions. For example, Docosahexaenoic acid (DHA) signalling, and Dermatan Sulphate biosynthesis are identified as significant in the dataset. The direction at which DHA signalling is regulated is not clear.

As the primary polyunsaturated fatty acid (PUFA) in the brain, DHA has been identified as key during brain development and for cognition later in life. Interestingly, DHA metabolism is impaired in AD patients (353). Furthermore, APOe4 mice have been found to uptake less DHA in comparison to APOe2 animals which may contribute to cognitive decline (354). This highlights another key pathway regulated through *Syk* signalling which may contribute to disease progression.

The top identified upstream regulator XBP1 is linked to the unfolded protein response (UPR). Interestingly, this response is detected when endoplasmic reticulum homeostasis is disrupted usually due to cellular stress (355). An interesting publication from the cancer field reveals that XBP1 is involved in activating myeloid cells through increase of cholesterol production (356). Some parallels can be drawn here where in the presented dataset a decrease of *Syk* leads to upregulation of XBP1 which in turn may promote cholesterol production and synthesis. This is particularly important in the context of AD where link to cholesterol metabolism exists. Additionally, this finding is further backed up by the presence of HDL as the top inhibited upstream regulator of these processes. Furthermore, XBP1 has been previously linked as an AD risk factor (357) and is thought to contribute to APP metabolism (358). Increase in XBP1 is seen as an early protective mechanism to attenuate ER stress, however if prolonged its expression is downregulated (359). Therefore, the increase of XBP1 in this dataset most likely signals that early response to stress caused by *Syk* deletion and alteration of pathways. Overall, the findings where XBP1 expression has been modulated in AD context are very conflicting (reviewed in (360)), therefore the exact impact remains to be determined, but the fact that it alters pathology remains conclusive.

Interestingly, in this dataset a predicted lowering of CTNNB1, which encodes for b-catenin is presented. However, an overall increase of Wnt/b-catenin pathway activation is predicted by the pathway analysis. This can be attributed to the fact that *Syk* deletion potentially leads to activation of some feedback compensatory mechanisms. A publication by Pons *et al.* demonstrates that upon CSF1R deletion, TREM2 and β-catenin are both upregulated indicating compensatory mechanism (361). Both CSF1R and TREM2 signal via SYK downstream, therefore the deletion might promote the other pathway. In our dataset, deletion of *Syk* is predicted to lead to increase in Wnt/β-catenin to compensate for lower

activation of SYK. Due to the importance of TREM2 for microglia disease state, this link in the pathway is particularly important.

Altogether these pathways and changes initiated by *Syk* deletion represent the versatile and complex responses which the gene can regulate. More importantly, this novel data represents the very immediate changes induced on a cellular level after cKO of *Syk*. Additionally, the detected response highlights that *Syk* is involved in the regulation of metabolic and biosynthetic pathways which are key for normal cellular functions but can also contribute to pathology development.

Overall, this data demonstrates that *Syk* does not only impact a single metabolic pathway, but an array of functions which are all associated with metabolic state and could potentially have a key role in determining functional responses. To put into context the importance of *Syk* for cell function we must consider what other intracellular proteins and second messengers it interacts with. In terms of AD risk, it is documented that both *TREM2* and *PLCG2*, AD risk genes, interact with SYK. This means that any dysfunction in these genes will ultimately result in altered SYK responses which can onset a variety of other cell pathways. For example, hypoactive TREM2 will lead to decreased SYK phosphorylation by DAP12, leading to reduced induction of pathways controlled by SYK through second messengers. The data here revealed some of these pathways might be linked to oxidative phosphorylation, therefore reduced *Syk* activity can lead to increase in inflammation and negatively impact other cell types such as neurons.

If the response here is to be summarised, in cells where *Syk* cKO has been induced, increase in DNA repair pathways occurs which in turn is compensated by increase in OXPHOS. Additionally, important anti-inflammatory pathways such as the Sitruin response are negatively regulated which can onset a variety of inflammatory mediators. In addition, molecules linked to synthesis of biochemical substrates are also altered which can negatively impact cells. Altogether, microglia cells lacking *Syk* are more likely to exhibit increased inflammatory response, potentially elevated apoptosis and negatively impact the microenvironment. How this initial shift can long-term impacts disease progression is still to be investigated.

Finally, it is important to consider that this data is derived from examining mRNA contents rather than protein expression which might not fully accurately depict the changes on a functional level and results need to be cautiously evaluated. This also highlights the need to functionally validate sequencing data to derive in depth conclusions about cellular responses.

5.3.4 The Cre-loxP model system

The Cre-LoxP model system represents a very useful research tool. Here it was utilised to generate *Syk* cKO, however there are some considerations in place when using this in transgenic animals. Multiple research papers demonstrate that the Cre recombinase can be spontaneously activated even in the absence of tamoxifen, therefore impede accurate interpretation of biological data. A paper by Kristiano *et al*. demonstrates that in mouse lines with UBC driven Cre-ERT2 system, a significant tamoxifen-independent Cre activity is observed in multiple tissues (362). Some of these findings are attributed to potential Cre expression differences in certain tissue types. This highlights the need to assess background Cre activity in the absence of tamoxifen.

More importantly, in the context of the presented experiments, Cx3cr1 expression and its impact need to be considered. Cx3cr1 is commonly used to restrict expression to cells with myeloid origin and specifically microglia within the CNS. There has been conflicting evidence about the specificity of Cx3cr1 and several studies have reported leakiness into neurons (363, 364), raising concerns about the reliability of the mouse model and the generated data. Similar findings have emerged from different Cre lines (365). It is unclear why there is variability in the leakiness between these lines. Further detailed examination of different Cre lines by Zhao and colleagues, demonstrates that the Cre-ERT2 line developed by Jung *et al*. (366) and used in this thesis, demonstrates some basal independent of tamoxifen enzymatic activity. However, the levels presented remain low and more importantly Cre-dependent expression is almost completely restricted to microglia (367).

5.3.5 Future directions

The transcriptomic data in this chapter highlights multiple pathways which role in AD could be particularly important. Therefore, any future work should be in the direction of exploring what are the functional consequences of modulating these pathways and understanding how they can contribute to disease progression.

Based on the multiple lines of evidence, including the modulation of the Sirtuin pathway, it will be particularly interesting to begin with investigating the inflammatory response in these cKO animals. Most of the identified pathways will lead to changes in inflammatory responses and evaluating the levels of both pro and anti-inflammatory cytokines might provide some important cues as to how microglia respond but also what signals they send to other cells in the microenvironment.

The transcriptomic data here also reveals that *Syk* might regulate some important metabolic pathways. Therefore, it would be beneficial to follow this work functionally and understand how changes in microglia metabolism early in disease development can impact amyloid pathology and overall disease progression. For example, using more human relevant models such as iPSC derived microglia-like cells might provide a way to further validate and translate these findings in humans. Microglia-like cells can be differentiated and a *Syk* KO achieved using GAPMERs or shRNAs. These cells can then be subjected to metabolic assays including the Seahorse platform to determine the ratio between glycolysis and oxidative phosphorylation. Alternatively, performing some histological analysis both in cultures and using tissue slices, mitochondria structure can be investigated together with mitochondrial membrane potential and depolarisation properties.

As described earlier, this cKO model is expected to impact other macrophage populations since they express Cx3cr1. Therefore, it will be particularly interesting to investigate how *Syk* cKO alters the BAM response specifically, especially with growing evidence supporting the role of BAMs in disease progression.

5.3.6 Conclusions

Overall, the work here demonstrates that using 100mg/kg tamoxifen in the APP^{NL-G-F} mouse model of AD to induce cKO of *Syk* is safe, efficient, and long-lasting at different stages of disease development. In addition, the results presented in this chapter point at the importance of *Syk* for microglia function and demonstrate some novel findings revealing key cellular pathways to be regulated by the kinase. The transcriptomic findings cumulatively suggest a role of *Syk* in regulating metabolic and immune pathways. To further explore the long-term effects of *Syk* cKO in AD and its impact on pathological hallmarks the next chapter will focus on investigating this in aged animals.

Chapter 6 Syk cKO alters microglia transcriptional profile and modulates AD pathology in aged APP^{NL-G-F} mice

6.1 Introduction

The *Syk* kinase which has been introduced in the previous chapter, can modulate a wide variety of cell signalling pathways within microglia. Currently in the literature there is no evidence demonstrating how cKO of *Syk* induced at different disease progression stages will impact microglia during disease development and how this will influence AD relevant phenotypes. It is important to compare the response of microglia at early and later disease development stages because this can provide cues to how microglia respond to the complex changes during disease progression and identify if and how they can contribute to propagation of disease. This is particularly important when trying to treat a complex disease like AD and selecting a precise treatment point which will best target the pathology. *Syk* has mainly been linked to tau pathology previously, but no conclusive evidence exists to indicate how *Syk* in microglia will impact Aβ deposition although some publications suggest a link (230).

Single-cell RNA sequencing (ScRNA-sequencing) has proven invaluable at distinguishing heterogenous cell populations. This method allows sequencing of the mRNA content of a full cell including the cytoplasm, which is not possible using more widely available single-nuclei RNA sequencing (SnRNA-seq). Some publications reveal that SnRNA-seq is not recommended for microglia populations and can result in loss of detection of important microglia related genes in humans (368). Examining microglia specifically will reveal the distribution of different microglia sub-populations. Transcriptomic analysis could be used to map genotype to phenotype and address some long-standing questions in the field. Overall, cells share the same genetic information, however transcriptomics can reveal unique genetic responses only in that particular set of cells. In comparison to conventional bulk sequencing, which only reveals the average expression response, single-cell transcriptomics provides unique cell to cell information. Single-cell technology was pioneered by Eberwine *et al*. and Iscove *et al.* who demonstrated expansion of complementary DNA (cDNA) from a single cell (369, 370). The method utilised in vitro transcription allowing linear amplification, followed by PCR to exponentially amplify the product. The first study using single-cell technologies based on next-generation sequencing was published in 2009 and focused on early development (371).

The ability of ScRNA-sequencing to resolve cell heterogeneity is particularly useful when researching microglia in AD, because from the literature it is evident that microglia are highly versatile population (137, 152, 336). The presence of different microglia populations including DAMs and IFNs during disease are hugely important for regulating progression of disease. Transcriptomics has also allowed the identification of specific genes which are associated with each of these groups and functional studies have further validated that loss and dysfunction of some of these can poorly impact disease progression. For example, TREM2 and APOE are both required for successful transition of homeostatic microglia to DAMs (152).

Importantly, ScRNA-sequencing provides cues about cell-cell interactions as well as pathways which can be activated and can impact functional responses. It is important to use transcriptomic findings and apply further phenotypic and functional characterisation to build a more complex picture of how subtle genetic changes can translate into induction of signalling responses which then result in pathological hallmarks as associated with amyloid accumulation.

This chapter focuses on examining transcriptomic changes occurring in microglia induced by cKO of *Syk* in the APP^{NL-G-F} AD model at different ages to reveal how *Syk* can impact disease progression. Additionally, we onset to investigate how transcriptomic changes are reflected phenotypically by exploring AD relevant pathology such as amyloid accumulation. The specific chapter aims are introduced bellow.

Chapter aims:

- Induce *Syk* cKO at either 8 or 16 weeks in APP^{NL-G-F} mice using tamoxifen
- Using the iCell8 technology investigate the transcriptomic response in aged *Syk* cKO mice and control mice
- Explore any AD-relevant histological differences between *Syk* cKO and control mice at 6 months old
- Compare the response of *Syk* cKO induced at either 8 or 16 weeks

6.2 Results

For this chapter Syk x APP and Syk x APP x Cre-ERT animals were utilised as defined previously. All experiments were conducted with 6-month-old male and female animals. To investigate the long-term effect of *Syk* cKO on disease progression and to evaluate its importance in respect to microglia, two experimental groups were developed. There was a group of animals which received tamoxifen at 8 weeks and a second group which received tamoxifen at 16 weeks instead, therefore inducing cKO of *Syk* at different disease development stage.

6.2.1 Animal welfare and injections

As in all previously described experiments, animal welfare checks were conducted for the duration of the injection period. In comparison to experiments presented in Chapter 5, here a modified monitoring schedule was applied. It was determined based on the previous trials that tamoxifen can be considered safe overall and it is not required to weigh animals twice daily since very rarely a decrease close to the endpoint is recorded. Therefore, here animals were weighed once daily at the same time as tamoxifen administration and then monitored with 2 visual checks instead. The summary weight charts can be seen in Figure 6.1. Interestingly, this demonstrates that when applying this monitoring schedule, the initial reduction in weight is not seen in most animals and overall, the anxiety scores are lower.

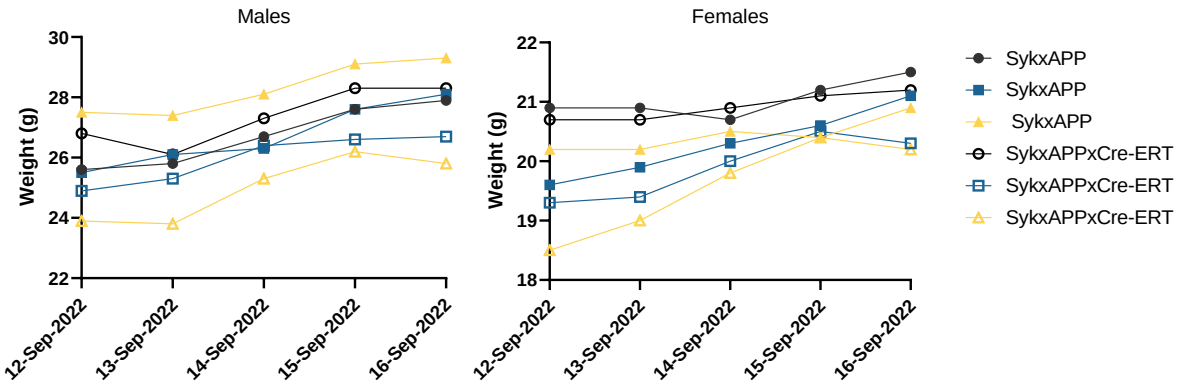

Figure 6.1: Weight change in animals treated with 100mg/kg tamoxifen used for ScRNA-sequencing experiments. Animals were treated for 5 consecutive days with 100mg/kg tamoxifen delivered I.P (n=3 male and female animals per genotype). Weight of all animals was recorded prior to injections each day.

6.2.2 Validation of cKO

In Chapter 5, it is demonstrated that *Syk* mRNA expression cannot be detected well using the utilised protocol for ScRNA-sequencing therefore there is no way to validate the cKO levels in the sequenced samples. As described there, the remainder of the sample which was not flow-cytometry sorted to generate the library was kept and utilised for RNA. Here, in Figure 6.2 the mRNA expression of *Syk* in the samples used to generate the data in the next section can be seen. This demonstrates that *Syk* cKO is efficient in these animals and the samples brought forward for sequencing show the expected decrease in expression. Some of the samples were depleted during initial analysis and could not be included in the qPCR validation.

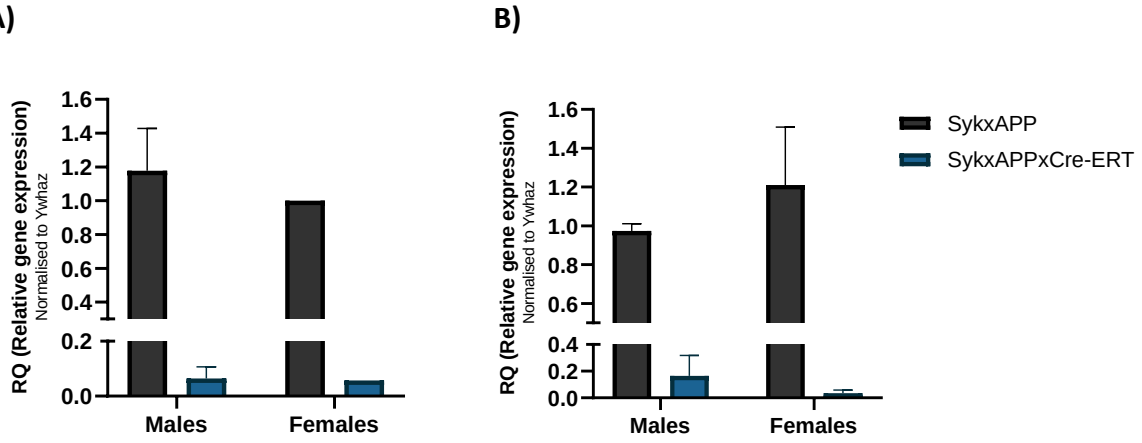

Figure 6.2: mRNA of Syk in samples used to generate ScRNA-sequencing library. (A) mRNA levels of *Syk* in 24-week-old animals treated with tamoxifen at 8 weeks of age quantified by RT-PCR. Bars represent mean ± SD (n=2 males, n=1 female). YWHAZ was used as endogenous control gene. **(B)** mRNA levels of *Syk* in 24-week-old animals treated with tamoxifen at 16 weeks of age quantified by RT-PCR. Bars represent mean ± SD (n=3/group). YWHAZ was used as an endogenous control gene.

6.2.3 ScRNA-sequencing

Libraries were generated using the iCell8 SMART-Seq® Pro Application kit (details in Methods). The libraries from both cohorts were generated and sequenced in parallel using the same reagents to reduce experimental variation. Once prepared, libraries were sequenced, and the data was bioinformatically analysed using DESeq2. All quality control steps for library preparation and examining the sequenced data can be found in the Appendix.

After initial identification of cell clusters, all contaminating cells, not labelled as microglia were excluded from the analysis based on marker expression. The samples were batch integrated and male and female samples were also combined. Clusters were identified using Seurat (Figure 6.3) and then mapped to existing microglia subtypes published by Sala-Frigerio et al. (2019) in the APP^{NL-G-F} model (137). Both microglia from mice treated at 8 and 16 weeks were analysed. Figure 6.4A presents the different microglia subpopulations and their distribution using UMAP plots to visualise the clusters. In addition, the number of cells assigned to each cluster are summarised in the table and visualised by the pie chart (Figure 6.4B). The data clearly demonstrates that in the Syk x APP x Cre-ERT animals a larger population of homeostatic cells is present. The proportion of activated response microglia (ARM) is significantly decreased in the cKO mice. This is replicated across both induction ages (Figure 6.4 and 6.5).

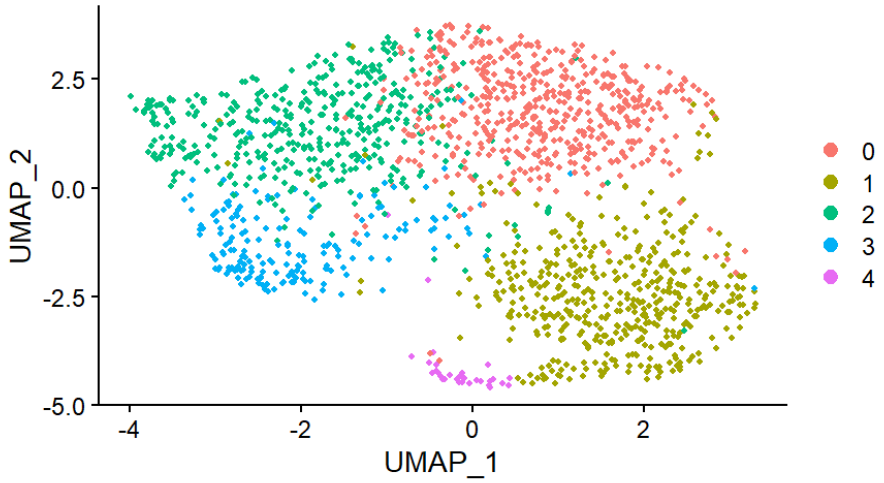

Figure 6.3: Identified Seurat clusters. UMAP plot representing the clusters of microglia identified in the ScRNA-sequencing experiment. Total of 5 clusters were identified using singleR.

A)

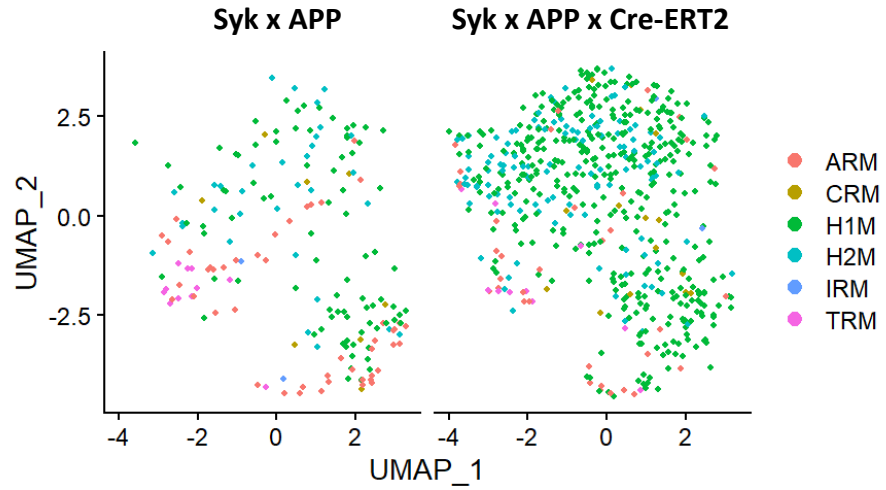

B)

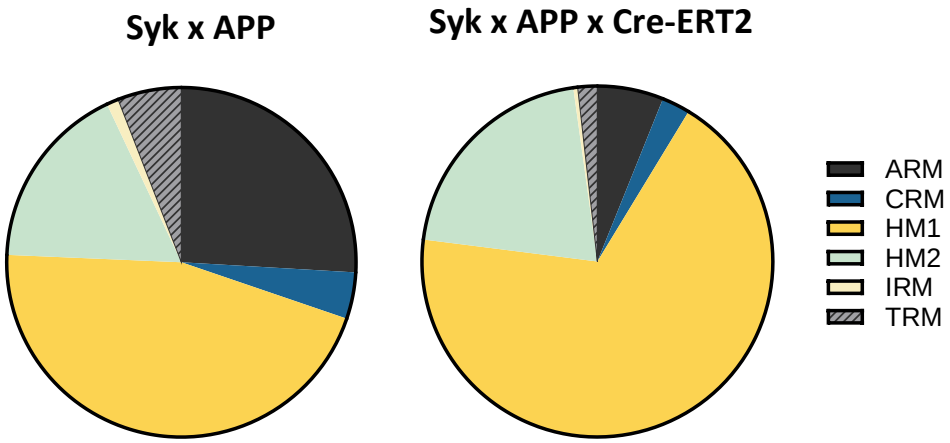

Cluster	Syk x APP (%)	Syk x APP x Cre-ERT2 (%)
ARM	25.94595	6.129597
CRM	4.324324	2.62697
HM1	45.40541	68.30123
HM2	17.2973	20.84063
IRM	1.081081	0.350263
TRM	5.945946	1.751313

Figure 6.4: Syk cKO microglia demonstrate distinct transcriptomic response when treated at 8 weeks. (A) Uniform Manifold Approximation and Projection (UMAP) plot visualising the single microglia cells which passed quality control. Cells are coloured according to clusters identified using Seurat's k-nearest neighbour approach. **(B)** Percentage of cells belonging to each cluster are presented as a pie chart. Activated response microglia (ARM), cycling and proliferating microglia (CRM), homeostatic microglia 1 (HM1), homeostatic microglia 2 (HM2), interferon response microglia (IRM), transitioning microglia (TRM). The exact numbers of each cluster based on genotype are summarised in the table.

A)

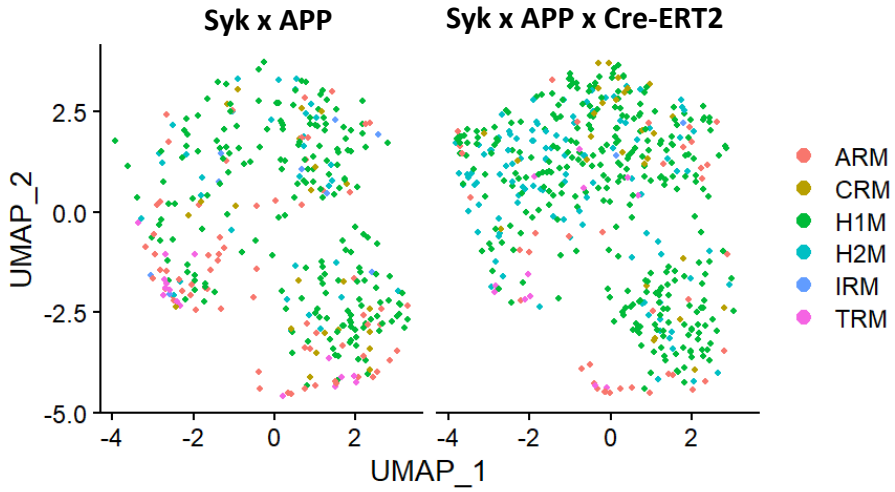

B)

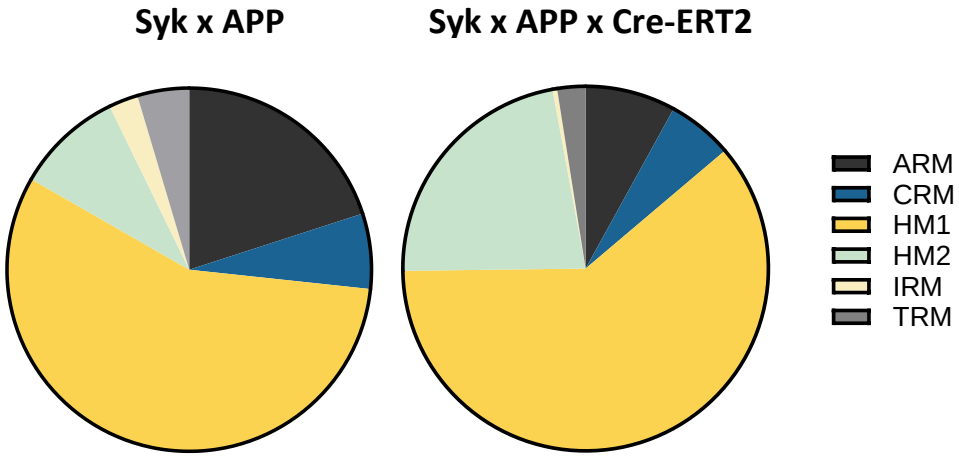

Cluster	Syk x APP (%)	Syk x APP x Cre-ERT2 (%)
ARM	20	8.041237
CRM	6.666667	5.773196
HM1	56.52174	61.03093
HM2	9.565217	22.26804
IRM	2.608696	0.412371
TRM	4.637681	2.474227

Figure 6.5: Syk cKO microglia demonstrate distinct transcriptomic response when treated at 16 weeks. (A) Uniform Manifold Approximation and Projection (UMAP) plot visualising the single microglia cells which passed quality control. Cells are coloured according to clusters identified using Seurat's k-nearest neighbour approach**. (B)** Percentage of cells belonging to each cluster are presented as a pie chart. Activated response microglia (ARM), cycling and proliferating microglia (CRM), homeostatic microglia 1 (HM1), homeostatic microglia 2 (HM2), interferon response microglia (IRM), transitioning microglia (TRM). The exact numbers of each cluster based on genotype are summarised in the table.

To investigate in more detail the apparent reduction of microglia clusters associated with increased expression in disease in the cKO animals, the data was compared to different DAM signatures (372-374). These are defined by the expression of specific markers associated with each state and function. For example, DAM microglia express genes such as *Csf1*, *Trem2*, *Clec7a*, *Axl* and *Apoe*. Figure 6.6 reveals that based on genotype, Syk cKO animals display a reduction in the number of DAM signature microglia cells.

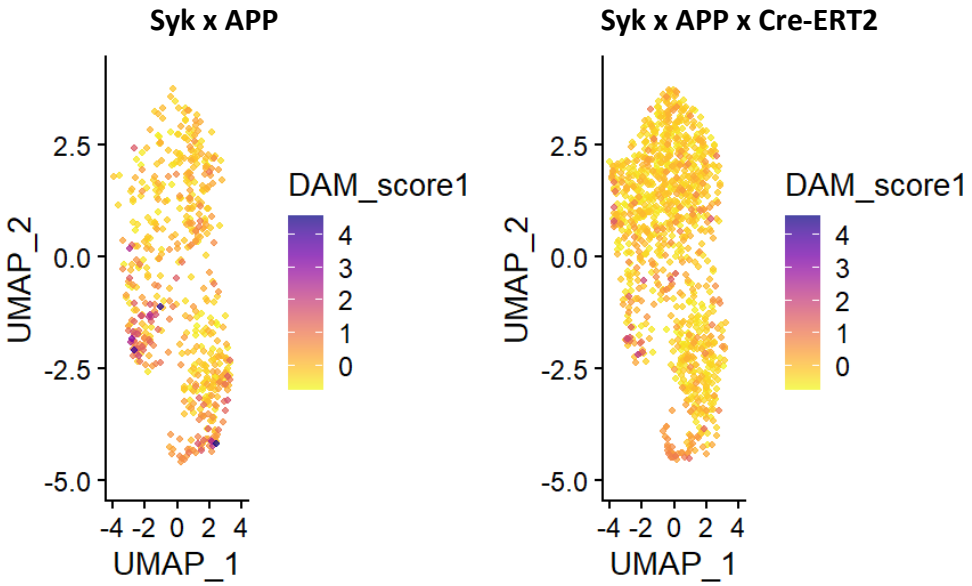

Figure 6.6: Expression of DAM signature across sequenced microglia based on genotype. Comparison between the expression of DAM score (associated with specific DAM gene signature) across sequenced microglia based on genotype. SA represents Syk x APP animals, whereas SAE stands for Syk x APP x Cre-ERT mice. The darker colour towards blue represents higher DAM score.

Further differential expression analysis comparing differences between *Syk*-deficient and *Syk*-sufficient animals revealed that there is a small number of differentially expressed genes. Total of 82 DEG were identified. The volcano plot in Figure 6.7 highlights the top DEGs based on p-value significance. Additional comparisons of differential expression were conducted based on sex or age of cKO induction (data not shown). However, few changes in expression were associated with the presence of *Syk* cKO.

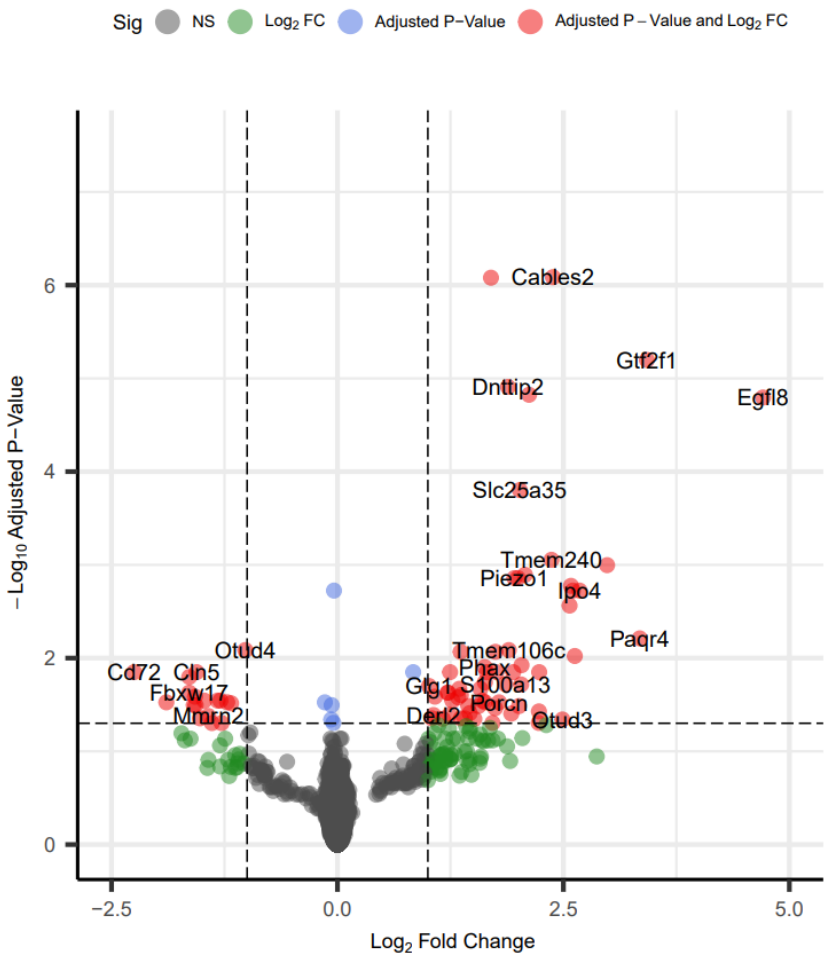

Figure 6.7: Differential expression analysis of Syk x APP and Syk x APP x Cre-ERT2 microglia. Genes highlighted in red are significant (p<0.05 and log2 fold change>1). Green dots represent genes with log2 fold change>1, but no p-value significance. Grey dots are non-significant, and blue have log2 fold change<1.

6.2.4 *Syk* cKO mice exhibit histological changes

Syk x APP and Syk x APP x Cre-ERT animals were treated with 5 doses of 100mg/kg tamoxifen at either 8 or 16 week of age according to the previously established protocol. The animals were then left to age until 24-25 weeks before tissue harvest. All tissue was processed simultaneously to avoid any batch-to-batch variability effects. Both male and female mice were included in the analysis to begin to identify and characterise any sexual-dependent effect results. In addition, both the hippocampus and the cortex are involved in memory retention and formation, therefore data for both regions were collected and analysed. The next sections will outline the observed changes in plaque burden, microglia morphology and astrocyte presence.

6.2.4.1 Microglia density is altered in *Syk* cKO mice

To explore the effect of *Syk* cKO on microglia in the APP^{NL-G-F} 6-month-old animals, sections were analysed using the well-established microglia marker Iba1. Both hippocampus and cortex regions were analysed (Figure 6.8A). Some differences between Syk x APP control mice and Syk x APP x Cre-ERT animals were already apparent based on the histological images. The data analysis revealed that in the cKO mice which were treated at 16-weeks, overall microglia number is significantly decreased both in the hippocampus and cortex (Figure 6.8B and C). Additionally, the nearest neighbour distance (NND) was increased which further validates the findings. This indicates that Syk x APP x Cre-ERT animals present with lower number of microglia cells which are distributed further away from each other. The percentage $Iba1^{+}$ immunoreactivity was not impacted in both regions of interest.

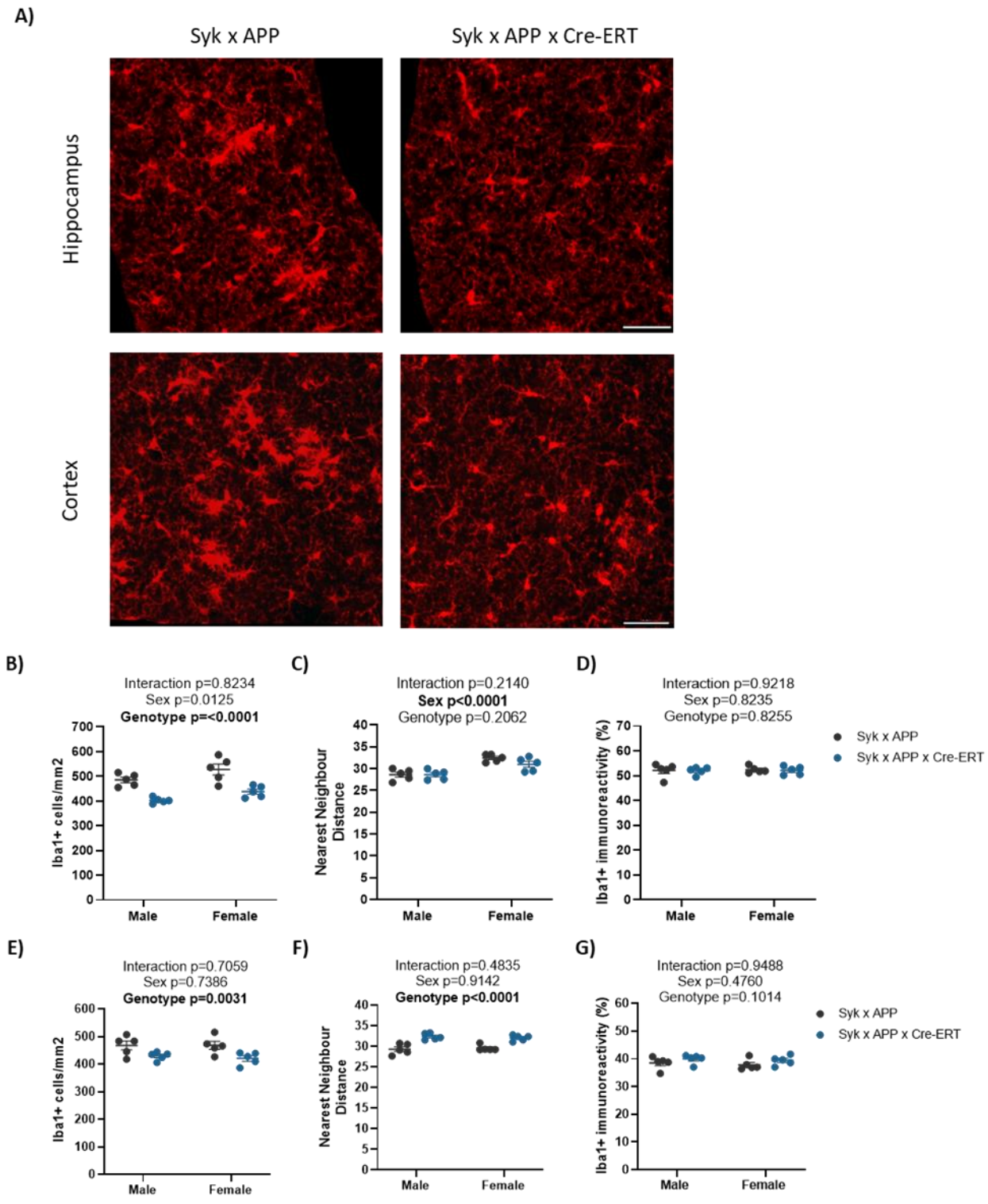

Figure 6.8: Induction of Syk cKO at 16 weeks alters microglia morphology in 6-month-old APP^{NL-G-F} animals. (A) Representative images of Syk x APP and Syk x APP x Cre-ERT sections stained for Iba1 in the CA1 region of the hippocampus (top) and cortex (bottom). Scale bar=50µm **(B-G)** Quantification of microglia. Microglia density **(B/E),** nearest neighbour distance (NND) **(C/F)** and Iba1 immunoreactivity **(D/G)** in Syk x APP and Syk x APP x Cre-ERT animals treated with tamoxifen at 16

weeks (n=5/group). Both hippocampus **(B-D)** and cortex **(E-G)** were analysed. In all graphs grey represents Syk x APP mice and blue represents Syk x APP x Cre-ERT animals. Each dot represents the average for 1 animal (1 image per hemisphere). Bars show mean ± SD. All data has been analysed via two-way ANOVA. Values are displayed above each graph, with significant values in **bold.**

Furthermore, the changes observed in the 16-week cohort seems to be replicated in the 8-week cohort as well. Figure 6.9A shows representative images of hippocampal and cortex region stained for Iba1. In Figure 6.9, the quantified data for both regions of interest suggest that these animals present with significantly lower microglia numbers, coupled with increase in the NND. The direction of change is same as the one identified in the 16-week treated cohort. Again, no significant difference in the Iba1 immunoreactivity was recorded.

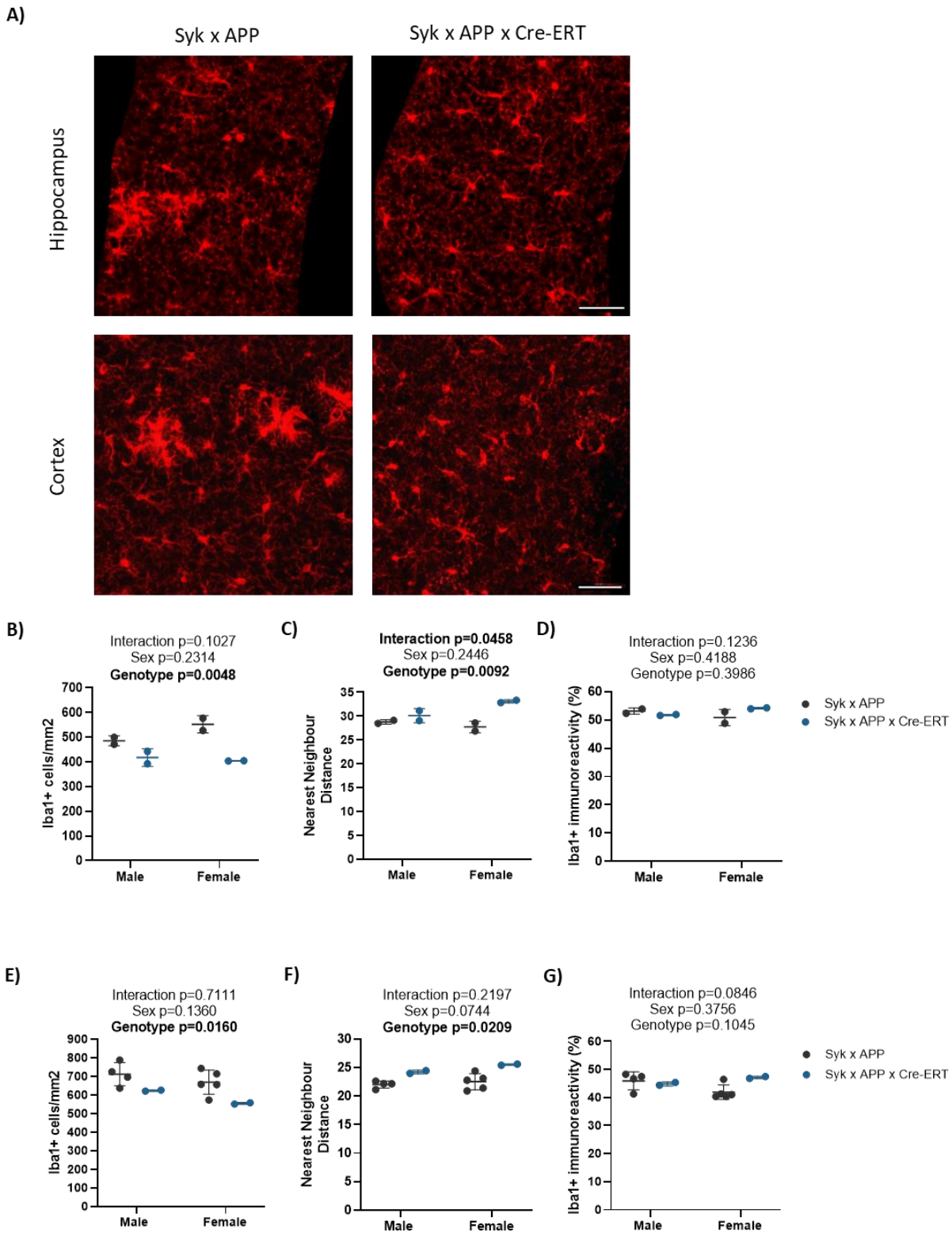

Figure 6.9: Syk cKO induced at 8 weeks alters microglia responses in 6-month-old APP^{NL-G-F} animals. **(A)** Representative images of Syk x APP and Syk x APP x Cre-ERT sections stained for Iba1 in the CA1 hippocampus region (top) and cortex (bottom) in Syk x APP and Syk x APP x Cre-ERT animals. Scale bar=50µm **(B-G)** Quantification of microglia. Microglia density **(B/E),** nearest neighbour distance (NND) **(C/F)** and Iba1 immunoreactivity **(D/G)** in Syk x APP and Syk x APP x Cre-ERT animals treated

with tamoxifen at 8 weeks (n=4/group Syk x APP cortex males, n=5/group Syk x APP cortex females 2/group for Syk x APP x Cre-ERT). Both hippocampus **(B-D)** and cortex **(E-G)** were analysed. In all graphs grey represents Syk x APP mice and blue represents Syk x APP x Cre-ERT animals. Each dot represents the average for 1 animal (1 image per hemisphere). Error bars show mean ± SD. All data has been analysed via two-way ANOVA. Values are displayed above each graph, with significant interactions in **bold.**

Interestingly, in images containing *Syk* cKO animals in both cohorts it was observed that no characteristic 'clustering' of the microglia occurred in comparison to Syk x APP control animals, where defined groups of cells can be seen in close proximity to each other.

Together these findings suggest that microglia surveillance and motility capabilities in *Syk* cKO mice might be impaired. Since this is a key microglia function which might impact disease progression, the next section will explore the amyloid deposition in both cohorts of animals.

6.2.4.2 Amyloid deposition

To explore the effect of *Syk* cKO in the APP^{NL-G-F} animals on one of the main hallmarks of AD, amyloid plaque deposition, brain sections were stained using Thioflavin S (ThioS) (Figure 6.10A). Area percentage (%) covered by ThioS, plaque size and number of plaques per mm^2 were used as relevant identification to detect any differences. The data from the 16-week treated cohort demonstrates no significant alteration of plaque deposition based on all readouts identified (Figure 6.10B and C). This applies both for hippocampal and cortex regions in all animals. Induction of cKO of *Syk* at this age does not alter the formation of plaques or the volume of the deposits. It is important to consider that ThioS stains both core and diffused plaque, therefore if any difference in the composition of plaques based on genotype are present, they might not have been identified here.

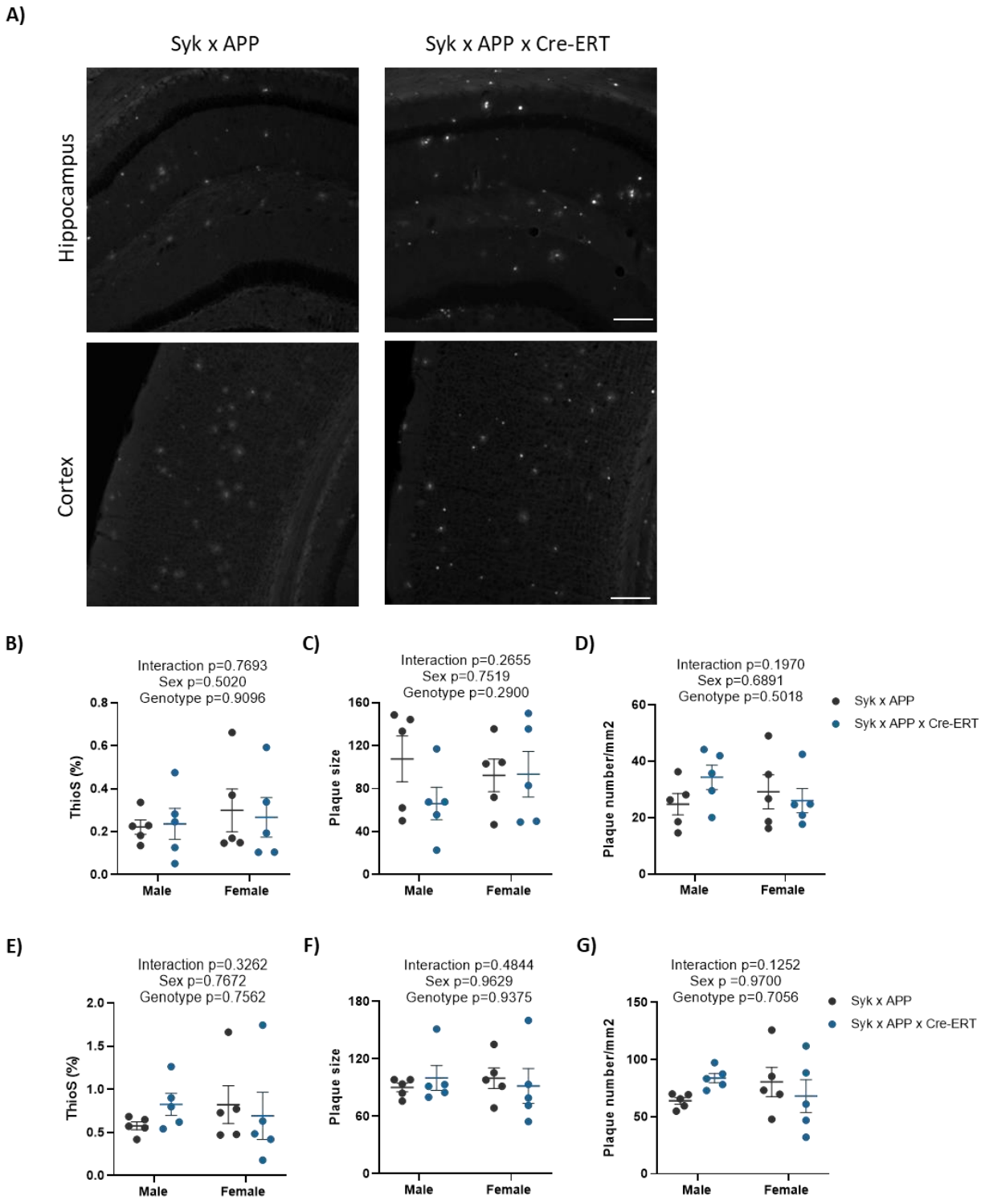

Figure 6.10: Syk cKO at 16 weeks does not alter plaque deposition in 6-month-old APP^{NL-G-F} animals. (A) Representative images of thioflavin S-stained sections in the hippocampus (top) and cortex (bottom) in Syk x APP and Syk x APP x Cre-ERT animals. Scale bar=100µm **(B-G)** Quantification of amyloid plaque deposition. Thioflavin S area % (B/E), plaque size (C/F) and plaque number per mm^2 (D/G) in Syk x APP and Syk x APP x Cre-ERT animals treated with tamoxifen at 16 weeks (n=5/group). Both hippocampus (B-D) and cortex (E-G) were analysed. In all graphs grey represents

Syk x APP mice and blue represents Syk x APP x Cre-ERT animals. Each dot represents the average for 1 animal (1 image per hemisphere). Bars show mean ± SD. All data has been analysed via two-way ANOVA. Values are displayed above each graph, with significant interactions in **bold.**

Interestingly, it appears that significant alteration of amyloid deposition is evident in the cortex of 8-week treated mice (Figure 6.11E-F). The cortex data suggests that in the Syk x APP x Cre-ERT animals have larger in size plaques which further correlates with significant increase in the percentage of ThioS staining. The data in the hippocampus presents with more variation, therefore not identifying any significant conclusive differences in the amyloid burden (Figure 6.11B-D).

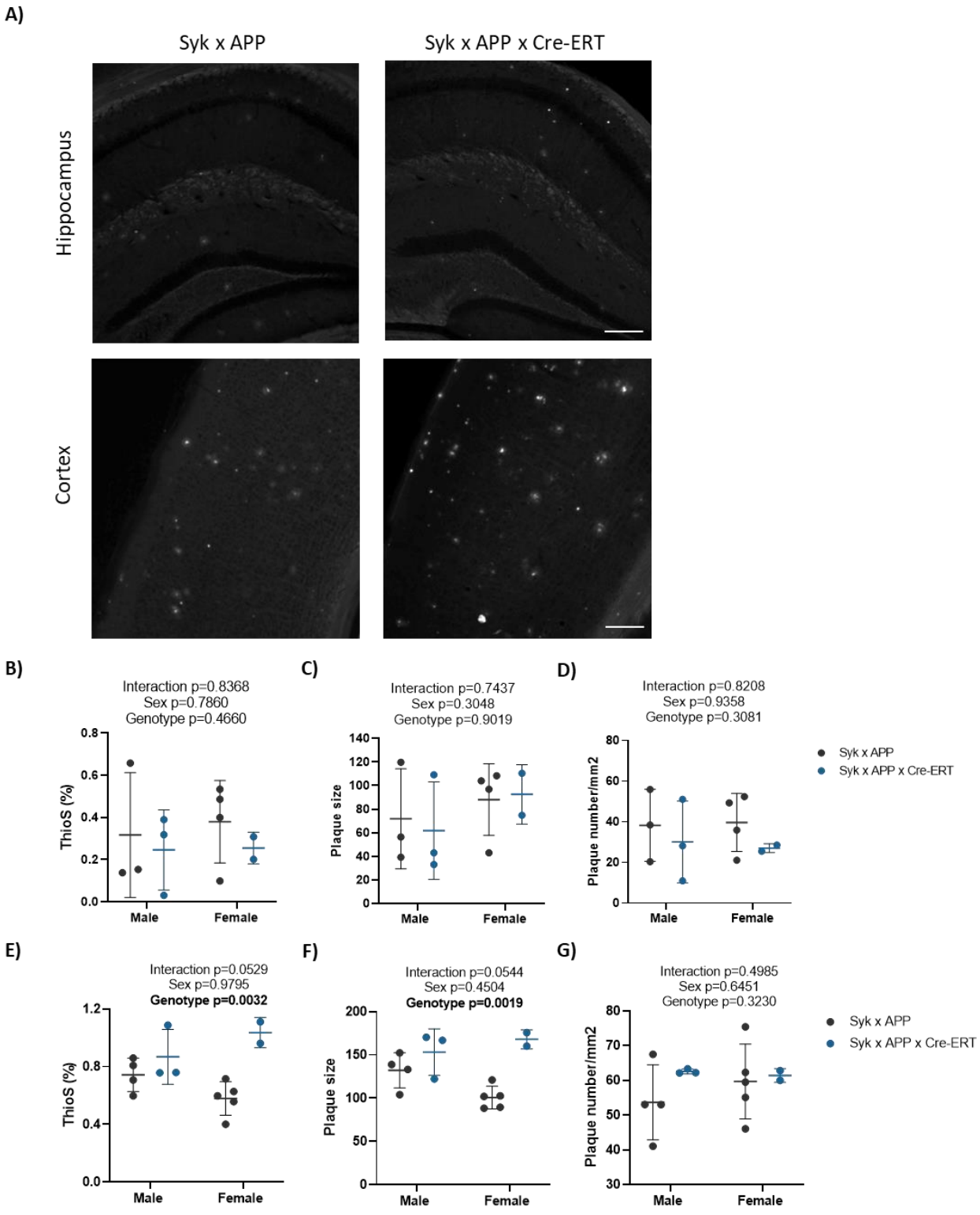

Figure 6.11: Syk cKO at 8 weeks alters plaque deposition in 6-month-old APP^{NL-G-F} animals. (A) Representative images of thioflavin S-stained sections in the hippocampus (top) and cortex (bottom) in Syk x APP and Syk x APP x Cre-ERT animals. Scale bar=100µm **(B-G)** Quantification of amyloid plaque deposition. Thioflavin S area % (B/E), plaque size (C/F) and plaque number per mm^2 (D/G) in Syk x APP and Syk x APP x Cre-ERT animals treated with tamoxifen at 8 weeks (n=4/group Syk x APP,

n=3/group male Syk x APP x Cre-ERT and 2/group female Syk x APP x Cre-ERT). Both hippocampus (B-D) and cortex (E-G) were analysed. In all graphs grey represents Syk x APP mice and blue represents Syk x APP x Cre-ERT animals. Each dot represents the average for 1 animal (1 image per hemisphere). Bars show mean ± SD. All data has been analysed via two-way ANOVA. Values are displayed above each graph, with significant interactions in **bold.**

6.2.4.3 Peri plaque analysis

The changes reported in the previous sections indicated that *Syk* cKO impacts microglia number and distribution in these animals. Microglia are known for one of their primary functions which involves surveying the surrounding environment and identifying targets for phagocytosis. They are known to respond to amyloid deposition through encirclement of the plaques. Therefore, to explore in more detail how the changes identified in the microglia of cKO mice can impact their ability to interact with plaques a high-magnification peri plaque analysis was conducted. This involved selecting a set number of plaques based on Amyloid Glo staining and counting the ratio detected between $Iba1^{+}$ expression and AmyloGlo in the vicinity of the plaque. Strikingly, the data revealed that microglia in Syk x APP x Cre-ERT mice are not migrating towards plaques and contain less plaque associated processes (Figure 6.12A and C). The analysis of the ratio between the microglia and amyloid stain showed a significant decrease in the overlap which points to functional defects in the *Syk* cKO microglia (Figure 6.12B and D). This was replicated both in the 16-week (A-B) and 8-week cohort (C-D).

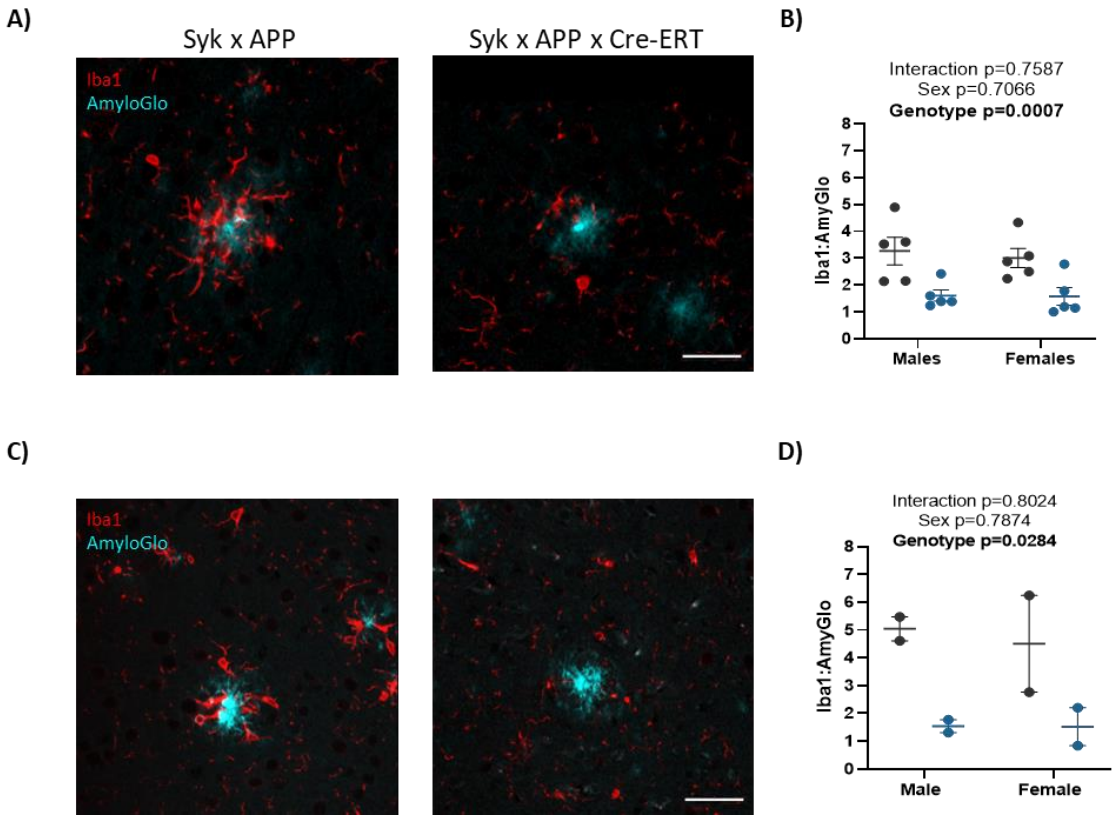

Figure 6.12: Peri plaque analysis in the cortex of Syk cKO animals at 6 months. (A) Representative 40X images of sections from Syk x APP and Syk x APP x Cre-ERT animals stained with Iba1 and AmyloGlo treated at 16 weeks. **(B)** Ratio between Iba1 and AmyloGlo staining present in the vicinity of the plaque. Bars represent mean ± SD (n=5/group). **(C)** Representative 40X images of sections from Syk x APP and Syk x APP x Cre-ERT animals stained with Iba1 and AmyloGlo treated at 8 weeks. **(D)** Ratio between Iba1 and AmyloGlo staining present in the vicinity of the plaque. Bars represent mean ± SD (n=2/group). Data was analysed with two-way ANOVA and significant values are highlighted in bold. The grey dots represent Syk x APP controls, whereas blue indicates Syk x APP x Cre-ERT animals. Each dot represents the average for 1 animal. Scale bar =30µm.

6.3.4.4 Astrocytes remain unchanged in cKO animals

Microglia communicate with various other cell types in the brain, therefore it is important to explore how changes in microglia phenotype recorded here impact on the other glial cells. Astrocyte presence was assessed using the Glial Fibrillary Acidic Protein (GFAP) as a marker (Figure 6.13A). Analysis was conducted only on hippocampal region as GFAP has been reported not to be an appropriate marker for astrocytic recognition in the cortex. No significant changes in GFAP immunoreactivity were reported in both cohorts. This suggests

that microglia alteration at this stage of disease development does not impact astrocyte density.

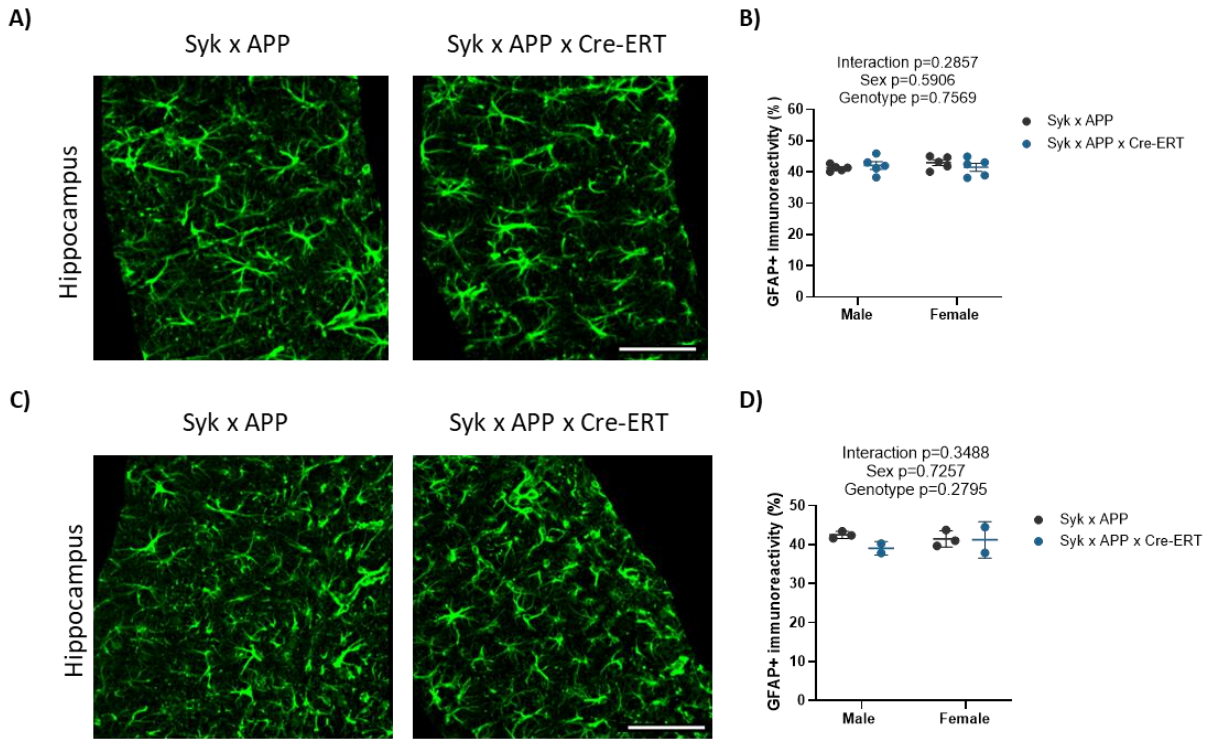

Figure 6.13: Syk cKO does not alter astrocyte responses in Syk x APP and Syk x APP x Cre-ERT 6-month-old animals. (A) Representative images of GFAP staining in the hippocampus of animals with *Syk* cKO induced at 16 weeks. Error bar=50µm **(B)** GFAP immunoreactivity in the hippocampus of 16-week treated Syk x APP and Syk x APP x Cre-ERT animals (n=5/group). **(C)** Representative images of GFAP staining in hippocampus of 6-month-old mice treated with tamoxifen at 8 weeks. **(D)** GFAP immunoreactivity in the hippocampus in 8-week treated Syk x APP and Syk x APP x Cre-ERT animals (n=3/group Syk x APP and 2/group Syk x APP x Cre-ERT). In each graph the grey dots show Syk x APP animals, whereas blue identify Syk x APP x Cre-ERT. Each dot represents the average for 1 animal. Error bars show mean ±SD. All analysis was completed via two-way ANOVA. Values are shown above each graph with any significant findings in **bold.**

6.3 Discussion

6.3.1 Summary

The following chapter set to investigate what are the changes occurring in microglia caused by conditional depletion of *Syk* in myeloid cells in aged APP^{NL-G-F} animals. Two distinct timepoints were selected to induce *Syk* cKO, 8 weeks and 16 weeks. Both cohorts were aged until the same age (6 months) before conducting further analysis to identify differential impacts of treatment regimen on the pathology. Transcriptomic analysis was conducted to identify distinct microglia populations and the results revealed some intriguing changes associated with the loss of *Syk* in this mouse model irrespective of the cKO induction age. Additionally, these findings were paired with histological analysis aiming to characterise *Syk* cKO microglia and its influence on amyloid pathology.

6.3.2 Syk cKO modifies microglia transcriptome

Using transcriptomic approaches, the profile of microglia derived from *Syk* cKO and control mice was evaluated in the presence of Alzheimer's disease pathology. Investigating in detail the distribution of microglia across different clusters revealed that in cKO animals there is a reduction in clusters associated with disease. A bigger proportion of homeostatic microglia is present, especially HM2 populations. These populations have previously been reported as associated with a more 'fragile' state and are the first to complete DAM transitioning (137). Additionally, the results clearly identify a reduction in ARM cells irrespective of the cKO induction age.

These results are in accordance with the already published work by other groups revealing a similar response in the absence of *Syk*. Interestingly, the Wang et al. publication demonstrates a complete ablation of the DAM cluster (238). This difference could be related the either the background genetic strain of disease model utilised, or the tissue regions analysed. Here experiments were conducted using microglia derived from whole brain, rather than cortex only such as in the publication. The addition of brain regions such as the cerebellum, which is affected by pathology spread later, might partially explain the discrepancy and why here a 'milder' effect is observed.

In addition, differential expression changes were detected in a very few genes between different genotypes and treatment ages. When comparing to previously published work, a larger number of differential transcripts were identified. A potential explanation for this

might reside within the utilised mouse model. In this chapter all experiments were performed in APP^{NL-G-F} animals which is considered a more physiologically relevant model. The use of models such as the 5xFAD animals might show changes which are linked to APP overexpression rather than the function of the gene alone. Additionally, as mentioned earlier, the utilised brain regions might impact those comparisons as wells.

Importantly the response observed, mainly defined by reduction of microglia which express disease-associated patterns and markers, is uniform for both 8-week and 16-week treated mice. No major differences between the way microglia transcriptionally respond to the loss of *Syk* was detected based on the age of induction. This means that the response is uniform to microglia and is not influenced by disease associated hallmarks such as Aβ accumulation. Considering that genes such as *Clec7a*, *Trem2* and *Csf1*, all of which upstream of *Syk* activation, associated with altered expression in disease, demonstrate a reduction in this model of cKO. Cumulatively this evidence demonstrates that manipulating *Syk* expression in microglia might be key to modifying key response during AD development.

6.3.3 Deletion of *Syk* alters microglia density

Overall, the histological findings reveal that irrespective of the induction age of *Syk* cKO significant changes in microglia morphology are identified. In the absence of *Syk*, animals present with lower microglia numbers and density and do not show accumulation around amyloid deposits. The peri plaque analysis reveals that less microglia processes are found in close proximity and associated with Aβ plaques. The results indicate that cKO microglia lack the ability to migrate towards the plaque or react to the presence of plaques. These results suggest that *Syk* is involved in regulating key microglia functions and responses relevant to AD development.

Interestingly, the impact on amyloid accumulation is different depending on the age at which *Syk* cKO was induced. Animals treated at 16-weeks demonstrate no significant changes in amyloid accumulation. Interestingly this can be potentially explained by the stage of disease progression. At 16 weeks plaque deposits, especially in the cortex, are well established in the APP^{NL-G-F} mice, inducing the absence of *Syk* at this time is potentially not causing a significant impact on plaque burden when the plaques are established, however it is impacting microglia accumulation at the plaque. Furthermore, it is possible that if assessed at 9 months, for example, additional changes in plaque burden may be evident as a

consequence of *Syk* manipulation. When looking at the 8-week treated cohort significant increase in plaque deposition were noted in the cortex of the Syk-deficient mice compared to Syk-sufficient animals, but not the hippocampus. This highlights that the presence of *Syk* early in pathology might be key for modifying disease progression and limiting the pathology that continues into later life. The difference between the two cohorts identifies a key aspect of AD, in the context of treatment. It is very important when pathology will be targeted because once some histological changes occur, modifying *Syk* function might not be beneficial.

When comparing these findings to the already existing literature one thing is apparent. The changes observed in this study are not as extreme as what is reported in the other publications at the same age of the animals. Here we report significant differences in microglia morphology in the cortex and hippocampus for 16 week treated animals and also for 8 weeks but not many significant findings related to plaque accumulation. The main cause for this effect is most likely the background mouse strain utilised for the studies. As previously mentioned, both publications utilise the 5XFAD model of AD which has quicker disease progression and multiple familial AD mutations. This highlights the huge importance of the model of choice and the conclusions derived from it. Most likely, if the histological comparison was drawn using the APP^{NL-F} model at 6 months the response will be even more subtle due to the slower disease progression in that model.

Furthermore, the current publications in the field focus on only one timepoint where tamoxifen is administered, at around 6 weeks which is similar to the first cohort presented here. However, again considering the differences in the models, 5XFAD mice at 8 weeks of age already demonstrate plaque accumulation, but more importantly studies report gliosis from 2 months (174). This indicates that most likely transcriptional changes are already underway in these cells when cKO is induced. The data here indicates a protective early role of *Syk*. The later intervention timepoint has not been previously studied and may suggest that treatment later in disease progression might be beneficial for preventing neuroinflammation and further microglia activation.

Additionally, one main criticism of the already published work which we clearly address here is the absence of sex separation in any of the samples. Therefore, it is not possible to

guarantee these experiments were not conducted in only one sex or that the numbers between male and female animals are equal.

The observations made here suggest that the microglia response to accumulation of plaques in the absence of *Syk* is greatly impaired. Publications suggest that macrophages lacking Syk have impaired phagocytosis, however here the histological findings reveal that microglia do not associate with plaques. Therefore, this effect is more likely attributed to impaired motility in the absence of Syk which prevents microglia to migrate towards plaques or inability to detect plaques, which will point to an impaired surveillance.

6.3.4 Limitations

One of the main limitations of the work generated here is the small number of animals used for the histological analysis of the 8-week-old cohort. Although the main trend is present in these animals, further validation is required in a larger group of mice.

Additionally, using thioflavin S as a marker of amyloid staining is an established and well documented method in the literature. However, ThioS staining does not allow the identification of condensed and core plaques, therefore not providing enough detail to be able to detect any differences in the ratio between these which more accurately depicts disease stage.

Cx3cr1 heterozygosity is an important genetic feature of this model which should not be neglected when considering results. Importantly, the publication by Ennerfelt *et al*. also suggests this as a limitation to their study (239). Due to the key role of Cx3cr1 in microglia homeostasis, the effect caused by replacing one allele should be examined. Interestingly a recent publication revealed that Cx3cr1 heterozygosity is linked to improved Aβ clearance and reduces overall plaque load (375). It is important to consider these findings were documented in the APP-PS1 mouse model, therefore it cannot be concluded that the same effect will be observed in the $APP^{NL\text{-}G\text{-}F}$ mouse model. Importantly, any future work must include more controls to account for the Cx3cr1 heterozygosity in the model and to exclude any impact on the generated results.

Finally, although ScRNA-sequencing is an excellent method to identify the heterogenous microglial populations, there are some limitations that should be considered. Like outlined

in the previous chapter methanol fixation can significantly impact the detection of certain genes, therefore this data might fail to identify other key genes which are impacted.

6.3.5 Future directions

The work presented here highlights some interesting findings and provides the base for future investigations. Considering the transcriptomic findings, it will be particularly interesting to further explore this response. Since one of the main disadvantages of single-cell transcriptomics is that the precise location of the cells cannot be defined using more advanced technologies such as spatial transcriptomics and identify if there are any region-specific microglia responses would be an intriguing new experiment. These technologies have already been applied and validate key concepts such as the association of DAM microglia to amyloid plaques (376).

Additionally, here changes in microglia numbers and area coverage were identified. However, this analysis represents only the basic morphological 2D structure and does not provide detailed enough reconstruction to analyse individual cell structure. Doing more in-depth analysis where microglia processes can be traced might provide a better insight into how they respond in the absence of *Syk* and how this is linked to amyloid accumulation. Furthermore, the more detailed peri plaque analysis identified that microglia tend to not migrate towards the plaque and do not extend their process in that direction. Therefore, understanding the structural differences between the homeostatic and disease-associated microglia might be key to unravelling their functional response. In terms of the histological analysis, as described earlier additional plaque stains such as 6E10 and 4G8 can be used to identify different plaque structures.

As mentioned in the previous chapter, here the focus is mainly on the microglia specific response. However, in this model BAMs are also affected therefore the changes that occur within different BAM subtypes in the absence of *Syk* can also be a factor in disease progression and might further contribute to the pathological hallmarks. Recently, publications suggested that PVMs can contribute to plaque development via communication with microglia. This communication between different cell types is key and therefore further investigations to understand how *Syk* impacts BAMs would be potentially key to understanding these responses better. Furthermore, PVMs in particular might be an interesting target since *Syk* is known to have a role in the vascular system during

development and is expressed in cells from the hematopoietic lineage. Potentially histologically analysing the brain blood vessels might be a good approach since other recent work identified that plaques could be accumulated in the vasculature as well.

Microglia are known for their role in communicating and supporting the function of other cell types such as neurons and astrocytes. Here, the impact on astrocytes was reported but neurons were not investigated. Some future experiments will inevitably include understanding how neurons are impacted by the changes documented in microglia. This can include assessing viability and structure, incorporating neuronal spine density.

Most of the previous work associated with the kinase was based on mouse tau hyperphosphorylation models. Although this provides an insight into how deletion of *Syk* impacts other pathological hallmarks, these studies do not identify the role of microglia. Therefore, it would be interesting to conduct similarly designed studies but in models expressing tau to compare the response and identify any differences between the two. This also brings up the point of using multiple mouse models. As argued above, the changes reported in the APP^{NL-G-F} mouse model are a lot less severe than those identified with the 5XFAD animals. Therefore, repeating these studies using additional mouse models might reveal further how this response is altered based on the background genetic strain.

Additionally, here only the GFAP area % was evaluated. Further investigations might include analysing astrocyte numbers and morphology in more detail. As observed in the data here, no change in Iba1 immunoreactivity is reported, however significant changes in cell number are reported. This indicates that even though overall changes in the marker expression are not detected, potentially other parameters might reveal significant changes.

Importantly, a high priority aim in the neurodegenerative field is to be able to identify targets which can be modulated by pharmacological treatments and ultimately takes further as treatment options. Therefore, it is key that the findings presented here are further validated and translated into more human relevant models.

6.3.6 Conclusions

The following chapter presents some novel evidence about the role of *Syk* in the APP^{NL-G-F} mouse model of AD. The transcriptomic results clearly demonstrate a change in the microglia profile defined by larger proportion of homeostatic cells in comparison to DAM

clusters in controls. In addition, using functional approaches, changes in microglia number and distribution are reported upon *Syk* deletion irrespective of the cKO induction age. Additionally, the data demonstrates that *Syk* cKO can impact amyloid deposition early in disease progression but does not affect levels once plaques are present. This evidence conclusively suggests that *Syk* has an important role in regulating microglia responses in AD.

Chapter 7 General Discussion

7.1 Introduction

The overarching theme of this thesis was to use functional approaches to investigate how 2 different genes of interest, namely *PILRa* and *Syk* can impact microglia responses and how this can relate to AD pathology. Although a direct functional interaction between these 2 genes does not exist, or has not yet been confirmed, their molecular functions and responses represent a crucial mechanisms of microglia activation and inhibition, demonstrating two opposing strands which ultimately regulate the overall cell response and dictate what functional pathways prevail. Genomic and functional data conclusively demonstrates the role of microglia in AD (36, 377). However, there is a need to understand how individual genes can impact microglia responses in disease context. From functional studies it is clear that many microglia risk genes converge in common pathways therefore understanding the contribution of individual genes is key in targeting specific responses linked to neuroinflammation (372).

The following sections will very briefly recapitulate the existing evidence for the role of the 2 genes in AD and highlighting why studying their role in microglia represents an important part of the field and our understanding towards how microglia contribute to AD pathology.

7.1.1 PILRa

The role of the PILRa inhibitory receptor was first investigated in terms of immune responses related to different cell types such as natural killer cells and monocytes (193, 194). It was not until 2013 when the Lambert *et al*. GWAS study revealed that the *ZWCWP1* locus confers increased risk to AD (35). Some functional work later mapped this risk to PILRa and confirmed the presence of the G78R SNP within PILRa (201). It was demonstrated that the R78 PILRa variant is hypofunctional due to conformational changes located in the ligand binding pocket of the receptor causing decreased binding and subsequent activation. PILRa contains two ITIM domains which upon activation cause phosphorylation of cytoplasmic phosphatases and inhibition of signalling pathways. As part of the sialic acid binding family of receptors, PILRa can recognise and successfully bind sialic acid residues. The receptor has several functionally identified ligands, including PANP and CD99, however potentially can bind a number of ligands which present the correct glycosylation pattern (204, 378). Interestingly, PILRa can facilitate viral entry of HSV-1 through association with gB (191). PILRa signals via two ITIM domains which activate downstream phosphatases and counteract

kinase functions. The information about the role of PILRa in dementia stems largely from genetic studies and does not provide a comprehensive functional understanding of the downstream changes associated with the G78R variant. Therefore, this thesis aimed to generate and validate appropriate functional models to be utilised for understanding the functional impact of the G78R SNP within PILRa.

7.1.2 Syk

SYK is expressed in a variety of immune cells and has been shown to have a wider function in the peripheral immune system. Importantly, SYK activity in macrophages has been linked to phagocytosis and inflammatory responses associated with cytokine release (219, 221). In the context of AD, SYK has been previously studied for its role in neurons and tau hyperphosphorylation where kinases with the ability to add a phosphate group might be of particular interest (230). *Syk* is not an identified risk gene, however, is a part of a wider signalling network which includes various disease associated variants either upstream or downstream, including key microglia homeostatic genes such as *CSF1R*. The kinase contains multiple phosphorylation sites and can also be auto phosphorylated (379). SYK can be activated by an array of upstream signalling molecules containing ITAM domains such as DAP12. Phosphorylation of the kinase initiates signalling cascade downstream which leads to modulation of variety of cellular functions. Some known downstream mediators of *Syk* function include PLCG2 and NF-κB. The role of the kinase in the context of amyloid pathology is largely understudied. Additionally, most published work focuses on SYK in neurons or peripheral cells with very little evidence about the functional role of the kinase in microglia specifically (230, 236). Therefore, this thesis aimed to answer questions about how modifying *Syk* function in microglia impacts their role and disease progression.

7.2 Main findings

The next sections will summarise some of the main findings from individual results chapters and explore their impact and contribution to the overall field of existing literature.

7.2.1 *In vitro* models to study the function of G78R PILRa

A large proportion of this thesis focused on generating appropriate models to investigate the role of the G78R SNP within PILRa in microglia-relevant context. An initial aim of this study was to generate models which are appropriate for studying PILRa impact in AD. To date there are no models demonstrating how G78 and R78 PILRa expression in microglia can

influence AD-relevant processes. The work focusing on G78R PILRa here utilised two different *in vitro* cell culture models. Initially macrophage precursor cell lines with stable PILRa overexpression were successfully generated and validated. Additionally, this thesis presents the first functional evidence for the role of PILRa in microglia using disease-relevant model comprising of iPSC-derived microglia-like cells. Firstly, using immortalised macrophage lines, overexpression of PILRa demonstrated some alteration of functional responses in relation to cytokine secretion and potentially a trend towards phagocytic increase. The functional assays were further repeated and validated using iPS derived microglia-like cells. Although these two models aimed to investigate the function of the same genetic variant, the approaches are fundamentally different. Using lentiviral overexpression does not mimic the natural expression seen in patients and we aimed to correct that using the iPSC derived cultures. Additionally, although macrophages and microglia share some common properties and functions, ultimately there are differences in their developmental origins which should not be neglected.

Firstly, focusing on the role of PILRa in modulating cytokine responses upon stimulation. The cytokine work demonstrates that IL-10 responses are modulated in both M-MOPs and iPS derived microglia-like cells. Interestingly overexpression of PILRa, irrespective of the variant causes decrease in IL-10 and homozygous G78 microglia-like cells demonstrate the same response showing lower IL-10 levels compared to homozygous R78 cells. Interestingly, this might reveal that PILRa is involved in regulation of the anti-inflammatory cytokine and suggest that the protection of the R78 variant might reside within its ability to modulate inflammation more effectively. Interestingly, high IL-10 levels have been corelated with increased phagocytosis via upregulation of TREM2 (380). This suggests that the IL-10 response is important not just for mediating inflammation but for essential microglia functions and if regulated by PILRa this can have disease relevant consequences. The potential role of R78 in mediating inflammation better is further enhanced by the increased levels of IL-1β noted in the G78 homozygous microglia-like cells.

Some of the data between the M-MOPs and microglia-like cells might suggest that PILRa can regulate the levels of IL-12p40 as well since differences in secretion levels are demonstrated in both datasets. Although the direction of that regulation is not conclusive, IL-12p40 is linked to IL-23 and can modulate responses such as NOS production in microglia (381).

Altogether this data suggests that PILRa may be involved in regulating the levels of important pro and anti-inflammatory cytokines which in turn have a key role in mediating cell responses.

Using these two cell culture models in parallel provided some interesting insights into the differences between mouse and human interactions. The literature demonstrates that PILRa ligands are most likely very abundant but small evolutionary changes might have led to diverse functions between mouse and human PILRa (382). Interestingly, as previously mentioned, mCD99 binds both mouse PILRa and human PILRa. However, human CD99 has not been identified as a ligand for PILRa (378). This does not mean that there is not another ligand present in human cells which most likely produces the same response as CD99 does. In this thesis it was identified that PANP, another reported ligand of PILRa, can bind PILRa in human but not mouse cells. This is particularly interesting because it raises the question if there are other unidentified mouse ligands which can be potentially secreted by macrophages which bind to human PILRa. It also identifies that if mouse macrophages express endogenous PILRa ligands, this model might be very useful to further study PILRa functions.

Importantly, comparing the findings in this thesis to others in the field it is important to highlight some key differences. For example, the early work which identified R78 PILRa as hypofunctional did not use microglia-relevant models and only utilised human derived macrophages to test the virus infection rates in cells collected from donors expressing either R78 or G78 PILRa (201). Importantly, the background genetics of patients used for this study was not considered. Although this functional evidence suggests that R78 cells are less efficient at uptake of viral particles and demonstrate lower infection rates this does not necessarily relate to AD context. The response to PILRa stimulation might differ based on the stimulant and virus uptake does not conclusively suggest that similar mechanism will occur in microglia. Additionally, the study does not provide any information about the functional outcome of PILRa activation. Functionally validating the ligand-receptor differences reported has proven challenging based on the experiments included in this thesis. Although a clear difference between mouse and human cell lines can be seen, the binding difference in iPS derived microglia-like cells clones with different PILRa variants was not conclusively different.

Additionally, trying to draw direct parallel between published studies on the role of PILRa and this thesis is challenging. Most work focusing on the role of the receptor is not considering the AD relevant SNP but utilized knock-out models in mice instead (193, 383). Although human and mouse PILRa might share similar function as previously discussed there are functionally reported differences between their ability to identify and bind ligands. This means that most likely the downstream signalling and initial activation linked to ligand presentation could be evolutionary different. There might be ligands on cell types present in mouse that have been evolutionary replaced in human and vice versa, so comparing this work will not necessarily provide relevant context.

Finally, no conclusive significant data from any of the other functional assays was reported, therefore it is important to consider additional approaches which will be outlined later in this chapter. To draw conclusions on the effect of the G78R SNP on microglia functions, more biological replicates of the differentiation and individual homozygous clones are required.

7.2.2 The role of *Syk* in microglia in AD mouse model

The second part of this thesis focused on validating *Syk* cKO mouse model and understanding the function of the gene in AD context. The work presented in Chapter 5 and 6 demonstrates convincing evidence for the efficiency of the cKO and provides a reproducible protocol to be used in mouse models.

The transcriptomic work identifies key responses in microglia where cKO of *Syk* was induced. Interestingly, microglia derived from animals which were *Syk*-deficient exhibited a shift in the transcriptomic profile towards homeostatic cells and decrease in ARM and overall DAM clusters. This response was recapitulated across all age groups. Combining this evidence with the results presented in Chapter 5, which are the only existing work focusing on the early response of microglia to *Syk* deletion, some speculations can be made. The pathways identified to be regulated shortly after *Syk* deletion all represented an overarching theme of metabolic regulation. Interestingly, modulation of some of these pathways might be linked to what is later observed in the aged cohort in Chapter 6. The decrease of DAM response is particularly intriguing due to its relevance for disease progression. Publications reveal that DAM transitioning is a two-stage process involving induction of different microglia genes (152). The initial stage is TREM2 independent and since TREM2 activation is linked to *Syk* activation this is of particular interest and expected to be impaired. The first stage in DAM

transitioning however is TREM2 independent but also seem to be impacted on a transcriptomic level. This points that *Syk* regulates pathways which are independent of TREM2 signalling and might be activated by other upstream receptors such as CSF1R (384). Also interestingly, the early transcriptional pathways linked to metabolism highlight changes in lipid processing in the *Syk*-deficient cells which has been identified previously as part of the DAM response (385).

In addition, the histological work demonstrates a very clear microglia phenotype in the absence of *Syk*. Interestingly *Syk* deletion ablates the ability of microglia to identify and migrate towards amyloid deposits. The altered microglia profile reported here is in conjunction with already reported findings in a different mouse model (239). This is particularly important because it shows that the findings are replicated, and the phenotype is reproducible in different genetic backgrounds. The differences between the two models are most apparent in relation to amyloid plaque deposition.

Recently published work suggested that *Syk* is a desirable treatment target (386), however this might be too optimistic. A lot more consideration needs to be given to the role of *Syk* in immune responses. Interestingly mutations linked to *Syk* hyperactivity can cause severe immune deficiency and dysregulated inflammation both in humans and mice (387). Furthermore, polymorphisms in *Syk* which lead to gain-of-function and high kinase activity have been linked to systemic inflammation (388). The study by Wang *et al*. demonstrates that both in human and mouse models, germline mutations enhancing *Syk* activity are linked to immunodeficiency and immune dysregulation of multiple pathways. This highlights that for *Syk* to be a viable treatment target, the treatment would need to be very selective and most likely will require prior screening.

Interestingly, *Syk* inhibition seems to be detrimental in terms of amyloid pathology but has shown some promising improvement regarding tau pathology and hyperphosphorylation levels (389, 390). This highlights the dual role the kinase might have depending on the cell type but also the drawbacks linked to using transgenic mouse models. Most studies use a model which either contains amyloid plaques or tangles but not both, which does not fully recapitulate the complexity of AD which occurs in patients. Using *Syk* as a treatment target might prove challenging and improve one disease aspect but worsen another. Just recently, a publication evaluated the use of Syk inhibitors in microglia culture in relation to neuronal

health (391). The study utilised a primary co-culture method and used LPS as a stimulant of inflammation. Interestingly the study reports that in the absence of LPS, microglia viability and density are impacted by Syk inhibition which is in accordance with *in vivo* data. Additionally, the authors report some findings linked to release of inflammatory cytokines which highlights the need to explore these responses more in depth using in vivo models.

As previously mentioned, *Syk* is not an AD risk gene as it does not reach genome wide significance. However, the kinase has been linked to other known AD risk targets. In a publication by Sierksma *et al*. using various sequencing methods, *Syk* is identified to belong to a wider network of genes involved in the Aβ response (336). The kinase and 17 other genes were found to be upregulated upon exposure to amyloid and were all identified in a common network regulated by *Spi1*, a known AD risk gene. Other genes identified were *CLU*, *PLCG2* and *CD33*. The publication further suggests that these genes might have an import role in contributing to the overall polygenic risk and that SYK can provide a potential link between amyloid and tau pathology. This highlights that the role of SYK is essential in regulating crucial microglia pathways in disease and that its function might have a key impact on disease progression and contribute to overall polygenic risk score.

Another very recent publication, also highlights the importance of *Syk* (392). Using single-cell transcriptomic approaches on human data, Syk is identified as a hub gene in a microglia network enriched during aging. This is of particular importance because aging remains the highest risk factor for developing AD. Interestingly, the network regulated by the gene includes other known AD targets such as *Spi1* and *Abi3*. This demonstrates that changes associated with *Syk* might result in regulation of other key microglia functions such as transcription and motility. Overall, when we assess the response of *Syk* in microglia, this should not be done in isolation. The experimental work conducted here demonstrates the vast number of pathways and processes which might be directly influenced by changes in *Syk* expression.

7.3 Balance between ITAM and ITIM signalling in microglia

The role of microglia has been the focus of extensive research since evidence from GWAS studies identified a large proportion of immune genes restricted to microglia were linked to increased risk of AD (36, 39, 377, 393). In the past decade, a high number of publications using both *in vivo* and *in vitro* approached have tried to dissect how microglia contribute and

regulate disease progression (reviewed in (394)). Transcriptomic studies recognised the heterogeneity of microglia and revealed how dynamic these cells are during AD progression as reviewed in (395). These findings coupled with better understanding of the different hallmarks present in AD suggest that microglia might have a dual role in disease development. Although considered protective based on their surveillance and phagocytic functions, many reports suggest that continued inflammation induced by cytokine release and synapse engulfment could contribute to pathology development and modulate severity (396). Therefore, it is key to identify at what stages targeting the microglia response will be helpful. Enhancing microglia functions might be beneficial in some cases but identifying ways to dampen the inflammatory response can also prove advantageous. Understanding how different genes regulate microglia activation and inhibition can provide better ways to target this. As demonstrated in this thesis, using transcriptomic approaches can provide a useful way to find precise pathways and the direction at which they are functionally controlled. The balance between activation and inhibition will ultimately determine the functional outcome. Research in the peripheral immune system has demonstrated that fine regulation is required for proper immune responses and dysfunction can lead to multiple disease conditions (397). Therefore, immune dysregulation in the CNS caused by a combination of genetic variants orchestrating microglia activation or inhibition can not only contribute to disease progression but most likely be involved in the onset of pathology. Most immune receptors evolutionary belong to a family where a different molecule would have evolved to counteract that function. PILRa is an accurate example of this as an inhibitory receptor with its paired PILRb signalling via DAP12 to deliver activation signals. Additionally, in the literature there is evidence that if some of these responses are lost, they can be overcome by compensatory mechanisms from a different pathway. For example, CSF1R conditional deletion leads to upregulation of TREM2 signalling (361).

The existing GWAS evidence suggests that defects in activation receptors are conferred to increase in AD risk (e.g., TREM2) (398) whereas defects in inhibitory receptors are associated with protective effect (e.g., CD33) (165). This highlights that microglia activation might be more important than inhibition for the onset of AD. Additionally, potentially chronically low microglia activation might be linked to quicker progression and more severe phenotype. This evidence might suggest that boosting microglia activation might be the correct approach to

treating AD and targeting associated pathological hallmarks (399). However, simply activating microglia will be an oversimplified approach disregarding the complex signalling pathways and the importance of balanced signalling. Prolonged microglia activation can have just as detrimental effect as low activation to disease progression leading to chronic inflammation. In normal healthy individual microglia responses are tightly regulated and well balanced through timed exposure of specific ligands and signals from surrounding cells in the microenvironment. Therefore, any future treatments targeting microglia and proteins which are involved in their regulation must be based on precise timed exposure, therefore highlighting the necessity for better understanding of the regulation of these pathways.

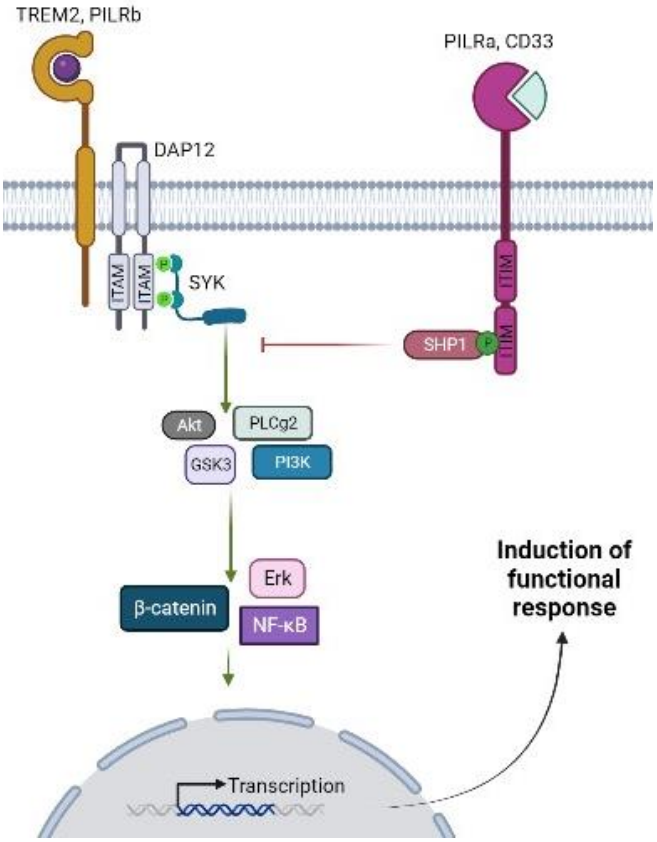

Figure 7.1: Regulation of microglia activation and inhibition. Signalling output is controlled by induction of activation and inhibition receptors. Activation of ITAM containing receptors (e.g., TREM2, PILRb) leads to recruitment of DAP12 and subsequent phosphorylation of SYK. SYK can activate multiple downstream targets and pathways, leading to induction of inflammatory gene expression and resulting in a functional response. Opposing this, ITIM receptors (e.g., PILRa, CD33) can activate phosphatases such as SHP1/2. Phosphatases dephosphorylate kinases leading to activation of alternative pathways and gene expression responses.

7.4 Future directions

7.4.1 PILRa

Based on the lack of conclusive functional response and irregularity between the responses of different homozygous clones, the future work to identify the role of PILRa in microglia needs to address these issues.

First, more homozygous clones expressing G78 PILRa will be generated. To potentially boost the CRISPR-Cas9 efficiency which proved to be very low with the utilised guide, additional guide can be designed, and the efficiency can be tested in advance using T7EI assay. Additionally, even if more clones are available to validate the results, no large changes in the response are reported, and this can be potentially attributed to the assays chosen here. The array of phenotypic assays was selected based on already established protocols in the lab and due to the relevance to microglia function. However, these assays only capture a small proportion of microglia function. For instance, in this thesis the role of phagocytosis was most widely explored, as well as including some endocytic assays. However, only one variation of cargo was used, therefore differences which might exist when more biologically relevant cargo is used could not be ruled out. For example, using apoptotic neurons and exploring other ways of uptake such as macropinocytosis might be a potential future investigation.

Furthermore, there is a possibility that PILRa regulates other microglia functions which were not captured here. To better identify pathways regulated by PILRa, ScRNA-sequencing can be completed which will reveal downstream molecular interactions and allow selection of more appropriate functional assays. This is a common trend when investigating single nucleotide polymorphisms where the changes observed are not as compelling as in KO models, therefore more targeted approach might be required. A publication by Hall-Roberts *et al*. exploring the R74H mutation in TREM2 using iPS derived microglia-like cells demonstrated no significant differences in the variant when using common microglia assays but managed to identify pathways linked to adhesion using sequencing methods (163). This highlights why sometimes more in-depth approaches are required and potentially why it is challenging to identify any significant changes driven by G78 expression.

Some recently published work demonstrates that PILRa might be linked to modulating APOE4 risk (209). Based on the heterogeneity of AD, it is important for such interactions to

be followed functionally and explored in more detail. Therefore, some future studies can include cell lines combining different risk variants of PILRa and APOE to investigate what the combinatorial effect associated with the increased risk might be.

Additionally, here some interesting findings regarding the PANP ligand in PILRa were identified. Since PILRa functions as an inhibitory receptor activated by a ligand on the cell surface, it is particularly important to study in more detail how the receptor will respond to different stimuli. This can potentially be done in a more complex co-culture system where PILRa expressing microglia is combined with astrocytes or neurons, which are predicted to express and secrete PILRa ligands (206). Such model system would mimic a more accurate *in vivo* environment and will enhance cell-cell interaction responses which might further contribute to identifying differences with the associated G78R variant.

Importantly, in this thesis most of the work related to validating and identifying a successful PILRa ligand was concerned with the cell-surface level binding and utilised flow-cytometric approaches to quantify this. However, it will be beneficial to conduct further studies which explore the intracellular consequences of PILRa activation. Using molecular techniques such as Western blotting, the levels of phosphatases downstream of PILRa can be identified as well as if their activity changes upon stimulation with a ligand which might provide more conclusive evidence of the direct interaction between receptor and ligand. Additionally, evaluating the levels of phosphorylated kinases like SYK which work in the opposing strand of the pathway might also reveal how PILRa interaction counteracts specific pathways and works in conjunction with activation receptors. More importantly, focusing on direct downstream targets will provide a more detailed picture of what molecules PILRa regulates and how induction is translated to functional responses. This will further reveal if there are downstream functional consequences linked to the G78R variant because all existing evidence focuses on the ligand binding site and predicts less binding, however a feedback mechanism might exist or activation of alternative receptor which can compensate for this effect.

7.4.2 Syk

The work presented here in relation to *Syk* function is focused on using a mouse model of AD. Taking into account the disadvantages linked to the use of mouse models and the

underlying genetic differences, ideally the data generated here would be replicated in more human relevant model such as iPSC derived microglia or chimeric models.

Since *Syk* has been linked to multiple AD risk variants and converges in many common microglia signalling pathways it is key to study the role of the gene in conjunction with the other variants. Combining different AD variants and modulating *Syk* function to understand how this can alter the functional response would be particularly useful. Because *Syk* lies downstream of many receptors any dysfunction in them might be overcome through altering the gene function.

Additionally, here the transcriptomic response has been investigated at two different disease development ages. It would be interesting to continue this work by conducting some proteomics studies as well. Although transcriptionally we see a lot of changes it would be useful to validate that these findings translate on a protein level. Additionally, since *Syk* has the ability of autophosphorylation itself it might be interesting the investigate what are the targets associated with activation of the kinase.

Furthermore, most of the presented data focused on microglia morphology and amyloid responses. Ideally some future experiments will focus on the effect of the altered microglia response on neuronal health and synapse functions to evaluate this in more detail.

7.4.3 Overall

As previously established, AD is a highly polygenic disease. Studying genes in isolation can be beneficial to identify their primary functions, especially when they are newly emerging targets in genetic studies. However, this approach does not fully recapitulate the complexity of the disease. Ultimately, targeting individual genes is very unlikely to produce significant response and modulate disease progression equally in every individual. Therefore, the need to study genetic networks in parallel is becoming more and more apparent. In the context of this thesis, both PILRa and Syk belong to a wider network of mediators and interact with multiple identified risk variants, therefore their role should not be observed in isolation. This also highlights the need to create more complex models where multiple genetic factors are combined and the overall outcome is evaluated, which can provide valuable information about which combination of genetic variants contributes more to the overall disease outcome.

7.5 Conclusions

The overarching theme of this project has linked opposing pathways, activation and inhibition and their role in regulating microglia functions. The balance between these functions determines the ultimate cell signalling response. The data presented in this thesis highlights the importance of using different models which best answer the identified research questions. It further highlights the complexity of both PILRa and *Syk* and the variation of pathways that these genes are able to regulate. The overall field of AD research needs to further focus on how microglia activation and inhibition can be altered by different genetic variants, to be able to design appropriate treatments, especially when targeting immune responses.

In this thesis the first human microglia relevant *in vitro* model to study the function of the G78R PILRa variant was presented, combined with the use of functional response to expand our understanding of the variant impact on disease relevant functions. Additionally, novel findings revealing the transcriptomic response in microglia associated with deletion of the *Syk* kinase in the APP^{NL-G-F} mouse model were presented. The data supports the role of the *Syk* kinase as key regulator of microglia responses in disease and its ability to modify amyloid pathology.

Bibliography

1. Masters CL, Bateman R, Blennow K, Rowe CC, Sperling RA, Cummings JL. Alzheimer's disease. Nature reviews Disease primers. 2015;1:15056. doi: 10.1038/nrdp.2015.56
2. Bondi MW, Edmonds EC, Salmon DP. Alzheimer's Disease: Past, Present, and Future. J Int Neuropsychol Soc. 2017;23(9-10):818-31. doi: 10.1017/s135561771700100x
3. Massoud F, Léger GC. Pharmacological treatment of Alzheimer disease. Canadian journal of psychiatry Revue canadienne de psychiatrie. 2011;56(10):579-88. doi: 10.1177/070674371105601003
4. Hampel H, Mesulam MM, Cuello AC, Farlow MR, Giacobini E, Grossberg GT, et al. The cholinergic system in the pathophysiology and treatment of Alzheimer's disease. Brain. 2018;141(7):1917-33. doi: 10.1093/brain/awy132
5. Budd Haeberlein S, Aisen PS, Barkhof F, Chalkias S, Chen T, Cohen S, et al. Two Randomized Phase 3 Studies of Aducanumab in Early Alzheimer's Disease. J Prev Alzheimers Dis. 2022;9(2):197-210. doi: 10.14283/jpad.2022.30
6. Takahashi RH, Nagao T, Gouras GK. Plaque formation and the intraneuronal accumulation of beta-amyloid in Alzheimer's disease. Pathology international. 2017;67(4):185-93. doi: 10.1111/pin.12520
7. Murphy MP, LeVine H, 3rd. Alzheimer's disease and the amyloid-beta peptide. Journal of Alzheimer's disease : JAD. 2010;19(1):311-23. doi: 10.3233/jad-2010-1221
8. Sgourakis NG, Yan Y, McCallum SA, Wang C, Garcia AE. The Alzheimer's peptides Abeta40 and 42 adopt distinct conformations in water: a combined MD / NMR study. J Mol Biol. 2007;368(5):1448-57. doi: 10.1016/j.jmb.2007.02.093
9. Du X, Wang X, Geng M. Alzheimer's disease hypothesis and related therapies. Transl Neurodegener. 2018;7:2. doi: 10.1186/s40035-018-0107-y
10. Medeiros R, Baglietto-Vargas D, LaFerla FM. The role of tau in Alzheimer's disease and related disorders. CNS Neurosci Ther. 2011;17(5):514-24. doi: 10.1111/j.1755-5949.2010.00177.x
11. Wu JW, Hussaini SA, Bastille IM, Rodriguez GA, Mrejeru A, Rilett K, et al. Neuronal activity enhances tau propagation and tau pathology in vivo. Nat Neurosci. 2016;19(8):1085-92. doi: 10.1038/nn.4328
12. Vossel KA, Beagle AJ, Rabinovici GD, Shu H, Lee SE, Naasan G, et al. Seizures and epileptiform activity in the early stages of Alzheimer disease. JAMA Neurol. 2013;70(9):1158-66. doi: 10.1001/jamaneurol.2013.136
13. Palop JJ, Chin J, Roberson ED, Wang J, Thwin MT, Bien-Ly N, et al. Aberrant excitatory neuronal activity and compensatory remodeling of inhibitory hippocampal circuits in mouse models of Alzheimer's disease. Neuron. 2007;55(5):697-711. doi: 10.1016/j.neuron.2007.07.025
14. Palop JJ, Mucke L. Epilepsy and cognitive impairments in Alzheimer disease. Arch Neurol. 2009;66(4):435-40. doi: 10.1001/archneurol.2009.15
15. Shankar GM, Bloodgood BL, Townsend M, Walsh DM, Selkoe DJ, Sabatini BL. Natural oligomers of the Alzheimer amyloid-beta protein induce reversible synapse loss by modulating an NMDA-type glutamate receptor-dependent signaling pathway. The Journal of neuroscience : the official journal of the Society for Neuroscience. 2007;27(11):2866-75. doi: 10.1523/jneurosci.4970-06.2007
16. Ghatak S, Dolatabadi N, Trudler D, Zhang X, Wu Y, Mohata M, et al. Mechanisms of hyperexcitability in Alzheimer's disease hiPSC-derived neurons and cerebral organoids vs isogenic controls. Elife. 2019;8. doi: 10.7554/eLife.50333
17. Larner AJ, Doran M. Clinical phenotypic heterogeneity of Alzheimer's disease associated with mutations of the presenilin-1 gene. Journal of neurology. 2006;253(2):139-58. doi: 10.1007/s00415-005-0019-5
18. Busch RM, Lineweaver TT, Naugle RI, Kim KH, Gong Y, Tilelli CQ, et al. ApoE-epsilon4 is associated with reduced memory in long-standing intractable temporal lobe epilepsy. Neurology. 2007;68(6):409-14. doi: 10.1212/01.wnl.0000253021.60887.db

19. Ponomareva NV, Selesneva ND, Jarikov GA. EEG alterations in subjects at high familial risk for Alzheimer's disease. Neuropsychobiology. 2003;48(3):152-9. doi: 10.1159/000073633
20. Tanaka S, Kondo H, Kanda K, Ashino T, Nakamachi T, Sekikawa K, et al. Involvement of interleukin-1 in lipopolysaccaride-induced microglial activation and learning and memory deficits. Journal of neuroscience research. 2011;89(4):506-14. doi: 10.1002/jnr.22582
21. Rogers JT, Morganti JM, Bachstetter AD, Hudson CE, Peters MM, Grimmig BA, et al. CX3CR1 deficiency leads to impairment of hippocampal cognitive function and synaptic plasticity. The Journal of neuroscience : the official journal of the Society for Neuroscience. 2011;31(45):16241-50. doi: 10.1523/jneurosci.3667-11.2011
22. Costello DA, Lyons A, Denieffe S, Browne TC, Cox FF, Lynch MA. Long term potentiation is impaired in membrane glycoprotein CD200-deficient mice: a role for Toll-like receptor activation. The Journal of biological chemistry. 2011;286(40):34722-32. doi: 10.1074/jbc.M111.280826
23. Cacace R, Sleegers K, Van Broeckhoven C. Molecular genetics of early-onset Alzheimer's disease revisited. Alzheimers Dement. 2016;12(6):733-48. doi: 10.1016/j.jalz.2016.01.012
24. Weggen S, Beher D. Molecular consequences of amyloid precursor protein and presenilin mutations causing autosomal-dominant Alzheimer's disease. Alzheimer's research & therapy. 2012;4(2):9. doi: 10.1186/alzrt107
25. Coon KD, Myers AJ, Craig DW, Webster JA, Pearson JV, Lince DH, et al. A high-density whole-genome association study reveals that APOE is the major susceptibility gene for sporadic late-onset Alzheimer's disease. J Clin Psychiatry. 2007;68(4):613-8. doi: 10.4088/jcp.v68n0419
26. Torres-Perez E, Ledesma M, Garcia-Sobreviela MP, Leon-Latre M, Arbones-Mainar JM. Apolipoprotein E4 association with metabolic syndrome depends on body fatness. Atherosclerosis. 2016;245:35-42. doi: 10.1016/j.atherosclerosis.2015.11.029
27. Huang Y, Mahley RW. Apolipoprotein E: structure and function in lipid metabolism, neurobiology, and Alzheimer's diseases. Neurobiol Dis. 2014;72 Pt A:3-12. doi: 10.1016/j.nbd.2014.08.025
28. Innerarity TL, Mahley RW. Enhanced binding by cultured human fibroblasts of apo-E-containing lipoproteins as compared with low density lipoproteins. Biochemistry. 1978;17(8):1440-7. doi: 10.1021/bi00601a013
29. Sienski G, Narayan P, Bonner JM, Kory N, Boland S, Arczewska AA, et al. APOE4 disrupts intracellular lipid homeostasis in human iPSC-derived glia. Sci Transl Med. 2021;13(583). doi: 10.1126/scitranslmed.aaz4564
30. Montagne A, Nikolakopoulou AM, Huuskonen MT, Sagare AP, Lawson EJ, Lazic D, et al. APOE4 accelerates advanced-stage vascular and neurodegenerative disorder in old Alzheimer's mice via cyclophilin A independently of amyloid-β. Nat Aging. 2021;1(6):506-20. doi: 10.1038/s43587-021-00073-z
31. Krasemann S, Madore C, Cialic R, Baufeld C, Calcagno N, El Fatimy R, et al. The TREM2-APOE Pathway Drives the Transcriptional Phenotype of Dysfunctional Microglia in Neurodegenerative Diseases. Immunity. 2017;47(3):566-81.e9. doi: 10.1016/j.immuni.2017.08.008
32. Lambert JC, Heath S, Even G, Campion D, Sleegers K, Hiltunen M, et al. Genome-wide association study identifies variants at CLU and CR1 associated with Alzheimer's disease. Nat Genet. 2009;41(10):1094-9. doi: 10.1038/ng.439
33. Naj AC, Jun G, Beecham GW, Wang LS, Vardarajan BN, Buros J, et al. Common variants at MS4A4/MS4A6E, CD2AP, CD33 and EPHA1 are associated with late-onset Alzheimer's disease. Nat Genet. 2011;43(5):436-41. doi: 10.1038/ng.801
34. Hollingworth P, Harold D, Sims R, Gerrish A, Lambert JC, Carrasquillo MM, et al. Common variants at ABCA7, MS4A6A/MS4A4E, EPHA1, CD33 and CD2AP are associated with Alzheimer's disease. Nat Genet. 2011;43(5):429-35. doi: 10.1038/ng.803
35. Lambert JC, Ibrahim-Verbaas CA, Harold D, Naj AC, Sims R, Bellenguez C, et al. Meta-analysis of 74,046 individuals identifies 11 new susceptibility loci for Alzheimer's disease. Nat Genet. 2013;45(12):1452-8. doi: 10.1038/ng.2802

36. Sims R, van der Lee SJ, Naj AC, Bellenguez C, Badarinarayan N, Jakobsdottir J, et al. Rare coding variants in PLCG2, ABI3, and TREM2 implicate microglial-mediated innate immunity in Alzheimer's disease. Nat Genet. 2017;49(9):1373-84. doi: 10.1038/ng.3916
37. Jansen IE, Savage JE, Watanabe K, Bryois J, Williams DM, Steinberg S, et al. Genome-wide meta-analysis identifies new loci and functional pathways influencing Alzheimer's disease risk. Nat Genet. 2019;51(3):404-13. doi: 10.1038/s41588-018-0311-9
38. Bellenguez C, Küçükali F, Jansen IE, Kleineidam L, Moreno-Grau S, Amin N, et al. New insights into the genetic etiology of Alzheimer's disease and related dementias. Nat Genet. 2022;54(4):412-36. doi: 10.1038/s41588-022-01024-z
39. Escott-Price V, Bellenguez C, Wang LS, Choi SH, Harold D, Jones L, et al. Gene-wide analysis detects two new susceptibility genes for Alzheimer's disease. PloS one. 2014;9(6):e94661. doi: 10.1371/journal.pone.0094661
40. Maurano MT, Humbert R, Rynes E, Thurman RE, Haugen E, Wang H, et al. Systematic localization of common disease-associated variation in regulatory DNA. Science. 2012;337(6099):1190-5. doi: 10.1126/science.1222794
41. Nott A, Holtman IR, Coufal NG, Schlachetzki JCM, Yu M, Hu R, et al. Brain cell type-specific enhancer-promoter interactome maps and disease-risk association. Science. 2019;366(6469):1134-9. doi: 10.1126/science.aay0793
42. Euesden J, Lewis CM, O'Reilly PF. PRSice: Polygenic Risk Score software. Bioinformatics. 2015;31(9):1466-8. doi: 10.1093/bioinformatics/btu848
43. Escott-Price V, Shoai M, Pither R, Williams J, Hardy J. Polygenic score prediction captures nearly all common genetic risk for Alzheimer's disease. Neurobiol Aging. 2017;49:214.e7-.e11. doi: 10.1016/j.neurobiolaging.2016.07.018
44. Jones L, Holmans PA, Hamshere ML, Harold D, Moskvina V, Ivanov D, et al. Genetic evidence implicates the immune system and cholesterol metabolism in the aetiology of Alzheimer's disease. PLoS One. 2010;5(11):e13950. doi: 10.1371/journal.pone.0013950
45. Carpanini SM, Torvell M, Morgan BP. Therapeutic Inhibition of the Complement System in Diseases of the Central Nervous System. Front Immunol. 2019;10:362. doi: 10.3389/fimmu.2019.00362
46. Cribbs DH, Berchtold NC, Perreau V, Coleman PD, Rogers J, Tenner AJ, et al. Extensive innate immune gene activation accompanies brain aging, increasing vulnerability to cognitive decline and neurodegeneration: a microarray study. J Neuroinflammation. 2012;9:179. doi: 10.1186/1742-2094-9-179
47. Raj D, Yin Z, Breur M, Doorduin J, Holtman IR, Olah M, et al. Increased White Matter Inflammation in Aging- and Alzheimer's Disease Brain. Front Mol Neurosci. 2017;10:206. doi: 10.3389/fnmol.2017.00206
48. Scheld M, Rüther BJ, Große-Veldmann R, Ohl K, Tenbrock K, Dreymüller D, et al. Neurodegeneration Triggers Peripheral Immune Cell Recruitment into the Forebrain. The Journal of neuroscience : the official journal of the Society for Neuroscience. 2016;36(4):1410-5. doi: 10.1523/jneurosci.2456-15.2016
49. Stalder AK, Ermini F, Bondolfi L, Krenger W, Burbach GJ, Deller T, et al. Invasion of hematopoietic cells into the brain of amyloid precursor protein transgenic mice. The Journal of neuroscience : the official journal of the Society for Neuroscience. 2005;25(48):11125-32. doi: 10.1523/jneurosci.2545-05.2005
50. Zuroff L, Daley D, Black KL, Koronyo-Hamaoui M. Clearance of cerebral Aβ in Alzheimer's disease: reassessing the role of microglia and monocytes. Cell Mol Life Sci. 2017;74(12):2167-201. doi: 10.1007/s00018-017-2463-7
51. Ferretti MT, Merlini M, Späni C, Gericke C, Schweizer N, Enzmann G, et al. T-cell brain infiltration and immature antigen-presenting cells in transgenic models of Alzheimer's disease-like cerebral amyloidosis. Brain Behav Immun. 2016;54:211-25. doi: 10.1016/j.bbi.2016.02.009

52. Merlini M, Kirabali T, Kulic L, Nitsch RM, Ferretti MT. Extravascular CD3+ T Cells in Brains of Alzheimer Disease Patients Correlate with Tau but Not with Amyloid Pathology: An Immunohistochemical Study. Neurodegener Dis. 2018;18(1):49-56. doi: 10.1159/000486200
53. Sweeney MD, Sagare AP, Zlokovic BV. Blood–brain barrier breakdown in Alzheimer disease and other neurodegenerative disorders. Nature Reviews Neurology. 2018;14(3):133-50. Available from: https://doi.org/10.1038/nrneurol.2017.188doi: 10.1038/nrneurol.2017.188
54. Iturria-Medina Y, Sotero RC, Toussaint PJ, Mateos-Pérez JM, Evans AC. Early role of vascular dysregulation on late-onset Alzheimer's disease based on multifactorial data-driven analysis. Nat Commun. 2016;7:11934. doi: 10.1038/ncomms11934
55. Xu X, Meng T, Wen Q, Tao M, Wang P, Zhong K, et al. Dynamic changes in vascular size and density in transgenic mice with Alzheimer's disease. Aging (Albany NY). 2020;12(17):17224-34. doi: 10.18632/aging.103672
56. Yang AC, Vest RT, Kern F, Lee DP, Agam M, Maat CA, et al. A human brain vascular atlas reveals diverse mediators of Alzheimer's risk. Nature. 2022;603(7903):885-92. doi: 10.1038/s41586-021-04369-3
57. Stassart RM, Möbius W, Nave KA, Edgar JM. The Axon-Myelin Unit in Development and Degenerative Disease. Front Neurosci. 2018;12:467. doi: 10.3389/fnins.2018.00467
58. Bartzokis G, Beckson M, Lu PH, Nuechterlein KH, Edwards N, Mintz J. Age-related changes in frontal and temporal lobe volumes in men: a magnetic resonance imaging study. Arch Gen Psychiatry. 2001;58(5):461-5. doi: 10.1001/archpsyc.58.5.461
59. Chu TH, Cummins K, Sparling JS, Tsutsui S, Brideau C, Nilsson KPR, et al. Axonal and myelinic pathology in 5xFAD Alzheimer's mouse spinal cord. PLoS One. 2017;12(11):e0188218. doi: 10.1371/journal.pone.0188218
60. McKenzie AT, Moyon S, Wang M, Katsyv I, Song WM, Zhou X, et al. Multiscale network modeling of oligodendrocytes reveals molecular components of myelin dysregulation in Alzheimer's disease. Mol Neurodegener. 2017;12(1):82. doi: 10.1186/s13024-017-0219-3
61. Lee JW, Lee YK, Yuk DY, Choi DY, Ban SB, Oh KW, et al. Neuro-inflammation induced by lipopolysaccharide causes cognitive impairment through enhancement of beta-amyloid generation. J Neuroinflammation. 2008;5:37. doi: 10.1186/1742-2094-5-37
62. Blasko I, Veerhuis R, Stampfer-Kountchev M, Saurwein-Teissl M, Eikelenboom P, Grubeck-Loebenstein B. Costimulatory effects of interferon-gamma and interleukin-1beta or tumor necrosis factor alpha on the synthesis of Abeta1-40 and Abeta1-42 by human astrocytes. Neurobiol Dis. 2000;7(6 Pt B):682-9. doi: 10.1006/nbdi.2000.0321
63. Habib N, McCabe C, Medina S, Varshavsky M, Kitsberg D, Dvir-Szternfeld R, et al. Disease-associated astrocytes in Alzheimer's disease and aging. Nat Neurosci. 2020;23(6):701-6. doi: 10.1038/s41593-020-0624-8
64. Veitch DP, Weiner MW, Aisen PS, Beckett LA, Cairns NJ, Green RC, et al. Understanding disease progression and improving Alzheimer's disease clinical trials: Recent highlights from the Alzheimer's Disease Neuroimaging Initiative. Alzheimers Dement. 2019;15(1):106-52. doi: 10.1016/j.jalz.2018.08.005
65. Dejakaisaya H, Harutyunyan A, Kwan P, Jones NC. Altered metabolic pathways in a transgenic mouse model suggest mechanistic role of amyloid precursor protein overexpression in Alzheimer's disease. Metabolomics. 2021;17(5):42. doi: 10.1007/s11306-021-01793-4
66. Swerdlow RH, Parks JK, Cassarino DS, Maguire DJ, Maguire RS, Bennett JP, Jr., et al. Cybrids in Alzheimer's disease: a cellular model of the disease? Neurology. 1997;49(4):918-25. doi: 10.1212/wnl.49.4.918
67. Ginhoux F, Lim S, Hoeffel G, Low D, Huber T. Origin and differentiation of microglia. Front Cell Neurosci. 2013;7:45. doi: 10.3389/fncel.2013.00045
68. Kitamura T, Miyake T, Fujita S. Genesis of resting microglia in the gray matter of mouse hippocampus. J Comp Neurol. 1984;226(3):421-33. doi: 10.1002/cne.902260310

69. Perry VH, Hume DA, Gordon S. Immunohistochemical localization of macrophages and microglia in the adult and developing mouse brain. Neuroscience. 1985;15(2):313-26. doi: 10.1016/0306-4522(85)90215-5
70. Ginhoux F, Greter M, Leboeuf M, Nandi S, See P, Gokhan S, et al. Fate mapping analysis reveals that adult microglia derive from primitive macrophages. Science (New York, NY). 2010;330(6005):841-5. doi: 10.1126/science.1194637
71. Chan WY, Kohsaka S, Rezaie P. The origin and cell lineage of microglia: new concepts. Brain Res Rev. 2007;53(2):344-54. doi: 10.1016/j.brainresrev.2006.11.002
72. Kierdorf K, Erny D, Goldmann T, Sander V, Schulz C, Perdiguero EG, et al. Microglia emerge from erythromyeloid precursors via Pu.1- and Irf8-dependent pathways. Nat Neurosci. 2013;16(3):273-80. doi: 10.1038/nn.3318
73. Monier A, Evrard P, Gressens P, Verney C. Distribution and differentiation of microglia in the human encephalon during the first two trimesters of gestation. J Comp Neurol. 2006;499(4):565-82. doi: 10.1002/cne.21123
74. Hoeffel G, Chen J, Lavin Y, Low D, Almeida FF, See P, et al. C-Myb(+) erythro-myeloid progenitor-derived fetal monocytes give rise to adult tissue-resident macrophages. Immunity. 2015;42(4):665-78. doi: 10.1016/j.immuni.2015.03.011
75. Tan YL, Yuan Y, Tian L. Microglial regional heterogeneity and its role in the brain. Mol Psychiatry. 2020;25(2):351-67. doi: 10.1038/s41380-019-0609-8
76. Zeisel A, Muñoz-Manchado AB, Codeluppi S, Lönnerberg P, La Manno G, Juréus A, et al. Brain structure. Cell types in the mouse cortex and hippocampus revealed by single-cell RNA-seq. Science (New York, NY). 2015;347(6226):1138-42. doi: 10.1126/science.aaa1934
77. Gosselin D, Skola D, Coufal NG, Holtman IR, Schlachetzki JCM, Sajti E, et al. An environment-dependent transcriptional network specifies human microglia identity. Science. 2017;356(6344). doi: 10.1126/science.aal3222
78. Butovsky O, Jedrychowski MP, Moore CS, Cialic R, Lanser AJ, Gabriely G, et al. Identification of a unique TGF-β-dependent molecular and functional signature in microglia. Nat Neurosci. 2014;17(1):131-43. doi: 10.1038/nn.3599
79. Lyons A, Lynch AM, Downer EJ, Hanley R, O'Sullivan JB, Smith A, et al. Fractalkine-induced activation of the phosphatidylinositol-3 kinase pathway attentuates microglial activation in vivo and in vitro. J Neurochem. 2009;110(5):1547-56. doi: 10.1111/j.1471-4159.2009.06253.x
80. Zujovic V, Benavides J, Vigé X, Carter C, Taupin V. Fractalkine modulates TNF-alpha secretion and neurotoxicity induced by microglial activation. Glia. 2000;29(4):305-15.
81. Koning N, Swaab DF, Hoek RM, Huitinga I. Distribution of the immune inhibitory molecules CD200 and CD200R in the normal central nervous system and multiple sclerosis lesions suggests neuron-glia and glia-glia interactions. J Neuropathol Exp Neurol. 2009;68(2):159-67. doi: 10.1097/NEN.0b013e3181964113
82. Hoek RM, Ruuls SR, Murphy CA, Wright GJ, Goddard R, Zurawski SM, et al. Down-regulation of the macrophage lineage through interaction with OX2 (CD200). Science. 2000;290(5497):1768-71. doi: 10.1126/science.290.5497.1768
83. Walker DG, Dalsing-Hernandez JE, Campbell NA, Lue LF. Decreased expression of CD200 and CD200 receptor in Alzheimer's disease: a potential mechanism leading to chronic inflammation. Exp Neurol. 2009;215(1):5-19. doi: 10.1016/j.expneurol.2008.09.003
84. Bohlen CJ, Bennett FC, Tucker AF, Collins HY, Mulinyawe SB, Barres BA. Diverse Requirements for Microglial Survival, Specification, and Function Revealed by Defined-Medium Cultures. Neuron. 2017;94(4):759-73.e8. doi: 10.1016/j.neuron.2017.04.043
85. Lenz KM, Nelson LH. Microglia and Beyond: Innate Immune Cells As Regulators of Brain Development and Behavioral Function. Front Immunol. 2018;9:698. doi: 10.3389/fimmu.2018.00698
86. Buttgereit A, Lelios I, Yu X, Vrohlings M, Krakoski NR, Gautier EL, et al. Sall1 is a transcriptional regulator defining microglia identity and function. Nature Immunology. 2016;17(12):1397-406. Available from: https://doi.org/10.1038/ni.3585doi: 10.1038/ni.3585

87. Bruttger J, Karram K, Wörtge S, Regen T, Marini F, Hoppmann N, et al. Genetic Cell Ablation Reveals Clusters of Local Self-Renewing Microglia in the Mammalian Central Nervous System. Immunity. 2015;43(1):92-106. doi: 10.1016/j.immuni.2015.06.012
88. Askew K, Li K, Olmos-Alonso A, Garcia-Moreno F, Liang Y, Richardson P, et al. Coupled Proliferation and Apoptosis Maintain the Rapid Turnover of Microglia in the Adult Brain. Cell Rep. 2017;18(2):391-405. doi: 10.1016/j.celrep.2016.12.041
89. Füger P, Hefendehl JK, Veeraraghavalu K, Wendeln AC, Schlosser C, Obermüller U, et al. Microglia turnover with aging and in an Alzheimer's model via long-term in vivo single-cell imaging. Nat Neurosci. 2017;20(10):1371-6. doi: 10.1038/nn.4631
90. Elmore MR, Najafi AR, Koike MA, Dagher NN, Spangenberg EE, Rice RA, et al. Colony-stimulating factor 1 receptor signaling is necessary for microglia viability, unmasking a microglia progenitor cell in the adult brain. Neuron. 2014;82(2):380-97. doi: 10.1016/j.neuron.2014.02.040
91. Harley SBR, Willis EF, Shaikh SN, Blackmore DG, Sah P, Ruitenberg MJ, et al. Selective Ablation of BDNF from Microglia Reveals Novel Roles in Self-Renewal and Hippocampal Neurogenesis. J Neurosci. 2021;41(19):4172-86. doi: 10.1523/jneurosci.2539-20.2021
92. Huttenlocher PR. Synaptic density in human frontal cortex - developmental changes and effects of aging. Brain research. 1979;163(2):195-205. doi: 10.1016/0006-8993(79)90349-4
93. Freeman SA, Grinstein S. Phagocytosis: receptors, signal integration, and the cytoskeleton. Immunol Rev. 2014;262(1):193-215. doi: 10.1111/imr.12212
94. Rosales C, Uribe-Querol E. Phagocytosis: A Fundamental Process in Immunity. BioMed research international. 2017;2017:9042851. doi: 10.1155/2017/9042851
95. Tahara K, Kim HD, Jin JJ, Maxwell JA, Li L, Fukuchi K. Role of toll-like receptor signalling in Abeta uptake and clearance. Brain. 2006;129(Pt 11):3006-19. doi: 10.1093/brain/awl249
96. Peng Q, Malhotra S, Torchia JA, Kerr WG, Coggeshall KM, Humphrey MB. TREM2- and DAP12-dependent activation of PI3K requires DAP10 and is inhibited by SHIP1. Sci Signal. 2010;3(122):ra38. doi: 10.1126/scisignal.2000500
97. Mecca C, Giambanco I, Donato R, Arcuri C. Microglia and Aging: The Role of the TREM2-DAP12 and CX3CL1-CX3CR1 Axes. International journal of molecular sciences. 2018;19(1). doi: 10.3390/ijms19010318
98. Okun E, Mattson MP, Arumugam TV. Involvement of Fc receptors in disorders of the central nervous system. Neuromolecular Med. 2010;12(2):164-78. doi: 10.1007/s12017-009-8099-5
99. Koizumi S, Shigemoto-Mogami Y, Nasu-Tada K, Shinozaki Y, Ohsawa K, Tsuda M, et al. UDP acting at P2Y6 receptors is a mediator of microglial phagocytosis. Nature. 2007;446(7139):1091-5. doi: 10.1038/nature05704
100. Lai MK, Tan MG, Kirvell S, Hobbs C, Lee J, Esiri MM, et al. Selective loss of P2Y2 nucleotide receptor immunoreactivity is associated with Alzheimer's disease neuropathology. Journal of neural transmission (Vienna, Austria : 1996). 2008;115(8):1165-72. doi: 10.1007/s00702-008-0067-y
101. Erb L, Cao C, Ajit D, Weisman GA. P2Y receptors in Alzheimer's disease. Biol Cell. 2015;107(1):1-21. doi: 10.1111/boc.201400043
102. Galloway DA, Phillips AEM, Owen DRJ, Moore CS. Phagocytosis in the Brain: Homeostasis and Disease. Front Immunol. 2019;10:790. doi: 10.3389/fimmu.2019.00790
103. Stephan AH, Madison DV, Mateos JM, Fraser DA, Lovelett EA, Coutellier L, et al. A dramatic increase of C1q protein in the CNS during normal aging. The Journal of neuroscience : the official journal of the Society for Neuroscience. 2013;33(33):13460-74. doi: 10.1523/jneurosci.1333-13.2013
104. Morgan BP. Complement in the pathogenesis of Alzheimer's disease. Semin Immunopathol. 2018;40(1):113-24. doi: 10.1007/s00281-017-0662-9
105. Pérez-Rodríguez DR, Blanco-Luquin I, Mendioroz M. The Participation of Microglia in Neurogenesis: A Review. Brain Sci. 2021;11(5). doi: 10.3390/brainsci11050658
106. Yu Z, Fukushima H, Ono C, Sakai M, Kasahara Y, Kikuchi Y, et al. Microglial production of TNF-alpha is a key element of sustained fear memory. Brain, Behavior, and Immunity. 2017;59:313-21.

Available from: https://www.sciencedirect.com/science/article/pii/S0889159116303907doi: https://doi.org/10.1016/j.bbi.2016.08.011
107. Greenberg DA, Jin K. From angiogenesis to neuropathology. Nature. 2005;438(7070):954-9. doi: 10.1038/nature04481
108. Rigato C, Buckinx R, Le-Corronc H, Rigo JM, Legendre P. Pattern of invasion of the embryonic mouse spinal cord by microglial cells at the time of the onset of functional neuronal networks. Glia. 2011;59(4):675-95. doi: 10.1002/glia.21140
109. Arnold T, Betsholtz C. The importance of microglia in the development of the vasculature in the central nervous system. Vasc Cell. 2013;5(1):4. doi: 10.1186/2045-824x-5-4
110. Yao C, Cao Y, Wang D, Lv Y, Liu Y, Gu X, et al. Single-cell sequencing reveals microglia induced angiogenesis by specific subsets of endothelial cells following spinal cord injury. Faseb j. 2022;36(7):e22393. doi: 10.1096/fj.202200337R
111. Dudvarski Stankovic N, Teodorczyk M, Ploen R, Zipp F, Schmidt MHH. Microglia-blood vessel interactions: a double-edged sword in brain pathologies. Acta Neuropathol. 2016;131(3):347-63. doi: 10.1007/s00401-015-1524-y
112. Matsumoto J, Dohgu S, Takata F, Nishioku T, Sumi N, Machida T, et al. Lipopolysaccharide-activated microglia lower P-glycoprotein function in brain microvascular endothelial cells. Neuroscience letters. 2012;524(1):45-8. doi: 10.1016/j.neulet.2012.07.004
113. Nimmerjahn A, Kirchhoff F, Helmchen F. Resting microglial cells are highly dynamic surveillants of brain parenchyma in vivo. Science (New York, NY). 2005;308(5726):1314-8. doi: 10.1126/science.1110647
114. Bernier LP, Bohlen CJ, York EM, Choi HB, Kamyabi A, Dissing-Olesen L, et al. Nanoscale Surveillance of the Brain by Microglia via cAMP-Regulated Filopodia. Cell Rep. 2019;27(10):2895-908.e4. doi: 10.1016/j.celrep.2019.05.010
115. Miyamoto A, Wake H, Ishikawa AW, Eto K, Shibata K, Murakoshi H, et al. Microglia contact induces synapse formation in developing somatosensory cortex. Nat Commun. 2016;7:12540. doi: 10.1038/ncomms12540
116. Basilico B, Pagani F, Grimaldi A, Cortese B, Di Angelantonio S, Weinhard L, et al. Microglia shape presynaptic properties at developing glutamatergic synapses. Glia. 2019;67(1):53-67. doi: 10.1002/glia.23508
117. Schafer DP, Lehrman EK, Kautzman AG, Koyama R, Mardinly AR, Yamasaki R, et al. Microglia sculpt postnatal neural circuits in an activity and complement-dependent manner. Neuron. 2012;74(4):691-705. doi: 10.1016/j.neuron.2012.03.026
118. Stevens B, Allen NJ, Vazquez LE, Howell GR, Christopherson KS, Nouri N, et al. The classical complement cascade mediates CNS synapse elimination. Cell. 2007;131(6):1164-78. doi: 10.1016/j.cell.2007.10.036
119. Chu Y, Jin X, Parada I, Pesic A, Stevens B, Barres B, et al. Enhanced synaptic connectivity and epilepsy in C1q knockout mice. Proc Natl Acad Sci U S A. 2010;107(17):7975-80. doi: 10.1073/pnas.0913449107
120. Scott-Hewitt N, Perrucci F, Morini R, Erreni M, Mahoney M, Witkowska A, et al. Local externalization of phosphatidylserine mediates developmental synaptic pruning by microglia. Embo j. 2020;39(16):e105380. doi: 10.15252/embj.2020105380
121. Li T, Chiou B, Gilman CK, Luo R, Koshi T, Yu D, et al. A splicing isoform of GPR56 mediates microglial synaptic refinement via phosphatidylserine binding. Embo j. 2020;39(16):e104136. doi: 10.15252/embj.2019104136
122. Martinon F, Burns K, Tschopp J. The inflammasome: a molecular platform triggering activation of inflammatory caspases and processing of proIL-beta. Mol Cell. 2002;10(2):417-26. doi: 10.1016/s1097-2765(02)00599-3
123. Burguillos MA, Deierborg T, Kavanagh E, Persson A, Hajji N, Garcia-Quintanilla A, et al. Caspase signalling controls microglia activation and neurotoxicity. Nature. 2011;472(7343):319-24. doi: 10.1038/nature09788

124. Brosseron F, Krauthausen M, Kummer M, Heneka MT. Body fluid cytokine levels in mild cognitive impairment and Alzheimer's disease: a comparative overview. Mol Neurobiol. 2014;50(2):534-44. doi: 10.1007/s12035-014-8657-1
125. Laws SM, Perneczky R, Wagenpfeil S, Müller U, Förstl H, Martins RN, et al. TNF polymorphisms in Alzheimer disease and functional implications on CSF beta-amyloid levels. Hum Mutat. 2005;26(1):29-35. doi: 10.1002/humu.20180
126. Heneka MT, Kummer MP, Stutz A, Delekate A, Schwartz S, Vieira-Saecker A, et al. NLRP3 is activated in Alzheimer's disease and contributes to pathology in APP/PS1 mice. Nature. 2013;493(7434):674-8. doi: 10.1038/nature11729
127. Shaked I, Tchoresh D, Gersner R, Meiri G, Mordechai S, Xiao X, et al. Protective autoimmunity: interferon-gamma enables microglia to remove glutamate without evoking inflammatory mediators. Journal of neurochemistry. 2005;92(5):997-1009. doi: 10.1111/j.1471-4159.2004.02954.x
128. Pascual O, Ben Achour S, Rostaing P, Triller A, Bessis A. Microglia activation triggers astrocyte-mediated modulation of excitatory neurotransmission. Proc Natl Acad Sci U S A. 2012;109(4):E197-205. doi: 10.1073/pnas.1111098109
129. Pocock JM, Kettenmann H. Neurotransmitter receptors on microglia. Trends Neurosci. 2007;30(10):527-35. doi: 10.1016/j.tins.2007.07.007
130. Graeber MB. Changing face of microglia. Science (New York, NY). 2010;330(6005):783-8. doi: 10.1126/science.1190929
131. Davalos D, Grutzendler J, Yang G, Kim JV, Zuo Y, Jung S, et al. ATP mediates rapid microglial response to local brain injury in vivo. Nat Neurosci. 2005;8(6):752-8. doi: 10.1038/nn1472
132. Hirbec H, Marmai C, Duroux-Richard I, Roubert C, Esclangon A, Croze S, et al. The microglial reaction signature revealed by RNAseq from individual mice. Glia. 2018;66(5):971-86. doi: 10.1002/glia.23295
133. Zhang Y, Chen K, Sloan SA, Bennett ML, Scholze AR, O'Keeffe S, et al. An RNA-sequencing transcriptome and splicing database of glia, neurons, and vascular cells of the cerebral cortex. J Neurosci. 2014;34(36):11929-47. doi: 10.1523/jneurosci.1860-14.2014
134. Hickman SE, Kingery ND, Ohsumi TK, Borowsky ML, Wang LC, Means TK, et al. The microglial sensome revealed by direct RNA sequencing. Nat Neurosci. 2013;16(12):1896-905. doi: 10.1038/nn.3554
135. Deczkowska A, Keren-Shaul H, Weiner A, Colonna M, Schwartz M, Amit I. Disease-Associated Microglia: A Universal Immune Sensor of Neurodegeneration. Cell. 2018;173(5):1073-81. doi: 10.1016/j.cell.2018.05.003
136. Mrdjen D, Pavlovic A, Hartmann FJ, Schreiner B, Utz SG, Leung BP, et al. High-Dimensional Single-Cell Mapping of Central Nervous System Immune Cells Reveals Distinct Myeloid Subsets in Health, Aging, and Disease. Immunity. 2018;48(2):380-95.e6. doi: 10.1016/j.immuni.2018.01.011
137. Sala Frigerio C, Wolfs L, Fattorelli N, Thrupp N, Voytyuk I, Schmidt I, et al. The Major Risk Factors for Alzheimer's Disease: Age, Sex, and Genes Modulate the Microglia Response to Aβ Plaques. Cell Rep. 2019;27(4):1293-306.e6. doi: 10.1016/j.celrep.2019.03.099
138. Masuda A, Kobayashi Y, Kogo N, Saito T, Saido TC, Itohara S. Cognitive deficits in single App knock-in mouse models. Neurobiol Learn Mem. 2016;135:73-82. doi: 10.1016/j.nlm.2016.07.001
139. Srinivasan K, Friedman BA, Etxeberria A, Huntley MA, van der Brug MP, Foreman O, et al. Alzheimer's Patient Microglia Exhibit Enhanced Aging and Unique Transcriptional Activation. Cell Rep. 2020;31(13):107843. doi: 10.1016/j.celrep.2020.107843
140. Domingues C, da Cruz ESOAB, Henriques AG. Impact of Cytokines and Chemokines on Alzheimer's Disease Neuropathological Hallmarks. Curr Alzheimer Res. 2017;14(8):870-82. doi: 10.2174/1567205014666170317113606
141. Chakrabarty P, Li A, Ceballos-Diaz C, Eddy JA, Funk CC, Moore B, et al. IL-10 alters immunoproteostasis in APP mice, increasing plaque burden and worsening cognitive behavior. Neuron. 2015;85(3):519-33. doi: 10.1016/j.neuron.2014.11.020

142. Chao CC, Hu S, Frey WH, 2nd, Ala TA, Tourtellotte WW, Peterson PK. Transforming growth factor beta in Alzheimer's disease. Clin Diagn Lab Immunol. 1994;1(1):109-10.
143. Spangenberg EE, Lee RJ, Najafi AR, Rice RA, Elmore MR, Blurton-Jones M, et al. Eliminating microglia in Alzheimer's mice prevents neuronal loss without modulating amyloid-β pathology. Brain. 2016;139(Pt 4):1265-81. doi: 10.1093/brain/aww016
144. Lee S, Xu G, Jay TR, Bhatta S, Kim KW, Jung S, et al. Opposing effects of membrane-anchored CX3CL1 on amyloid and tau pathologies via the p38 MAPK pathway. J Neurosci. 2014;34(37):12538-46. doi: 10.1523/jneurosci.0853-14.2014
145. Dworzak J, Renvoisé B, Habchi J, Yates EV, Combadière C, Knowles TP, et al. Neuronal Cx3cr1 Deficiency Protects against Amyloid β-Induced Neurotoxicity. PLoS One. 2015;10(6):e0127730. doi: 10.1371/journal.pone.0127730
146. Rojo R, Raper A, Ozdemir DD, Lefevre L, Grabert K, Wollscheid-Lengeling E, et al. Deletion of a Csf1r enhancer selectively impacts CSF1R expression and development of tissue macrophage populations. Nat Commun. 2019;10(1):3215. doi: 10.1038/s41467-019-11053-8
147. Kiani Shabestari S, Morabito S, Danhash EP, McQuade A, Sanchez JR, Miyoshi E, et al. Absence of microglia promotes diverse pathologies and early lethality in Alzheimer's disease mice. Cell Rep. 2022;39(11):110961. doi: 10.1016/j.celrep.2022.110961
148. Utz SG, See P, Mildenberger W, Thion MS, Silvin A, Lutz M, et al. Early Fate Defines Microglia and Non-parenchymal Brain Macrophage Development. Cell. 2020;181(3):557-73.e18. doi: 10.1016/j.cell.2020.03.021
149. Masuda T, Amann L, Monaco G, Sankowski R, Staszewski O, Krueger M, et al. Specification of CNS macrophage subsets occurs postnatally in defined niches. Nature. 2022;604(7907):740-8. doi: 10.1038/s41586-022-04596-2
150. Goldmann T, Wieghofer P, Jordão MJ, Prutek F, Hagemeyer N, Frenzel K, et al. Origin, fate and dynamics of macrophages at central nervous system interfaces. Nat Immunol. 2016;17(7):797-805. doi: 10.1038/ni.3423
151. De Schepper S, Ge JZ, Crowley G, Ferreira LSS, Garceau D, Toomey CE, et al. Perivascular cells induce microglial phagocytic states and synaptic engulfment via SPP1 in mouse models of Alzheimer's disease. Nat Neurosci. 2023;26(3):406-15. doi: 10.1038/s41593-023-01257-z
152. Keren-Shaul H, Spinrad A, Weiner A, Matcovitch-Natan O, Dvir-Szternfeld R, Ulland TK, et al. A Unique Microglia Type Associated with Restricting Development of Alzheimer's Disease. Cell. 2017;169(7):1276-90.e17. doi: 10.1016/j.cell.2017.05.018
153. Karch CM, Goate AM. Alzheimer's disease risk genes and mechanisms of disease pathogenesis. Biol Psychiatry. 2015;77(1):43-51. doi: 10.1016/j.biopsych.2014.05.006
154. Shaw BC, Katsumata Y, Simpson JF, Fardo DW, Estus S. Analysis of Genetic Variants Associated with Levels of Immune Modulating Proteins for Impact on Alzheimer's Disease Risk Reveal a Potential Role for SIGLEC14. Genes (Basel). 2021;12(7). doi: 10.3390/genes12071008
155. Song WM, Joshita S, Zhou Y, Ulland TK, Gilfillan S, Colonna M. Humanized TREM2 mice reveal microglia-intrinsic and -extrinsic effects of R47H polymorphism. J Exp Med. 2018;215(3):745-60. doi: 10.1084/jem.20171529
156. Paloneva J, Kestilä M, Wu J, Salminen A, Böhling T, Ruotsalainen V, et al. Loss-of-function mutations in TYROBP (DAP12) result in a presenile dementia with bone cysts. Nat Genet. 2000;25(3):357-61. doi: 10.1038/77153
157. Kleinberger G, Yamanishi Y, Suárez-Calvet M, Czirr E, Lohmann E, Cuyvers E, et al. TREM2 mutations implicated in neurodegeneration impair cell surface transport and phagocytosis. Sci Transl Med. 2014;6(243):243ra86. doi: 10.1126/scitranslmed.3009093
158. Cheng Q, Danao J, Talreja S, Wen P, Yin J, Sun N, et al. TREM2-activating antibodies abrogate the negative pleiotropic effects of the Alzheimer's disease variant Trem2(R47H) on murine myeloid cell function. The Journal of biological chemistry. 2018;293(32):12620-33. doi: 10.1074/jbc.RA118.001848

159. Kober DL, Alexander-Brett JM, Karch CM, Cruchaga C, Colonna M, Holtzman MJ, et al. Neurodegenerative disease mutations in TREM2 reveal a functional surface and distinct loss-of-function mechanisms. Elife. 2016;5. doi: 10.7554/eLife.20391
160. Wang Y, Ulland TK, Ulrich JD, Song W, Tzaferis JA, Hole JT, et al. TREM2-mediated early microglial response limits diffusion and toxicity of amyloid plaques. J Exp Med. 2016;213(5):667-75. doi: 10.1084/jem.20151948
161. Gratuze M, Leyns CEG, Holtzman DM. New insights into the role of TREM2 in Alzheimer's disease. Mol Neurodegener. 2018;13(1):66. doi: 10.1186/s13024-018-0298-9
162. Brendel M, Kleinberger G, Probst F, Jaworska A, Overhoff F, Blume T, et al. Increase of TREM2 during Aging of an Alzheimer's Disease Mouse Model Is Paralleled by Microglial Activation and Amyloidosis. Front Aging Neurosci. 2017;9:8. doi: 10.3389/fnagi.2017.00008
163. Hall-Roberts H, Agarwal D, Obst J, Smith TB, Monzón-Sandoval J, Di Daniel E, et al. TREM2 Alzheimer's variant R47H causes similar transcriptional dysregulation to knockout, yet only subtle functional phenotypes in human iPSC-derived macrophages. Alzheimer's research & therapy. 2020;12(1):151. doi: 10.1186/s13195-020-00709-z
164. Malik M, Simpson JF, Parikh I, Wilfred BR, Fardo DW, Nelson PT, et al. CD33 Alzheimer's risk-altering polymorphism, CD33 expression, and exon 2 splicing. The Journal of neuroscience : the official journal of the Society for Neuroscience. 2013;33(33):13320-5. doi: 10.1523/jneurosci.1224-13.2013
165. Griciuc A, Serrano-Pozo A, Parrado AR, Lesinski AN, Asselin CN, Mullin K, et al. Alzheimer's disease risk gene CD33 inhibits microglial uptake of amyloid beta. Neuron. 2013;78(4):631-43. doi: 10.1016/j.neuron.2013.04.014
166. Butler CA, Thornton P, Brown GC. CD33M inhibits microglial phagocytosis, migration and proliferation, but the Alzheimer's disease-protective variant CD33m stimulates phagocytosis and proliferation, and inhibits adhesion. J Neurochem. 2021;158(2):297-310. doi: 10.1111/jnc.15349
167. Bhattacherjee A, Rodrigues E, Jung J, Luzentales-Simpson M, Enterina JR, Galleguillos D, et al. Repression of phagocytosis by human CD33 is not conserved with mouse CD33. Commun Biol. 2019;2:450. doi: 10.1038/s42003-019-0698-6
168. Angata T, Kerr SC, Greaves DR, Varki NM, Crocker PR, Varki A. Cloning and Characterization of Human Siglec-11: A RECENTLY EVOLVED SIGNALING MOLECULE THAT CAN INTERACT WITH SHP-1 AND SHP-2 AND IS EXPRESSED BY TISSUE MACROPHAGES, INCLUDING BRAIN MICROGLIA*210. Journal of Biological Chemistry. 2002;277(27):24466-74. Available from: https://www.sciencedirect.com/science/article/pii/S0021925819666238doi: https://doi.org/10.1074/jbc.M202833200
169. Liao H, Winkler J, Wißfeld J, Shahraz A, Klaus C, Neumann H. Low molecular weight polysialic acid prevents lipopolysaccharide-induced inflammatory dopaminergic neurodegeneration in humanized SIGLEC11 transgenic mice. Glia. 2021;69(12):2845-62. doi: 10.1002/glia.24073
170. Wang Y, Neumann H. Alleviation of neurotoxicity by microglial human Siglec-11. J Neurosci. 2010;30(9):3482-8. doi: 10.1523/jneurosci.3940-09.2010
171. Pluvinage JV, Haney MS, Smith BAH, Sun J, Iram T, Bonanno L, et al. CD22 blockade restores homeostatic microglial phagocytosis in ageing brains. Nature. 2019;568(7751):187-92. doi: 10.1038/s41586-019-1088-4
172. Aires V, Coulon-Bainier C, Pavlovic A, Ebeling M, Schmucki R, Schweitzer C, et al. CD22 Blockage Restores Age-Related Impairments of Microglia Surveillance Capacity. Front Immunol. 2021;12:684430. doi: 10.3389/fimmu.2021.684430
173. Morshed N, Ralvenius WT, Nott A, Watson LA, Rodriguez FH, Akay LA, et al. Phosphoproteomics identifies microglial Siglec-F inflammatory response during neurodegeneration. Mol Syst Biol. 2020;16(12):e9819. doi: 10.15252/msb.20209819
174. Oakley H, Cole SL, Logan S, Maus E, Shao P, Craft J, et al. Intraneuronal beta-amyloid aggregates, neurodegeneration, and neuron loss in transgenic mice with five familial Alzheimer's

disease mutations: potential factors in amyloid plaque formation. J Neurosci. 2006;26(40):10129-40. doi: 10.1523/jneurosci.1202-06.2006
175. Saito T, Matsuba Y, Mihira N, Takano J, Nilsson P, Itohara S, et al. Single App knock-in mouse models of Alzheimer's disease. Nat Neurosci. 2014;17(5):661-3. doi: 10.1038/nn.3697
176. Das A, Kim SH, Arifuzzaman S, Yoon T, Chai JC, Lee YS, et al. Transcriptome sequencing reveals that LPS-triggered transcriptional responses in established microglia BV2 cell lines are poorly representative of primary microglia. J Neuroinflammation. 2016;13(1):182. doi: 10.1186/s12974-016-0644-1
177. Timmerman R, Burm SM, Bajramovic JJ. An Overview of in vitro Methods to Study Microglia. Front Cell Neurosci. 2018;12:242. doi: 10.3389/fncel.2018.00242
178. Zuiderwijk-Sick EA, van der Putten C, Bsibsi M, Deuzing IP, de Boer W, Persoon-Deen C, et al. Differentiation of primary adult microglia alters their response to TLR8-mediated activation but not their capacity as APC. Glia. 2007;55(15):1589-600. doi: 10.1002/glia.20572
179. Turano A, Lawrence JH, Schwarz JM. Activation of neonatal microglia can be influenced by other neural cells. Neuroscience letters. 2017;657:32-7. doi: 10.1016/j.neulet.2017.07.052
180. Zhang Y, Sloan SA, Clarke LE, Caneda C, Plaza CA, Blumenthal PD, et al. Purification and Characterization of Progenitor and Mature Human Astrocytes Reveals Transcriptional and Functional Differences with Mouse. Neuron. 2016;89(1):37-53. doi: 10.1016/j.neuron.2015.11.013
181. Takahashi K, Yamanaka S. Induction of pluripotent stem cells from mouse embryonic and adult fibroblast cultures by defined factors. Cell. 2006;126(4):663-76. doi: 10.1016/j.cell.2006.07.024
182. Haenseler W, Rajendran L. Concise Review: Modeling Neurodegenerative Diseases with Human Pluripotent Stem Cell-Derived Microglia. Stem Cells. 2019;37(6):724-30. doi: 10.1002/stem.2995
183. Fournier N, Chalus L, Durand I, Garcia E, Pin JJ, Churakova T, et al. FDF03, a novel inhibitory receptor of the immunoglobulin superfamily, is expressed by human dendritic and myeloid cells. Journal of immunology (Baltimore, Md : 1950). 2000;165(3):1197-209. doi: 10.4049/jimmunol.165.3.1197
184. Lu Q, Lu G, Qi J, Wang H, Xuan Y, Wang Q, et al. PILRalpha and PILRbeta have a siglec fold and provide the basis of binding to sialic acid. Proc Natl Acad Sci U S A. 2014;111(22):8221-6. doi: 10.1073/pnas.1320716111
185. Tato CM, Joyce-Shaikh B, Banerjee A, Chen Y, Sathe M, Ewald SE, et al. The myeloid receptor PILRβ mediates the balance of inflammatory responses through regulation of IL-27 production. PLoS One. 2012;7(3):e31680. doi: 10.1371/journal.pone.0031680
186. Mousseau DD, Banville D, L'Abbe D, Bouchard P, Shen SH. PILRalpha, a novel immunoreceptor tyrosine-based inhibitory motif-bearing protein, recruits SHP-1 upon tyrosine phosphorylation and is paired with the truncated counterpart PILRbeta. J Biol Chem. 2000;275(6):4467-74. doi: 10.1074/jbc.275.6.4467
187. Tabata S, Kuroki K, Maita N, Wang J, Shiratori I, Arase H, et al. Expression, crystallization and preliminary X-ray diffraction analysis of human paired Ig-like type 2 receptor alpha (PILRalpha). Acta Crystallogr Sect F Struct Biol Cryst Commun. 2008;64(Pt 1):44-6. doi: 10.1107/s1744309107065384
188. Kuroki K, Wang J, Ose T, Yamaguchi M, Tabata S, Maita N, et al. Structural basis for simultaneous recognition of an O-glycan and its attached peptide of mucin family by immune receptor PILRα. Proc Natl Acad Sci U S A. 2014;111(24):8877-82. doi: 10.1073/pnas.1324105111
189. Satoh T, Arii J, Suenaga T, Wang J, Kogure A, Uehori J, et al. PILRalpha is a herpes simplex virus-1 entry coreceptor that associates with glycoprotein B. Cell. 2008;132(6):935-44. doi: 10.1016/j.cell.2008.01.043
190. Wang J, Fan Q, Satoh T, Arii J, Lanier LL, Spear PG, et al. Binding of herpes simplex virus glycoprotein B (gB) to paired immunoglobulin-like type 2 receptor alpha depends on specific sialylated O-linked glycans on gB. J Virol. 2009;83(24):13042-5. doi: 10.1128/jvi.00792-09

191. Arii J, Uema M, Morimoto T, Sagara H, Akashi H, Ono E, et al. Entry of herpes simplex virus 1 and other alphaherpesviruses via the paired immunoglobulin-like type 2 receptor alpha. J Virol. 2009;83(9):4520-7. doi: 10.1128/jvi.02601-08
192. Wang J, Shiratori I, Uehori J, Ikawa M, Arase H. Neutrophil infiltration during inflammation is regulated by PILRalpha via modulation of integrin activation. Nat Immunol. 2013;14(1):34-40. doi: 10.1038/ni.2456
193. Kohyama M, Matsuoka S, Shida K, Sugihara F, Aoshi T, Kishida K, et al. Monocyte infiltration into obese and fibrilized tissues is regulated by PILRalpha. Eur J Immunol. 2016;46(5):1214-23. doi: 10.1002/eji.201545897
194. Ophir Y, Duev-Cohen A, Yamin R, Tsukerman P, Bauman Y, Gamliel M, et al. PILRalpha binds an unknown receptor expressed primarily on CD56bright and decidual-NK cells and activates NK cell functions. Oncotarget. 2016;7(27):40953-64. doi: 10.18632/oncotarget.8397
195. Sun Y, Caplazi P, Zhang J, Mazloom A, Kummerfeld S, Quinones G, et al. PILRα negatively regulates mouse inflammatory arthritis. J Immunol. 2014;193(2):860-70. doi: 10.4049/jimmunol.1400045
196. Zheng L, Han X, Yao S, Zhu Y, Klement J, Wu S, et al. The CD8α-PILRα interaction maintains CD8(+) T cell quiescence. Science. 2022;376(6596):996-1001. doi: 10.1126/science.aaz8658
197. Patel T, Brookes KJ, Turton J, Chaudhury S, Guetta-Baranes T, Guerreiro R, et al. Whole-exome sequencing of the BDR cohort: evidence to support the role of the PILRA gene in Alzheimer's disease. Neuropathol Appl Neurobiol. 2018;44(5):506-21. doi: 10.1111/nan.12452
198. Schwartzentruber J, Cooper S, Liu JZ, Barrio-Hernandez I, Bello E, Kumasaka N, et al. Genome-wide meta-analysis, fine-mapping and integrative prioritization implicate new Alzheimer's disease risk genes. Nat Genet. 2021;53(3):392-402. doi: 10.1038/s41588-020-00776-w
199. Heath L, Earls JC, Magis AT, Kornilov SA, Lovejoy JC, Funk CC, et al. Manifestations of Alzheimer's disease genetic risk in the blood are evident in a multiomic analysis in healthy adults aged 18 to 90. Sci Rep. 2022;12(1):6117. doi: 10.1038/s41598-022-09825-2
200. Auton A, Brooks LD, Durbin RM, Garrison EP, Kang HM, Korbel JO, et al. A global reference for human genetic variation. Nature. 2015;526(7571):68-74. doi: 10.1038/nature15393
201. Rathore N, Ramani SR, Pantua H, Payandeh J, Bhangale T, Wuster A, et al. Paired Immunoglobulin-like Type 2 Receptor Alpha G78R variant alters ligand binding and confers protection to Alzheimer's disease. PLoS Genet. 2018;14(11):e1007427. doi: 10.1371/journal.pgen.1007427
202. Kikuchi M, Hara N, Hasegawa M, Miyashita A, Kuwano R, Ikeuchi T, et al. Enhancer variants associated with Alzheimer's disease affect gene expression via chromatin looping. BMC Med Genomics. 2019;12(1):128. doi: 10.1186/s12920-019-0574-8
203. Chapuis J, Flaig A, Grenier-Boley B, Eysert F, Pottiez V, Deloison G, et al. Genome-wide, high-content siRNA screening identifies the Alzheimer's genetic risk factor FERMT2 as a major modulator of APP metabolism. Acta Neuropathol. 2017;133(6):955-66. doi: 10.1007/s00401-016-1652-z
204. Kogure A, Shiratori I, Wang J, Lanier LL, Arase H. PANP is a novel O-glycosylated PILRα ligand expressed in neural tissues. Biochem Biophys Res Commun. 2011;405(3):428-33. doi: 10.1016/j.bbrc.2011.01.047
205. Agostini S, Costa AS, Mancuso R, Guerini FR, Nemni R, Clerici M. The PILRA G78R Variant Correlates with Higher HSV-1-Specific IgG Titers in Alzheimer's Disease. Cell Mol Neurobiol. 2019;39(8):1217-21. doi: 10.1007/s10571-019-00712-5
206. Smith AM, Davey K, Tsartsalis S, Khozoie C, Fancy N, Tang SS, et al. Diverse human astrocyte and microglial transcriptional responses to Alzheimer's pathology. Acta Neuropathol. 2022;143(1):75-91. doi: 10.1007/s00401-021-02372-6
207. O'Day DH, Huber RJ. Calmodulin binding proteins and neuroinflammation in multiple neurodegenerative diseases. BMC Neurosci. 2022;23(1):10. doi: 10.1186/s12868-022-00695-y

208. Logue MW, Schu M, Vardarajan BN, Farrell J, Lunetta KL, Jun G, et al. Search for age-related macular degeneration risk variants in Alzheimer disease genes and pathways. Neurobiol Aging. 2014;35(6):1510.e7-18. doi: 10.1016/j.neurobiolaging.2013.12.007
209. Lopatko Lindman K, Jonsson C, Weidung B, Olsson J, Pandey JP, Prokopenko D, et al. PILRA polymorphism modifies the effect of APOE4 and GM17 on Alzheimer's disease risk. Sci Rep. 2022;12(1):13264. doi: 10.1038/s41598-022-17058-6
210. Tsang E, Giannetti AM, Shaw D, Dinh M, Tse JK, Gandhi S, et al. Molecular mechanism of the Syk activation switch. J Biol Chem. 2008;283(47):32650-9. doi: 10.1074/jbc.M806340200
211. Deindl S, Kadlecek TA, Brdicka T, Cao X, Weiss A, Kuriyan J. Structural basis for the inhibition of tyrosine kinase activity of ZAP-70. Cell. 2007;129(4):735-46. doi: 10.1016/j.cell.2007.03.039
212. Furlong MT, Mahrenholz AM, Kim KH, Ashendel CL, Harrison ML, Geahlen RL. Identification of the major sites of autophosphorylation of the murine protein-tyrosine kinase Syk. Biochim Biophys Acta. 1997;1355(2):177-90. doi: 10.1016/s0167-4889(96)00131-0
213. Wang L, Duke L, Zhang PS, Arlinghaus RB, Symmans WF, Sahin A, et al. Alternative splicing disrupts a nuclear localization signal in spleen tyrosine kinase that is required for invasion suppression in breast cancer. Cancer Res. 2003;63(15):4724-30.
214. Turner M, Mee PJ, Costello PS, Williams O, Price AA, Duddy LP, et al. Perinatal lethality and blocked B-cell development in mice lacking the tyrosine kinase Syk. Nature. 1995;378(6554):298-302. doi: 10.1038/378298a0
215. Lee YG, Chain BM, Cho JY. Distinct role of spleen tyrosine kinase in the early phosphorylation of inhibitor of kappaB alpha via activation of the phosphoinositide-3-kinase and Akt pathways. Int J Biochem Cell Biol. 2009;41(4):811-21. doi: 10.1016/j.biocel.2008.08.011
216. Miller YI, Choi SH, Wiesner P, Bae YS. The SYK side of TLR4: signalling mechanisms in response to LPS and minimally oxidized LDL. Br J Pharmacol. 2012;167(5):990-9. doi: 10.1111/j.1476-5381.2012.02097.x
217. Yoon JY, Jeong HY, Kim SH, Kim HG, Nam G, Kim JP, et al. Methanol extract of Evodia lepta displays Syk/Src-targeted anti-inflammatory activity. Journal of ethnopharmacology. 2013;148(3):999-1007. doi: 10.1016/j.jep.2013.05.030
218. Yang Y, Yu T, Lee YG, Yang WS, Oh J, Jeong D, et al. Methanol extract of Hopea odorata suppresses inflammatory responses via the direct inhibition of multiple kinases. Journal of ethnopharmacology. 2013;145(2):598-607. doi: 10.1016/j.jep.2012.11.041
219. Hamerman JA, Tchao NK, Lowell CA, Lanier LL. Enhanced Toll-like receptor responses in the absence of signaling adaptor DAP12. Nat Immunol. 2005;6(6):579-86. doi: 10.1038/ni1204
220. Ziegenfuss JS, Biswas R, Avery MA, Hong K, Sheehan AE, Yeung YG, et al. Draper-dependent glial phagocytic activity is mediated by Src and Syk family kinase signalling. Nature. 2008;453(7197):935-9. doi: 10.1038/nature06901
221. Tabata H, Morita H, Kaji H, Tohyama K, Tohyama Y. Syk facilitates phagosome-lysosome fusion by regulating actin-remodeling in complement-mediated phagocytosis. Sci Rep. 2020;10(1):22086. doi: 10.1038/s41598-020-79156-7
222. Abtahian F, Guerriero A, Sebzda E, Lu MM, Zhou R, Mocsai A, et al. Regulation of blood and lymphatic vascular separation by signaling proteins SLP-76 and Syk. Science. 2003;299(5604):247-51. doi: 10.1126/science.1079477
223. Bertozzi CC, Schmaier AA, Mericko P, Hess PR, Zou Z, Chen M, et al. Platelets regulate lymphatic vascular development through CLEC-2-SLP-76 signaling. Blood. 2010;116(4):661-70. doi: 10.1182/blood-2010-02-270876
224. Finney BA, Schweighoffer E, Navarro-Núñez L, Bénézech C, Barone F, Hughes CE, et al. CLEC-2 and Syk in the megakaryocytic/platelet lineage are essential for development. Blood. 2012;119(7):1747-56. doi: 10.1182/blood-2011-09-380709
225. Liu D, Mamorska-Dyga A. Syk inhibitors in clinical development for hematological malignancies. J Hematol Oncol. 2017;10(1):145. doi: 10.1186/s13045-017-0512-1

226. Mullard A. FDA approves first-in-class SYK inhibitor. Nature Reviews Drug Discovery. 2018;17(6):385-. Available from: https://doi.org/10.1038/nrd.2018.96doi: 10.1038/nrd.2018.96
227. McDonald DR, Brunden KR, Landreth GE. Amyloid fibrils activate tyrosine kinase-dependent signaling and superoxide production in microglia. J Neurosci. 1997;17(7):2284-94. doi: 10.1523/jneurosci.17-07-02284.1997
228. Combs CK, Karlo JC, Kao SC, Landreth GE. beta-Amyloid stimulation of microglia and monocytes results in TNFalpha-dependent expression of inducible nitric oxide synthase and neuronal apoptosis. J Neurosci. 2001;21(4):1179-88. doi: 10.1523/jneurosci.21-04-01179.2001
229. Lebouvier T, Scales TM, Hanger DP, Geahlen RL, Lardeux B, Reynolds CH, et al. The microtubule-associated protein tau is phosphorylated by Syk. Biochim Biophys Acta. 2008;1783(2):188-92. doi: 10.1016/j.bbamcr.2007.11.005
230. Paris D, Ait-Ghezala G, Bachmeier C, Laco G, Beaulieu-Abdelahad D, Lin Y, et al. The spleen tyrosine kinase (Syk) regulates Alzheimer amyloid-β production and Tau hyperphosphorylation. The Journal of biological chemistry. 2014;289(49):33927-44. doi: 10.1074/jbc.M114.608091
231. Schweig JE, Yao H, Beaulieu-Abdelahad D, Ait-Ghezala G, Mouzon B, Crawford F, et al. Alzheimer's disease pathological lesions activate the spleen tyrosine kinase. Acta Neuropathol Commun. 2017;5(1):69. doi: 10.1186/s40478-017-0472-2
232. Hu W, Wen L, Cao F, Wang Y. Down-Regulation of Mir-107 Worsen Spatial Memory by Suppressing SYK Expression and Inactivating NF-KB Signaling Pathway. Curr Alzheimer Res. 2019;16(2):135-45. doi: 10.2174/1567205016666181212154347
233. Schweig JE, Yao H, Coppola K, Jin C, Crawford F, Mullan M, et al. Spleen tyrosine kinase (SYK) blocks autophagic Tau degradation in vitro and in vivo. J Biol Chem. 2019;294(36):13378-95. doi: 10.1074/jbc.RA119.008033
234. Schweig JE, Yao H, Jin C, Crawford F, Mullan M, Paris D. Neuronal Spleen tyrosine kinase (SYK) mediates cytokine release in Transgenic Tau P301S mice organotypic brain slice cultures. Neurosci Lett. 2020;729:134992. doi: 10.1016/j.neulet.2020.134992
235. Krisenko MO, Higgins RL, Ghosh S, Zhou Q, Trybula JS, Wang WH, et al. Syk Is Recruited to Stress Granules and Promotes Their Clearance through Autophagy. J Biol Chem. 2015;290(46):27803-15. doi: 10.1074/jbc.M115.642900
236. Ghosh S, Geahlen RL. Stress Granules Modulate SYK to Cause Microglial Cell Dysfunction in Alzheimer's Disease. EBioMedicine. 2015;2(11):1785-98. doi: 10.1016/j.ebiom.2015.09.053
237. Morin A, Mouzon B, Ferguson S, Paris D, Browning M, Stewart W, et al. Nilvadipine suppresses inflammation via inhibition of P-SYK and restores spatial memory deficits in a mouse model of repetitive mild TBI. Acta Neuropathol Commun. 2020;8(1):166. doi: 10.1186/s40478-020-01045-x
238. Wang S, Sudan R, Peng V, Zhou Y, Du S, Yuede CM, et al. TREM2 drives microglia response to amyloid-β via SYK-dependent and -independent pathways. Cell. 2022;185(22):4153-69.e19. doi: 10.1016/j.cell.2022.09.033
239. Ennerfelt H, Frost EL, Shapiro DA, Holliday C, Zengeler KE, Voithofer G, et al. SYK coordinates neuroprotective microglial responses in neurodegenerative disease. Cell. 2022;185(22):4135-52.e22. doi: 10.1016/j.cell.2022.09.030
240. Weiss A, Wiskocil RL, Stobo JD. The role of T3 surface molecules in the activation of human T cells: a two-stimulus requirement for IL 2 production reflects events occurring at a pre-translational level. J Immunol. 1984;133(1):123-8.
241. DuBridge RB, Tang P, Hsia HC, Leong PM, Miller JH, Calos MP. Analysis of mutation in human cells by using an Epstein-Barr virus shuttle system. Mol Cell Biol. 1987;7(1):379-87. doi: 10.1128/mcb.7.1.379-387.1987
242. Palacios R, Steinmetz M. Il-3-dependent mouse clones that express B-220 surface antigen, contain Ig genes in germ-line configuration, and generate B lymphocytes in vivo. Cell. 1985;41(3):727-34. doi: 10.1016/s0092-8674(85)80053-2

243. Daley GQ, Baltimore D. Transformation of an interleukin 3-dependent hematopoietic cell line by the chronic myelogenous leukemia-specific P210bcr/abl protein. Proc Natl Acad Sci U S A. 1988;85(23):9312-6. doi: 10.1073/pnas.85.23.9312
244. Skarnes WC, Pellegrino E, McDonough JA. Improving homology-directed repair efficiency in human stem cells. Methods. 2019;164-165:18-28. doi: 10.1016/j.ymeth.2019.06.016
245. Hildebrandt MR, Reuter MS, Wei W, Tayebi N, Liu J, Sharmin S, et al. Precision Health Resource of Control iPSC Lines for Versatile Multilineage Differentiation. Stem Cell Reports. 2019;13(6):1126-41. doi: 10.1016/j.stemcr.2019.11.003
246. Pantazis CB, Yang A, Lara E, McDonough JA, Blauwendraat C, Peng L, et al. A reference human induced pluripotent stem cell line for large-scale collaborative studies. Cell Stem Cell. 2022;29(12):1685-702.e22. doi: 10.1016/j.stem.2022.11.004
247. Demaison C, Parsley K, Brouns G, Scherr M, Battmer K, Kinnon C, et al. High-level transduction and gene expression in hematopoietic repopulating cells using a human immunodeficiency [correction of imunodeficiency] virus type 1-based lentiviral vector containing an internal spleen focus forming virus promoter. Hum Gene Ther. 2002;13(7):803-13. doi: 10.1089/10430340252898984
248. Saijo K, Schmedt C, Su IH, Karasuyama H, Lowell CA, Reth M, et al. Essential role of Src-family protein tyrosine kinases in NF-kappaB activation during B cell development. Nat Immunol. 2003;4(3):274-9. doi: 10.1038/ni893
249. Yona S, Kim KW, Wolf Y, Mildner A, Varol D, Breker M, et al. Fate mapping reveals origins and dynamics of monocytes and tissue macrophages under homeostasis. Immunity. 2013;38(1):79-91. doi: 10.1016/j.immuni.2012.12.001
250. Gautier EL, Shay T, Miller J, Greter M, Jakubzick C, Ivanov S, et al. Gene-expression profiles and transcriptional regulatory pathways that underlie the identity and diversity of mouse tissue macrophages. Nat Immunol. 2012;13(11):1118-28. doi: 10.1038/ni.2419
251. Love MI, Huber W, Anders S. Moderated estimation of fold change and dispersion for RNA-seq data with DESeq2. Genome Biol. 2014;15(12):550. doi: 10.1186/s13059-014-0550-8
252. Schenkel AR, Mamdouh Z, Chen X, Liebman RM, Muller WA. CD99 plays a major role in the migration of monocytes through endothelial junctions. Nat Immunol. 2002;3(2):143-50. doi: 10.1038/ni749
253. Sun Y, Senger K, Baginski TK, Mazloom A, Chinn Y, Pantua H, et al. Evolutionarily conserved paired immunoglobulin-like receptor α (PILRα) domain mediates its interaction with diverse sialylated ligands. The Journal of biological chemistry. 2012;287(19):15837-50. doi: 10.1074/jbc.M111.286633
254. Kogure A, Shiratori I, Wang J, Lanier LL, Arase H. PANP is a novel O-glycosylated PILRalpha ligand expressed in neural tissues. Biochem Biophys Res Commun. 2011;405(3):428-33. doi: 10.1016/j.bbrc.2011.01.047
255. Balcaitis S, Weinstein JR, Li S, Chamberlain JS, Möller T. Lentiviral transduction of microglial cells. Glia. 2005;50(1):48-55. doi: 10.1002/glia.20146
256. Lois C, Hong EJ, Pease S, Brown EJ, Baltimore D. Germline transmission and tissue-specific expression of transgenes delivered by lentiviral vectors. Science (New York, NY). 2002;295(5556):868-72. doi: 10.1126/science.1067081
257. Arnone MI, Dmochowski IJ, Gache C. Using reporter genes to study cis-regulatory elements. Methods Cell Biol. 2004;74:621-52. doi: 10.1016/s0091-679x(04)74025-x
258. Nair AK, Baier LJ. Using Luciferase Reporter Assays to Identify Functional Variants at Disease-Associated Loci. Methods Mol Biol. 2018;1706:303-19. doi: 10.1007/978-1-4939-7471-9_17
259. Love PE, Hayes SM. ITAM-mediated signaling by the T-cell antigen receptor. Cold Spring Harbor perspectives in biology. 2010;2(6):a002485. doi: 10.1101/cshperspect.a002485
260. Riley JK, Takeda K, Akira S, Schreiber RD. Interleukin-10 receptor signaling through the JAK-STAT pathway. Requirement for two distinct receptor-derived signals for anti-inflammatory action. J Biol Chem. 1999;274(23):16513-21. doi: 10.1074/jbc.274.23.16513

261. He J, Yang Q, Chang LJ. Dynamic DNA methylation and histone modifications contribute to lentiviral transgene silencing in murine embryonic carcinoma cells. J Virol. 2005;79(21):13497-508. doi: 10.1128/jvi.79.21.13497-13508.2005
262. Mok HP, Javed S, Lever A. Stable gene expression occurs from a minority of integrated HIV-1-based vectors: transcriptional silencing is present in the majority. Gene Ther. 2007;14(9):741-51. doi: 10.1038/sj.gt.3302923
263. Banasik MB, McCray PB, Jr. Integrase-defective lentiviral vectors: progress and applications. Gene Ther. 2010;17(2):150-7. doi: 10.1038/gt.2009.135
264. Pierson TC, Kieffer TL, Ruff CT, Buck C, Gange SJ, Siliciano RF. Intrinsic stability of episomal circles formed during human immunodeficiency virus type 1 replication. J Virol. 2002;76(8):4138-44. doi: 10.1128/jvi.76.8.4138-4144.2002
265. Butler SL, Johnson EP, Bushman FD. Human immunodeficiency virus cDNA metabolism: notable stability of two-long terminal repeat circles. J Virol. 2002;76(8):3739-47. doi: 10.1128/jvi.76.8.3739-3747.2002
266. Wang F, Zhang S, Jeon R, Vuckovic I, Jiang X, Lerman A, et al. Interferon Gamma Induces Reversible Metabolic Reprogramming of M1 Macrophages to Sustain Cell Viability and Pro-Inflammatory Activity. EBioMedicine. 2018;30:303-16. doi: 10.1016/j.ebiom.2018.02.009
267. Shoji T, Higuchi H, Nishijima K, Iijima S. Effects of Siglec on the expression of IL-10 in the macrophage cell line RAW264. Cytotechnology. 2015;67(4):633-9. doi: 10.1007/s10616-014-9717-0
268. Chang YC, Olson J, Beasley FC, Tung C, Zhang J, Crocker PR, et al. Group B Streptococcus engages an inhibitory Siglec through sialic acid mimicry to blunt innate immune and inflammatory responses in vivo. PLoS Pathog. 2014;10(1):e1003846. doi: 10.1371/journal.ppat.1003846
269. Dharmadhikari G, Stolz K, Hauke M, Morgan NG, Varki A, de Koning E, et al. Siglec-7 restores β-cell function and survival and reduces inflammation in pancreatic islets from patients with diabetes. Sci Rep. 2017;7:45319. doi: 10.1038/srep45319
270. Siddiqui SS, Springer SA, Verhagen A, Sundaramurthy V, Alisson-Silva F, Jiang W, et al. The Alzheimer's disease-protective CD33 splice variant mediates adaptive loss of function via diversion to an intracellular pool. J Biol Chem. 2017;292(37):15312-20. doi: 10.1074/jbc.M117.799346
271. Cooper AM, Khader SA. IL-12p40: an inherently agonistic cytokine. Trends Immunol. 2007;28(1):33-8. doi: 10.1016/j.it.2006.11.002
272. Columba-Cabezas S, Serafini B, Ambrosini E, Sanchez M, Penna G, Adorini L, et al. Induction of macrophage-derived chemokine/CCL22 expression in experimental autoimmune encephalomyelitis and cultured microglia: implications for disease regulation. J Neuroimmunol. 2002;130(1-2):10-21. doi: 10.1016/s0165-5728(02)00170-4
273. Matsukawa A, Hogaboam CM, Lukacs NW, Lincoln PM, Evanoff HL, Kunkel SL. Pivotal role of the CC chemokine, macrophage-derived chemokine, in the innate immune response. J Immunol. 2000;164(10):5362-8. doi: 10.4049/jimmunol.164.10.5362
274. Wang N, Liu W, Zheng Y, Wang S, Yang B, Li M, et al. CXCL1 derived from tumor-associated macrophages promotes breast cancer metastasis via activating NF-κB/SOX4 signaling. Cell Death Dis. 2018;9(9):880. doi: 10.1038/s41419-018-0876-3
275. Serdar M, Kempe K, Herrmann R, Picard D, Remke M, Herz J, et al. Involvement of CXCL1/CXCR2 During Microglia Activation Following Inflammation-Sensitized Hypoxic-Ischemic Brain Injury in Neonatal Rats. Front Neurol. 2020;11:540878. doi: 10.3389/fneur.2020.540878
276. Seok J, Warren HS, Cuenca AG, Mindrinos MN, Baker HV, Xu W, et al. Genomic responses in mouse models poorly mimic human inflammatory diseases. Proc Natl Acad Sci U S A. 2013;110(9):3507-12. doi: 10.1073/pnas.1222878110
277. Ngwa C, Qi S, Mamun AA, Xu Y, Sharmeen R, Liu F. Age and sex differences in primary microglia culture: A comparative study. J Neurosci Methods. 2021;364:109359. doi: 10.1016/j.jneumeth.2021.109359

278. Henn A, Lund S, Hedtjärn M, Schrattenholz A, Pörzgen P, Leist M. The suitability of BV2 cells as alternative model system for primary microglia cultures or for animal experiments examining brain inflammation. Altex. 2009;26(2):83-94. doi: 10.14573/altex.2009.2.83
279. Semb H. Human embryonic stem cells: origin, properties and applications. Apmis. 2005;113(11-12):743-50. doi: 10.1111/j.1600-0463.2005.apm_312.x
280. Evans MJ, Kaufman MH. Establishment in culture of pluripotential cells from mouse embryos. Nature. 1981;292(5819):154-6. doi: 10.1038/292154a0
281. Adewumi O, Aflatoonian B, Ahrlund-Richter L, Amit M, Andrews PW, Beighton G, et al. Characterization of human embryonic stem cell lines by the International Stem Cell Initiative. Nat Biotechnol. 2007;25(7):803-16. doi: 10.1038/nbt1318
282. De Miguel MP, Fuentes-Julián S, Alcaina Y. Pluripotent stem cells: origin, maintenance and induction. Stem Cell Rev Rep. 2010;6(4):633-49. doi: 10.1007/s12015-010-9170-1
283. Wesselschmidt RL. The teratoma assay: an in vivo assessment of pluripotency. Methods Mol Biol. 2011;767:231-41. doi: 10.1007/978-1-61779-201-4_17
284. Silva J, Nichols J, Theunissen TW, Guo G, van Oosten AL, Barrandon O, et al. Nanog is the gateway to the pluripotent ground state. Cell. 2009;138(4):722-37. doi: 10.1016/j.cell.2009.07.039
285. Kaji K, Norrby K, Paca A, Mileikovsky M, Mohseni P, Woltjen K. Virus-free induction of pluripotency and subsequent excision of reprogramming factors. Nature. 2009;458(7239):771-5. doi: 10.1038/nature07864
286. Ye L, Swingen C, Zhang J. Induced pluripotent stem cells and their potential for basic and clinical sciences. Curr Cardiol Rev. 2013;9(1):63-72. doi: 10.2174/157340313805076278
287. Kim JB, Zaehres H, Wu G, Gentile L, Ko K, Sebastiano V, et al. Pluripotent stem cells induced from adult neural stem cells by reprogramming with two factors. Nature. 2008;454(7204):646-50. doi: 10.1038/nature07061
288. Rowe RG, Daley GQ. Induced pluripotent stem cells in disease modelling and drug discovery. Nat Rev Genet. 2019;20(7):377-88. doi: 10.1038/s41576-019-0100-z
289. Fyfe I. Mutation-specific amyloid-β processing in iPSC-derived neurons. Nat Rev Neurol. 2019;15(6):310. doi: 10.1038/s41582-019-0195-z
290. Haenseler W, Sansom SN, Buchrieser J, Newey SE, Moore CS, Nicholls FJ, et al. A Highly Efficient Human Pluripotent Stem Cell Microglia Model Displays a Neuronal-Co-culture-Specific Expression Profile and Inflammatory Response. Stem Cell Reports. 2017;8(6):1727-42. doi: 10.1016/j.stemcr.2017.05.017
291. Washer SJ, Bassett AR, Cowley SA. Variation on a theme: mapping microglial heterogeneity. Trends Genet. 2021;37(12):1050-2. doi: 10.1016/j.tig.2021.09.004
292. Ji J, Ng SH, Sharma V, Neculai D, Hussein S, Sam M, et al. Elevated coding mutation rate during the reprogramming of human somatic cells into induced pluripotent stem cells. Stem Cells. 2012;30(3):435-40. doi: 10.1002/stem.1011
293. Gore A, Li Z, Fung HL, Young JE, Agarwal S, Antosiewicz-Bourget J, et al. Somatic coding mutations in human induced pluripotent stem cells. Nature. 2011;471(7336):63-7. doi: 10.1038/nature09805
294. Rouhani F, Kumasaka N, de Brito MC, Bradley A, Vallier L, Gaffney D. Genetic background drives transcriptional variation in human induced pluripotent stem cells. PLoS Genet. 2014;10(6):e1004432. doi: 10.1371/journal.pgen.1004432
295. Cong L, Zhang F. Genome engineering using CRISPR-Cas9 system. Methods Mol Biol. 2015;1239:197-217. doi: 10.1007/978-1-4939-1862-1_10
296. Gupta D, Bhattacharjee O, Mandal D, Sen MK, Dey D, Dasgupta A, et al. CRISPR-Cas9 system: A new-fangled dawn in gene editing. Life Sci. 2019;232:116636. doi: 10.1016/j.lfs.2019.116636
297. Cui Y, Xu J, Cheng M, Liao X, Peng S. Review of CRISPR/Cas9 sgRNA Design Tools. Interdiscip Sci. 2018;10(2):455-65. doi: 10.1007/s12539-018-0298-z
298. Doudna JA, Charpentier E. Genome editing. The new frontier of genome engineering with CRISPR-Cas9. Science. 2014;346(6213):1258096. doi: 10.1126/science.1258096

299. Symington LS, Gautier J. Double-strand break end resection and repair pathway choice. Annu Rev Genet. 2011;45:247-71. doi: 10.1146/annurev-genet-110410-132435
300. Symington LS. Mechanism and regulation of DNA end resection in eukaryotes. Crit Rev Biochem Mol Biol. 2016;51(3):195-212. doi: 10.3109/10409238.2016.1172552
301. Cradick TJ, Fine EJ, Antico CJ, Bao G. CRISPR/Cas9 systems targeting β-globin and CCR5 genes have substantial off-target activity. Nucleic Acids Res. 2013;41(20):9584-92. doi: 10.1093/nar/gkt714
302. Washer SJ, Perez-Alcantara M, Chen Y, Steer J, James WS, Trynka G, et al. Single-cell transcriptomics defines an improved, validated monoculture protocol for differentiation of human iPSC to microglia. Sci Rep. 2022;12(1):19454. doi: 10.1038/s41598-022-23477-2
303. Liang X, Potter J, Kumar S, Ravinder N, Chesnut JD. Enhanced CRISPR/Cas9-mediated precise genome editing by improved design and delivery of gRNA, Cas9 nuclease, and donor DNA. J Biotechnol. 2017;241:136-46. doi: 10.1016/j.jbiotec.2016.11.011
304. Yu C, Liu Y, Ma T, Liu K, Xu S, Zhang Y, et al. Small molecules enhance CRISPR genome editing in pluripotent stem cells. Cell Stem Cell. 2015;16(2):142-7. doi: 10.1016/j.stem.2015.01.003
305. Maruyama T, Dougan SK, Truttmann MC, Bilate AM, Ingram JR, Ploegh HL. Increasing the efficiency of precise genome editing with CRISPR-Cas9 by inhibition of nonhomologous end joining. Nat Biotechnol. 2015;33(5):538-42. doi: 10.1038/nbt.3190
306. Srivastava M, Nambiar M, Sharma S, Karki SS, Goldsmith G, Hegde M, et al. An inhibitor of nonhomologous end-joining abrogates double-strand break repair and impedes cancer progression. Cell. 2012;151(7):1474-87. doi: 10.1016/j.cell.2012.11.054
307. Yang D, Scavuzzo MA, Chmielowiec J, Sharp R, Bajic A, Borowiak M. Enrichment of G2/M cell cycle phase in human pluripotent stem cells enhances HDR-mediated gene repair with customizable endonucleases. Sci Rep. 2016;6:21264. doi: 10.1038/srep21264
308. Lin Y, Cradick TJ, Brown MT, Deshmukh H, Ranjan P, Sarode N, et al. CRISPR/Cas9 systems have off-target activity with insertions or deletions between target DNA and guide RNA sequences. Nucleic Acids Res. 2014;42(11):7473-85. doi: 10.1093/nar/gku402
309. Young MA, Larson DE, Sun CW, George DR, Ding L, Miller CA, et al. Background mutations in parental cells account for most of the genetic heterogeneity of induced pluripotent stem cells. Cell Stem Cell. 2012;10(5):570-82. doi: 10.1016/j.stem.2012.03.002
310. Sugiura M, Kasama Y, Araki R, Hoki Y, Sunayama M, Uda M, et al. Induced pluripotent stem cell generation-associated point mutations arise during the initial stages of the conversion of these cells. Stem Cell Reports. 2014;2(1):52-63. doi: 10.1016/j.stemcr.2013.11.006
311. Yoshihara M, Hayashizaki Y, Murakawa Y. Genomic Instability of iPSCs: Challenges Towards Their Clinical Applications. Stem Cell Rev Rep. 2017;13(1):7-16. doi: 10.1007/s12015-016-9680-6
312. Laurent LC, Ulitsky I, Slavin I, Tran H, Schork A, Morey R, et al. Dynamic changes in the copy number of pluripotency and cell proliferation genes in human ESCs and iPSCs during reprogramming and time in culture. Cell Stem Cell. 2011;8(1):106-18. doi: 10.1016/j.stem.2010.12.003
313. Le Scouarnec S, Gribble SM. Characterising chromosome rearrangements: recent technical advances in molecular cytogenetics. Heredity (Edinb). 2012;108(1):75-85. doi: 10.1038/hdy.2011.100
314. Pagnamenta AT, Lise S, Harrison V, Stewart H, Jayawant S, Quaghebeur G, et al. Exome sequencing can detect pathogenic mosaic mutations present at low allele frequencies. J Hum Genet. 2012;57(1):70-2. doi: 10.1038/jhg.2011.128
315. Chang YC, Olson J, Louie A, Crocker PR, Varki A, Nizet V. Role of macrophage sialoadhesin in host defense against the sialylated pathogen group B Streptococcus. J Mol Med (Berl). 2014;92(9):951-9. doi: 10.1007/s00109-014-1157-y
316. Scholz CC, Cavadas MA, Tambuwala MM, Hams E, Rodríguez J, von Kriegsheim A, et al. Regulation of IL-1β-induced NF-κB by hydroxylases links key hypoxic and inflammatory signaling pathways. Proc Natl Acad Sci U S A. 2013;110(46):18490-5. doi: 10.1073/pnas.1309718110
317. Thornton P, Pinteaux E, Gibson RM, Allan SM, Rothwell NJ. Interleukin-1-induced neurotoxicity is mediated by glia and requires caspase activation and free radical release. J Neurochem. 2006;98(1):258-66. doi: 10.1111/j.1471-4159.2006.03872.x

318. Ye T, Duan Y, Tsang HWS, Xu H, Chen Y, Cao H, et al. Efficient manipulation of gene dosage in human iPSCs using CRISPR/Cas9 nickases. Commun Biol. 2021;4(1):195. doi: 10.1038/s42003-021-01722-0
319. Speicher AM, Wiendl H, Meuth SG, Pawlowski M. Generating microglia from human pluripotent stem cells: novel in vitro models for the study of neurodegeneration. Mol Neurodegener. 2019;14(1):46. doi: 10.1186/s13024-019-0347-z
320. Abud EM, Ramirez RN, Martinez ES, Healy LM, Nguyen CHH, Newman SA, et al. iPSC-Derived Human Microglia-like Cells to Study Neurological Diseases. Neuron. 2017;94(2):278-93.e9. doi: 10.1016/j.neuron.2017.03.042
321. Mócsai A, Ruland J, Tybulewicz VL. The SYK tyrosine kinase: a crucial player in diverse biological functions. Nat Rev Immunol. 2010;10(6):387-402. doi: 10.1038/nri2765
322. Kerrigan AM, Brown GD. Syk-coupled C-type lectin receptors that mediate cellular activation via single tyrosine based activation motifs. Immunol Rev. 2010;234(1):335-52. doi: 10.1111/j.0105-2896.2009.00882.x
323. Obst J, Hall-Roberts HL, Smith TB, Kreuzer M, Magno L, Di Daniel E, et al. PLCγ2 regulates TREM2 signalling and integrin-mediated adhesion and migration of human iPSC-derived macrophages. Sci Rep. 2021;11(1):19842. doi: 10.1038/s41598-021-96144-7
324. Chihara K, Kimura Y, Honjo C, Takeuchi K, Sada K. Syk inhibitors. Nihon Rinsho Meneki Gakkai Kaishi. 2013;36(4):197-202. doi: 10.2177/jsci.36.197
325. Cheng AM, Rowley B, Pao W, Hayday A, Bolen JB, Pawson T. Syk tyrosine kinase required for mouse viability and B-cell development. Nature. 1995;378(6554):303-6. doi: 10.1038/378303a0
326. Schwenk F, Kuhn R, Angrand PO, Rajewsky K, Stewart AF. Temporally and spatially regulated somatic mutagenesis in mice. Nucleic Acids Res. 1998;26(6):1427-32. doi: 10.1093/nar/26.6.1427
327. Kim H, Kim M, Im SK, Fang S. Mouse Cre-LoxP system: general principles to determine tissue-specific roles of target genes. Lab Anim Res. 2018;34(4):147-59. doi: 10.5625/lar.2018.34.4.147
328. Indra AK, Warot X, Brocard J, Bornert JM, Xiao JH, Chambon P, et al. Temporally-controlled site-specific mutagenesis in the basal layer of the epidermis: comparison of the recombinase activity of the tamoxifen-inducible Cre-ER(T) and Cre-ER(T2) recombinases. Nucleic Acids Res. 1999;27(22):4324-7. doi: 10.1093/nar/27.22.4324
329. Jordan VC. The role of tamoxifen in the treatment and prevention of breast cancer. Curr Probl Cancer. 1992;16(3):129-76. doi: 10.1016/0147-0272(92)90002-6
330. Crewe HK, Notley LM, Wunsch RM, Lennard MS, Gillam EM. Metabolism of tamoxifen by recombinant human cytochrome P450 enzymes: formation of the 4-hydroxy, 4'-hydroxy and N-desmethyl metabolites and isomerization of trans-4-hydroxytamoxifen. Drug Metab Dispos. 2002;30(8):869-74. doi: 10.1124/dmd.30.8.869
331. Jahn HM, Kasakow CV, Helfer A, Michely J, Verkhratsky A, Maurer HH, et al. Refined protocols of tamoxifen injection for inducible DNA recombination in mouse astroglia. Sci Rep. 2018;8(1):5913. doi: 10.1038/s41598-018-24085-9
332. Zhong ZA, Sun W, Chen H, Zhang H, Lay YE, Lane NE, et al. Optimizing tamoxifen-inducible Cre/loxp system to reduce tamoxifen effect on bone turnover in long bones of young mice. Bone. 2015;81:614-9. doi: 10.1016/j.bone.2015.07.034
333. Donocoff RS, Teteloshvili N, Chung H, Shoulson R, Creusot RJ. Optimization of tamoxifen-induced Cre activity and its effect on immune cell populations. Sci Rep. 2020;10(1):15244. doi: 10.1038/s41598-020-72179-0
334. Citron M, Oltersdorf T, Haass C, McConlogue L, Hung AY, Seubert P, et al. Mutation of the beta-amyloid precursor protein in familial Alzheimer's disease increases beta-protein production. Nature. 1992;360(6405):672-4. doi: 10.1038/360672a0
335. Lichtenthaler SF, Wang R, Grimm H, Uljon SN, Masters CL, Beyreuther K. Mechanism of the cleavage specificity of Alzheimer's disease gamma-secretase identified by phenylalanine-scanning mutagenesis of the transmembrane domain of the amyloid precursor protein. Proc Natl Acad Sci U S A. 1999;96(6):3053-8. doi: 10.1073/pnas.96.6.3053

336. Sierksma A, Lu A, Mancuso R, Fattorelli N, Thrupp N, Salta E, et al. Novel Alzheimer risk genes determine the microglia response to amyloid-β but not to TAU pathology. EMBO Mol Med. 2020;12(3):e10606. doi: 10.15252/emmm.201910606
337. Wang X, Yu L, Wu AR. The effect of methanol fixation on single-cell RNA sequencing data. BMC Genomics. 2021;22(1):420. doi: 10.1186/s12864-021-07744-6
338. Wu QJ, Zhang TN, Chen HH, Yu XF, Lv JL, Liu YY, et al. The sirtuin family in health and disease. Signal Transduct Target Ther. 2022;7(1):402. doi: 10.1038/s41392-022-01257-8
339. Woo SJ, Noh HS, Lee NY, Cheon YH, Yi SM, Jeon HM, et al. Myeloid sirtuin 6 deficiency accelerates experimental rheumatoid arthritis by enhancing macrophage activation and infiltration into synovium. EBioMedicine. 2018;38:228-37. doi: 10.1016/j.ebiom.2018.11.005
340. Kim D, Park W, Lee S, Kim W, Park SK, Kang KP. Absence of Sirt3 aggravates cisplatin nephrotoxicity via enhanced renal tubular apoptosis and inflammation. Mol Med Rep. 2018;18(4):3665-72. doi: 10.3892/mmr.2018.9350
341. Perone I, Ghena N, Wang J, Mackey C, Wan R, Malla S, et al. Mitochondrial SIRT3 Deficiency Results in Neuronal Network Hyperexcitability, Accelerates Age-Related Aβ Pathology, and Renders Neurons Vulnerable to Aβ Toxicity. Neuromolecular Med. 2023;25(1):27-39. doi: 10.1007/s12017-022-08713-2
342. Liu Y, Cheng A, Li YJ, Yang Y, Kishimoto Y, Zhang S, et al. SIRT3 mediates hippocampal synaptic adaptations to intermittent fasting and ameliorates deficits in APP mutant mice. Nat Commun. 2019;10(1):1886. doi: 10.1038/s41467-019-09897-1
343. Yeung F, Hoberg JE, Ramsey CS, Keller MD, Jones DR, Frye RA, et al. Modulation of NF-kappaB-dependent transcription and cell survival by the SIRT1 deacetylase. Embo j. 2004;23(12):2369-80. doi: 10.1038/sj.emboj.7600244
344. Zhang L, Guo XQ, Chu JF, Zhang X, Yan ZR, Li YZ. Potential hippocampal genes and pathways involved in Alzheimer's disease: a bioinformatic analysis. Genet Mol Res. 2015;14(2):7218-32. doi: 10.4238/2015.June.29.15
345. Brace LE, Vose SC, Stanya K, Gathungu RM, Marur VR, Longchamp A, et al. Increased oxidative phosphorylation in response to acute and chronic DNA damage. NPJ Aging Mech Dis. 2016;2:16022. doi: 10.1038/npjamd.2016.22
346. Liu R, Jagannathan R, Sun L, Li F, Yang P, Lee J, et al. Tead1 is essential for mitochondrial function in cardiomyocytes. Am J Physiol Heart Circ Physiol. 2020;319(1):H89-h99. doi: 10.1152/ajpheart.00732.2019
347. Marczuk-Krynicka D, Hryniewiecki T, Piatek J, Paluszak J. The effect of brief food withdrawal on the level of free radicals and other parameters of oxidative status in the liver. Med Sci Monit. 2003;9(3):Br131-5.
348. Nolan DA, Chen B, Michon AM, Salatka E, Arndt D. A Rasmussen encephalitis, autoimmune encephalitis, and mitochondrial disease mimicker: expanding the DNM1L-associated intractable epilepsy and encephalopathy phenotype. Epileptic Disord. 2019;21(1):112-6. doi: 10.1684/epd.2019.1036
349. Abdelmohsen K, Pullmann R, Jr., Lal A, Kim HH, Galban S, Yang X, et al. Phosphorylation of HuR by Chk2 regulates SIRT1 expression. Mol Cell. 2007;25(4):543-57. doi: 10.1016/j.molcel.2007.01.011
350. Conti V, Corbi G, Simeon V, Russomanno G, Manzo V, Ferrara N, et al. Aging-related changes in oxidative stress response of human endothelial cells. Aging Clinical and Experimental Research. 2015;27(4):547-53. Available from: https://doi.org/10.1007/s40520-015-0357-9doi: 10.1007/s40520-015-0357-9
351. Koo JH, Kang EB, Oh YS, Yang DS, Cho JY. Treadmill exercise decreases amyloid-β burden possibly via activation of SIRT-1 signaling in a mouse model of Alzheimer's disease. Exp Neurol. 2017;288:142-52. doi: 10.1016/j.expneurol.2016.11.014

352. Feng X, Liang N, Zhu D, Gao Q, Peng L, Dong H, et al. Resveratrol inhibits β-amyloid-induced neuronal apoptosis through regulation of SIRT1-ROCK1 signaling pathway. PloS one. 2013;8(3):e59888. doi: 10.1371/journal.pone.0059888
353. Astarita G, Jung KM, Berchtold NC, Nguyen VQ, Gillen DL, Head E, et al. Deficient liver biosynthesis of docosahexaenoic acid correlates with cognitive impairment in Alzheimer's disease. PLoS One. 2010;5(9):e12538. doi: 10.1371/journal.pone.0012538
354. Vandal M, Alata W, Tremblay C, Rioux-Perreault C, Salem N, Jr., Calon F, et al. Reduction in DHA transport to the brain of mice expressing human APOE4 compared to APOE2. J Neurochem. 2014;129(3):516-26. doi: 10.1111/jnc.12640
355. Hetz C, Zhang K, Kaufman RJ. Mechanisms, regulation and functions of the unfolded protein response. Nat Rev Mol Cell Biol. 2020;21(8):421-38. doi: 10.1038/s41580-020-0250-z
356. Yang Z, Huo Y, Zhou S, Guo J, Ma X, Li T, et al. Cancer cell-intrinsic XBP1 drives immunosuppressive reprogramming of intratumoral myeloid cells by promoting cholesterol production. Cell Metab. 2022;34(12):2018-35.e8. doi: 10.1016/j.cmet.2022.10.010
357. Liu SY, Wang W, Cai ZY, Yao LF, Chen ZW, Wang CY, et al. Polymorphism -116C/G of human X-box-binding protein 1 promoter is associated with risk of Alzheimer's disease. CNS Neurosci Ther. 2013;19(4):229-34. doi: 10.1111/cns.12064
358. Reinhardt S, Schuck F, Grösgen S, Riemenschneider M, Hartmann T, Postina R, et al. Unfolded protein response signaling by transcription factor XBP-1 regulates ADAM10 and is affected in Alzheimer's disease. Faseb j. 2014;28(2):978-97. doi: 10.1096/fj.13-234864
359. Lin JH, Li H, Yasumura D, Cohen HR, Zhang C, Panning B, et al. IRE1 signaling affects cell fate during the unfolded protein response. Science. 2007;318(5852):944-9. doi: 10.1126/science.1146361
360. Gerakis Y, Hetz C. Emerging roles of ER stress in the etiology and pathogenesis of Alzheimer's disease. Febs j. 2018;285(6):995-1011. doi: 10.1111/febs.14332
361. Pons V, Lévesque P, Plante MM, Rivest S. Conditional genetic deletion of CSF1 receptor in microglia ameliorates the physiopathology of Alzheimer's disease. Alzheimers Res Ther. 2021;13(1):8. doi: 10.1186/s13195-020-00747-7
362. Kristianto J, Johnson MG, Zastrow RK, Radcliff AB, Blank RD. Spontaneous recombinase activity of Cre-ERT2 in vivo. Transgenic Res. 2017;26(3):411-7. doi: 10.1007/s11248-017-0018-1
363. Haimon Z, Volaski A, Orthgiess J, Boura-Halfon S, Varol D, Shemer A, et al. Re-evaluating microglia expression profiles using RiboTag and cell isolation strategies. Nat Immunol. 2018;19(6):636-44. doi: 10.1038/s41590-018-0110-6
364. Zhang B, Zou J, Han L, Beeler B, Friedman JL, Griffin E, et al. The specificity and role of microglia in epileptogenesis in mouse models of tuberous sclerosis complex. Epilepsia. 2018;59(9):1796-806. doi: 10.1111/epi.14526
365. Hwang HW, Saito Y, Park CY, Blachère NE, Tajima Y, Fak JJ, et al. cTag-PAPERCLIP Reveals Alternative Polyadenylation Promotes Cell-Type Specific Protein Diversity and Shifts Araf Isoforms with Microglia Activation. Neuron. 2017;95(6):1334-49.e5. doi: 10.1016/j.neuron.2017.08.024
366. Jung S, Aliberti J, Graemmel P, Sunshine MJ, Kreutzberg GW, Sher A, et al. Analysis of fractalkine receptor CX(3)CR1 function by targeted deletion and green fluorescent protein reporter gene insertion. Mol Cell Biol. 2000;20(11):4106-14. doi: 10.1128/mcb.20.11.4106-4114.2000
367. Zhao XF, Alam MM, Liao Y, Huang T, Mathur R, Zhu X, et al. Targeting Microglia Using Cx3cr1-Cre Lines: Revisiting the Specificity. eNeuro. 2019;6(4). doi: 10.1523/eneuro.0114-19.2019
368. Thrupp N, Sala Frigerio C, Wolfs L, Skene NG, Fattorelli N, Poovathingal S, et al. Single-Nucleus RNA-Seq Is Not Suitable for Detection of Microglial Activation Genes in Humans. Cell Rep. 2020;32(13):108189. doi: 10.1016/j.celrep.2020.108189
369. Eberwine J, Yeh H, Miyashiro K, Cao Y, Nair S, Finnell R, et al. Analysis of gene expression in single live neurons. Proc Natl Acad Sci U S A. 1992;89(7):3010-4. doi: 10.1073/pnas.89.7.3010
370. Representative in Vitro cDNA Amplification From Individual Hemopoietic Cells and Colonies. 1990.

371. Tang F, Barbacioru C, Wang Y, Nordman E, Lee C, Xu N, et al. mRNA-Seq whole-transcriptome analysis of a single cell. Nat Methods. 2009;6(5):377-82. doi: 10.1038/nmeth.1315
372. Song WM, Colonna M. The identity and function of microglia in neurodegeneration. Nature Immunology. 2018;19(10):1048-58. Available from: https://doi.org/10.1038/s41590-018-0212-1doi: 10.1038/s41590-018-0212-1
373. Lambracht-Washington D, Fu M, Manouchehri N, Hynan LS, Stuve O, Rosenberg RN. Glial cell transcriptome analyses in 3xTg-AD mice: Effects of aging, disease progression, and anti-Aβ immunotherapy. Aging Brain. 2023;3:100066. Available from: https://www.sciencedirect.com/science/article/pii/S2589958923000038doi: https://doi.org/10.1016/j.nbas.2023.100066
374. Marsh SE, Walker AJ, Kamath T, Dissing-Olesen L, Hammond TR, de Soysa TY, et al. Dissection of artifactual and confounding glial signatures by single-cell sequencing of mouse and human brain. Nature Neuroscience. 2022;25(3):306-16. Available from: https://doi.org/10.1038/s41593-022-01022-8doi: 10.1038/s41593-022-01022-8
375. Hickman SE, Allison EK, Coleman U, Kingery-Gallagher ND, El Khoury J. Heterozygous CX3CR1 Deficiency in Microglia Restores Neuronal β-Amyloid Clearance Pathways and Slows Progression of Alzheimer's Like-Disease in PS1-APP Mice. Front Immunol. 2019;10:2780. doi: 10.3389/fimmu.2019.02780
376. Chen WT, Lu A, Craessaerts K, Pavie B, Sala Frigerio C, Corthout N, et al. Spatial Transcriptomics and In Situ Sequencing to Study Alzheimer's Disease. Cell. 2020;182(4):976-91.e19. doi: 10.1016/j.cell.2020.06.038
377. Kunkle BW, Grenier-Boley B, Sims R, Bis JC, Damotte V, Naj AC, et al. Genetic meta-analysis of diagnosed Alzheimer's disease identifies new risk loci and implicates Abeta, tau, immunity and lipid processing. Nat Genet. 2019;51(3):414-30. doi: 10.1038/s41588-019-0358-2
378. Tabata S, Kuroki K, Wang J, Kajikawa M, Shiratori I, Kohda D, et al. Biophysical characterization of O-glycosylated CD99 recognition by paired Ig-like type 2 receptors. The Journal of biological chemistry. 2008;283(14):8893-901. doi: 10.1074/jbc.M709793200
379. Cottat M, Yasukuni R, Homma Y, Lidgi-Guigui N, Varin-Blank N, Lamy de la Chapelle M, et al. Phosphorylation impact on Spleen Tyrosine kinase conformation by Surface Enhanced Raman Spectroscopy. Scientific Reports. 2017;7(1):39766. Available from: https://doi.org/10.1038/srep39766doi: 10.1038/srep39766
380. Yi S, Jiang X, Tang X, Li Y, Xiao C, Zhang J, et al. IL-4 and IL-10 promotes phagocytic activity of microglia by up-regulation of TREM2. Cytotechnology. 2020;72(4):589-602. doi: 10.1007/s10616-020-00409-4
381. Jana M, Dasgupta S, Pal U, Pahan K. IL-12 p40 homodimer, the so-called biologically inactive molecule, induces nitric oxide synthase in microglia via IL-12R beta 1. Glia. 2009;57(14):1553-65. doi: 10.1002/glia.20869
382. Furukawa A, Kakita K, Yamada T, Ishizuka M, Sakamoto J, Hatori N, et al. Structural and thermodynamic analyses reveal critical features of glycopeptide recognition by the human PILRalpha immune cell receptor. The Journal of biological chemistry. 2017;292(51):21128-36. doi: 10.1074/jbc.M117.799239
383. Sun Y, Caplazi P, Zhang J, Mazloom A, Kummerfeld S, Quinones G, et al. PILRalpha negatively regulates mouse inflammatory arthritis. Journal of immunology (Baltimore, Md : 1950). 2014;193(2):860-70. doi: 10.4049/jimmunol.1400045
384. Tsukui D, Kimura Y, Kono H. GM-CSF receptor/SYK/JNK/FOXO1/CD11c signaling promotes atherosclerosis. iScience. 2023;26(8):107293. doi: 10.1016/j.isci.2023.107293
385. Claes C, Danhash EP, Hasselmann J, Chadarevian JP, Shabestari SK, England WE, et al. Plaque-associated human microglia accumulate lipid droplets in a chimeric model of Alzheimer's disease. Molecular Neurodegeneration. 2021;16(1):50. Available from: https://doi.org/10.1186/s13024-021-00473-0doi: 10.1186/s13024-021-00473-0

386. Wang S, Colonna M. The microglial immunoreceptor tyrosine-based motif-Syk signaling pathway is a promising target of immunotherapy for Alzheimer's disease. Clin Transl Med. 2023;13(2):e1200. doi: 10.1002/ctm2.1200
387. Aksentijevich I. The sickening consequences of too much SYK signaling. Nature Genetics. 2021;53(4):432-4. Available from: https://doi.org/10.1038/s41588-021-00837-8doi: 10.1038/s41588-021-00837-8
388. Wang L, Aschenbrenner D, Zeng Z, Cao X, Mayr D, Mehta M, et al. Gain-of-function variants in SYK cause immune dysregulation and systemic inflammation in humans and mice. Nature Genetics. 2021;53(4):500-10. Available from: https://doi.org/10.1038/s41588-021-00803-4doi: 10.1038/s41588-021-00803-4
389. Schweig JE, Yao H, Coppola K, Jin C, Crawford F, Mullan M, et al. Spleen tyrosine kinase (SYK) blocks autophagic Tau degradation in vitro and in vivo. Journal of Biological Chemistry. 2019;294(36):13378-95. Available from: https://www.sciencedirect.com/science/article/pii/S0021925820303926doi: https://doi.org/10.1074/jbc.RA119.008033
390. Yamaguchi T, Hamano T, Sada K, Kanaan NM, Sasaki H, Yen S-H, et al. Syk inhibitor reduces oligomeric tau associated with GSK3β inactivation and autophagy activation. Alzheimer's & Dementia. 2020;16(S3):e042633. [accessed 2023/10/22]. Available from: https://doi.org/10.1002/alz.042633doi: https://doi.org/10.1002/alz.042633
391. Birkle TJY, Brown GC. Syk inhibitors protect against microglia-mediated neuronal loss in culture. Front Aging Neurosci. 2023;15:1120952. doi: 10.3389/fnagi.2023.1120952
392. Andrew CG, Eftychia B, Janet CH, Umran Y, Meral C, Naciye M, et al. Genetic variation associated with human longevity and Alzheimer's disease risk act through microglia and oligodendrocyte cross-talk. medRxiv. 2023:2023.03.30.23287975. Available from: http://medrxiv.org/content/early/2023/04/03/2023.03.30.23287975.abstractdoi: 10.1101/2023.03.30.23287975
393. Lambert JC, Ibrahim-Verbaas CA, Harold D, Naj AC, Sims R, Bellenguez C, et al. Meta-analysis of 74,046 individuals identifies 11 new susceptibility loci for Alzheimer's disease. Nat Genet. 2013;45(12):1452-8. doi: 10.1038/ng.2802
394. Leng F, Edison P. Neuroinflammation and microglial activation in Alzheimer disease: where do we go from here? Nature Reviews Neurology. 2021;17(3):157-72. Available from: https://doi.org/10.1038/s41582-020-00435-ydoi: 10.1038/s41582-020-00435-y
395. Chew G, Petretto E. Transcriptional Networks of Microglia in Alzheimer's Disease and Insights into Pathogenesis. Genes (Basel). 2019;10(10). doi: 10.3390/genes10100798
396. Fleiss B, Van Steenwinckel J, Bokobza C, I KS, Ross-Munro E, Gressens P. Microglia-Mediated Neurodegeneration in Perinatal Brain Injuries. Biomolecules. 2021;11(1). doi: 10.3390/biom11010099
397. Pisetsky DS. Pathogenesis of autoimmune disease. Nature Reviews Nephrology. 2023;19(8):509-24. Available from: https://doi.org/10.1038/s41581-023-00720-1doi: 10.1038/s41581-023-00720-1
398. Korvatska O, Leverenz JB, Jayadev S, McMillan P, Kurtz I, Guo X, et al. R47H Variant of TREM2 Associated With Alzheimer Disease in a Large Late-Onset Family: Clinical, Genetic, and Neuropathological Study. JAMA Neurol. 2015;72(8):920-7. doi: 10.1001/jamaneurol.2015.0979
399. Muzio L, Viotti A, Martino G. Microglia in Neuroinflammation and Neurodegeneration: From Understanding to Therapy. Frontiers in neuroscience. 2021;15:742065. doi: 10.3389/fnins.2021.742065

Appendices

Appendix 1

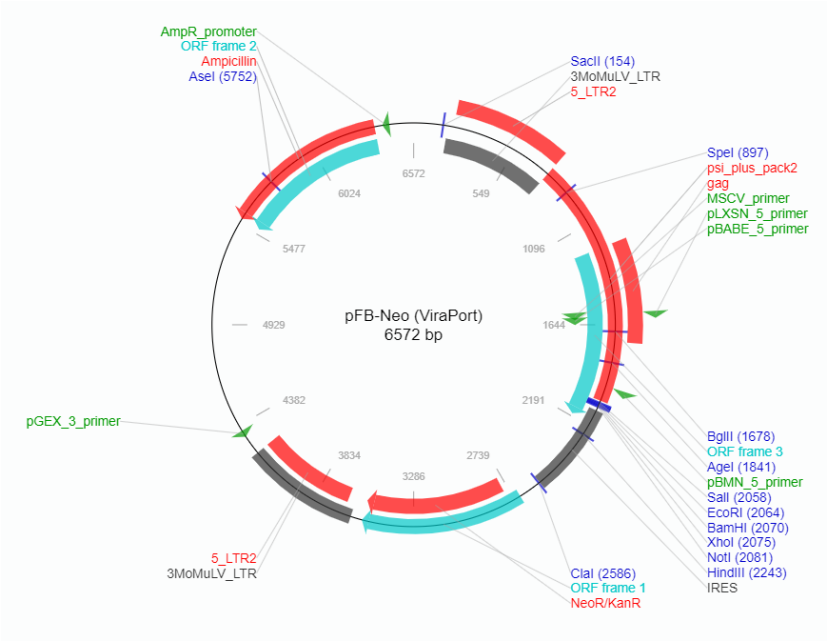

Appendix 1: pFB-Neo vector map (Addgene).

Appendix 2

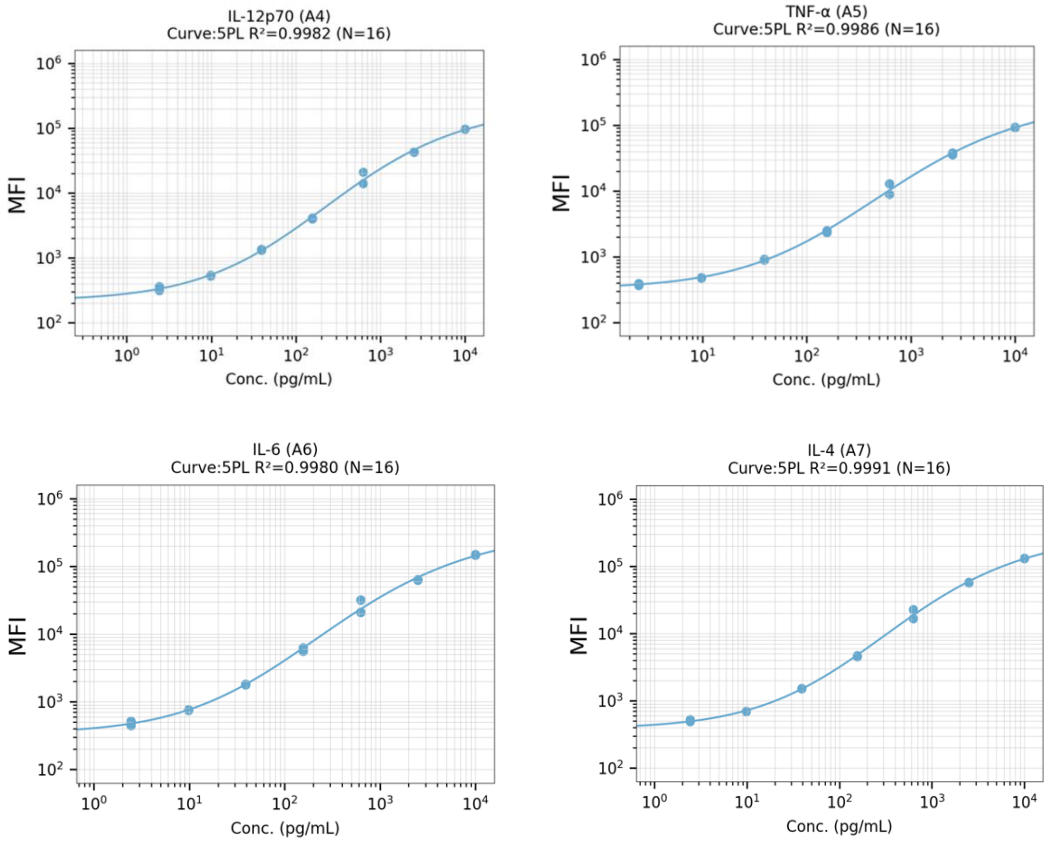

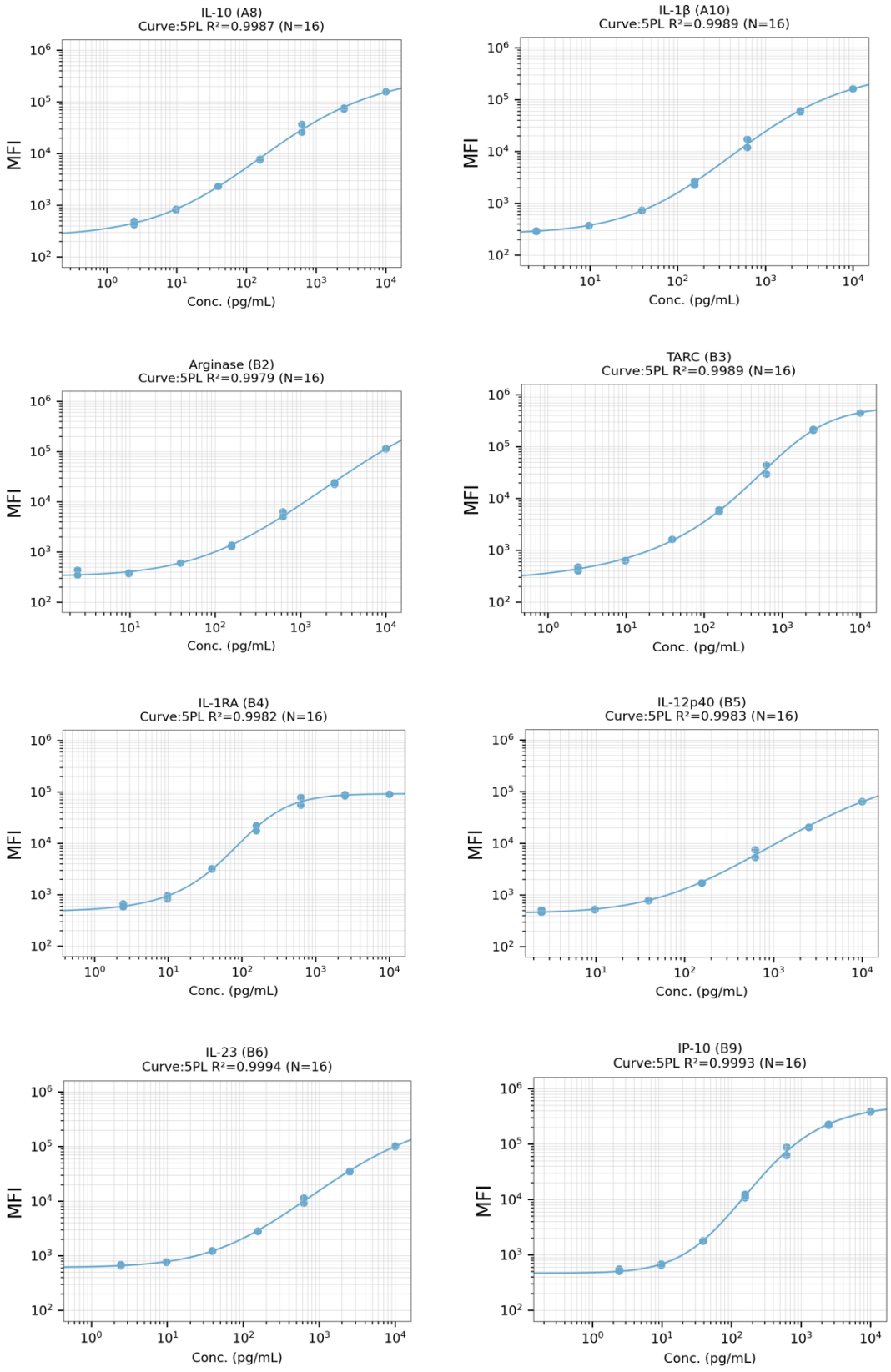

Appendix 2: Standard curves of cytokines included in the Legendplex assay.

Appendix 3

Detailed version of the code used to process the ScRNA-sequencing data in this thesis can be found here: Files · main · TaylorGroup / single-cell RNA seq icell8 pipeline · GitLab (cardiff.ac.uk). The code was developed by Dr Ruth Jones. Additional changes and adjustments have been made by Dr Mateus Bernardo Harrington and Dr Carolina Toste.

Appendix 3: Differentially expressed genes (DEGs) in Syk x APP x Cre-ERT mice compared to Syk x APP animals.

Gene	baseMean	log2FoldChange	lfcSE	pvalue	padj
Gm10800	1720527	-0.3782	0.016992	########	########
2410004B18Rik	396.2349	-5.4169	0.644969	2.24E-18	1.98E-14
Rfxap	385.0764	-4.63702	0.569861	1.87E-17	1.10E-13
Timm10	232.1327	5.154221	0.642768	6.82E-17	3.02E-13
Cryab	315.0001	5.167531	0.669636	6.44E-16	2.28E-12
Cnp	170.668	4.279706	0.569846	3.68E-15	1.08E-11
Tbx6	139.0923	4.464853	0.621689	4.52E-14	1.14E-10
Slc1a2	4838.138	1.878979	0.263607	6.16E-14	1.36E-10
Nradd	118.4249	4.062149	0.589694	3.72E-13	7.31E-10
Gnl1	254.5944	3.455561	0.524972	2.34E-12	4.14E-09
Cox6a1	807.5869	2.632323	0.413297	9.68E-12	1.43E-08
Hsdl1	579.6937	4.864438	0.765551	9.41E-12	1.43E-08
Atg10	218.4019	-3.22889	0.511796	1.32E-11	1.80E-08
Cd48	82.57846	3.752877	0.60174	3.09E-11	3.91E-08
Flt3l	131.0849	3.609976	0.586524	4.12E-11	4.56E-08
Bcl2a1a	98.28846	3.537301	0.572503	3.88E-11	4.56E-08
Ahcyl1	820.9478	2.866695	0.478071	9.47E-11	9.86E-08
Tmcc2	144.6744	3.785809	0.640133	1.69E-10	1.62E-07
Imp3	98.71001	3.6021	0.607122	1.74E-10	1.62E-07
Mad2l2	153.6381	3.924444	0.667591	2.07E-10	1.67E-07
D11Wsu47e	115.088	3.823576	0.647274	1.92E-10	1.67E-07
Cluap1	117.532	3.137915	0.532464	2.01E-10	1.67E-07
Ppdpf	146.2067	-4.68783	0.802762	2.41E-10	1.78E-07
1700123O20Rik	47.20886	-3.8682	0.655641	2.37E-10	1.78E-07
Lrrc8a	220.1204	3.013849	0.520546	3.43E-10	2.43E-07
Fgf11	58.80715	4.070936	0.698378	5.21E-10	3.55E-07
Ppp1r1b	86.67063	4.611143	0.80327	6.60E-10	4.32E-07
Ywhag	522.5138	3.389069	0.599572	7.42E-10	4.65E-07
Kdelr2	279.6664	3.990154	0.70707	7.63E-10	4.65E-07
Mpv17	459.3115	4.492568	0.798234	7.92E-10	4.67E-07
Tma7	135.3403	3.021296	0.540772	1.18E-09	6.74E-07
Themis2	473.2089	2.799954	0.506005	1.53E-09	8.46E-07
Rsl24d1	93.65805	-2.76367	0.500466	1.67E-09	8.94E-07
Rpain	346.366	4.442182	0.810261	1.82E-09	9.45E-07
Tmem184b	477.7667	3.052049	0.556876	2.00E-09	1.01E-06

Lsm1	192.8497	2.819707	0.515188	2.19E-09	1.08E-06
Fam207a	250.6298	-3.67427	0.676168	2.37E-09	1.13E-06
Fbxw9	89.40211	-3.54619	0.654267	2.72E-09	1.27E-06
Hs6st1	85.01207	-2.74316	0.510525	3.77E-09	1.70E-06
Cct6a	712.9957	2.296824	0.427204	3.85E-09	1.70E-06
Slc25a51	226.1473	2.784155	0.522537	4.72E-09	2.04E-06
Xpa	171.9579	2.960016	0.557292	5.26E-09	2.17E-06
Nipsnap2	225.3963	-3.13424	0.592036	5.28E-09	2.17E-06
Ndufs2	488.295	3.210478	0.611527	6.94E-09	2.79E-06
Kcnn4	176.6938	4.03155	0.770557	7.68E-09	3.02E-06
Ctf2	95.73075	-3.41045	0.654485	8.41E-09	3.23E-06
Nrm	252.5723	3.964215	0.762485	8.68E-09	3.27E-06
Rmi1	490.846	3.468535	0.676459	1.28E-08	4.71E-06
Tbc1d10b	419.6084	2.693385	0.529813	1.74E-08	6.27E-06
Calhm2	243.7523	3.011764	0.597638	2.13E-08	7.55E-06
Cstb	287.2464	5.902587	1.205729	3.90E-08	1.33E-05
Gm3164	85.33581	2.897956	0.585647	3.92E-08	1.33E-05
Bag6	122.8398	2.724544	0.555192	4.55E-08	1.52E-05
Tnfrsf4	61.78513	-2.50124	0.511199	4.99E-08	1.64E-05
9130401M01Rik	64.53162	3.401085	0.694796	5.65E-08	1.79E-05
Mcrs1	68.22785	2.843403	0.58196	5.62E-08	1.79E-05
Irf1	294.2084	2.98793	0.617242	5.89E-08	1.80E-05
Zfp950	1067.678	2.002928	0.411397	5.90E-08	1.80E-05
Iqcc	129.9707	3.018261	0.628377	7.36E-08	2.17E-05
Fabp7	131.467	4.141046	0.863232	7.26E-08	2.17E-05
Mtif3	175.4091	-2.40215	0.507337	1.02E-07	2.96E-05
Pafah2	100.0315	-2.3882	0.509865	1.35E-07	3.85E-05
Rraga	105.6177	-2.95826	0.636229	1.48E-07	4.16E-05
Tmem221	116.902	4.111757	0.8946	1.91E-07	5.27E-05
Spty2d1	483.8804	2.200188	0.476802	1.94E-07	5.27E-05
Stk16	327.4772	-2.75981	0.603904	2.07E-07	5.50E-05
Camk2b	139.0372	2.400881	0.522113	2.08E-07	5.50E-05
Gadd45gip1	57.56297	5.054633	1.072274	2.27E-07	5.92E-05
Nefm	151.5233	2.388185	0.525362	2.66E-07	6.72E-05
Ppp1r21	971.6981	2.775864	0.613379	2.65E-07	6.72E-05
Rps6kc1	617.3071	-2.22512	0.491973	2.76E-07	6.88E-05
Pf4	182.9512	4.003834	0.89024	2.83E-07	6.95E-05
Fam72a	129.7494	2.500174	0.553195	2.97E-07	7.19E-05
Hmces	315.2982	3.160021	0.705784	3.23E-07	7.71E-05
Gm21738	194372.6	-0.33225	0.067099	3.92E-07	9.24E-05
Cd3eap	41.74597	2.824467	0.62542	4.06E-07	9.28E-05
Mrpl17	400.483	-2.36007	0.531525	4.02E-07	9.28E-05
Cyp46a1	87.34147	2.593554	0.582219	4.09E-07	9.28E-05
Bad	236.5223	-4.83353	1.112538	4.71E-07	1.06E-04
Ccdc102a	59.06487	-2.65771	0.608825	5.71E-07	1.26E-04
Acadl	355.044	2.531063	0.582617	6.23E-07	1.36E-04

Gnpat	410.7566	2.567084	0.590888	6.37E-07	1.38E-04
Natd1	83.17236	-2.1351	0.490791	6.58E-07	1.40E-04
Myl12a	96.32976	2.611002	0.601884	6.88E-07	1.45E-04
Pcdhga2	85.45812	2.347838	0.540722	7.15E-07	1.47E-04
Ndufv1	284.8989	3.167703	0.737018	7.12E-07	1.47E-04
Zbtb12	60.19912	-4.71455	1.100212	7.97E-07	1.62E-04
Ss18l2	271.8495	3.478334	0.816122	8.10E-07	1.63E-04
Rexo4	366.4699	2.603483	0.608299	8.38E-07	1.67E-04
Zcchc3	112.2331	-2.94415	0.692193	8.57E-07	1.69E-04
Tcf7l2	922.6764	1.753944	0.410018	9.40E-07	1.83E-04
Rnf227	57.0861	2.467576	0.575816	9.84E-07	1.89E-04
Ercc2	187.3629	3.052532	0.723974	1.04E-06	1.98E-04
Fxr2	371.4945	2.285716	0.538501	1.05E-06	1.98E-04
Ptpmt1	288.6517	3.757216	0.906283	1.29E-06	2.40E-04
Dhrs4	93.3508	2.661703	0.638759	1.41E-06	2.57E-04
Amdhd2	100.4942	-2.15831	0.517281	1.40E-06	2.57E-04
Akt1	129.2121	2.766254	0.666825	1.46E-06	2.64E-04
Stk38	1303.971	2.102455	0.505928	1.56E-06	2.78E-04
Ppia	144.8107	2.936872	0.712773	1.62E-06	2.84E-04
Vat1	71.2604	-3.08415	0.750894	1.61E-06	2.84E-04
Zfp91	1037.351	-1.60835	0.389334	1.95E-06	3.37E-04
Rpl6	125.8469	2.185263	0.534178	2.07E-06	3.56E-04
Gm10718	146780.5	-0.34816	0.076255	2.30E-06	3.92E-04
Ube2c	98.77399	3.304572	0.822228	2.48E-06	4.18E-04
Reep4	106.5707	3.46875	0.866088	2.56E-06	4.28E-04
Sparcl1	1200.507	1.651431	0.406579	2.66E-06	4.39E-04
Lyrm2	165.4894	-2.72892	0.684885	2.73E-06	4.46E-04
Rabggta	95.69247	2.343663	0.583169	2.77E-06	4.46E-04
Ak6	69.25878	2.849411	0.709949	2.76E-06	4.46E-04
Ndufb4	50.97607	2.61857	0.649632	2.87E-06	4.57E-04
Mfsd12	203.1873	3.497518	0.887444	3.11E-06	4.83E-04
Rps19bp1	94.15846	4.119907	1.040729	3.08E-06	4.83E-04
Men1	84.88396	3.262494	0.822789	3.11E-06	4.83E-04
Tifa	273.0689	2.0605	0.517444	3.27E-06	5.04E-04
Yif1a	24.60674	3.012539	0.730012	3.37E-06	5.14E-04
Cpe	2881.965	2.310781	0.585604	3.74E-06	5.66E-04
Sdf2l1	112.4782	2.041818	0.517618	3.93E-06	5.90E-04
Cdc123	247.5908	2.380406	0.610849	4.21E-06	6.26E-04
Klhl21	165.2025	3.566521	0.924924	4.32E-06	6.37E-04
Phyhip	269.569	4.808335	1.262362	4.45E-06	6.50E-04
Gps1	54.87542	2.078962	0.529519	4.63E-06	6.71E-04
Armcx3	36.47604	-2.49402	0.641687	4.84E-06	6.97E-04
Wrap53	39.33041	2.668316	0.681972	5.04E-06	7.19E-04
Btd	42.28473	3.393231	0.871209	5.22E-06	7.39E-04
AA467197	30.72174	-2.29408	0.593512	5.63E-06	7.90E-04
Oxsr1	392.746	1.934723	0.50449	6.00E-06	8.36E-04

Morf4l2	295.1757	2.829868	0.748469	6.26E-06	8.65E-04
Cd300c2	370.2878	3.273189	0.874237	6.71E-06	9.21E-04
Rpp14	130.7474	-2.66397	0.710386	6.97E-06	9.49E-04
Gar1	57.04934	2.078858	0.548768	7.92E-06	0.00107
Llgl1	31.97447	2.351351	0.616641	8.46E-06	0.001134
Plpp3	919.505	1.996974	0.533966	8.58E-06	0.001135
Bckdk	158.7794	2.974514	0.805208	8.60E-06	0.001135
Zbtb17	89.01055	2.454922	0.6614	8.96E-06	0.001174
Rac1	408.7609	3.482796	0.956562	9.48E-06	0.001233
Xpot	672.0162	-2.49845	0.683118	9.85E-06	0.001263
Zcchc10	150.4517	2.586785	0.703788	9.80E-06	0.001263
Trp53rkb	72.09334	2.191743	0.59161	1.01E-05	0.001289
Dnajc30	564.966	-3.59959	1.002522	1.03E-05	0.001299
Ndp	355.6223	-0.23799	0.47437	1.05E-05	0.001317
1700066M21Rik	79.80963	-1.98529	0.541165	1.12E-05	0.00139
Zfp955b	328.5407	2.219739	0.607968	1.13E-05	0.0014
Prorsd1	111.1981	-2.05749	0.564243	1.16E-05	0.001425
Ndufs8	43.235	3.248506	0.88414	1.17E-05	0.001425
Dnajb2	57.74118	1.889962	0.511641	1.18E-05	0.001429
Cox5b	117.5866	2.84041	0.786708	1.20E-05	0.001449
Scnm1	209.2211	2.726418	0.757965	1.26E-05	0.001485
Plaur	98.51454	2.21055	0.608025	1.26E-05	0.001485
Zfp707	95.70335	-2.09898	0.578502	1.24E-05	0.001485
Tnni3	76.76415	-2.933	0.818514	1.29E-05	0.001488
Wdr24	37.10011	2.104096	0.569896	1.28E-05	0.001488
Ranbp3	318.3761	2.413345	0.667678	1.28E-05	0.001488
Nkap	204.9263	2.65879	0.741782	1.34E-05	0.001538
Gys1	131.0541	1.887191	0.520543	1.39E-05	0.00159
Pcnp	177.2481	2.243944	0.623842	1.40E-05	0.00159
Gsk3a	170.5998	-3.28323	0.932242	1.42E-05	0.001597
Nosip	109.7423	2.370855	0.660467	1.44E-05	0.001611
Oxnad1	200.9064	-1.93885	0.539602	1.45E-05	0.001617
Ctbs	412.2291	2.541091	0.713009	1.47E-05	0.001631
Cmc1	42.07145	-1.8761	0.521077	1.59E-05	0.00173
Gadd45g	50.56562	3.314509	0.928181	1.58E-05	0.00173
Myc	50.96413	-2.27836	0.639693	1.59E-05	0.00173
Taf4	385.0203	1.926925	0.543952	1.83E-05	0.001972
Lysmd1	46.06348	2.952765	0.835339	1.88E-05	0.002014
Rsad1	132.6682	-2.27774	0.651057	1.89E-05	0.002016
Vps9d1	634.2754	2.055108	0.582608	1.95E-05	0.002069
Rexo1	120.6667	-1.80615	0.512698	1.99E-05	0.002098
Gna11	61.38378	2.309572	0.659271	2.10E-05	0.002193
Rhbdd3	117.2196	3.835478	1.120871	2.13E-05	0.002193
Sox10	84.43053	-0.31055	0.63656	2.11E-05	0.002193
Tuba1a	394.411	3.04732	0.887206	2.14E-05	0.002193
Mmut	177.0911	1.789632	0.509448	2.14E-05	0.002193

Cldn11	200.3574	-2.91023	0.852549	2.19E-05	0.002226
Unc45a	131.3678	2.064744	0.594848	2.32E-05	0.002343
Fbxo22	170.2186	3.02314	0.88695	2.36E-05	0.002377
Spint1	397.9456	1.944113	0.560678	2.43E-05	0.002427
Sgms2	152.8806	1.81686	0.522924	2.46E-05	0.002427
Bbc3	88.55806	-2.10304	0.610131	2.44E-05	0.002427
H4c4	143.8588	-1.99752	0.582506	2.59E-05	0.00255
Ppm1m	177.5341	3.623983	1.081706	2.66E-05	0.0026
Ncstn	89.14048	1.819035	0.527159	2.74E-05	0.002658
Utp4	185.5361	2.033359	0.594364	2.75E-05	0.002658
Naa10	85.57586	-2.42405	0.71666	2.83E-05	0.002704
Iqsec2	170.8757	2.37132	0.699781	2.81E-05	0.002704
Pmvk	58.47381	2.526986	0.741479	2.84E-05	0.002706
Zbtb40	617.0779	-1.80267	0.527842	2.86E-05	0.002706
Dhdds	223.5199	1.861773	0.545358	3.01E-05	0.002831
Fkbp2	176.9445	2.650468	0.790885	3.04E-05	0.002849
Pdia4	360.9226	-1.72329	0.507907	3.20E-05	0.002969
Elp6	85.36263	1.749725	0.512188	3.19E-05	0.002969
Sgsh	262.211	2.469756	0.740288	3.27E-05	0.003009
Fam216a	499.4545	5.024058	1.567027	3.29E-05	0.003012
Max	293.7093	2.234104	0.667275	3.37E-05	0.003078
Rbm7	298.297	-1.76676	0.525278	3.48E-05	0.003162
Ndor1	63.12239	3.688329	1.114226	3.52E-05	0.003169
Clpx	387.7802	2.279813	0.685839	3.53E-05	0.003169
Crip2	296.9177	4.022254	1.243134	3.55E-05	0.003169
Qrfp	48.62637	-2.1105	0.632982	3.73E-05	0.003318
Khdc3	72.29083	-0.28555	0.566894	3.87E-05	0.003424
Mocs3	81.60329	2.130341	0.642163	4.00E-05	0.003494
S100a13	70.05999	2.576316	0.782068	3.97E-05	0.003494
Sf3a1	285.4303	1.962155	0.590285	4.01E-05	0.003494
Ccdc28b	30.72125	3.201745	0.952497	4.08E-05	0.003501
Lsm4	143.0085	3.90478	1.215297	4.07E-05	0.003501
Trappc12	592.1631	-2.11213	0.643323	4.04E-05	0.003501
Eps15	787.3849	1.826841	0.5511	4.19E-05	0.003578
Vps51	41.32693	2.068311	0.622615	4.46E-05	0.003792
Poc1b	139.8699	1.694924	0.513749	4.74E-05	0.004009
Slc45a4	116.6047	2.043342	0.629835	5.04E-05	0.004243
Ppp6r1	725.5008	1.573272	0.478098	5.09E-05	0.004255
Ccdc124	77.9856	-1.88024	0.578384	5.10E-05	0.004255
Sema4a	187.1568	2.739868	0.860619	5.24E-05	0.00435
BC024978	278.3406	2.931584	0.92654	5.26E-05	0.00435
Csnk1d	921.5525	-1.62385	0.498657	5.31E-05	0.004367
Fam214b	120.5706	2.093519	0.65017	5.39E-05	0.004411
Nsun6	382.2723	-2.0782	0.650523	5.48E-05	0.004462
Fam222a	153.4051	5.405217	1.761605	5.50E-05	0.004462
Wscd1	102.3023	1.748919	0.53861	5.58E-05	0.00451

Tmem14c	125.6237	2.659677	0.840703	5.73E-05	0.004576
Hgh1	84.40168	1.947503	0.605098	5.70E-05	0.004576
Mydgf	210.5577	-1.84	0.573634	5.74E-05	0.004576
Lrmp	323.1009	-1.95697	0.613798	5.82E-05	0.004618
Rab9	285.9944	4.611891	1.51929	5.94E-05	0.004691
Epn3	111.5614	3.6964	1.191033	6.03E-05	0.004744
Gcsh	103.5895	2.243436	0.710188	6.39E-05	0.005
Gpd1	36.44742	-3.94922	1.270413	6.48E-05	0.005047
Ccdc84	331.9301	-2.60381	0.843989	6.77E-05	0.005251
Tspan13	808.2105	1.468139	0.457558	6.83E-05	0.005252
Treml1	116.4016	2.494922	0.799566	6.82E-05	0.005252
Bud13	153.6998	-2.01161	0.64154	6.86E-05	0.005253
2610002M06Rik	128.0775	2.482034	0.800008	7.24E-05	0.005519
Mrpl38	187.1285	2.306345	0.742511	7.30E-05	0.005546
Tsc22d1	264.7868	1.813602	0.577669	7.55E-05	0.005712
Gm10801	151165.8	-0.36289	0.09526	7.72E-05	0.005784
Nrxn2	105.1561	1.689034	0.535158	7.70E-05	0.005784
Cherp	121.123	2.610359	0.853494	7.99E-05	0.005963
Sae1	160.9195	-2.26273	0.742436	8.36E-05	0.006134
Lat	39.83705	-3.25144	1.073684	8.31E-05	0.006134
Evl	193.3445	-1.86643	0.604065	8.28E-05	0.006134
Rab5a	276.8696	-1.77565	0.573062	8.34E-05	0.006134
Sltm	2771.821	1.299168	0.412058	8.59E-05	0.006254
Tspo	177.8534	3.972536	1.34576	8.58E-05	0.006254
Fut11	137.4322	1.969871	0.63969	8.71E-05	0.006318
Grk6	491.0079	2.346908	0.771832	8.77E-05	0.00633
Cidea	23.63234	-2.4497	0.796276	9.00E-05	0.006474
Znrd1as	63.74208	1.960437	0.636873	9.18E-05	0.006577
Mrpl36	27.73087	-1.91737	0.619542	9.23E-05	0.006586
Trappc4	402.7021	3.131979	1.065702	9.93E-05	0.007058
Arf1	263.9646	1.903149	0.626645	1.00E-04	0.007101
Zfpl1	19.26222	2.513428	0.7919	1.01E-04	0.007101
Mamdc4	71.51063	1.588884	0.514098	1.02E-04	0.007158
Slc48a1	76.39244	3.226802	1.090582	1.02E-04	0.007158
Fam45a	639.005	-1.75428	0.580296	1.04E-04	0.007236
Trmt10a	421.6937	2.499981	0.842905	1.05E-04	0.007253
Parp6	520.2464	1.570101	0.511362	1.05E-04	0.007253
Erlin2	398.9027	1.726326	0.568455	1.07E-04	0.007368
Itgb2	370.0698	-1.75673	0.583582	1.09E-04	0.007503
Gpatch4	86.81788	1.966233	0.653493	1.12E-04	0.00761
mt-Nd6	38726.29	-0.60369	0.175905	1.11E-04	0.00761
1600014C10Rik	117.3891	1.72522	0.570249	1.12E-04	0.00762
Tmem63b	76.095	-1.74327	0.579057	1.15E-04	0.007772
Mt3	519.7085	1.483897	0.489288	1.16E-04	0.007819
Pskh1	150.821	2.531498	0.86498	1.19E-04	0.007884
Acot13	179.8841	4.137427	1.464746	1.19E-04	0.007884

Kat5	62.99265	1.857146	0.617393	1.19E-04	0.007884
Myd88	187.7596	2.74522	0.943837	1.20E-04	0.007937
Sox18	150.6695	4.645242	1.65971	1.21E-04	0.007961
Ech1	114.0412	3.25758	1.131652	1.21E-04	0.007961
Dtx3	64.35172	1.770469	0.5873	1.21E-04	0.007961
Map4k2	467.1272	1.651125	0.549958	1.23E-04	0.008045
B4galt7	170.0633	-3.33301	1.18025	1.25E-04	0.008121
Tlk2	361.7645	1.532773	0.509283	1.29E-04	0.008331
Dusp2	221.4193	-0.12645	0.352883	1.31E-04	0.008434
Rfc2	477.2018	-1.78393	0.605154	1.31E-04	0.008435
Ak1	141.4947	2.395162	0.826658	1.36E-04	0.008686
Acsbg1	253.3663	2.006086	0.685288	1.36E-04	0.008691
Hypk	124.4849	-2.23884	0.779792	1.44E-04	0.009157
Prpf31	193.2375	2.06154	0.713304	1.47E-04	0.009325
H2aw	230.7086	2.132249	0.739014	1.49E-04	0.009406
Trpc4ap	726.508	-1.35371	0.454402	1.51E-04	0.009477
Abhd4	94.36788	1.947348	0.67117	1.52E-04	0.009484
Gm35339	134.2219	-2.33538	0.822028	1.51E-04	0.009484
Rps27	2417.105	1.087038	0.358393	1.56E-04	0.009696
Zfp1	115.7076	-2.36026	0.834696	1.57E-04	0.009696
Esd	250.963	2.343269	0.824395	1.56E-04	0.009696
Armcx2	173.4502	2.150132	0.751463	1.58E-04	0.009721
Fkbp14	155.7255	-1.73433	0.598883	1.59E-04	0.009721
Egln1	59.24543	1.750288	0.597805	1.59E-04	0.009721
Lipt1	51.26777	1.94441	0.671692	1.64E-04	0.009869
Trappc3	59.0943	2.430737	0.8528	1.62E-04	0.009869
Grwd1	51.29658	-2.06898	0.723136	1.62E-04	0.009869
Id2	352.1675	-1.73197	0.601319	1.64E-04	0.009869
Slc38a6	480.3211	1.861703	0.644373	1.64E-04	0.009869
Cacfd1	155.7457	-2.2976	0.81924	1.69E-04	0.010153
Tlr8	151.1748	3.016975	1.093951	1.73E-04	0.010366
Phactr4	318.7945	1.651602	0.572443	1.75E-04	0.010417
Hipk2	435.347	-1.91179	0.676616	1.78E-04	0.010482
2310022A10Rik	97.77124	1.56633	0.539269	1.78E-04	0.010482
H1f2	1207.92	1.652819	0.573333	1.78E-04	0.010482
Dcaf12	386.4774	-1.96383	0.698321	1.81E-04	0.010634
Ndufa8	153.6047	2.151912	0.765339	1.83E-04	0.010696
Snx21	177.238	3.435545	1.272047	1.84E-04	0.01077
Nrros	572.6268	-1.51078	0.52487	1.85E-04	0.010783
Tor2a	86.5228	-0.31603	0.641409	1.93E-04	0.011201
Rps3	520.4571	2.668082	0.975072	1.94E-04	0.011201
Treml2	169.9354	-1.86226	0.664563	1.96E-04	0.011291
Stx5a	556.0478	1.995128	0.711732	1.97E-04	0.011291
Idh3b	209.0631	-2.35911	0.862368	1.99E-04	0.011388
Ppp1r8	229.1779	2.890529	1.069694	2.03E-04	0.011571
Stxbp3	585.275	-1.47106	0.515747	2.04E-04	0.011608

Rundc1	74.43338	2.968312	1.094206	2.08E-04	0.011782
Grhpr	35.66535	2.001036	0.710156	2.19E-04	0.012358
Ndufa13	399.3172	3.081939	1.165243	2.24E-04	0.012567
Trap1	230.862	1.717276	0.613827	2.23E-04	0.012567
Igsf6	195.9406	1.916884	0.696089	2.27E-04	0.012733
Scpep1	536.0884	-1.45708	0.51842	2.31E-04	0.012885
Cd99l2	309.458	1.966098	0.715722	2.33E-04	0.012955
Tapbpl	64.21744	2.569139	0.954546	2.41E-04	0.013308
Laptm4b	262.3877	1.497952	0.534267	2.41E-04	0.013308
Snapc2	126.1782	-0.20746	0.427389	2.45E-04	0.013441
Rab40b	191.104	-0.18875	0.405745	2.44E-04	0.013441
Surf4	152.5265	1.775678	0.648172	2.52E-04	0.01374
Ubl4a	362.3886	2.526494	0.95289	2.51E-04	0.01374
Fgr	140.9144	1.91588	0.704216	2.56E-04	0.013934
Chst14	45.56835	1.981543	0.724702	2.61E-04	0.014168
Pradc1	59.69765	2.903647	1.099739	2.62E-04	0.014193
Atp6ap2	778.4108	1.224265	0.435856	2.73E-04	0.014697
Kti12	216.9357	4.305755	1.75023	2.73E-04	0.014697
Fcer1g	1620.978	1.213584	0.429158	2.77E-04	0.014857
Kif2a	480.3641	1.827575	0.680374	2.83E-04	0.015113
Qrich1	453.3166	1.469222	0.533959	2.87E-04	0.015293
Rabif	155.313	2.602242	1.001508	2.89E-04	0.015326
Prdm11	117.7624	1.627715	0.599458	2.90E-04	0.015326
Rtl5	62.26162	2.219417	0.837748	2.90E-04	0.015326
Arv1	184.0582	3.168889	1.249469	2.91E-04	0.015326
Prcc	146.8709	-2.39533	0.929429	2.98E-04	0.015666
Whamm	124.6465	-1.91755	0.728069	3.05E-04	0.015949
Blcap	201.6463	-1.79467	0.680297	3.14E-04	0.016408
Ncoa3	1079.288	1.21063	0.435912	3.20E-04	0.016559
Siglecf	65.78287	1.438343	0.526067	3.19E-04	0.016559
Arl1	784.2135	1.951489	0.744171	3.19E-04	0.016559
Strap	170.2772	2.254989	0.873781	3.24E-04	0.016721
Dus3l	165.9558	1.613174	0.602932	3.29E-04	0.016901
mt-Nd4	122333.8	-0.42971	0.13215	3.30E-04	0.016941
Eme2	17.20378	2.277994	0.821771	3.34E-04	0.017064
Smim15	451.8556	2.394034	0.938603	3.36E-04	0.017146
Zfp46	130.5629	1.836273	0.699536	3.40E-04	0.017223
Izumo4	151.4404	4.25132	1.78919	3.43E-04	0.017223
Gdf9	73.54885	2.294791	0.891283	3.41E-04	0.017223
Uqcrb	434.7949	3.9064	1.641271	3.42E-04	0.017223
Tagap1	142.7954	2.598003	1.026558	3.40E-04	0.017223
Pithd1	114.5865	-2.69322	1.082446	3.45E-04	0.01724
Kctd2	768.7581	1.335857	0.49165	3.45E-04	0.01724
Pla2g5	86.49638	2.210655	0.861639	3.49E-04	0.017385
Aldh1b1	89.24088	-0.22036	0.443564	3.55E-04	0.017645
P2ry1	73.43267	1.423672	0.529731	3.62E-04	0.017895

Cks1b	51.10985	3.440876	1.381238	3.63E-04	0.017895
Get1	229.085	2.007656	0.780421	3.63E-04	0.017895
Trim3	84.06749	1.971947	0.764808	3.69E-04	0.018135
N4bp3	92.92425	-0.28972	0.567305	3.72E-04	0.018183
Itgb1bp1	134.1939	-2.14737	0.852057	3.72E-04	0.018183
Ficd	66.9918	2.462766	0.976571	3.76E-04	0.018237
Bub3	520.4872	-1.30759	0.488373	3.75E-04	0.018237
Pik3cg	1416.418	-1.40805	0.535875	3.75E-04	0.018237
Armcx5	48.0711	1.855798	0.712598	3.77E-04	0.018238
Raly	508.5153	2.971717	1.223149	3.85E-04	0.01858
Dnajc16	303.304	1.740477	0.674523	3.89E-04	0.018697
Psmg3	73.88594	-1.68646	0.654275	3.94E-04	0.018904
Gimap3	94.78069	-1.90318	0.750661	3.96E-04	0.018929
Aasdhppt	255.4899	2.342448	0.941565	3.98E-04	0.018997
Crkl	191.8703	1.662023	0.641715	4.01E-04	0.019052
Ccdc6	231.7617	2.165357	0.867009	4.07E-04	0.019245
Txnl4b	47.04037	1.773924	0.684648	4.07E-04	0.019245
Fth1	1237.206	1.803926	0.705696	4.08E-04	0.019245
Smarcal1	240.1086	1.852319	0.727678	4.11E-04	0.019339
Btg2	2294.228	0.993463	0.361155	4.19E-04	0.019469
Mllt11	166.7779	-1.89519	0.754491	4.16E-04	0.019469
Sema4b	215.4739	-1.56255	0.60796	4.19E-04	0.019469
Polr1c	51.41648	1.850518	0.720689	4.16E-04	0.019469
Mbd1	114.9661	1.386659	0.526578	4.18E-04	0.019469
Ppp2r1a	404.8032	1.617555	0.630378	4.29E-04	0.019848
Atp6ap1	1780.455	-1.16806	0.437416	4.32E-04	0.019947
Wipf2	293.6184	1.763718	0.69654	4.41E-04	0.020315
Orm2	30.65763	2.649	1.057583	4.47E-04	0.020511
Parvb	148.866	2.599821	1.077048	4.48E-04	0.020511
Trem3	124.8257	3.055772	1.291257	4.49E-04	0.020511
Zmat2	894.1886	-1.22837	0.467062	4.54E-04	0.020725
Dnm1l	681.989	1.472956	0.570807	4.57E-04	0.02079
Efemp2	94.83286	-0.21302	0.433419	4.58E-04	0.02079
Irgm2	157.5886	-1.52721	0.600723	4.63E-04	0.020906
Tmem18	174.3492	-0.30003	0.590829	4.63E-04	0.020906
Mrps27	77.21776	1.613265	0.634852	4.68E-04	0.021073
Ebf4	72.30137	1.46842	0.569873	0.000471	0.02113
Tmppe	102.5572	-0.22219	0.445501	4.72E-04	0.02113
Fbxw2	539.4981	-1.43002	0.56228	4.77E-04	0.021296
Snx9	102.6596	1.856496	0.745859	4.79E-04	0.021344
Slc35a4	115.7721	2.159775	0.885714	4.80E-04	0.021344
Nat8l	101.2301	2.107352	0.861903	4.82E-04	0.02137
Entpd2	31.23438	-2.57276	1.068293	4.88E-04	0.021531
Foxk1	216.9555	-1.75391	0.710085	4.88E-04	0.021531
Zfp942	259.901	1.601701	0.636863	4.90E-04	0.021561
Lamtor2	283.6946	3.321397	1.460101	4.96E-04	0.02161

1700094D03Rik	47.71223	2.236998	0.916406	5.00E-04	0.02161
Rnpc3	256.2707	-1.42665	0.563879	5.05E-04	0.02161
Pex14	65.15235	1.693715	0.677569	5.05E-04	0.02161
Vamp8	1866.085	-0.91132	0.332517	5.02E-04	0.02161
Tmem135	962.0208	1.258977	0.486362	5.11E-04	0.02161
AB124611	178.1139	2.629332	1.119572	5.07E-04	0.02161
Prss42	17.96771	2.108596	0.813804	5.09E-04	0.02161
Ccdc88a	865.5171	1.354447	0.527387	5.03E-04	0.02161
Dvl2	89.14957	2.776883	1.178	4.97E-04	0.02161
B3galt4	72.85228	3.652813	1.599114	5.10E-04	0.02161
Mrpl14	57.19471	1.755483	0.702135	5.01E-04	0.02161
Gpr108	482.9364	-2.70538	1.172165	4.97E-04	0.02161
Rbm4	30.05416	1.783695	0.700412	4.99E-04	0.02161
Ddb1	559.9838	1.907637	0.775536	5.04E-04	0.02161
Ubtd1	85.37841	3.505782	1.533833	5.07E-04	0.02161
Tgif1	325.037	1.477929	0.583812	5.20E-04	0.021961
Myl2	40.15019	1.587283	0.625733	5.22E-04	0.021973
Pecr	70.41547	1.545864	0.614719	5.28E-04	0.022127
Cetn2	107.1177	1.653035	0.665702	5.28E-04	0.022127
Isoc1	335.0808	2.013387	0.834531	5.31E-04	0.022196
Fbxo48	50.10419	-1.61644	0.651424	5.35E-04	0.022322
Rragd	191.0401	1.621983	0.656096	5.41E-04	0.022494
Rnf111	1320.858	1.792382	0.731482	5.43E-04	0.022494
Nubp2	305.8555	-1.40946	0.562588	5.44E-04	0.022494
Gm17018	215.4092	-2.62652	1.149749	5.43E-04	0.022494
Castor1	107.6242	-0.14936	0.368767	5.52E-04	0.022785
Spred1	659.401	1.466727	0.585122	5.54E-04	0.022807
Atad3a	433.3915	-2.07411	0.882457	5.58E-04	0.022893
Slc35a2	102.1833	-1.66223	0.681822	5.63E-04	0.022958
Fgfr3	463.9246	-0.16381	0.380719	5.63E-04	0.022958
E030018B13Rik	35.01226	1.903602	0.773142	5.62E-04	0.022958
Fndc5	54.29682	1.585453	0.640984	5.83E-04	0.023727
Amd2	112.2909	1.995621	0.841032	5.86E-04	0.023759
Gp1ba	124.825	-0.26161	0.507232	5.87E-04	0.023759
Prelid2	80.99714	1.669149	0.683579	5.89E-04	0.02379
Flot1	240.6344	1.757479	0.731669	6.03E-04	0.024293
Ago4	303.3408	1.355089	0.543459	6.05E-04	0.024329
Dnajc24	139.1764	1.861831	0.785806	6.21E-04	0.024792
Tceanc2	231.1638	-2.09876	0.911266	6.21E-04	0.024792
Gzma	236.7795	-0.15461	0.372874	6.19E-04	0.024792
Cmss1	147.3301	1.655368	0.686074	6.24E-04	0.024861
Fam131a	141.6703	3.570307	1.670935	6.29E-04	0.024998
Klhl11	142.6364	-0.25724	0.499116	6.30E-04	0.025009
Galnt12	292.7777	-1.69468	0.715402	6.35E-04	0.025074
Prpf38a	176.0791	-1.34507	0.545518	6.34E-04	0.025074
Mrpl44	57.21821	-1.27764	0.511664	6.37E-04	0.025082

Fxyd1	46.50081	2.064321	0.872836	6.38E-04	0.025097
Id3	120.9961	2.822956	1.275162	6.50E-04	0.025517
Nup133	304.6957	1.354721	0.548506	6.58E-04	0.025766
Pml	171.6648	1.572884	0.655431	6.61E-04	0.025807
C2cd4c	168.4671	-0.25251	0.490713	6.73E-04	0.026238
Eif5	1662.575	-1.25243	0.507074	6.76E-04	0.02627
Kcmf1	546.5026	-1.73636	0.745876	6.78E-04	0.026288
Phf11b	230.9121	2.806165	1.282388	6.80E-04	0.026288
Cox8a	190.528	-1.76318	0.75762	6.80E-04	0.026288
Tusc1	24.00549	-2.12103	0.912755	6.89E-04	0.026449
Usp5	324.8327	-1.42126	0.590715	6.86E-04	0.026449
Mettl23	157.9845	2.449562	1.09818	6.89E-04	0.026449
Pld2	210.2467	-1.33495	0.54955	6.93E-04	0.026555
Pdcd6	291.184	2.324751	1.040604	7.02E-04	0.026818
Mlc1	156.6955	2.216369	0.988513	7.18E-04	0.027397
Naa80	92.20719	-1.40839	0.58915	7.30E-04	0.027732
Daxx	282.6868	-0.32964	0.669644	7.30E-04	0.027732
A430005L14Rik	17.89346	1.914209	0.780944	7.39E-04	0.027765
Dyrk4	258.0165	1.677623	0.720571	7.40E-04	0.027765
Mesd	262.9088	1.885775	0.82553	7.41E-04	0.027765
Slc22a17	161.9855	2.280066	1.024322	7.34E-04	0.027765
Sap30bp	430.0343	1.730252	0.745945	7.34E-04	0.027765
Hps6	71.01419	3.424218	1.621794	7.40E-04	0.027765
Egfl7	86.3461	-0.24424	0.476698	7.49E-04	0.02803
Agfg2	386.0867	-1.49196	0.636357	7.52E-04	0.02808
Cln6	260.4653	2.401073	1.098013	7.54E-04	0.028099
Snrnp35	100.4009	2.95614	1.389863	7.57E-04	0.028132
Map2k5	252.8085	1.329388	0.552597	7.65E-04	0.028321
Tmed9	299.836	1.284736	0.530386	7.65E-04	0.028321
Setd3	850.565	-1.39408	0.59081	7.71E-04	0.028492
Lage3	123.873	2.568898	1.188858	7.76E-04	0.028526
Nap1l2	46.84649	2.833281	1.296815	7.74E-04	0.028526
Dut	175.7468	-0.25496	0.494297	7.77E-04	0.028529
Rbpjl	508.3839	-0.17486	0.390513	7.81E-04	0.028533
Cyth2	85.11059	1.510765	0.641494	7.80E-04	0.028533
Srp68	162.699	1.648627	0.714465	7.87E-04	0.028706
Hey1	89.7294	-0.30689	0.603447	7.95E-04	0.028924
Syvn1	87.45009	1.692699	0.73839	8.08E-04	0.029356
Ube2l6	29.27338	-1.87107	0.82616	8.16E-04	0.02951
Xlr4a	73.95566	3.227481	1.558748	8.17E-04	0.02951
Sclt1	451.3805	1.264522	0.528264	8.19E-04	0.02951
Tapbp	928.9951	1.59619	0.694386	8.18E-04	0.02951
Fxyd5	515.8379	1.309136	0.550347	8.24E-04	0.029649
Slc35e2	540.0927	-1.77869	0.798648	8.28E-04	0.029668
Cwc27	256.3342	-1.70617	0.759704	8.30E-04	0.029668
Tmem191c	101.1833	-0.25169	0.488515	8.29E-04	0.029668

Ccdc32	92.28231	-1.44635	0.622492	8.32E-04	0.029672
Azi2	418.8476	1.34699	0.570212	8.34E-04	0.029672
Tmem168	306.9169	-1.44092	0.622875	8.36E-04	0.0297
Spry2	40.39122	1.50378	0.638728	8.38E-04	0.029712
Rab43	183.8137	2.569229	1.2205	8.44E-04	0.029851
Gipc1	36.47769	2.513121	1.145796	8.47E-04	0.029927
Nek3	270.927	2.10443	0.964044	8.52E-04	0.030034
Imp4	224.6281	1.349839	0.574004	8.55E-04	0.030058
Mmp14	557.0722	2.095444	0.960523	8.58E-04	0.030118
Slc35a1	319.7245	2.048461	0.938796	8.69E-04	0.030421
Eif3c	1097.096	-1.29829	0.553462	8.70E-04	0.030421
Tmem218	185.3888	2.419176	1.146406	8.81E-04	0.030731
Impact	415.726	-1.44441	0.632461	8.93E-04	0.031091
Tubb4b	68.04737	3.030751	1.481267	9.02E-04	0.031285
Tpm2	52.64775	1.801942	0.805975	9.04E-04	0.031285
Ptges3	703.3123	1.852581	0.842017	9.05E-04	0.031285
Ksr1	118.6019	1.996551	0.916805	9.05E-04	0.031285
Bag1	367.7055	2.053469	0.95862	9.32E-04	0.032129
Ccr2	924.9432	1.353077	0.585595	9.35E-04	0.032181
Sh2d3c	101.2448	1.352534	0.583994	9.47E-04	0.03241
Zic2	34.82901	2.064688	0.938881	9.49E-04	0.03241
Peak1	545.7426	-1.40986	0.62207	9.48E-04	0.03241
Sp7	25.43096	2.620841	1.196779	9.47E-04	0.03241
Eva1a	79.79153	1.801061	0.82158	9.63E-04	0.032697
Ifitm1	72.52066	2.781839	1.366512	9.62E-04	0.032697
Arl11	64.74018	2.803144	1.367526	9.60E-04	0.032697
Srp14	103.2861	2.878456	1.439345	9.65E-04	0.032713
Gnao1	335.6464	1.828411	0.841482	9.68E-04	0.032749
Gm4924	256.3642	-1.42759	0.633901	9.72E-04	0.032832
Gle1	297.1369	-1.43427	0.63803	9.76E-04	0.032838
Erp44	340.3345	1.658804	0.753423	9.76E-04	0.032838
AI837181	173.6249	1.942085	0.909585	9.91E-04	0.033262
Dad1	241.1837	1.860673	0.86659	1.00E-03	0.033508
1700001C19Rik	98.06469	-0.21401	0.433048	0.001003	0.033535
Mphosph6	101.6446	-1.71825	0.798198	0.001017	0.033885
Utp23	76.39453	2.24608	1.077795	0.001017	0.033885
Rpl7a	568.6913	2.127604	1.017264	0.00102	0.033926
Ppm1f	76.20363	1.670969	0.764903	0.001034	0.034337
Letmd1	544.9499	-1.85748	0.886423	0.001044	0.034577
Mtss1	979.7283	1.185657	0.508468	0.001048	0.034643
Hmox1	91.32033	-1.78863	0.8424	0.001057	0.03488
Upk1b	126.1747	1.405896	0.626724	0.001061	0.034944
Ndufb2	184.7832	1.33862	0.592567	0.001066	0.035007
Zfhx2	177.2018	-1.40982	0.635619	0.001065	0.035007
Zfp553	60.7454	2.099781	1.00445	0.001072	0.035108
Repin1	99.3012	2.064975	0.99466	0.001083	0.03542

B3gat2	116.7427	2.370993	1.180084	0.0011	0.035608
Atg4a	99.07307	1.287237	0.567016	0.001101	0.035608
Wnt4	122.5827	-0.22931	0.453225	0.0011	0.035608
Pus1	37.11902	1.529668	0.684963	0.001095	0.035608
Cep164	415.299	1.691216	0.78908	0.001091	0.035608
Zfp672	282.2073	2.211209	1.091243	0.001095	0.035608
Pheta1	181.8412	3.825158	2.250425	0.001103	0.035624
Eif4a3	157.3353	2.828335	1.479087	0.001109	0.035752
Serpinh1	82.24921	3.020748	1.587313	0.001116	0.035848
AI467606	82.24617	2.351002	1.169968	0.001116	0.035848
Nr1h3	269.1692	3.33464	1.874084	0.001129	0.036006
Commd8	1351.398	1.068087	0.454192	0.001128	0.036006
Fkbp6	59.74501	2.273302	1.11773	0.001128	0.036006
Yars2	133.497	2.195057	1.08576	0.001127	0.036006
Dnajb5	63.46052	1.331359	0.591922	0.001135	0.036066
H2bc6	181.9173	-1.57823	0.739746	0.001135	0.036066
Disp1	179.7308	-1.79983	0.874256	0.001163	0.036868
Znrd1	143.7964	2.174577	1.082254	0.001166	0.036901
Ccdc58	95.56238	2.11748	1.049142	0.001178	0.037225
Zic5	147.4808	2.050694	1.015206	0.001186	0.037334
Slc16a13	47.84011	3.106077	1.626048	0.001186	0.037334
Mrps36	106.4984	2.551967	1.32285	0.001188	0.037334
Mrps21	112.011	3.256192	1.812759	0.00119	0.037341
Mrps15	451.8811	2.194436	1.104655	0.0012	0.037572
Brd3os	26.78766	-2.50884	1.273231	0.001219	0.038118
Slc16a1	145.4727	1.316614	0.597115	0.001222	0.038118
Xylt2	82.10588	1.325108	0.60023	0.001231	0.038291
Rce1	26.22474	1.677869	0.771297	0.00123	0.038291
Smyd2	46.25191	1.788199	0.858369	0.00125	0.038783
Snrnp25	90.77662	-0.17652	0.391492	0.001252	0.038783
Atp6v1g1	284.3488	2.225631	1.144608	0.001259	0.038834
Smad3	539.8484	-1.21738	0.549994	0.001259	0.038834
B4galt6	630.4574	1.160436	0.513956	0.00126	0.038834
Edn1	33.1386	-1.32077	0.599377	0.001268	0.039003
Hmgcr	381.8811	-1.2005	0.542989	0.001282	0.039368
Trim45	267.767	-0.31717	0.625055	0.001289	0.039469
Svbp	26.66687	1.608607	0.742031	0.001288	0.039469
Trim30b	227.3988	1.425652	0.668388	0.001303	0.039821
Cops5	1283.834	1.526494	0.728611	0.001331	0.040608
Myl6	350.0398	1.811446	0.903918	0.001338	0.040673
Ostf1	519.508	1.447987	0.685999	0.001336	0.040673
Chst2	129.4171	1.153404	0.520089	0.001399	0.042468
Slc40a1	1071.621	1.189733	0.536341	0.001402	0.042471
Prrg2	120.9247	-2.01891	1.064338	0.001419	0.042912
Unc13d	128.6904	1.654287	0.820707	0.001433	0.043262
Atp1a1	540.3822	-1.43194	0.696115	0.001441	0.043424

Caprin1	1279.686	-1.37968	0.666088	0.001452	0.043684
Hipk1	673.8315	1.359115	0.648011	0.001467	0.044079
Sh3tc1	88.08976	1.252067	0.582763	0.00148	0.044266
Pirb	285.1644	1.67075	0.83864	0.00148	0.044266
Fkbp11	96.6514	2.474156	1.368028	0.001481	0.044266
Hdc	216.995	1.522665	0.750488	0.00151	0.044993
Nudt1	58.41365	2.245179	1.202085	0.001512	0.044993
Ms4a6b	610.4062	1.460344	0.710366	0.001513	0.044993
Sec22b	1079.453	-1.22831	0.582886	0.001536	0.045607
Cab39	539.0882	-1.18826	0.558443	0.001545	0.045627
4933436I01Rik	18.95046	-1.43662	0.684545	0.001542	0.045627
Serf1	72.69784	2.651396	1.509883	0.001543	0.045627
Sowahc	1312.995	1.070329	0.481277	0.001555	0.04585
Slc12a7	210.2446	1.213792	0.569061	0.001561	0.045964
Neurod6	63.36965	-1.9829	1.065122	0.001567	0.046042
Tlcd2	126.8414	-2.03327	1.112011	0.001573	0.046064
Nhlrc2	319.6407	1.322778	0.636681	0.001572	0.046064
Cox11	38.77524	2.112664	1.108979	0.001579	0.046169
Cyb5d2	173.7361	1.663604	0.850963	0.001606	0.046896
Fdxr	119.0149	2.363192	1.338538	0.001618	0.047158
Gpt2	194.6398	1.977999	1.066371	0.001624	0.047256
Zdhhc4	115.3091	1.231092	0.583406	0.001634	0.047481
Mrfap1	1319.805	1.344123	0.657831	0.001655	0.047989
Klhl15	115.3084	-1.25838	0.609043	0.001667	0.048274
Slc25a27	183.3467	1.568431	0.800083	0.001671	0.048323
Timp3	280.3597	-1.77043	0.956701	0.001692	0.048753
Tirap	220.3864	1.864995	1.003215	0.00169	0.048753
Med9	79.3237	2.272507	1.286431	0.001704	0.049028
BC031181	216.616	-1.46385	0.748056	0.001713	0.049197
Edf1	89.27053	2.381544	1.378962	0.001721	0.049358
Ly6c2	84.95334	1.660135	0.865846	0.00173	0.049518
Esam	175.6821	-0.19243	0.406969	0.001736	0.049625
Gm19935	134.3745	2.364526	1.3851	0.001748	0.049875
Dlx1	66.74606	2.346834	1.355836	0.001766	0.049914
Acot9	156.5224	2.024047	1.131077	0.001762	0.049914
Erp29	2340.779	-0.84544	0.367467	0.001764	0.049914
Ptov1	309.6359	2.269781	1.317554	0.001756	0.049914
Mcm5	116.4884	-1.38391	0.698366	0.001757	0.049914
Otub1	146.4147	1.365769	0.679925	0.001763	0.049914

Appendix 4

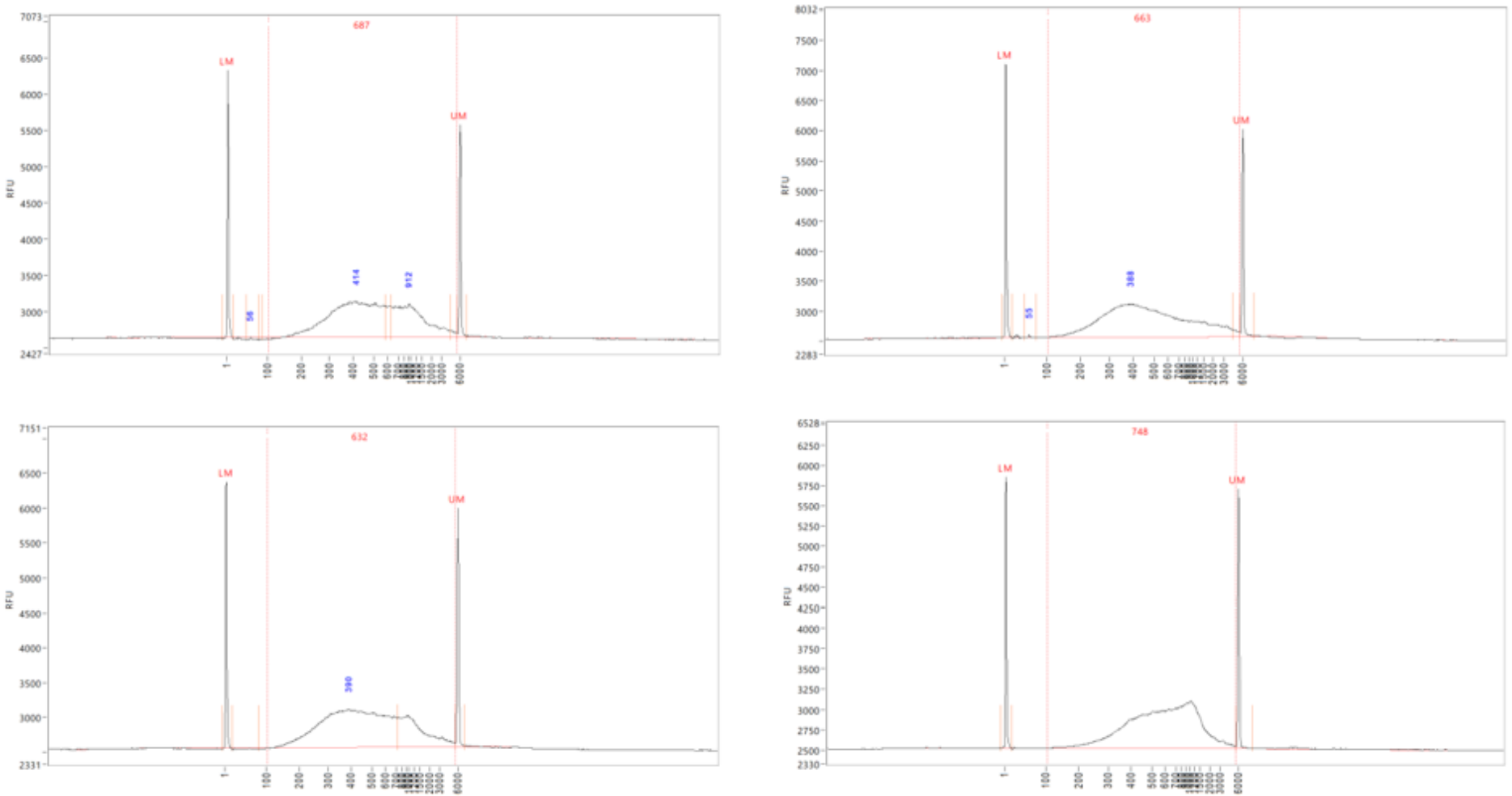

Appendix 4: Fragment analysis of generated libraries.

Appendix 5

Appendix 5: Differentially expressed genes (DEGs) in Syk x APP x Cre-ERT mice compared to Syk x APP animals when treated at 16 weeks.

Gene	baseMean	log2FoldChange	lfcSE	pvalue	padj
Cables2	157.9105106	2.383577312	0.390662468	4.78E-11	8.21E-07
Tmx1	215.7869057	1.698510988	0.285247503	9.69E-11	8.32E-07
Gtf2f1	131.6034031	3.423297268	0.624976907	1.11E-09	6.34E-06
Dnttip2	140.8451856	1.886427585	0.348153973	2.87E-09	1.23E-05
Lrpap1	259.364443	2.119559906	0.399836618	4.36E-09	1.50E-05
Egfl8	20.38927041	4.707997838	0.906509208	5.60E-09	1.60E-05
Slc25a35	60.33110146	2.017000259	0.458976748	6.43E-08	0.000157686
Tmem240	42.8038149	2.367844258	0.548854488	4.11E-07	0.000882478
Plscr3	226.7070002	2.983297333	0.741150579	5.28E-07	0.001007768
Polr1c	114.0577884	2.074797638	0.499343039	7.44E-07	0.001278773
Piezo1	121.8896073	1.958054913	0.463758931	9.69E-07	0.001386569
Wdr5b	105.4811507	1.995956422	0.485579043	9.08E-07	0.001386569
Ngdn	101.3469752	2.584148499	0.628177855	1.27E-06	0.001679583
Zfp775	79.85953528	2.604195927	0.724437317	1.66E-06	0.001887945
Ipo4	56.6081144	2.678596804	0.761872673	1.76E-06	0.001887945
Ccl7	160.8629499	-0.038522231	0.120507786	1.54E-06	0.001887945
Yif1a	46.99787231	2.568233828	0.652394359	2.71E-06	0.002733851
Paqr4	42.74937693	3.344401528	0.903223955	6.44E-06	0.006149281
Otud4	437.2062303	-1.02022906	0.273181546	9.55E-06	0.008204741
Tmem106c	112.0216913	1.896132085	0.526912965	9.10E-06	0.008204741
Speer4d	31.34046448	1.362626255	0.375881809	1.09E-05	0.008565927
Tbcb	100.6113559	1.747750881	0.493716856	1.10E-05	0.008565927

H1f0	206.6587317	2.626049749	0.834815619	1.27E-05	0.009497604
Lzic	88.69831162	2.036443	0.655920607	1.66E-05	0.011914304
Phax	114.102251	1.628422658	0.489785147	1.82E-05	0.012481989
Zfp687	100.6689624	1.245772077	0.383641885	2.67E-05	0.014153897
Cd72	26.83214547	-2.249513247	0.647763247	2.42E-05	0.014153897
Mark4	101.5249516	1.944160642	0.665766823	2.46E-05	0.014153897
Thap11	88.83691784	1.758202847	0.528963268	2.53E-05	0.014153897
Borcs8	33.40359897	2.231995746	0.681634152	2.48E-05	0.014153897
Cln5	304.2325505	-1.558439829	0.52235418	2.39E-05	0.014153897
Leo1	111.9096333	1.651430003	0.531356417	2.72E-05	0.014153897
Arap3	1198.831656	0.837714176	0.249866116	2.70E-05	0.014153897
Chmp5	262.2859862	-1.63977766	0.483394155	3.15E-05	0.015923946
S100a9	290.0068591	1.631392314	0.514328675	3.71E-05	0.018208072
S100a13	94.01914628	1.856789715	0.672231012	3.98E-05	0.018995325
Dusp18	83.26750306	2.032377011	0.641333918	4.13E-05	0.019192485
Glg1	429.3807438	1.013829309	0.318748667	4.41E-05	0.019938517
Plpp3	424.9692414	1.347545562	0.428591762	4.91E-05	0.021370382
Gm21083	42.05096606	1.581384152	0.492431763	4.98E-05	0.021370382
Arhgap1	95.3808837	1.216148887	0.412300513	5.83E-05	0.023477501
Gm21190	45.12802712	1.225503888	0.391971632	5.82E-05	0.023477501
Fbxw17	95.69905706	-1.640851654	0.516028596	5.88E-05	0.023477501
Rbbp9	77.73573815	1.36528849	0.469414793	6.38E-05	0.024900205
Arrdc4	111.1681582	-1.576580807	0.502296872	6.83E-05	0.025942392
Srr	54.97499707	1.078077479	0.359361068	6.95E-05	0.025942392
Fxr1	377.2006021	1.336163201	0.441359361	7.23E-05	0.026416991

Mospd1	45.05407263	-1.473293113	0.493805356	8.47E-05	0.028576235
Jade3	85.90488461	-1.295794936	0.426102195	8.15E-05	0.028576235
Tomm7	137.7424318	-1.326288381	0.425257513	8.35E-05	0.028576235
Sumo3	371.8271652	1.270787771	0.421048972	8.50E-05	0.028576235
Polr1h	97.94374045	1.603359845	0.55093737	8.65E-05	0.028576235
Rhno1	78.97562866	1.631229679	0.702021064	9.32E-05	0.029760744
Axl	206.4960812	-1.220383116	0.410040958	9.35E-05	0.029760744
Porcn	29.6455316	1.787808184	0.635980281	9.88E-05	0.029832925
Pmf1	65.10087819	-0.139868198	0.362528448	9.90E-05	0.029832925
Ifit3	96.53782765	-1.893506289	0.684789091	9.87E-05	0.029832925
Gstz1	219.4588214	-1.177345433	0.383165643	0.000102923	0.030484591
Timm10	98.33835604	-0.064333908	0.139671787	0.000112953	0.0319735
Ctla2a	41.98922885	-1.590457495	0.567889724	0.000113533	0.0319735
Dusp5	27.78624707	-1.569649383	0.515385536	0.000109819	0.0319735
Lcmt2	46.41810416	1.560502731	0.576131318	0.000120873	0.032698672
Ap1m1	132.2454888	2.009154178	0.734178561	0.000118697	0.032698672
Rnf135	185.1888299	1.448628163	0.540409344	0.000121818	0.032698672
Mllt11	96.63157342	1.744222692	0.756102242	0.000130457	0.034478809
S100g	39.6774863	2.229062149	0.86199515	0.00014331	0.037301985
Atg101	166.4120481	1.463616629	0.606479455	0.000151903	0.038948411
nan-ENSMUSG00002075981-	17.48111007	1.92346593	0.894125444	0.000155907	0.039387147
Mcm9	225.6945598	1.238379828	0.457417217	0.000163491	0.040704451
Derl2	355.6839038	1.062426774	0.380514738	0.000166329	0.040819632
Mmrn2	40.51114536	-1.429565817	0.537198049	0.000172669	0.041778696
Gm10354	45.07897002	1.044681279	0.374356151	0.000193481	0.044317355

Coq5	63.10575461	1.366123363	0.538343292	0.000191532	0.044317355
Otx2	31.69848141	-1.520647398	0.54884939	0.000187898	0.044317355
Vps28	208.5746898	1.407864481	0.592157464	0.000191402	0.044317355
Gm9758	29.56498119	1.163928033	0.416851127	0.000198044	0.044765652
Snapc5	84.44720861	1.514409432	0.650124249	0.000201685	0.044996632
Alpl	74.10710932	-0.068956117	0.14494852	0.000207557	0.045572789
Otud3	81.50445867	2.488907096	1.031964018	0.000209573	0.045572789
Unc119b	69.55539268	2.226673205	0.869369043	0.0002367	0.04958871
Gatd3a	88.78827765	-0.045713417	0.123994458	0.000233434	0.04958871
Smim15	235.0347764	1.715499738	0.654326009	0.000236013	0.04958871
Aph1a	70.25081351	-1.282928035	0.461166404	0.000240384	0.049750238
Rbm22	233.1019251	-1.389437575	0.687145549	0.000243263	0.049750238